Fun With Ferrocene

Synthesis of Polyiron Complexes Using 1,1'-Diaminoferrocene Based Ligands

by

Fraser Stanley Pick

B.Sc.(H) Chemistry, University of Alberta, 2010

A THESIS SUBMITTED IN PARTIAL FULFILLMENT
OF THE REQUIREMENTS FOR THE DEGREE OF

Doctor of Philosophy

in

THE FACULTY OF GRADUATE AND POSTDOCTORAL STUDIES
(Chemistry)

The University of British Columbia
(Vancouver)

July 2017

Abstract

Reactions of an amidophosphine supported ditantalum tetrahydride, $([NPN^{Si}]Ta)_2(\mu\text{-}H)_4$ and CO_x (x = 1, 2) were studied and all products were fully characterized. Selective deuteration allows for the production of two deuterated isotopomers which were used in low temperature NMR and GC-MS experiments in order to support a computationally determined mechanism.

Iron and cobalt complexes of a ferrocene linked bis(phosphinoamide) were synthesized and characterized by X-ray crystallography and Mössbauer spectroscopy. The cobalt complex contains a Co–Fe bond that was absent in the all-iron complex. The Co–Fe bond was further studied using DFT calculations, which suggest that the bond is comprised of donation from the iron center to the cobalt center (Fe $\rightarrow$ Co) and back donation from the cobalt center to antibonding orbitals in the ferrocene backbone (Co $\rightarrow$ fc*). A putative nickel complex supported by the same bis(phosphinoamide) ligand underwent a reductive elimination of the amidophosphine groups forming a new P-N bond.

Reactions between the aforementoned iron complex and H_2, CO_2 and other electrophiles were studied and the products of these reactions were fully characterized. The products of these reactions show that the iron phosphinoamides can cooperativley activate a variety of bonds without changing the oxidation state at

iron. Upon reduction, the iron complex forms an Fe–Fe bond while remaining in a high spin state. The cleavage of the N=N double bond of azobenzene was achieved under photolytic conditions using the same iron phosphinoamide and is thought to involve formation of a putative iron imido which migrates to the phosphinoamide groups. Due to the tendency of iron phosphinoamides to activate substrates using ligand cooperativity, an alternative ligand using amidophosphine donors was syntheisized and initial coordination studies were performed.

Lay Summary

Coordination chemistry is the study of metal complexes containing a metal center and a ligand. A ligand is a molecule which protects and supports the metal center. Some of these metal-ligand complexes function as catalysts, which make chemical transformations more energy efficient and in some cases reduce the amount of waste produced in certain chemical reactions. Enzymes found in all living things, are biological catalysts and typically they contain more than one metal center. Often those metal centers are iron. These enzymes can perform impressive chemical transformations beyond the abilities of metal-ligand complexes made by scientists. In this dissertation we attempt to simulate some of the chemical transformations facilitated by enzymes in nature by designing new iron complexes that contain more than one iron center.

Preface

Section 2.1 is from Ballmann, J.; Pick, F. S.; Castro, L.; Fryzuk, M. D.; Maron, L. *Organometallics* **2012**, *31*, 8516. My contributions were the design and execution of the isotopic labeling studies, characterization of **2.1-d_{12}** and complete characterization of **2.4**. The original discovery of **2.4** was made by Dr. Joachim Ballmann, the manuscript was written by Prof. Michael Fryzuk and the DFT calculations were performed by Ludovic Castro under the supervision of Prof. Laurent Maron. Section 2.2 is from Ballmann, J.; Pick, F. S.; Castro, L.; Fryzuk, M. D.; Maron, L. *Inorg. Chem.* **2013**, *52*, 1685. My contributions were completing the characterization of **2.5**, and attempting to observe predicted intermediates by low temperature NMR monitoring. The inital discovery of **2.5** was made by Dr. Joachim Ballmann, the manuscript was written by Prof. Michael Fryzuk and the DFT calculations were preformed by Ludovic Castro under the supervision of Prof. Laurent Maron. The computational details for sections 2.1 and 2.2 are available at pubs.acs.org.

Section 3.1 is from Pick, F. S.; Thompson, J. R.; Savard, D. S.; Leznoff, D. B.; Fryzuk, M. D. *Inorg. Chem.* **2016**, *55*, 4509. J. R. Thompson and D. S. Savard recorded the Mössbauer and VT-SQUID data respectively for compounds **1.50**, **3.2**, **3.3** and **3.4**. All synthesis and DFT calculations were preformed by F. S. Pick. The manuscript was written by F. S. Pick with contributions from M. D. Fryzuk

Section 4.2 is a manuscript which will be submitted for publication. All synthesis were preformed by F. S. Pick and the manuscript was written by F. S. Pick with contributions from M.D. Fryzuk. The syntheses of **4.8** and **4.9** in section 4.3 were performed by an undergraduate student, Garrion Hicks, under the direct supervision of F. S. Pick.

Table of Contents

List of Tables

List of Figures

List of Schemes

List of Abbreviations

Cp Cyclopentadienyl

DFT Density Functional Theory

ECP Effective Core Potential

fc ferrocene

GC-MS Gas Chromatography Mass Spectrometry

HMDSO Hexamethyldisiloxane

HOMO Highest Occupied Molecular Orbital

HS High Spin

IRC Intrinsic Reaction Coordinate

LS Low Spin

LUMO Lowest Unoccupied Molecular Orbital

ORTEP Oak Ridge Thermal Ellipsoid Plot

NBO Natural Bond Order

NMR Nuclear Magnetic Resonance

ppm Parts Per Million

TEM Transmission Electron Tomography

TOF Turnover Frequency

VT Variable Temperature

Acknowledgments

First and foremost I would like to thank Prof. Mike Fryzuk for allowing me the opportunity to work in his lab and for the guidance he has provided throughout my degree. To all of the group members I have crossed paths with, Kyle, Nathan, Brian, Truman, Lee, Alyssa, Nick and Amanda, it has been a pleasure working alongside you. In addition I have had the pleasure of working with many outstanding post-doctoral fellows Yogi, Dominik, Thomas, Vince, Rich and Tiko. You have all a taught me a great deal.

The work herein would not have been possible without the excellent support staff at the University of British Columbia. In particular Dr. Brian Patrick (X-ray), Ms. Anita Lam (PXRD), Ms. Maria Ezhova (NMR), Dr. Paul Xia (NMR), Mr. Marshal Lapawa and Mr. Ken Love have been generous with their time throughout my degree.

I have become a practitioner of density functional theory, and a small fraction of that work is included in this thesis. I am indebted to JM, Aleks, Eric, and Damon for their never ending patience answering all of my questions.

Finally I would like to thank my family for their continual support of my education. To my parents Heather and Gary, grandparents Phyllis and Brian and siblings Petrina, Jolleen, Matthew, Trevor, and Kathleen thank you for you support and confidence in me. To Sonia, you have provided me with the love and strength to complete this chapter of my life and I will forever be thankful that you were there to support me. I could not have done it without you.

Chapter 1

Introduction

If I have seen farther it is by standing on the shoulders of Giants.
— Sir Isaac Newton

1.1 Base Metals

1.1.1 Economic and Biological Motivations

Small molecule activation and catalysis reside at the heart of synthetic inorganic chemistry. While noble metals (Ru, Os, Rh, Ir, Pd, Pt) have revealed tremendous capabilities that have revolutionized a variety of chemical based industries, the base metals (Fe, Co, Ni) have, until recently, received less attention.[1–6] The cost differential between the base metals and their heavier congeners, the noble metals, is striking. For example, iron is more than 2000 times cheaper than ruthenium, one of the least expensive noble metals (Table 1.1). In addition to their economic advantages, base metals have lower toxicity than the heavy metals of groups 8, 9 and 10. This is particularly useful in the pharmaceutical industry, as catalyst recovery does not have to be as rigorous when using the less toxic base metals.[7] With these advantages in mind, it is clear that replacing noble metal catalysts with

base metal catalysts is a worthwhile pursuit.

Table 1.1: Prices of group 8, 9 and 10 transition metals

Metal	Price ($ / kg)[a]	Abundance (ppm)[b]
Iron Ore	0.05	56 300
Ruthenium	1 350.00	0.001
Osmium	12 860.00	0.0015
Cobalt	23.76	25
Rhodium	23 467.46	0.001
Iridium	22 089.48	0.001
Nickel	8.83	24
Palladium	22 039.96	0.015
Platinum	31 342.77	0.005

[a]Three month averages in USD from the London Metal Exchange for base metals and the Engelhard Industrial Bullion Prices for noble metals (September 10th - December 10th 2016)
[b]Mass abundance taken from the CRC Handbook[8]

While the utilization of base metals offers substantial benefits in terms of both cost and environmental impact, noble metals continue to dominate in many streams of synthetic methodology, and with good reason. Catalysts based on noble metals are the gold standard in transformations such as C-H activation,[9–11] alkene metathesis,[12,13] hydrosilylation,[14,15] and a variety of cross-coupling reactions.[16,17] Precious metals offer numerous advantageous over base metal complexes: (i) Noble metals readily undergo 2e- reduction and oxidation events and many catalytic cycles[18–20] involve oxidative addition and reductive elimination steps, therefore, these cycles are readily accessed using noble metals. The tendency for iron and cobalt complexes to undergo one-electron redox events has traditionally impeded the utilization of their complexes in such catalytic cycles;[21] (ii) Noble metals form stronger metal-ligand bonds, when compared to base metals.[22–27] This allows for more stable complexes that are less prone to ligand redistribution, and eventual de-

composition; (iii) Noble metals are usually found in Low Spin (LS) electron configurations resulting in diamagnetic compounds for the common oxidation states, which allows characterization by routine Nuclear Magnetic Resonance (NMR) spectroscopy. In addition, some of the noble metals (^{195}Pt, ^{103}Rh) are spin active, providing additional spectroscopic handles. The paramagnetic nature of base metal complexes combined with their relative instability leads to a situation where base metal complexes are often very difficult to characterize, requiring multiple techniques and large amounts of material. It should be noted that paramagnetic NMR spectroscopy is available for some base metal complexes, however, the amount of information provided is limited; (iv) Finally, the dearth of soluble starting materials, both commercially available and reported in the literature, presents a challenge when synthesizing base metal complexes.[28,29] For these reasons the chemistry of the base metals is less developed than that of the noble metals.

Considering the limitations previously mentioned it may seem like folly to think iron, cobalt, and nickel could replace many of the noble metal systems we currently utilize. Indeed, the goals of exploring base metal chemistry should be more than simply replicating established reaction manifolds with base metals, but in addition, finding new reaction pathways that offer access to new transformations or selectivities. As is often the case, nature provides insight into what can be accomplished with these metals. Many impressive enzymatic transformations occur in enzymes containing a metallic cofactor and most often these cofactors contain multiple base metal centers. Examples include the [FeFe]hydrogenase family, the cytochrome P450 family, and [FeMo]nitrogenase whose principal cofactors contain 2, 1, and 7 iron atoms respectively (Scheme 1.1). The family of [FeFe]hydrogenases are excellent catalysts for proton reduction, out performing

platinum in terms of required overpotential and TON.[30] Cytochrome P450 is able to oxidize unactivated C-H bonds in hydrocarbons,[31] and [FeMo]nitrogenase is able to perform the complete reduction of dinitrogen to ammonia under mild conditions.[32,33] Clearly, in the enzymatic environment base metals can be used to perform complex and valuable transformations.

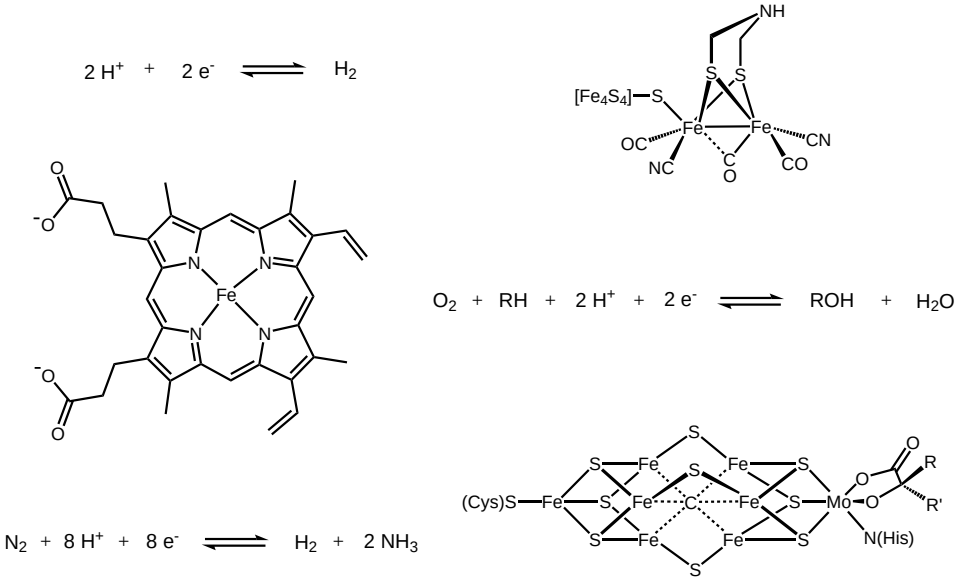

Scheme 1.1: (Top) Active site of [FeFe]Hydrogenase. (Middle) Heme cofactor, active site of cytochrome P450. (Bottom) Iron molybdenum cofactor (FeMoco), site of N_2 reduction in [FeMo]nitrogenase.

Enzymes with iron cofactors can be divided into two categories, heme and non-heme. Both types of cofactors illustrate biological examples of ligand design strategies, *vide infra*. Heme cofactors contain iron centers imbeded in porphyrin macrocycles like the cofactor for cytochrome P450 in Scheme 1.1. These non-innocent heme ligands allow the complex to take on a higher oxidation state than would normally be stable under biological conditions.[31] The non-heme cofactors

display a wide variety of structural motifs and supporting ligands but they typically contain multiple iron centers. One advantage of assembling multiple iron centers is the wide range of redox potentials available to the cluster in comparison to an isolated iron center. For example, the family of iron-sulfur clusters, which facilitate electron transfer in many proteins, is ubiquitous in biological systems and will not be reviewed here other than to point out that the [4Fe-4S] clusters have redox potentials ranging from -650 mV to +450 mV.[34] A second advantage of polynuclear systems is an increase in the number of possible coordination modes. For example, site-directed mutagenesis studies have suggested that the site of N_2 binding is a tetra-iron face of FeMoco.[35] This advantage of polymetallic binding has also been realized in synthetic molecular systems, *vide infra*. Nature assembles clusters of base metals or monomeric cofactors with redox active ligands to tune redox potentials, transfer electrons, and activate substrates; these concepts of polynuclearity and redox active ligands should be used as a guide for designing ligands for base metals.

Drawing on the insights provided by nature, discrete polynuclear base metal complexes are worthwhile synthetic targets. In the next sections we will look at some examples of mononuclear and polynuclear base metal complexes, however, it should be mentioned that heterogeneous catalysts containing base metals are also poised to utilize these same polynuclear advantages. Many researchers have been working on heterogeneous systems in recent years and, while difficult to study, these systems are typically more robust than their soluble molecular cousins. In order to gain insights about how polynuclear base metal complexes bind substrates we have chosen to study discrete homogeneous systems that are more amenable to characterization.

1.1.2 Iron Complexes: Catalysis and Small Molecule Activation

Discrete homogeneous complexes of iron have been shown to catalyze many important reactions including ethylene polymerization, alkene hydrogenation, ketone hydrogenation and transfer hydrogenation, and carbon-carbon cross coupling reactions. These systems contain a diverse array of ligand sets not so different from ligand sets employed by the 2nd and 3rd row transition metals. In this section, we will survey a few notable iron complexes suitable for catalysis and small molecule activation, finding commonalities that will guide future ligand design.

Hydrogenation of alkenes and ketones using base metals was reported as early as the 1960's using metal carbonyls such as $Fe(CO)_5$ and $Co_2(CO)_8$.[36–39] A few years later, transfer hydrogenations with complexes of the form $MX_2(PPh_3)_2$ were discovered[40] where M = Fe, Co, Ni and X = Cl, Br, I. However, all of these systems suffer from harsh reaction conditions, poor chemoselectivity and substrate scope. A breakthrough was made by Bianchini and co-workers when they found that they could catalyze the hydrogenation of terminal alkynes to alkenes under mild conditions (1 atm H_2 RT) using a tetraphosphine ligated iron(II) center, **1.1** in Scheme 1.2.[41,42] Years later, the same complex was shown to be active in transfer hydrogenation of arylalkynes producing styrene derivatives using cyclopentanol as the hydrogen source.[43] The Peters group modified the tetraphosphine ligand framework by removing one P-donor and replacing it with a borane, producing a neutral triphosphinoborane ligand and corresponding iron complex, **1.2**. This complex was able to hydrogenate alkenes to alkanes under mild conditions (1 atm H_2 RT) with Turnover Frequency (TOF) up to 15 h^{-1}.[44]

A major step forward in iron catalysis was the development of the bisiminopyri-

dine ligand. First reported by the Brookhart group, these ligands were coordinated to Fe(II) salts and the resulting complexes were the first iron based homogeneous catalysts for ethylene polymerization.[45] The Chirik group has since developed many iron complexes using these ligands. In regards to alkene hydrogenation, the reduced dinitrogen complex **1.3** is a hydrogenation catalyst with TOF up to 1814 h^{-1} for 1-hexene .[46,47] Not only was compound **1.3** a catalyst for direct alkene hydrogenation, it was also shown to oxidatively add carbon-carbon bonds using one electron from the metal one from the ligand.[48] A recent review sumarizes the reactivity of base metal complexes of bisiminopyridine ligands.[3] The bisiminopyridine ligand represents a synthetic example of a biological design strategy discussed in section 1.1.1, that is, pairing base metals with redox active ligands.

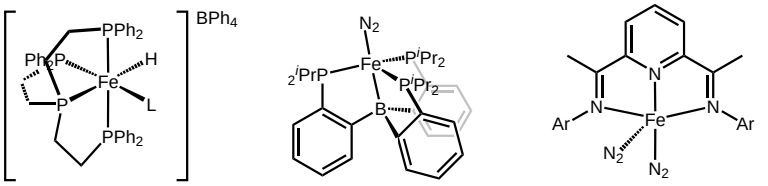

1.1 **1.2** **1.3**

Scheme 1.2: Selected alkene hydrogenation catalysts

Selective hydrogenation and hydrogen transfer reactions of ketones and aldehydes are important reactions for both bulk and fine chemical processes.[49] In recognition of their contributions to the field, half of the 2001 Nobel prize was split between Professor Ryoji Noyori and Professor William Knowles for their work on catalytic asymmetric hydrogenation reactions, with the other half awarded to Professor Barry Sharpless for his work on catalytic asymmetric oxidations. Professor Knowles pioneered the use of rhodium complexes containing chiral auxiliary

phosphines. In particular compound **1.4** catalyzes the asymmetric alkene hydrogenation step for the production of L-DOPA.[50] Professor Noyori pioneered the use of a ruthenium catalyst (**1.5**) containing asymmetric phosphines as auxiliary ligands and a diamine ligand which acts cooperatively in the outer-sphere hydrogenation of ketones.[51] Efforts toward using iron in place of ruthenium in these transformations have been ongoing for a number of years. Beller and co-workers found that by adding phosphine ligands, the *in situ* iron carbonyl catalysts were much more effective in transfer hydrogenation.[52] The groups of Casey and Beller made significant improvements to the selectivity, functional group tolerance and reaction conditions by using Knölker-type complexes,[53,54] compounds **1.6** and **1.7** in Scheme 1.4, which are closely related to the organoruthenium Shvo complex.[55]

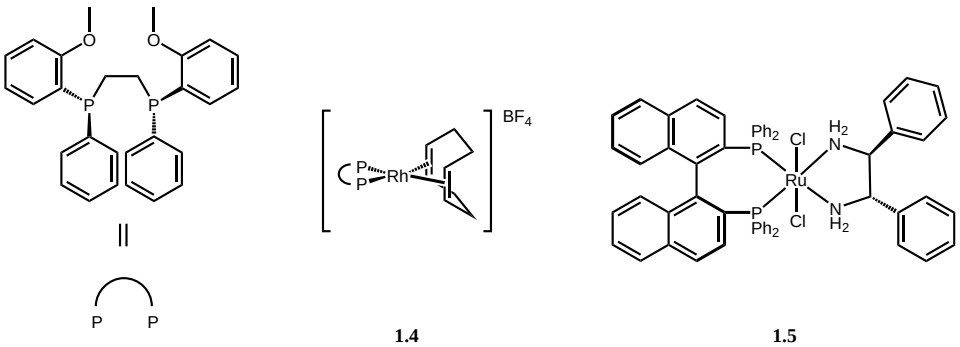

1.4 **1.5**

Scheme 1.3: Catalysts for asymmetric hydrogenation

Morris and co-workers have recently developed a family of tetradentate ligands containing phosphine, amine, and imine functionalities. These ligands are active catalysts for asymmetric hydrogenation of ketones.[56–58] A representitive example, **1.8**, is shown in Scheme 1.4. These complexes are reminiscent of **1.5** with two phosphine and two amine donors. In the case of **1.8**, all four donors are tethered producing a very stable compelx. In the Morris and Noyori systems previ-

ously mentioned, the dihydrogen molecule (or dihydrogen equivalent in the case of transfer hydrogenation) is split between the nitrogen donor and the iron center creating an Fe–H, N–H pair which then interacts with the incoming ketone.[59] We can see from these examples that when ligand cooperativity is a key component of the reaction mechanism iron can substitute for ruthenium quite readily, however, for the highly active species (**1.8** and **1.9**), tri- and tetradentate ligands must be used to overcome the lower stability of iron complexes. A new form of ligand metal cooperativity has recently been reported by the Milstein group. This new cooperativity is proposed to be driven by an aromatization-dearomatization cycle[60] and complexes including **1.9** (Scheme 1.4) are active catalysts for the hydrogenation of ketones[61] and carbon dioxide.[62] Deprotonation of these complexes occurs at the benzyl linker, to generate systems that can cleave dihydrogen between the iron center and the backbone of the ligand producing an Fe–H, C–H pair, like the one shown in compound **1.9**.

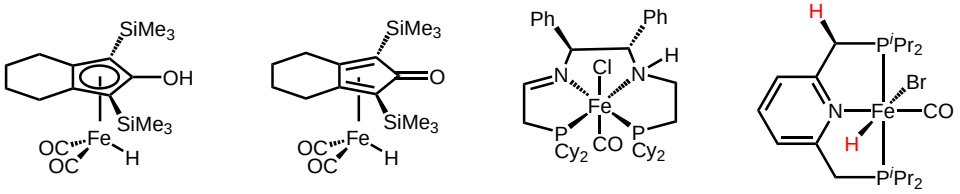

1.6 **1.7** **1.8** **1.9**

Scheme 1.4: Selected carbonyl hydrogenation catalysts

There has been increasing interest in using iron-based systems for activation and functionalization of small molecules including NO,[63] O_2,[64] and CO_2.[65] Of particular interest to the Fryzuk research group is the activation of N_2. The earliest report of an iron dinitrogen compound is from 1976.[66] Over the next two decades

additional examples were sparsely reported.[67–71] Only a few of these compounds were structurally characterized and for all examples the N-N bond lengths (1.102 Å- 1.139 Å) are not substantially elongated compared to free dinitrogen (1.0975 Å), indicating minimal activation upon binding to the metal center.[72] Another commonality between these early examples is that all of these species are LS with coordination numbers of 5 or 6. In the last two decades a number of High Spin (HS) iron dinitrogen complexes were reported with coordination numbers less than 5. We will now examine several examples of these low valent iron dinitrogen complexes and illustrate how they have led to progressively more activated dinitrogen and stoichiometric functionalization of the N_2 unit.

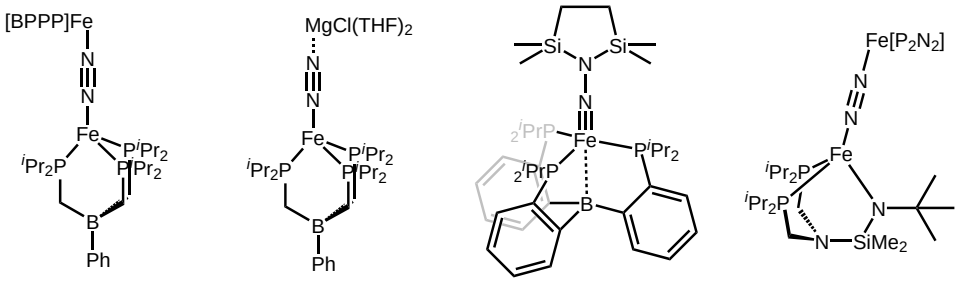

1.10 **1.11** **1.12** **1.13**

Scheme 1.5: Selected iron dinitrogen complexes with tetrahedral coordination geometries

The first tetrahedral iron compounds containing a dinitrogen ligand were reported in 2003 by Peters and co-workers (**1.10**) using the tripodal ligand $[PhB(CH_2P^iPr_2)_3]^-$.[73] In contrast to previously reported iron N_2 complexes, compound **1.10** displays a bridging end-on coordination mode for the N_2 ligand, and moderate activation (N–N = 1.171 Å). Interestingly, while **1.10** forms upon reduction of the iron chloride complex $[PhB(CH_2P^iPr_2)_3]FeCl$ with sodium, reduction with mag-

nesium leads to a monomeric end-on ate complex, **1.11**. This report represents a breakthrough in iron dinitrogen activation because treating compound **1.11** with MeOTf results in the formation of a nitrogen-carbon bond. A few years later a neutral ligand with *ortho*-phenylene linkers, $B(C_6H_4P^iPr_2)_3$, was utilized to form another dinitrogen compound, $[B(C_6H_4P^iPr_2)_3]Fe(N_2)$, which, when treated with 1,2-(dimethylchlorosilyl)ethane results in N_2 functionalization producing **1.12**.[74] Unfortunately, total N-N bond cleavage could not be achieved by further reduction of **1.12**. It should be noted that the Arnold group also developed an anionic tridentate ligand that showed a similar tetrahedral iron center and N_2 activation *via* a diiron system, compound **1.13**.[75] However, functionalization of the N_2 unit has not been reported for this system.

Moving to even lower coordination numbers, the Holland group has been developing iron complexes that bind, activate, and in some cases cleave N_2.[5] The ligand framework used in all of this chemistry contains a 1,3-diketiminato, NacNac, system, which can be sterically tuned by appropriate choice of N-aryl substituent.[76] Utilizing salt metathesis, three coordinate complexes of the type (NacNac)FeCl have been reported for a variety of NacNac derivatives. Upon reduction, these complexes bind dinitrogen in a bridging end-on coordination geometry illustrated by **1.14** in Scheme 1.6.[77] Interestingly, further reduction of this neutral complex yields the dianionic ate complex **1.15**, which shows even greater N-N bond elongation.[77] Attempts to functionalize the N_2 unit in **1.14** or **1.15** were unsuccessful as the complexes react by displacing N_2 and binding other neutral ligands such as PR_3, CO and C_6H_6.[78] Modifying the ligand architecture by reducing the steric bulk led to a different product. When complex **1.16** was reduced with potassium graphite, the trinuclear complex **1.17** was formed. In compound **1.17**, the N–N bond has been

completely cleaved by a 6-electron reduction, resulting in two nitrido ligands.[79] The first nitrido is bound by three (NacNac)Fe moieties and the second bridges two of the aforementioned centers and two potassium ions. A fourth equivalent of (NacNac)Fe is bound through chloride bridges to the potassium promoters; computational studies suggest that the potassium atoms play a role in the dinitrogen activation.[80] This result is hugely important as it shows that by tuning the steric profile of the supporting ligands, cluster formation can be encouraged and in these high nuclearity complexes the N-N bond of dinitrogen can be cleaved.

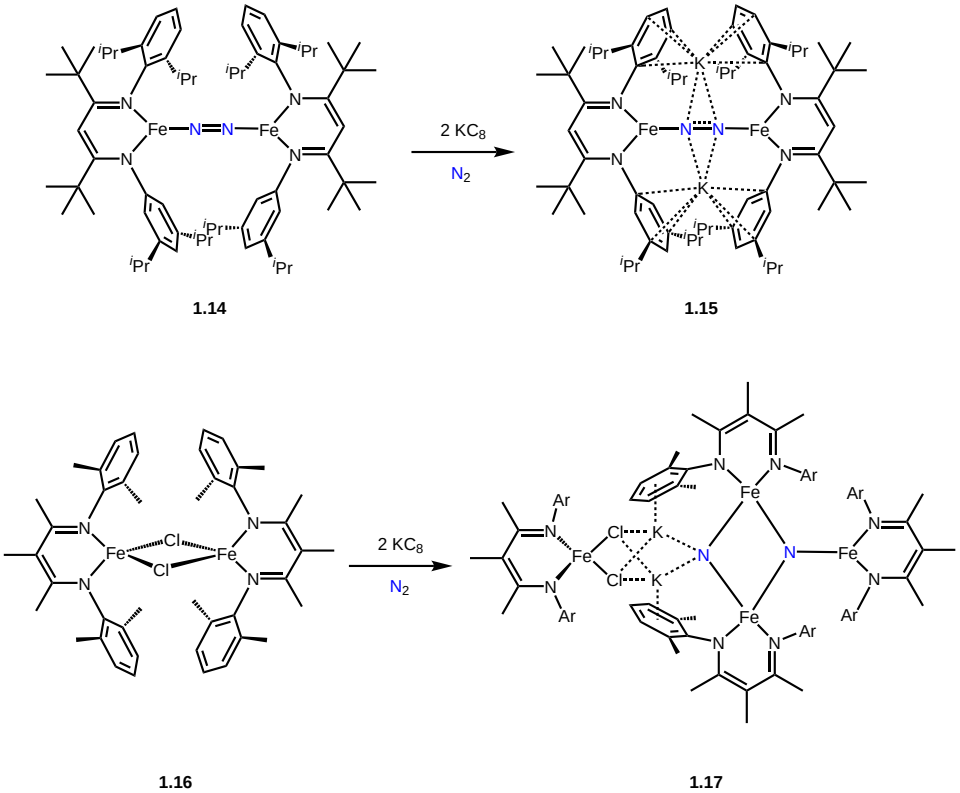

1.14 **1.15**

1.16 **1.17**

Scheme 1.6: Low coordinate iron complexes cleave dinitrogen with alkali metal promoters

To examine the effect of the reductant, MC_8 reagents were used where M = Rb, and Cs. These reagents have similar reduction potentials to KC_8 so the analogous trinuclear clusters would have been expected. For Rb, the analogous complex is obtained, however, using CsC_8 no N-N bond cleavage is observed and the product is a trinuclear dinitrogen complex with three equivalents of dinitrogen bridging the metal centers.[5] The different outcomes of reactions of **1.16** with MC_8 (M = K, Rb, Cs) suggest that these alkali cations play a crucial role in assembling the unobserved (NacNac)Fe(I) intermediates into polynuclear reaction sites. These reports from the Holland group show that high spin iron complexes with low coordination number and low oxidation states should be targets for dinitrogen activation. The fortuitous cluster formation templated by alkali metal cations suggests that polynuclear reaction sites are another fruitful avenue for investigation, and construction of more complex ligand sets could alleviate the need for spontaneous self assembly.

Recently, ligand scaffolds specifically designed for coordinating multiple metal centers have been gaining attention. These ligand sets have been used to systematically study metal metal bonding,[81–84]and to activate small molecules.[85–89] Most relevant to iron dinitrogen activation are the ligand sets developed by the Betley and Murray research groups. Both ligand sets consist of three donor pockets bound together such that the open coordination sites of each metal are pointed towards the center of the ligand scaffold. In the Betley system the ligand is hexaanionic and when three Fe(II) ions are installed the neutral compound displays short iron–iron distances, which are best described as weak interactions (**1.18** in Scheme 1.7). Compound **1.18** does not spontaneously react with N_2. However, treatment of **1.18** with azobenzene results in cleavage of the N–N double bond, producing compound **1.19** with two phenyl imido ligands.[90]

Betley 2013

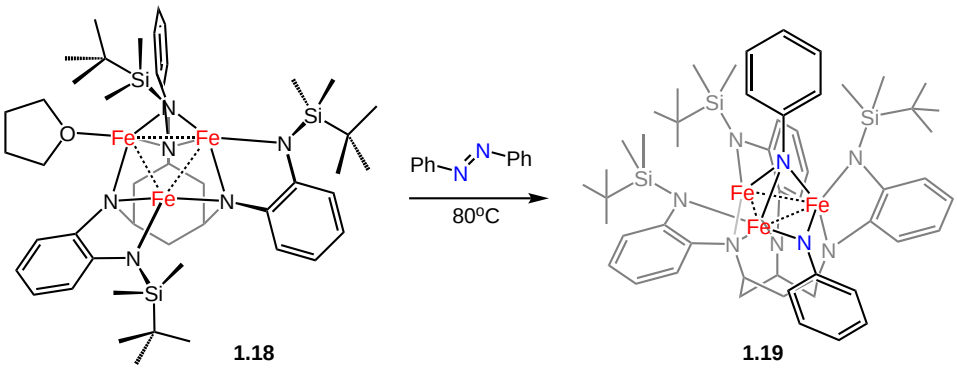

1.18 **1.19**

Murray 2015

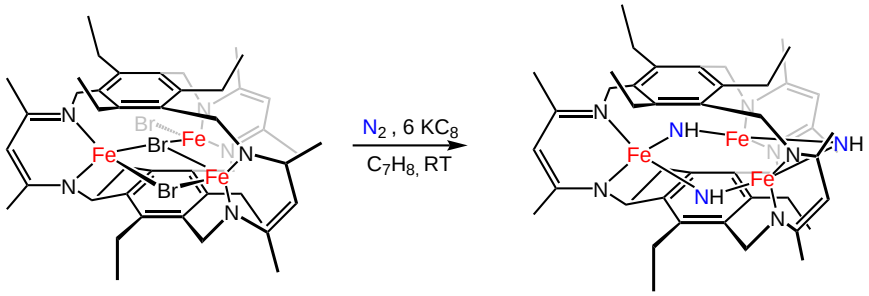

1.20 **1.21**

Scheme 1.7: Polynuclear iron complexes through ligand design

In contrast, the ligand set developed by the Murray group is a trianionic ligand that effectively tethers three NacNac ligands into a trigonal array. Based on reports from the Holland group, *vide supra*, this trigonal system should be competent in N_2 reduction. Indeed, reducing the iron bromide complex, **1.20**, results in complete N–N bond cleavage and formation of a complex containing three bridging imidos, **1.21**.[91] While the H atom source and mechanism of formation remain unclear, labeling studies have shown that these imidos originate from atmospheric nitrogen.[91] Both of the examples shown in Scheme 1.7 illustrate the utility of polynuclear com-

plexes.

Examining some of the iron complexes from above, a few design features are common: i) low-coordinate complexes allow for stronger substrate activation; ii) high-spin complexes display higher degrees of N-N bond elongation, although low-spin complexes are excellent hydrogenation catalysts; iii) non-innocent ligands can be helpful when promoting 2-electron chemistry in base metal complexes; and iv) polymetallic clusters are crucial for the cleavage of strong bonds such as the N-N triple bond in dinitrogen. When designing new ligands to be used for iron-based small molecule activation, these design features should be kept in mind. In the following sections we will look at previous ligand design in the Fryzuk group and introduce the phosphinoamide ligand.

1.2 Ligand Design

1.2.1 Ligand Design in the Fryzuk Group

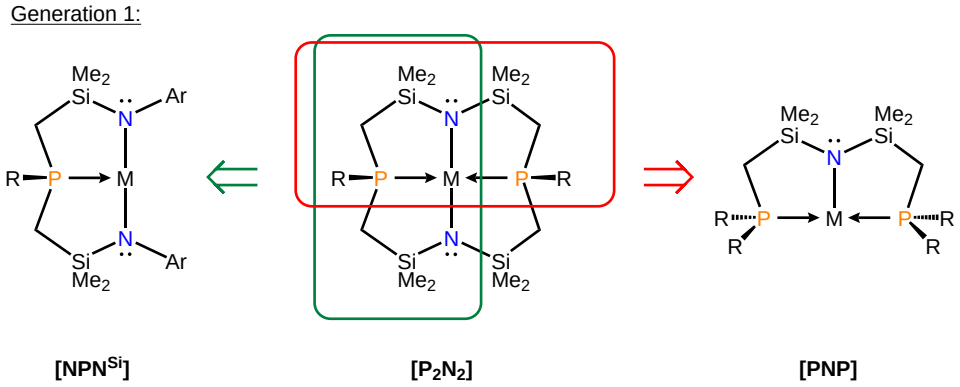

Figure 1.1: First generation ligand design in the Fryzuk group

Ligands designed in the Fryzuk group typically combine "hard" amido and "soft" phosphine donors into chelating arrays.[92] The central hypothesis is that us-

ing a mixed donor system allows for the formation of hard-soft acid-base mismatches, which affords a more reactive metal complex. For example, these hybrid ligands (Figure 1.1) have been coordinated to early and late transition metals and have resulted in the first examples of early metal-phosphine and late metal-amido linkages.[93,94] The first generation of hybrid ligands utilized silyl methylene linkers to connect the disparate donor environments. Three versions of the first generation ligands were investigated: a dianionic pincer **[NPN^{Si}]**, a monoanionic pincer **[PNP]**, and a dianionic macrocycle **[P$_2$N$_2$]**. Early transiton metal complexes of **[NPN^{Si}]** and **[P$_2$N$_2$]** have shown remarkable N_2 activation and the N_2 units can be hydrogenated[95] and functionalized[96–98] (Scheme 1.8). A problem with the first generation ligands was that the N-Si linkers in the the ligand backbone were labile and in many cases the ligand as well as the dinitrogen units were functionalized.

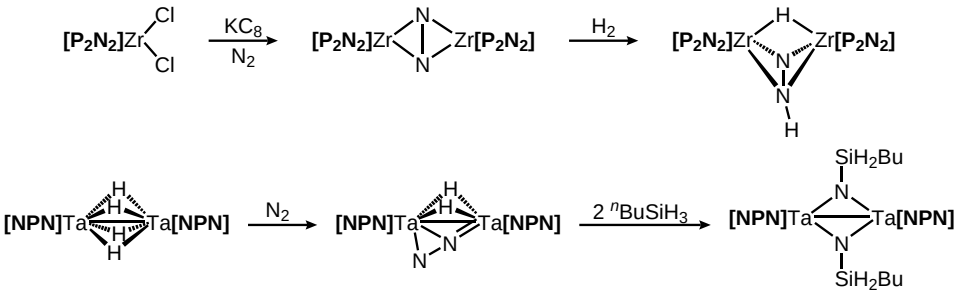

Scheme 1.8: Dinitrogen functionalization with hybrid ligands

To avoid ligand rearrangments, modifications were made to the linkers of the first generation **[NPN^{Si}]** ligands. Aryl **[^{Ar}NPN*]**,[99–101] alkenyl **[NPN^{cp}]**,[102,103] and *o*-thiophene **[NPN^{S}]**[104] linked amidophosphine ligands have been synthesized and coordinated to a variety of transition metals (Figure 1.2). In some cases dinitrogen complexes have been made, however, none of these complexes have been able to functionalize dinitrogen like the complexes of the first generation ligands. More-

over, none of these second generation ligands allowed for any kind of catalytic functionalization of dinitrogen. More recently, linkerless donor sets were studied in our lab. In particular, complexes of the group 3 and 4 metals were investigated for a variety of transformations. The following section will explore the history of the linkerless ligand sets and their incorporation into larger ligand scaffolds.

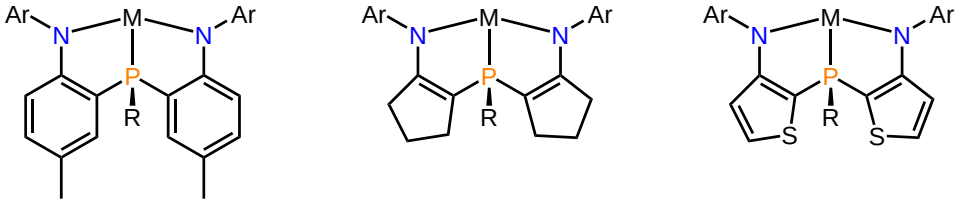

[^{Ar}NPN*] **[NPN^{cp}]** **[NPN^{S}]**

Figure 1.2: Second generation ligand design in the Fryzuk group

1.2.2 Phosphinoamides as Ligands

Neutral phosphine (P-C) and phosphite (P-O) ligands are ubiquitous P donors in organometallic chemistry, both as monodentate donors, and as part of a larger chelating ligand set. A new class of phosphine donor that is gaining increased attention is the phosphinoamine ligand containing a P-N bond.[105] These P-N bonds are relatively easy to construct from the appropriate amine and chlorophosphine in the presence of an external base (Scheme 1.9). For some sterically demanding derivatives an alkali amido precursor may be required.[105] These phosphinoamines have been used as ligands for late transition metals including a rhodium complex capable of catalytic hydroformylation.[106] Asymmetric phosphinoamines have been synthesized and the resulting copper complexes catalyze enantioselective nucleophilic addition to enones.[107]

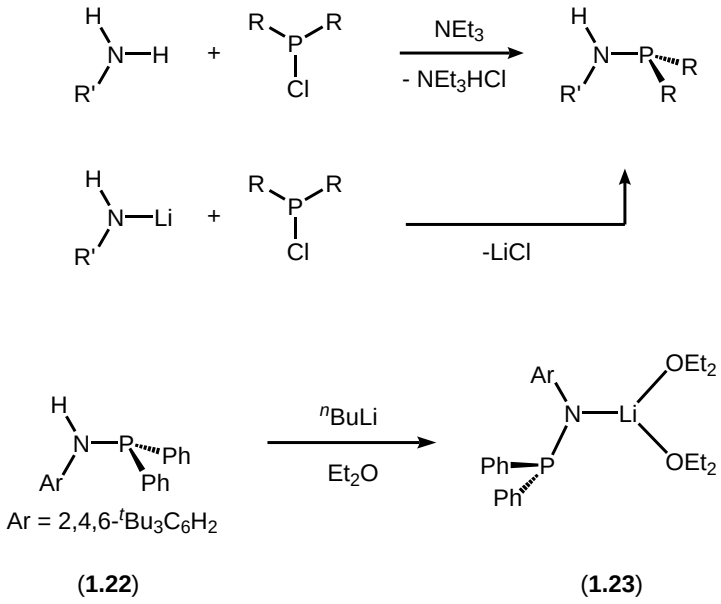

Scheme 1.9: Synthesis of phosphinoamides

More relevant to this thesis, phosphinoamines serve as precursors to the anionic phosphinoamide functional group. Treatment of the phosphinoamine (**1.22**) with alkyl lithium reagents generates the lithium phosphinoamide (**1.23**) as shown in Scheme 1.9. The amidophosphine anion has several important structural features. The first feature is the short P-N bond length in the $[RNPR'_2]^-$ anion. The short bond is due to a combination of phosphinoamide (**A**) and iminophosphide (**B**) resonance forms (see Figure 1.3). Computational modeling suggests that the phosphinoamide resonance structure (**A**) is the major contributor, except when particularly electron withdrawing groups are attatched to phosphorus.[108] The delocalization is best described as a nitrogen based lone pair donating into the σ^*_{PR} orbital. The N–P bond length in phosphinoamides ($\sim$ 1.70 Å) is substantially longer than the P=N double bond ($\sim$ 1.60 Å) in phosphinimines (also known as iminophosphoranes).

Due to the partial double bond character between the nitrogen and phosphorus atoms, *cis* and *trans* stereoisomers are possible (Figure 1.3). Computational studies suggest that the two stereoisomers are nearly degenerate when all steric bulk is removed, however, there is a significant barrier to interconversion (7.4 kcal/mol for H_2PNH^-).[108] There are four binding modes which have been observed for phosphinoamides. Both κ^1 - (N) and κ^1 - (P) coordination modes are possible. In addition η^2 - (NP) is common[109] and phosphinoamides have the potential to bridge two metal centers in the μ binding mode.[110,111]

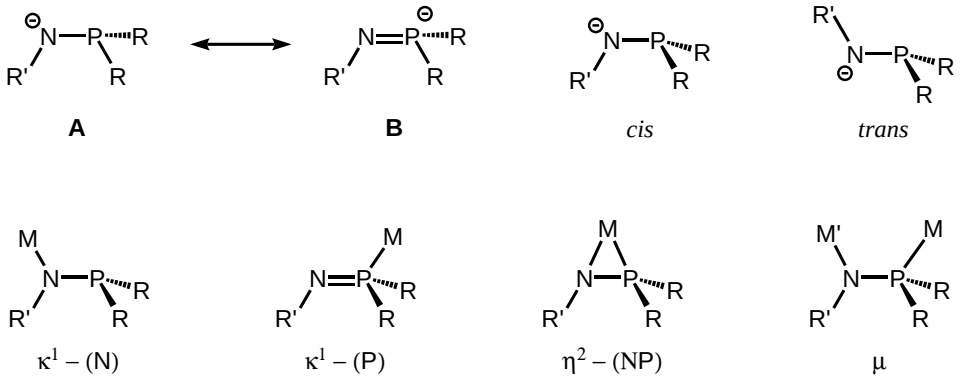

Figure 1.3: Resonance forms, stereoisomers and common binding modes of amidophosphines

Phosphinoamide complexes of rare earth metals have been reported by our group and others. Anionic 'ate' complexes can be formed by salt metathesis of lithium phosphinoamides with MCl_3 (M = Y, Yb, Lu),[112] however, neutral complexes are more easily accessed by protonolysis of metal alkyl precursors $M(CH_2SiMe_3)_3$ (M = Sc, Y) with phosphinoamines (See Figure 1.4).[109] Based on the highly symmetric ^{31}P NMR spectrum displaying a small $^2J_{PY}$ coupling, complex **1.24** is thought to have all four phosphinoamides bound κ^1 - (N) in solution. The

neutral compounds **1.25** and **1.26** were found to undergo deleterious ligand exchange reactions and therefore were not suitable for small molecule activation studies.

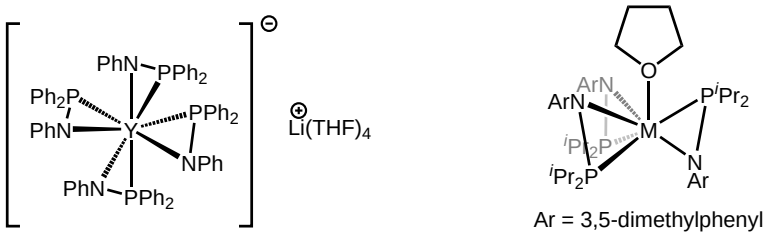

Figure 1.4: Phosphinoamide complexes of rare earth metals

Phosphinoamide complexes of the mid to late transition metals are more commonly dinuclear, displaying the μ-(NP) binding mode. Phosphinoamide complexes of chromium have been synthesized and can be dinuclear (**1.27**), or tetranuclear (**1.28**) depending on the stoichiometry of the reaction (Scheme 1.10). These chromium complexes are active catalysts for ethylene oligermization.[113] Reduction of the tetramer leads to a dinuclear Cr(I)/Cr(II) complex **1.29**, which is an ethylene trimerization catalyst.[114] Recently the Thomas group has extended the use of phosphinoamides, making dinuclear complexes of iron (**1.30**) and manganese (**1.31**).[111] The iron complex, **1.30**, can be reduced to give a mixed valent Fe(I/II) system, **1.32**, which is best described as a delocalized $[Fe_2]^{3+}$ unit. Compound **1.32** reacts with organic azides to produce the C_3 symmetric iron imido (**1.33**), however, no group transfer reactivity has been reported.[115]

Utilizing the disparate phosphine and amido donors, heterobimetallic complexes have been constructed using phosphinoamides. The Nagashima group pioneered the strategy of using phosphinoamide complexes of group IV transition

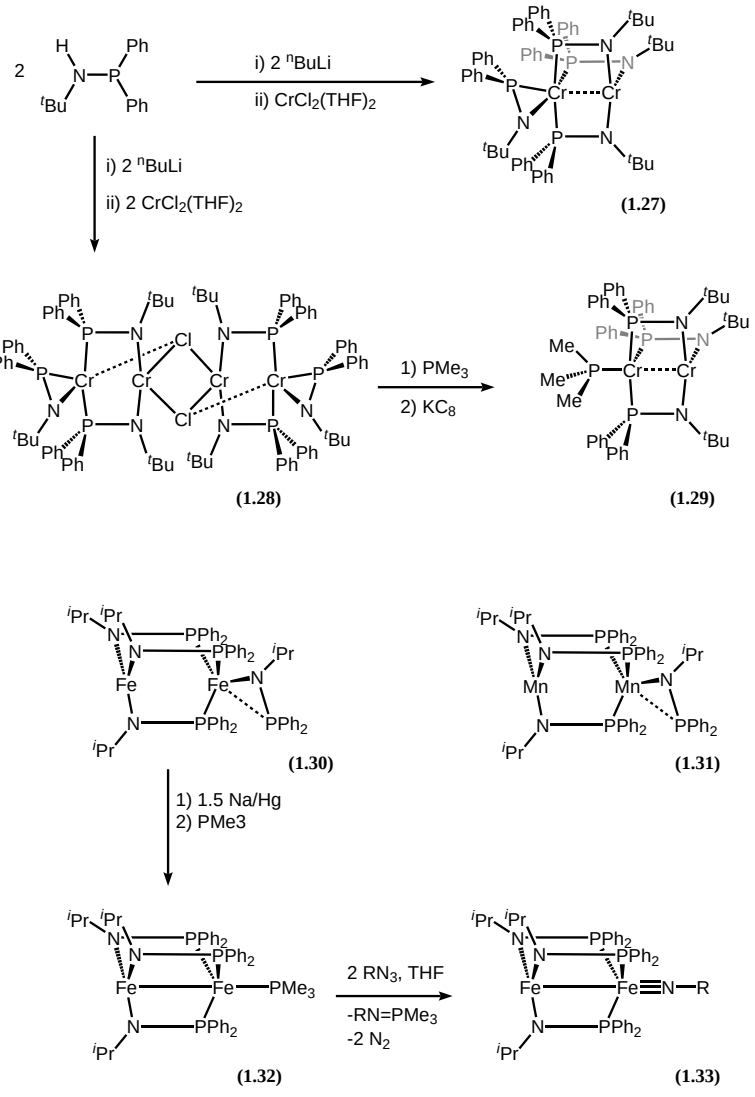

Scheme 1.10: Phosphinoamide complexes of the mid to late transition metals

metals as 'metalloligands'(ligands containing a metal atom) for late transtion metals. The first example of this strategy utilized the metalloligand (^{t}BuNPPh$_2$)$_2$TiCl$_2$ (**1.34**) to coordinate Pt(II) precursors forming heterobimetallics containing a Pt $\rightarrow$ Ti interaction, compound **1.35** in Scheme 1.11.[116] Later work from the Nagashima group extended this methodology to ruthenium, copper and molybdenum.[117,118] They were able to synthesize a platinum allyl complex, **1.36**, and show that the dative Pt $\rightarrow$ Ti interaction generates increased electrophilicity at the π-allyl moiety, *trans* to the titanium center.[119] Building off this methodology, the Thomas group has examined early-late heterobimetallics containing Co $\rightarrow$ Zr interactions **1.37**. This open shell system contains three amidophosphine ligands and binds dinitrogen to the cobalt center upon reduction, forming **1.38**.[110] If the reduction of **1.37** is performed under argon, compound **1.39** is obtained, which upon exposure to CO_2, cleaves one of the carbon oxygen bonds forming compound **1.40**.[120–122] It should be noted that **1.38** is a catalyst for the hydrosilyation of ketones.[123] The work by the Nagashima and Thomas groups illustrates the utility of phosphinoamides in constructing heterobimetallic complexes across the periodic table.

It is clear from the examples in Scheme 1.11 that phosphinoamides can be used to build early/late heterobimetallic frameworks. As discussed previously, we would like to be able to build polymetallic base metal complexes. Recently the Thomas group has shown that not only can these ligands form homobimetallic compounds of iron, *vide supra*, but heterobimetallics can be formed between iron and other mid transition metals.[124–126] These complexes are formed with control over the binding site for each metal, and there are no reports of metal or ligand scrambling within theses complexes. The Cr/Fe and V/Fe (**1.41** and **1.42**) complexes allowed for detailed study of the metal-metal multiple bond upon reduction and oxidation

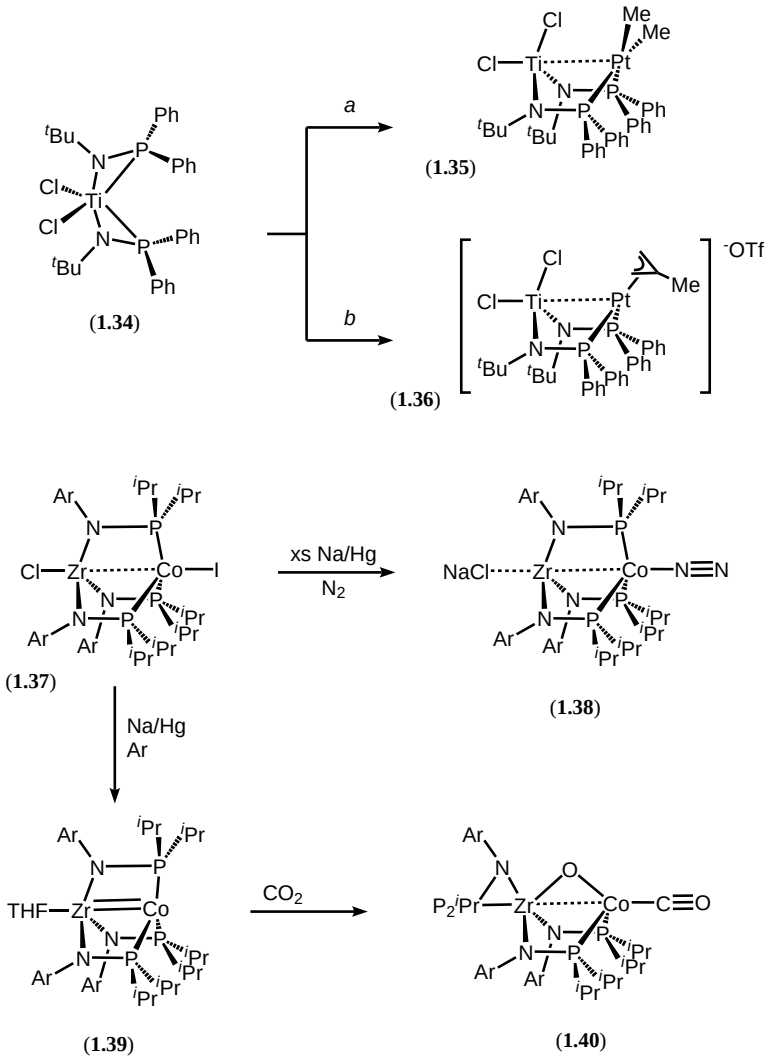

Scheme 1.11: Early/late heterobimetallic complexes of phosphinoamide ligands. Ar = 2,4,6-trimethylphenyl. [a]: $((PtMe_2)(\mu\text{ - }SMe_2))_2$, [b]: $[((CH_3)_2CO)_2Pt(C_4H_8)]OTf$

(**1.43**, **1.44**, **1.45**).[122] This work provides an excellent comparison to the Cr/Fe V/Fe heterobimetallics (amongst others) that have been developed in the Lu lab (See Scheme 1.12). We will not explore the systems developed by the Lu lab in detail because they do not employ phosphinoamide ligands.

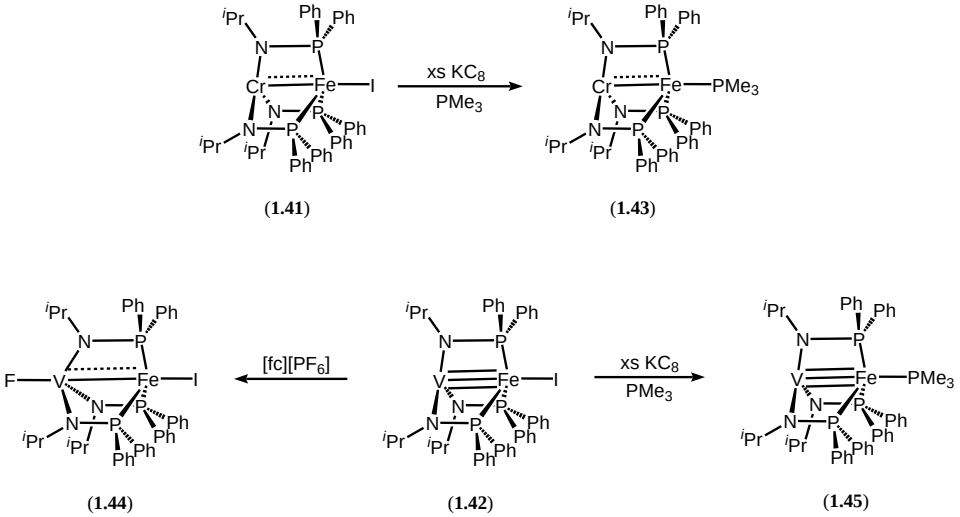

(**1.41**) (**1.43**) (**1.44**) (**1.42**) (**1.45**)

Scheme 1.12: Heterobimetallic complexes of phosphinoamide ligands.

1.2.3 Tethered Phosphinoamides

Phosphinoamide ligands are typically labile, easily interconverting between binding modes. This lability creates a situation where control of stoichiometry in $M(R_2PNR)_x$ compounds is difficult, and ligand redistribution is common.[109] In an effort to control the coordination modes and number of bound ligands, researchers have begun designing multidentate ligands containing multiple phosphinoamide groups. The Stephan group has developed bis(phosphinoamide) ligands with aliphatic linkers ($R_2PNH(CH_2)_nNHPR_2$) where n = 2 or 3. When mixed with nickel halides these ligands were found to coordinate nickel in the aminophos-

phine/phosphinoamide (κ^3-P,η^2-N,P; **1.46**) or bis(aminophosphine) (κ^3-P,C,P; **1.47**) coordination modes (Figure 1.5).[127] A second generation of these ligands were designed with a neutral amine donor tethering three aminophosphine donors. Ruthenium complexes of this tris(phosphinoamine) were synthesized and deprotonation of the complex leads to compound **1.48** containing one η^2 phosphinoamide and two phosphinoamine donors. This complex was shown to activate CO_2 cooperatively between the nucleophilic phosphorus atom and the electrophilic ruthenium center, and is an active catalyst for the hydroboration of CO_2.[128] A third iteration, again pioneered by the Stephan group, contained two phosphinoamine donors flanking a central thiol donor. Protonolysis with $Hf(CH_2Ph)_4$ led to the formation of compound **1.49**, which is the first example of a tethered bis(phosphinoamide) complex. This complex was found to activate CO_2 cooperatively, analogous to the ruthenium system.[129] However, no catalytic hydroboration was reported for this complex, presumably due to the stronger M-O bond in the hafnium system. The high degree of flexibility in the backbone of the ligands developed by the Stephan group has led to C-H bond activation in the case of nickel, and ligand dissociation in the case of ruthenium. However, an interesting feature of these systems is the nucleophilicity of the P atom in the phosphinoamides, and their ability to act cooperatively with a metal center to activate CO_2.

Our group has investigated the use of phosphinoamide ligands with rare earth elements and discovered that ligand redistribution was common.[109] In order to avoid this challenge we searched for an appropriate linker. Our attention soon turned to work done by the Arnold and Diaconescu groups which utilized 1,1'-diaminoferrocene based ligands such as $fc(NH_2)_2$,[130,131] $fc(NHSiR_3)_2$[132–135] and $fc(NHAr)_2$.[136] Using these ligands, complexes of zirconium and ruthenium could

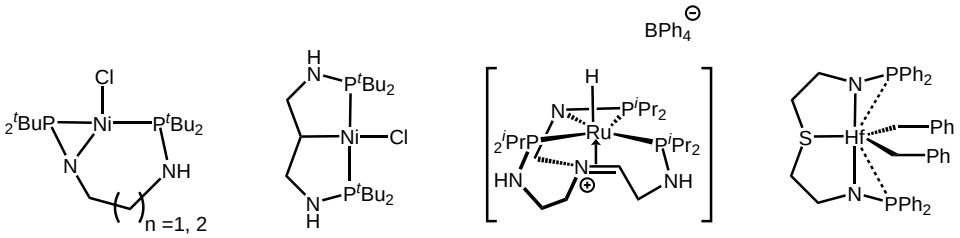

(**1.46**) (**1.47**) (**1.48**) (**1.49**)

Figure 1.5: Coordination modes of alkyl linked phosphinoamides

be developed, which were active catalysts for olefin polymerization and transfer hydrogenation, respectivley.[131,136] Utilizing the same ferrocene (fc) linker we constructed the bis(aminophosphine) ligand 1,1'-fc(NHP^iPr_2)$_2$ (**1.50**). With **1.50** in hand, a scandium alkyl complex, **1.51**, could be formed, via protonolysis. Unlike previous scandium alkyls supported by phosphinoamide ligands, compound **1.51** cleanly reacts with dihydrogen to produce a rare scandium hydride, **1.52**.[137] We wondered whether this bis(phosphinoamide) ligand set would be a good candidate for supporting polymetallic complexes of the base metals.

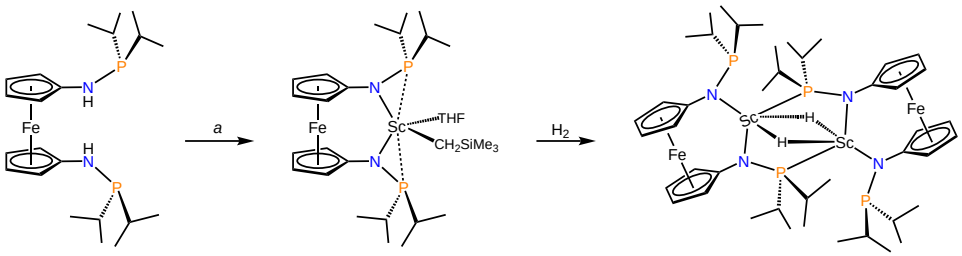

(**1.50**) (**1.51**) (**1.52**)

Scheme 1.13: Hydrogenation of a scandium alkyl. [a]: $Sc(CH_2SiMe_3)_3(THF)_3$

1.3 Scope of Thesis

Examining the bis(phosphinoamine), **1.50**, while considering the design features mentioned in section 1.1.2, we thought that this ligand would be useful for synthesizing polynuclear base metal complexes. Phosphinoamide donors have been shown to bridge multiple metal centers, including iron. The ferrocene linker provides a rigid backbone that will enable the controlled assembly of metal complexes containing only two phosphinoamide donors, yielding low coordinate complexes. In addition the ferrocene backbone is potentially redox non-innocent.[138] A direct N–M bond between this ligand set and an appropriate metal has the potential to react with hydrogen in a cooperative fashion, similar to the Noyori and Morris systems (Scheme 1.4).

This thesis will discuss the coordination chemistry of hybrid amidophosphine donors with transition metals. Chapter 2 contains mechanistic studies of reactions between a tantalum tetrahydride supported with the 1st generation **[NPN^{Si}]** ligands and C_1 sources, CO_2 and CO. Chapter 3 focuses on the synthesis of base metal complexes supported by the new ferrocene linked bis(phosphinoamide) ligand, **1.50**. Chapter 4 examines the reactivity of a dimeric iron complex with a wide array of small molecules. Chapter 5 discusses future directions for the compounds reported in this thesis as well as new ligand designs.

Chapter 2

Reduction of Carbon Monoxide and Carbon Dioxide by a Ditantalumtetrahydride

Education is what remains after one has forgotten what one has learned in school — Albert Einstein

2.1 Complete Reduction of Carbon Monoxide

2.1.1 Introduction

The analogy between carbon monoxide (CO) and dinitrogen (N_2) is often made to rationalize their relative abilities to be activated by transition metal complexes.[139] Even though these molecules are isoelectronic, the more polar CO is a much better ligand than N_2 largely because of the smaller energy gap between the Highest Occupied Molecular Orbital (HOMO) and Lowest Unoccupied Molecular Orbital (LUMO) for CO as compared to N_2, which allows better overlap of these orbitals with appropriate transition metal *d*-orbitals. In addition, unlike dinitrogen, carbon

monoxide undergoes migratory insertion processes, which are key to a number of industrial catalytic processes such as hydroformylation, Fischer Tropsch, and the acetic acid synthesis;[140] by comparison, the only industrial process that utilizes N_2 as a feedstock is the Haber-Bosch ammonia synthesis,[141] which does not involve any migratory insertion steps with intact dinitrogen.[142]

We recently described the facile activation of dinitrogen (N_2) by a dinuclear tantalum tetrahydride, ([NPN]Ta)$_2$(μ−H)$_4$ **2.1** to generate the side-on end-on di-tantalum dinitrogen complex, ([NPN]Ta)$_2$($\mu - \eta^2 : \eta^1$−N_2)(μ−H)$_2$ **2.2**.[143,144] As this N_2 complex displays a rich reactivity that results in E-N bond formation (E = B, C, Al, Si) and even N-N bond cleavage,[143] we wondered if a similar kind of activation process could be realized for carbon monoxide (CO) by reaction with tetrahydride **2.1** (i.e., formation of **2.3** in Scheme 2.1). What we discovered was that CO can be activated by an apparent series of migratory insertion processes involving **2.1** in a manner quite different from its isoelectronic analogue, N_2.

2.1.2 Results and Discussion

While the reaction of **2.1** with N_2 proceeds smoothly with excess N_2,[144,145] the corresponding reaction of **2.1** with CO requires stoichiometric addition of CO as excess carbon monoxide results in a complicated mixture of products. Addition of exactly 1 equiv of CO to **2.1** results in the formation of a dark brown solution from which red crystals could be obtained in reasonable yield (54%). The spectroscopic characteristics of the isolated material show that it is an unsymmetrical species with inequivalent phosphorus-31 nuclei (two sharp singlets at δ 20.2 and 12.1 in the $^{31}P\{^1H\}$ NMR spectrum) and a very complicated ^1H NMR spectrum with eight distinct silyl methyl groups, consistent with C_1 symmetry. These patterns alone

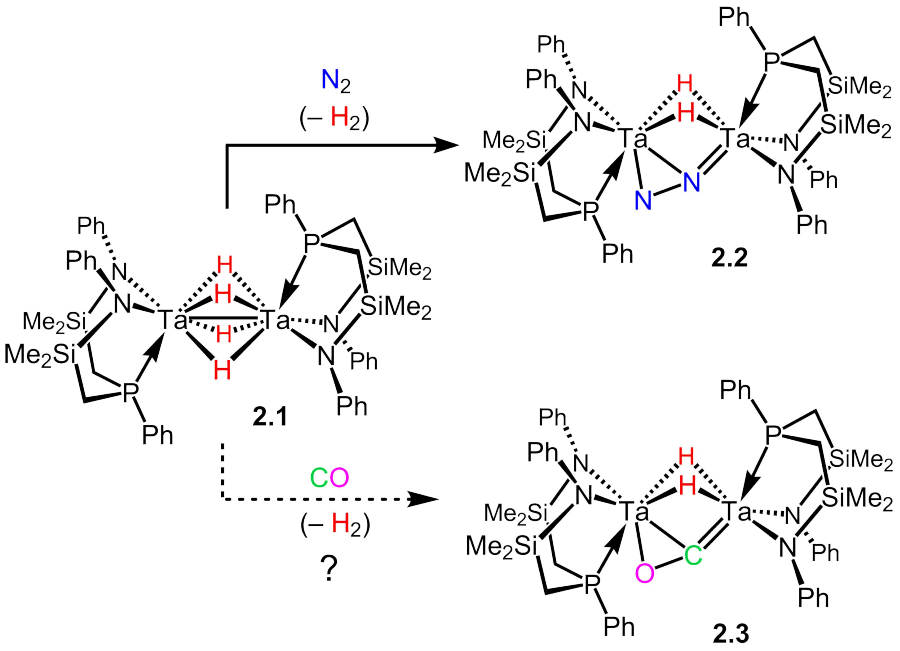

Scheme 2.1

made it clear that this product was not **2.3** (Scheme 2.1), the anticipated analogue of the side-on end-on N_2 complex **2.2**, as both species would have C_s symmetry. In particular, no peaks were observed in the ^{1}H NMR spectrum of the product in the downfield region between δ 8-18, which is diagnostic for a bridging hydride of the type $Ta_2(\mu\text{-H})_x$. Moreover, the aromatic protons displayed a complicated upfield-shifted pattern of four coupled resonances in the range of δ $4.8 - 6.4$. The use of carbon-13 labeled carbon monoxide (^{13}CO) was confusing as the isolated product did not display any isotope-enhanced peaks in the ^{13}C NMR spectrum. However, we did observe an intense peak at δ -4.5 when the solution and gas phase were carefully analyzed by ^{13}C NMR spectroscopy before separation of the product from the crude reaction mixture; this peak corresponds to $^{13}CH_4$. The reaction of

the polydeuteride (**2.1**-$\mathbf{d}_{12}$, *vide infra*) with 1 equiv of CO resulted in the formation of an isotopologue of the final product, whose upfield ^{1}H NMR resonance at δ 4.98 is absent. While a number of possible structures were considered, particularly in light of previous studies wherein upfield shifted aromatic proton resonances of a cyclometalated N-Ph unit were observed,[146] the isolation of suitable crystals for X-ray analysis provided an unequivocal answer.

As shown in Figure 2.1, the product **2.4** has a dinuclear structure and there is both a bridging hydride unit and a bridging oxo. Also interesting is the π-bound cyclometalated N-C_6H_4 group of one of the amido donors; this feature in **2.4** rationalizes the upfield shifted proton resonances observed as they are due to this unique cyclometalated ring. As a resonance for the bridging hydride was not detected in the range from δ -20 to +50 in the ^{1}H NMR spectrum, we suggest that it is buried under the aromatic resonances. Attempts to confirm this using the various deuterated forms of **2.1** (cf., **2.1**-$\boldsymbol{d}_{12}$ or **2.1**-$\boldsymbol{d}_x$) were inconclusive.

A mechanism for the formation of **2.4** is proposed in Scheme 2.2 that takes advantage of previous studies on the reaction of carbon monoxide with tantalum hydrides.[147–149] The structure of the initial adduct of CO with the tetrahydride, $\mathbf{Ta_2H_4{\bullet}CO}$, could not be detected and therefore its formulation is speculatively shown as a simple end-on CO bound to one of the Ta centers of the dinuclear tetrahydride. Subsequent migratory insertion generates the bridging η^2-formyl, $\mathbf{Ta_2H_3{\bullet}CHO}$, which is then converted to the methylene-oxy species, $\mathbf{Ta_2H_2{\bullet}CH_2O}$, via migratory insertion. The next step is a reductive ring opening of a ditantalamethylene oxy 4-membered ring to generate a coordinated methylidene and tantalum-oxo species. Another migratory insertion of the methylidene and one of the hydrides generates the methyl-μ-oxo hydride, $\mathbf{Ta_2H{\bullet}CH_3O}$, which upon

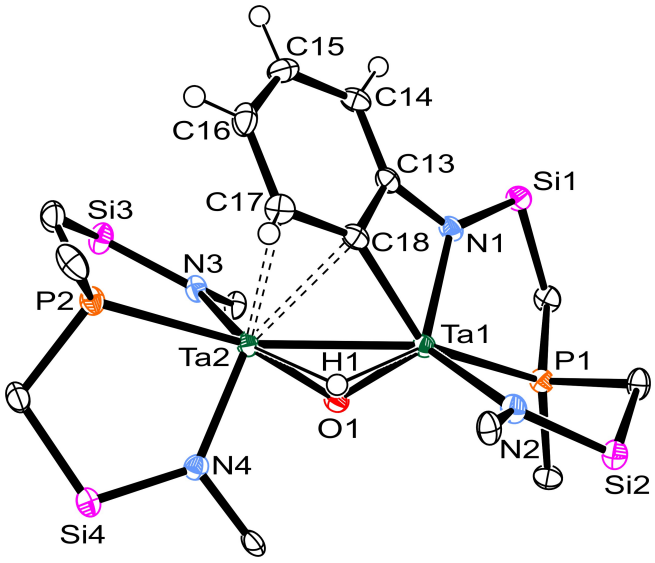

Figure 2.1: ORTEP diagram of **2.4** (silylmethyls omitted and only ipso carbons of the N- and P-phenyls are shown, except for the cyclometallated phenyl). Selected bond lengths (Å) and bond angles (°): Ta1-Ta2 2.7240(6), Ta1-C18 2.095(4), Ta2-C18 2.399(4), Ta-C17 2.501(4), Ta1-O1 1.925(3), Ta2-O1 2.009(3), Ta1-H1 1.96(5), Ta2-H1 1.92(5), Ta1-N1 2.127(3), Ta1-N2 2.081(4), Ta1-P1 2.6706(12), Ta2-N3 2.043(4), Ta2-N4 2.068(3), Ta2-P2 2.6154(12), Ta1-N1-C13 94.8(2), N1-C13-C18 104.4(3), Ta1-C18-C13 95.0(3), C18-Ta1-N1 64.81(14), C17-C18-Ta1 143.2(3), Ta1-C18-Ta2 74.29(13), Ta1-O1-Ta2 87.60(11), O1-Ta1-N1 107.72(12), O1-Ta1-N2 126.07(13), O1-Ta1-C18 100.74(14), N2-Ta1-C18 116.15(15), N2-Ta1-N1 122.77(13), N3-Ta2-N4 113.35(13), N3-Ta2-C18 102.07(14), N4-Ta2-C18 144.54(14), O1-Ta2-N3 91.87(12), O1-Ta2-N4 88.40(12), O1-Ta2-C18 88.85(13)

reductive elimination of CH_4 would generate the highly coordinatively unsaturated species $\mathbf{Ta_2O}$; it is this species that we propose undergoes activation of the N-Ph moiety to generate the observed cyclometalated derivative **2.4**.

Carbon monoxide can be cleaved by both mononuclear and multinuclear early transition metal[150] and lanthanide complexes.[151] In certain cases, the systems utilized are low oxidation early transition metal complexes, such as $Ta(silox)_3$[152]

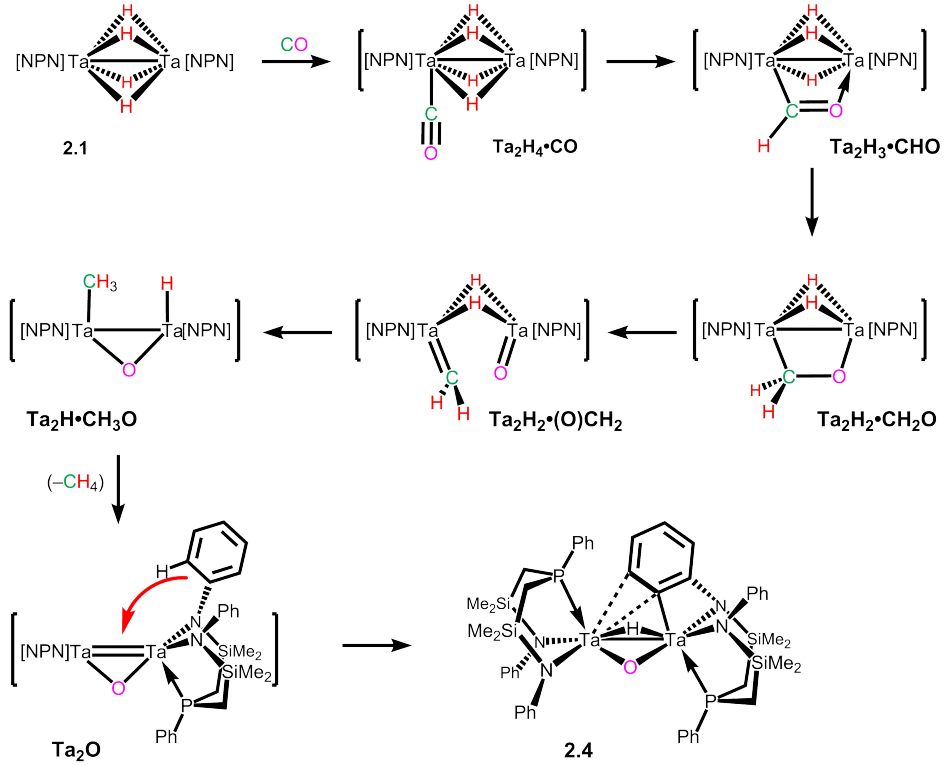

Scheme 2.2: Proposed mechanism for CO reduction by **2.1**

or $W_2(silox)_4Cl_2$[153] (where silox = $OSiBu^t_3$), and the cleavage process operates via reduction of the CO.[154] Other examples include multistep processes involving migratory insertion,[147–149] sometimes through the intermediacy of a coordinated formyl unit. As proposed above in Scheme 2.2, the dinuclear ditantalum system cleaves CO by a combination of migratory insertion steps and a reductive cleavage step. In an effort to better understand the mechanism of the reaction of tetrahydride **2.1** with CO, we examined possible intermediates and transition states computationally.

Computational Details

Tantalum atoms were treated with the small core Stuttgart-Dresden relativistic Effective Core Potential (ECP) in combination with its adapted basis set.[155,156] Carbon, oxygen, nitrogen and hydrogen atoms have been described with a 6-31G(d,p) double-ζ basis set.[157] Silicon and phosphorus atoms were treated with the Stuttgart-Dresden ECP in combination with its adapted basis set and additional *d* polarization functions.[158,159] Calculations were carried out at the Density Functional Theory (DFT) level of theory using the hybrid functional B3PW91.[160,161] Geometry optimizations were performed without any symmetry restrictions and the nature of the extremes (minima and transition states) was verified with analytical frequency calculations. Gibbs free energies were obtained at T = 298.15 K within the harmonic approximation. Intrinsic Reaction Coordinate (IRC) calculations were performed to confirm the connections of the optimized transition states. DFT calculations were carried out with the Gaussian09 suite program.[162] The electronic density (at the DFT level) has been analyzed using the Natural Bond Order (NBO) technique.[163] Calculations have been realized in the gas-phase and the real NPN ligands have been computed.

To begin, we computed the structure of the ditantalum tetrahydride **2.1** and compared it to an incomplete X-ray crystal structure (see Appendix, Figure A.1). The computed structure is presented in Figure 2.2 with selected bond lengths and angles. It confirms the presence of four bridging hydrides and the global structure matches the structure observed experimentally[164] for the complex $([P_2N_2]Ta)_2(\mu\text{-}H)_4$. The NBO analysis is consistent with the presence of the Ta(IV) oxidation state and the presence of a Ta-Ta bond. This is further confirmed by analyzing the molecular orbitals. Indeed, the HOMO of this complex corresponds to the σ-

interaction of two *d* orbitals of tantalum (Figure 2.3), suggesting that the electrons stored in the Ta-Ta bond can be used to reduce substrates.

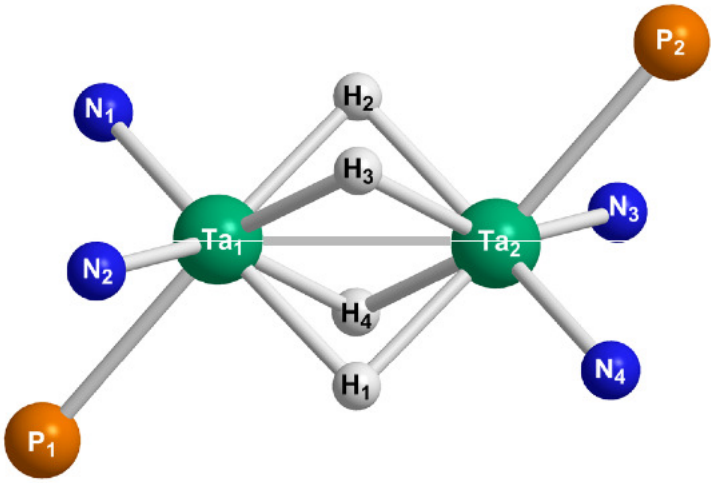

Figure 2.2: Computed structure of complex **2.1**. NPN ligands have been simplified for clarity. Selected bond distances (Å), bond angles (deg) and torsion angles (deg) ; comparisons to the incomplete structure of **2.1** (see Supporting Information) are given where applicable in brackets: Ta1-Ta2 2.589 [2.57], Ta-P 2.605, Ta1-N1 2.104 [2.08], Ta1-N2 2.124 [2.09], Ta2-N3 2.124 [2.09], Ta2-N4 2.104 [2.08], Ta1-H1 1.965, Ta1-H2 1.918, Ta1-H3 1.978, Ta1-H4 1.909, Ta2-H1 1.918, Ta2-H2 1.965, Ta2-H3 1.909, Ta2-H4 1.978, P1-Ta1-P2 154.57, Ta2-Ta1-P1 128.97, Ta2-Ta1-N1 122.69, Ta1-H1-Ta2 83.61, P1-Ta1-Ta2-P2 179.99 [180], N1-Ta1-Ta2-N4 179.98.

The reaction between **2.1** and CO is complex. The first part of the Gibbs free energy profile of the reaction between **2.1** and CO is presented in Figure 2.4. Each minimum of the profile has been optimized in its singlet and triplet spin-states and the singlet spin-states are also found to be the most stable for all minima, by 8∼30 kcal/mol. Thus, the reactivity takes place on the singlet potential energy surface.

The first step of the reaction is the coordination of CO to **2.1** involving both Ta centers. Interestingly, two of bridging hydride groups have become terminal in

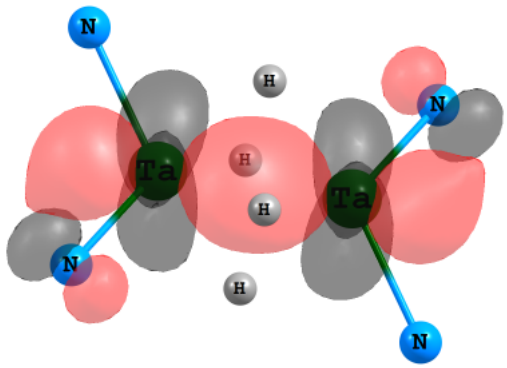

Figure 2.3: Schematic depiction of the HOMO for complex **2.1**, corresponding to the metal-metal overlap.

order to allow the coordination; this was not considered in the original proposed mechanism shown in Scheme 2.2. The coordination mode shows the CO to be unsymmetrically bridging in a μ-η^1-η^1 mode with quite different Ta1-C and Ta2-C distances of 2.08 Åand 2.43 Å, respectively. The C-O bond length is 1.19 Å, which is elongated with respect to free CO (1.13 Å), which supports some π-back-donation from the two tantalum centers. The HOMO of this system corresponds to the interaction between the Ta centers and CO and is depicted in Figure 2.5. The coordination of CO is exergonic by -7.8 kcal/mol. Interestingly, this resembles the aforementioned product of CO activation shown in Scheme 2.1, by analogy to the

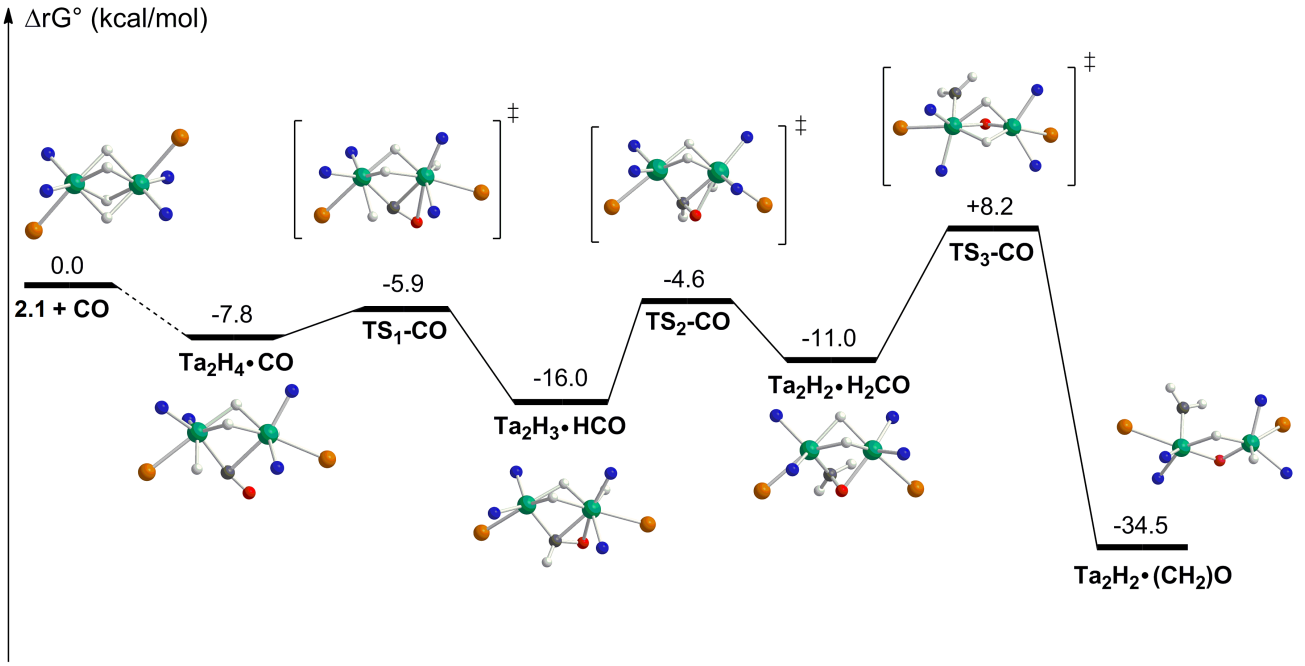

Figure 2.4: Gibbs free energy profile of the reaction between the tetrahydride complex **2.1** and CO. NPN ligands have been simplified for clarity. Atoms colors: Ta: green, P: orange, N: blue, O: red, C: black, H: white. For atom numbering, Ta1 is on the left while Ta2 is on the right.

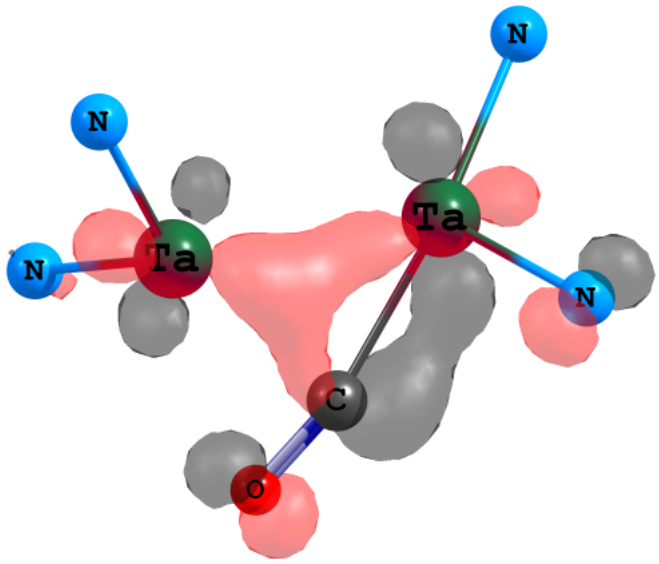

Figure 2.5: Schematic depiction of the HOMO for **Ta_2H_4•CO**, corresponding to the metal-CO overlaps; the bridging hydrides are not shown and most of the ligands except for the two amido donors on each tantalum are omitted.

N_2 activation; however, in this calculation the side-on, end-on CO species, loss of H_2 does not occur as in the case of dinitrogen activation. Rather, the adduct **Ta_2H_4•CO** easily undergoes migratory insertion of CO into a terminal Ta-H bond. Indeed, the transition state of insertion lies at only +1.9 kcal/mol above the adduct, and the formation of the corresponding formyl, **Ta_2H_3•HCO**, is exergonic by -8.2 kcal/mol with respect to **Ta_2H_4•CO**. The structure of the first transition state, **TS_1-CO**, has the hydride poised for migratory insertion to generate the formyl group in a μ-η^1-η^2 coordination mode.

The next step of the reaction is the facile migration of the other terminal hydride (transition state **TS_2-CO** at +11.4 kcal/mol), which generates **Ta_2H_2•H_2CO** that contains a coordinated formaldehyde unit, whose formation is slightly ender-

gonic by +5.0 kcal/mol with respect to the formyl **Ta_2H_3•HCO**. The formaldehyde group is unsymmetrically bridging the two Ta centers, with the Ta1-C, Ta2-C, Ta1-O, and Ta2-O distances being 2.16 Å, 2.41 Å, 2.24 Å, and 2.16 Å, respectively. At this point, the Ta-Ta distance is equal to 2.66 Å, consistent with the presence of a Ta-Ta bond and the Ta(IV) formal oxidation state. This intermediate can further react by breaking the C-O bond of the formaldehyde moiety with concomitant oxidation of both Ta(IV) centers to Ta(V). Overcoming this third transition state, **TS_3-CO**, is the most difficult part of the reaction since the activation barrier is equal to +19.2 kcal/mol with respect to **Ta_2H_2•H_2CO**; interestingly, the overall barrier can be defined as the conversion of **Ta_2H_3•HCO** to **TS_3-CO**, and requires +24.2 kcal/mol. However, the next intermediate is **Ta_2H_2•(CH_2)O**, which is exergonic by -23.5 kcal/mol with respect to **Ta_2H_2•H_2CO**. **Ta_2H_2•(CH_2)O** displays a bridging μ-oxo group as well as a bridging hydride, a terminal methylene group on Ta1 and a terminal hydride on Ta2. From this point on, different pathways have been examined computationally in order to generate the experimentally observed product **2.4**, but only three were found to be competitive and these are summarized schematically in Figure 2.6.

The three pathways **A**, **B**, and **C**, in Figure 2.6, differ in the order of the migratory insertion of the methylene unit and the activation of the N-phenyl moiety, which results in differences on where the *ortho* proton of the activated N-phenyl group ends up. In path **A**, the *ortho*-C-H ends up as the bridging hydride, whereas in paths **B** and **C**, one of the original bridging hydrides of **2.1** remains in the bridging position. We anticipated that testing this would be straightforward based on our earlier report[144] on the preparation of ([NPN]Ta)$_2$(μ-D)$_4$, **2.1-*d*^{4}** which should generate CD_4 via path **A**, whereas both paths **B** and **C** generate CD_3H. However,

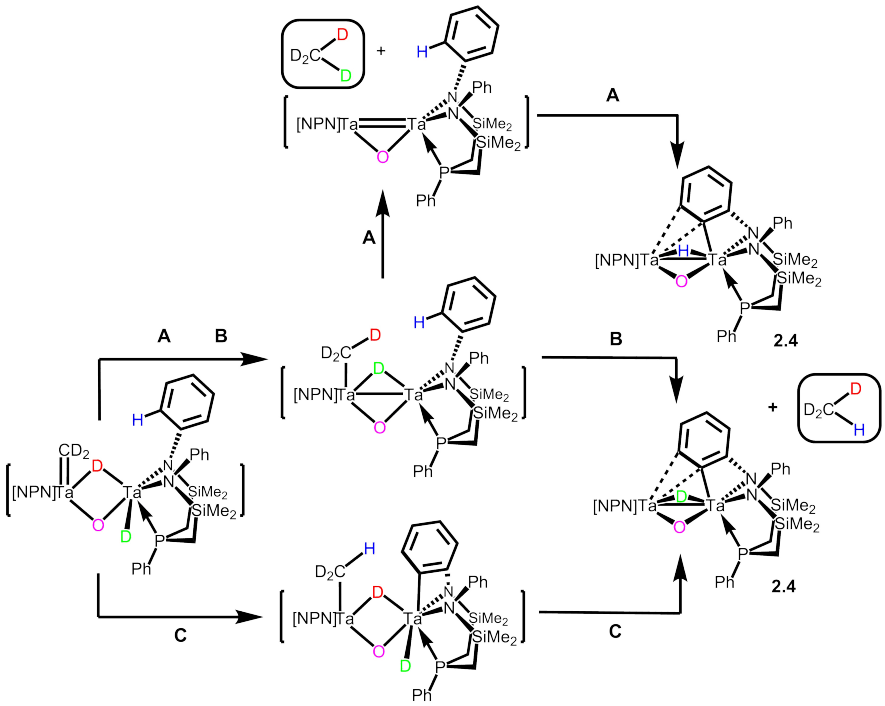

Figure 2.6: Starting with the putative tetradeuteride, $([NPN]Ta)_2(\mu-D)_4$; three proposed pathways leading to the experimental product with concomitant release of deuterated methane from $\mathbf{Ta_2H_2{\bullet}(CH_2)O}$. In pathways **B** and **C**, CD_3H is produced whereas in path **A**, CD_4 would result.

we have since discovered that the preparation of **2.1**-$\boldsymbol{d}_4$ by addition of excess D_2 to the precursor trimethyl [NPN]$TaMe_3$ is more complicated and actually results in the formation of **2.1**-$\boldsymbol{d}_{12}$, wherein all eight of the *ortho*-C-H units on the N-Ph moieties have also been deuterated, in addition to formation of the four bridging deuterides (Scheme 2.3). None of *ortho*-C-Hs of the phenyl on the phosphine moiety are exchanged. To distinguish paths **A-C** in Figure 2.6, the use of **2.1**-$\boldsymbol{d}_{12}$ would not be useful as CD_4 would result in all cases.

However, we have determined that the deuteration of the trimethyl complex in hexanes results in less deuterium incorporation; this arises from precipitation of the

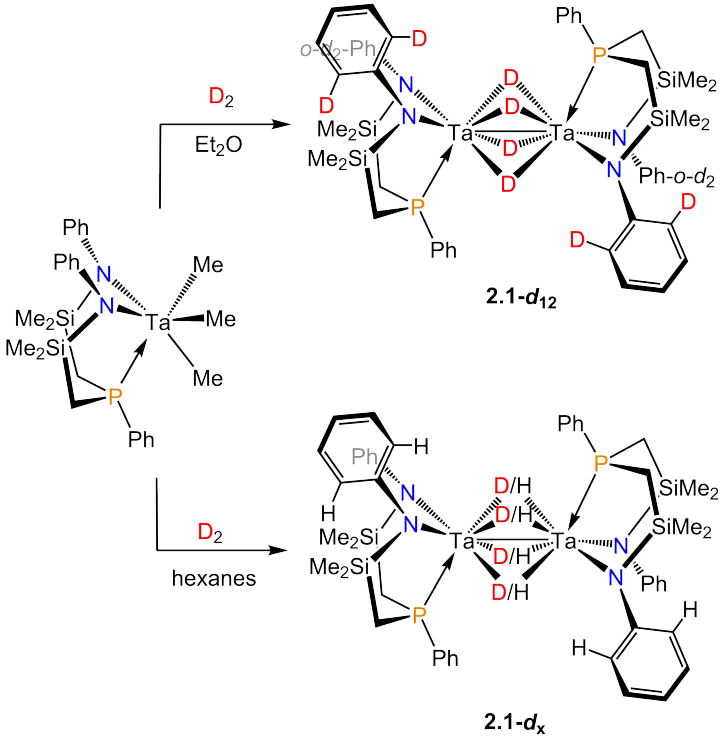

Scheme 2.3

partially deuterated complex, which presumably intercepts the isotopic incorporation process. By ^{1}H NMR spectroscopy, there is no incorporation of deuterium into the *ortho*-C-H positions of the N-Ph groups, and partial deuteration of the bridging tantalum hydrides (Scheme 2.3). In fact, the formation of a mixture of isotopologues ([NPN]Ta)$_2$(μ-D)$_{4-x}$(μ-H)$_x$ (x = 0-4) can easily be determined by the isotopically perturbed signals in the ^{1}H NMR spectrum in the tantalum hydride region.[144,148] While the mechanism of this process is currently under investigation, by correlating the number of deuterium atoms of the partially deuterated dinuclear

hydride **2.1**-$\boldsymbol{d}_x$ to the amount of deuterium contained in the methane product, we are able to provide some support for one of the pathways. By Gas Chromatography Mass Spectrometry (GC-MS) analysis, we observe the formation of approximately equal amounts of CD_4 and CD_3H from the reaction of **2.1**-$\boldsymbol{d}_x$ with CO; CD_2H_2 is also likely produced but its parent ion overlaps with CD_3^+ ions from CD_4. The deuteration of the trimethyl complex in Et_2O is homogeneous throughout, which likely promotes exchange of both the bridging hydrides and the *ortho*-C-H bonds (Scheme 2.3). Reaction of CO with the fully deuterated material **2.1**-$\boldsymbol{d}_{12}$ results in the formation of CD_4 exclusively as expected.

While the other pathways are found to be energetically accessible, only the Gibbs free energy profile for path **A** is shown in detail. The Gibbs free energy profile of pathway **A** is presented in Figure 2.7. It begins by the migration of the bridging hydride group of $\mathbf{Ta_2H_2{\bullet}(CH_2)O}$ to the carbene group in order to form $\mathbf{Ta_2H{\bullet}(CH_3)O}$. The activation barrier is equal to +16.1 kcal/mol with respect to $\mathbf{Ta_2H_2{\bullet}(CH_2)O}$ and the energetic gain is only 2.3 kcal/mol. The Ta-Ta distance has decreased from 3.15 Å in $\mathbf{Ta_2H_2{\bullet}(CH_2)O}$ to 2.83 Å in $\mathbf{Ta_2H{\bullet}(CH_3)O}$ which is consistent with the passage from Ta(V) to Ta(IV). The terminal hydride becomes a bridging hydride in order to slightly stabilize the complex. Then, this new bridging hydride can also migrate towards the methyl group in order to release a methane molecule and form the Ta(III) μ-oxo complex $\mathbf{Ta_2O}$. This latter complex presents a bent Ta-O-Ta angle of 89.1° allowing the formation of a double Ta-Ta bond. This is confirmed by analyzing the HOMO and HOMO-1 of the complex, which correspond respectively to one π and one σ orbital arising from the overlap of the *d* orbitals of the metal centers (Figure 2.8).

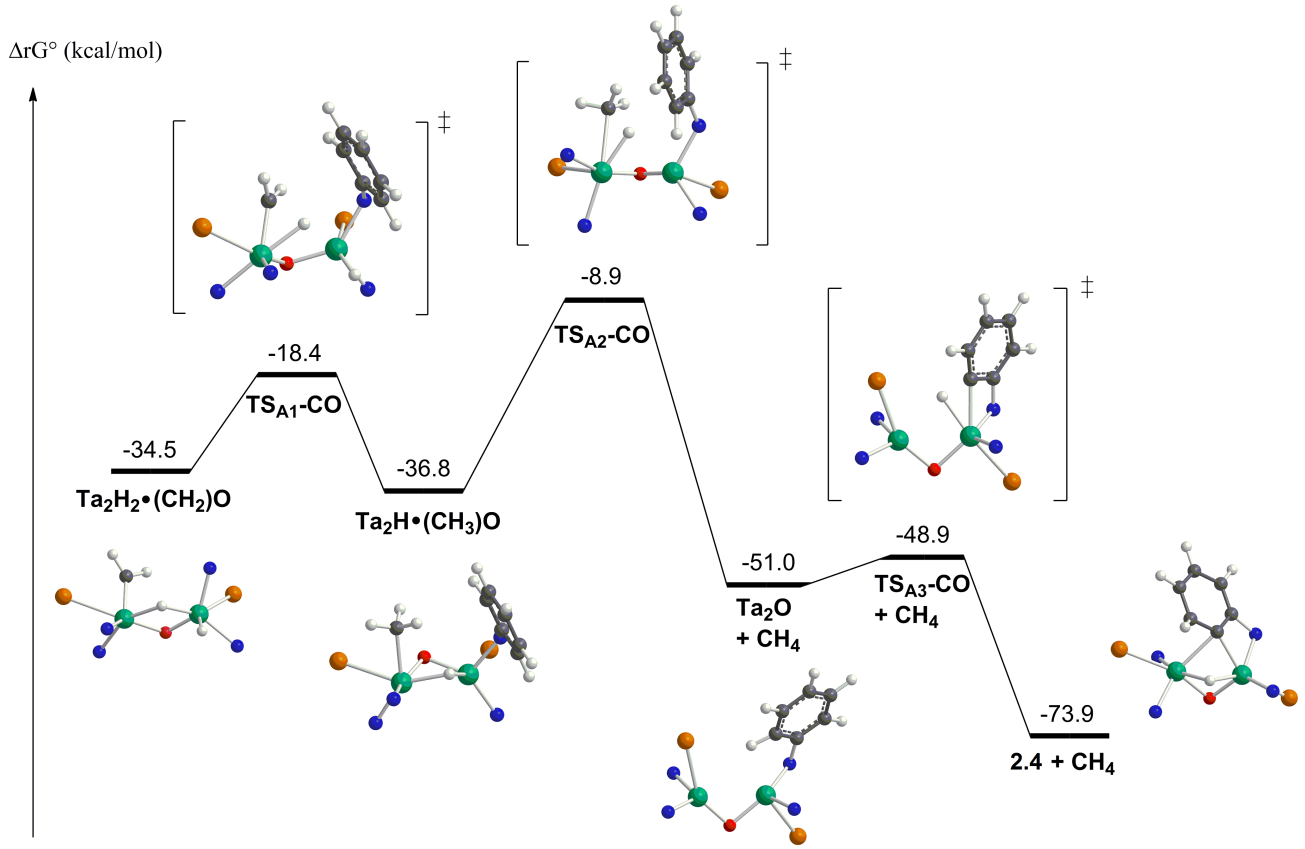

Figure 2.7: Gibbs free energy profile of pathway **A**. NPN ligands have been simplified for clarity. Atoms colors: Ta: green, P: orange, N: blue, O: red, C: black, H: white. For atom numbering, Ta1 is on the left while Ta2 is on the right.

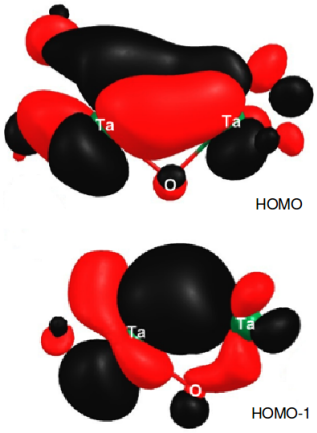

Figure 2.8: The calculated HOMO (top) and HOMO-1 (bottom) for the Ta=Ta of the putative intermediate $\mathbf{Ta_2O}$

The activation barrier corresponding to its formation is equal to +27.9 kcal/mol and the reaction is exergonic by -14.2 kcal/mol, both with respect to $\mathbf{Ta_2H{\bullet}(CH_3)O}$. This thermodynamic gain is mainly due to the formation of the stable methane molecule along with the entropic gain due to the release of a small molecule (TΔS estimated to 10$\sim$15 kcal/mol at room temperature).[165] Thus, the formation of the coordinately unsaturated $\mathbf{Ta_2O}$ complex itself is not a favorable process, otherwise the energetic gain would be much larger than the 14.2 kcal/mol calculated. In order to stabilize the complex, the last step of the reaction is the C-H activation of the *ortho* C-H bond of an N-phenyl group of the NPN ligand, leading to the observed product **2.4**. The transition state lies only at +2.1 kcal/mol above the oxo complex and the reaction is exergonic by -22.9 kcal/mol with respect to $\mathbf{Ta_2O}$, which is consistent with the low stability of $\mathbf{Ta_2O}$. The product exhibits a bridging oxo group (Ta1-O bond length of 2.02 Å and Ta2-O bond length of 1.95 Å, versus 2.009(3) and 1.925(3) exp.), a bridging hydride (Ta1-H bond length of 2.02 Å and Ta2-H

bond length of 1.92 Å, versus 1.92(5) and 1.96(5) exp.) and a phenyl bridging ligand, coordinated by the *ortho*-carbon (Ta1-C bond length of 2.42 Å and Ta2-C bond length of 2.11 Å versus 2.399(4) and 2.095(4) exp.). It is thus a Ta(IV) complex, which is confirmed by the short Ta-Ta bond distance (2.75 Å versus 2.7240(6) exp.). It is noteworthy that the quintet spin-state of the Ta(III) μ-oxo complex is more stable than the singlet spin-state by 3.6 kcal/mol, but in the first case, the Ta-O-Ta angle becomes linear, which would make the last reaction step forbidden. We can thus assume without risk that there is equilibrium between the singlet and the quintet spin-states, and that the singlet spin-state complex **Ta_2O** reacts directly to generate **2.4**.

2.1.3 Conclusions

The reaction of CO with the highly reducing ditantalum tetrahydride complex **2.1** proceeds by a series of migratory insertion reactions. Of particular interest for this process is how CO interacts with the starting hydride. By using a computational approach, an adduct structure is proposed that involves CO interacting with tetrahydride **2.1** wherein two of the bridging hydrides isomerize to terminal hydrides, presumably to open up a coordination site. In fact, one of the interesting insights that is suggested from these calculations is the importance of the terminal hydride unit in the migratory insertion processes documented in this work. While the starting tetrahydride **2.1** contains four bridging hydrides in its ground state, each insertion process involves a terminal hydride interacting with a small organic moiety in a bridging position. While dinuclear complexes have offered unique activation modes for small molecules, mainly by invoking simultaneous interactions with two metal centers,[154,166,167] in this work, we show that a strongly reducing

dinuclear center in concert with available hydrides for migratory insertion can convert an important C_1 molecule, CO, into CH_4 via complete utilization of the four bridging hydrides.

2.2 Reduction of Carbon Dioxide Promoted by a Dinuclear Tantalum Tetrahydride Complex

2.2.1 Introduction

Carbon dioxide (CO_2) is potentially a plentiful C_1 source that continues to occupy discussions related to climate change.[168] While conversion of CO_2 to higher-value carbon-based materials is a worthy goal, it is clear that these kinds of approaches are not realistic as a way to sequester this greenhouse gas,[169] particularly if dihydrogen (H_2) derived via steam reforming is involved. Nevertheless, from a fundamental point of view, discovering systems that can transform CO_2 with[170–172] or without H_2[173] is of considerable interest[174–176] and may provide hints on ways to better utilize this ever-more-abundant resource.[177]

We have described the facile activation of dinitrogen (N_2) by dinuclear tantalum tetrahydride, $([NPN]Ta)_2(\mu\text{-}H)_4$ (**2.1**, where NPN = $PhP(CH_2SiMe_2NPh)_2$), to generate the side-on end-on ditantalum dinitrogen complex $([NPN]Ta)_2(\mu\text{-}\eta^2{:}\eta^1\text{-}N_2)(\mu\text{-}H)_2$ (**2.2**;[143,144] Scheme 2.4). Given that N_2 is a very stable, inert molecule, the question arose as to what the outcome would be in the reaction of tetrahydride **2.1** with the very stable CO_2 molecule. Herein we report our efforts to examine the reactivity of CO_2 with the strongly reducing ditantalum tetrahydride complex **2.1**. What emerges from this work is a rare example of a dinuclear metal hydride system that functionalizes CO_2 and retains its dinuclearity.

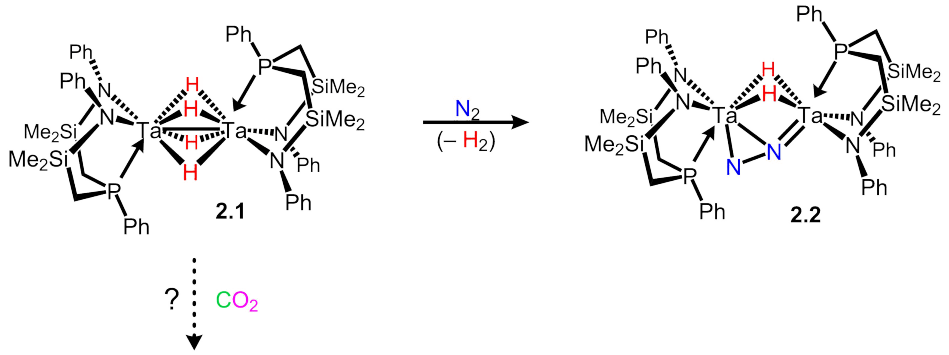

Scheme 2.4

2.2.2 Results and Discussion

Our initial inspiration to examine the activation of CO_2 was based on the report that certain zirconium and hafnium dinitrogen complexes react productively with CO_2 to generate new N-C bonds and regiospecific hydrazides.[178] However, the reaction of CO_2 and the tantalum side-on end-on N_2 complex **2.2** led to the formation of a multitude of products even when the stoichiometry of added CO_2 was controlled. Undaunted, we turned to the reaction of the ditantalum tetrahydride **2.1** with CO_2 and discovered that a single product could be obtained provided that strict control of the stoichiometry was followed. For example, if excess CO_2 is used, very complicated spectra are obtained, indicative of a mixture of products, perhaps a consequence of migratory insertion of CO_2 in the tantalum-amido linkages of the NPN ligand. However, if exactly 1 equiv of CO_2 is employed, a clean reaction ensues with the formation of only one very symmetrical product (60% recrystallized yield) on the basis of a singlet at δ -13.1 observed in the ^{31}P NMR spectrum. The corresponding ^{1}H NMR spectrum shows a triplet resonance downfield at δ 6.81, which simplifies to a singlet upon ^{31}P decoupling and integrates to two H atoms.

Analysis by heteronuclear single quantum coherence indicates that these H atoms are not C-bound, consistent with the presence of bridging tantalum hydrides, and are likely a $Ta_2(\mu\text{-}H)_2$ moiety. Also diagnostic in the ^{1}H NMR spectrum is a singlet at δ 6.11 that again integrates for two H atoms. That these two sets of proton resonances are derived from the bridging hydrides of **2.1** was confirmed by the use of **2.1**-d_{12}, in which all four bridging hydrides and all eight of the *o*-NPh protons are deuterated (See Scheme 2.3); in this reaction, the peaks at δ 6.81 and 6.11 both disappear in the ^{1}H NMR spectrum, as does a peak at δ 6.89 due to the *o*-H atoms of the NPh moiety of the NPN ligand. When ^{13}C-labeled CO_2 was utilized, the resonance at δ 6.11 becomes a doublet with $^1J_{CH}$ = 110 Hz. Given our earlier publication[179] of the complete disassembly of CS_2 to generate the ditantalum species with a bridging methylene, an analogous structure was considered. However, there are no bridging hydrides in the CS_2 disassembly product, and the chemical shift of the resonance due to the bridging methylene of this material occurs at δ 4.5 in the ^{1}H NMR spectrum, which is considerably upfield of the methylene resonance observed for the CO_2 product **2.5**. In fact, a recent report of the reaction of CO_2 with a mononuclear tantalum hydride to generate a ditantalum species with a methylene diolate fragment proved to be a better analogy.[180]

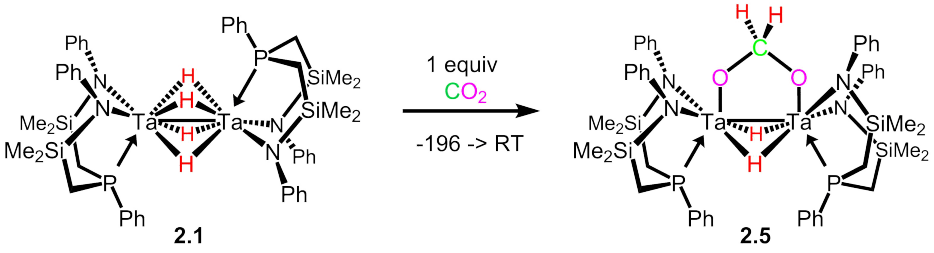

Scheme 2.5: Reduction of CO_2 using **2.1**

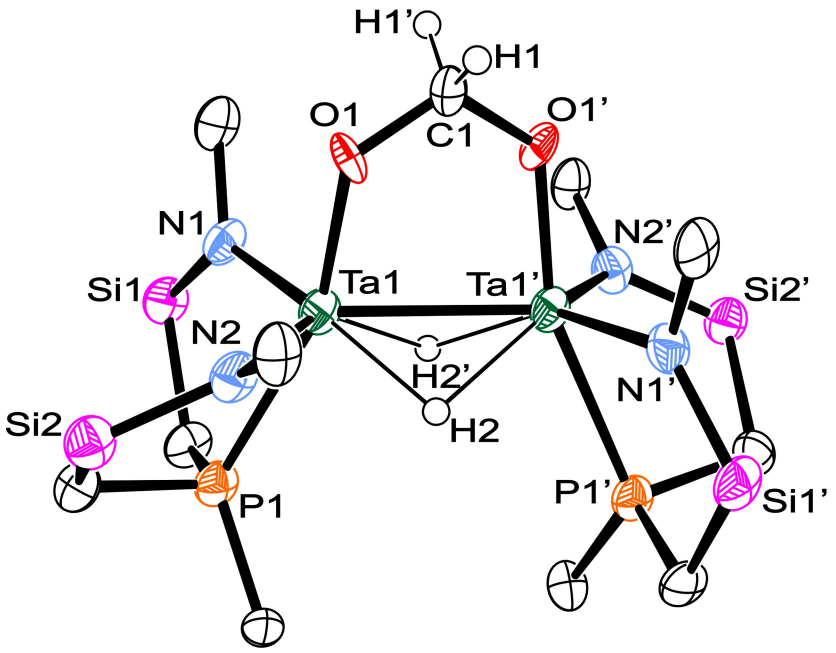

Figure 2.9: Selected bond lengths (Å) and bond angles (deg) for **2.5**: Ta1 - N1 2.091(7), Ta1 - N2 2.062(6), Ta1 - P1 2.628(2), Ta1 - O1 1.980(5), Ta1 - Ta1 2.7688(7), N1 - Si1 1.742(7), N2 - Si2 1.739(7), C1 - O1 1.384(7); O1 - C1 - O1 117.0(9), Ta1 - O1 - C1 126.4(5), O1 - Ta1 - O1 117.0(9), O1 - Ta1 - N1 91.6(2), O1 - Ta1 - N2 91.6(2), N1 - Ta1 - N2 118.2(3), O1 - Ta1 - P1 160.99(15), N1 - Ta1 - P1 77.82(19), N2 - Ta1 - P1 79.08(19), O1 - Ta1 - Ta1 83.45(14).

The solid-state structure of this complex (**2.5**) is shown in Figure 2.9, along with the transformation in Scheme 2.5; the most notable feature of **2.5** is the bridging methylene diolate unit between the two Ta centers. The Ta1-O1 bond length of **2.5** of 1.980(5) Å is slightly longer that the Ta-O bonds of 1.929(5) and 1.917(2) Å found in two dinuclear methylene diolate complexes formed via intermolecular processes.[180] The other parameters of this μ-OCH_2O unit compare unremarkably to other examples of this rare kind of fragment with the exception that the O-C-O angle in **2.5** of 117.0(9)° is larger than the aforementioned dinuclear systems [cf.

111.4(7) and 109.7(3)°][180] and a tetrayttrium cluster [cf. 107.6(3)°][181] that contain this unit.

The formation of **2.5** likely involves hydride addition reactions most probably through a formate-type intermediate.[62,170] In an effort to shed light on this process, possible structures of intermediates and transition states were examined computationally. DFT [B3PW91//SDDALl(Ta,P)/6-31G** (other atoms)] calculations were carried out on the full system.

The Gibbs free-energy profile of the reaction between **2.1** and CO_2 is presented in Figure 2.10. For each minimum, singlet and triplet spin states have been considered, and the singlet spin states are always the most stable, by 20-50 kcal/mol. Thus, the reactivity takes place on the singlet potential energy surface.

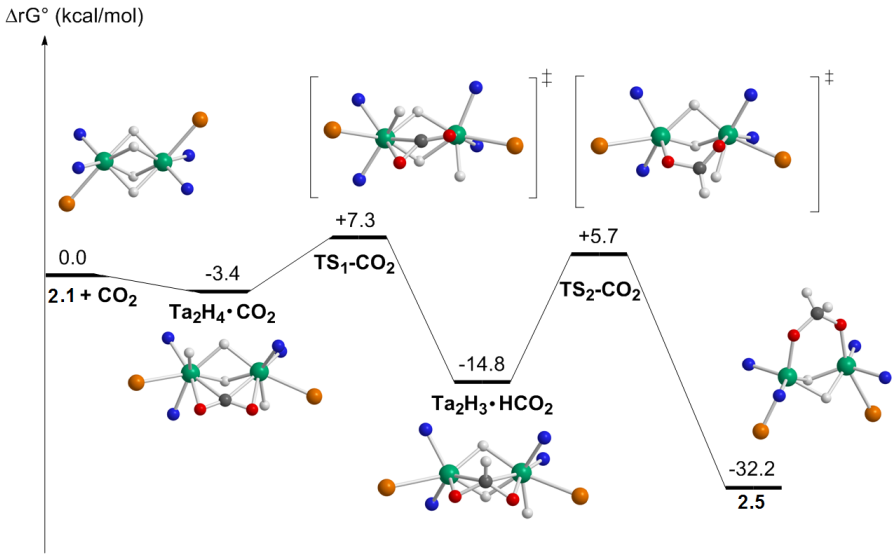

Figure 2.10: Gibbs free-energy profile of the reaction between the tetrahydride complex **2.1** and CO_2. NPN ligands have been simplified for clarity. Atoms colors: Ta, green; P, orange; N, blue; O, red; C, black; H, white. For atom numbering, Ta1 is on the left, while Ta2 is on the right.

The first step of the reaction is coordination of CO_2 to **2.1**, involving the two Ta centers. In $\mathbf{Ta_2H_4{\bullet}CO_2}$, two bridging hydride groups have become terminal in order to liberate one coordination site on each Ta center and thus allow the μ-η^2:η^2-coordination mode of CO_2, all of which happens in a concerted fashion. The computed O-C-O angle is 132.8° and both C-O bonds are equal to 1.26 Å, suggesting that CO_2 has been reduced by **2.1**. The Ta-Ta distance has increased from 2.59 to 3.01 Å so that the Ta-Ta bond has been broken. This is confirmed by NBO analysis, which gives an oxidation state of +5 for each Ta, suggestive of the presence of ${CO_2}^{2-}$, at least formally. NPA charges show that the C atom of CO_2 is strongly positively charged (+0.70). The formation of this adduct is slightly exergonic by -3.4 kcal/mol, but it readily transforms to give the dinuclear μ-η^2:η^2-formato $\mathbf{Ta_2H_3{\bullet}HCO_2}$. Indeed, the transition state corresponding to the hydrogen transfer from one Ta center to CO_2 lies at only +10.7 kcal/mol with respect to $\mathbf{Ta_2H_4{\bullet}CO_2}$, while the formation of $\mathbf{Ta_2H_3{\bullet}HCO_2}$ is exergonic by -11.4 kcal/mol with respect to the adduct. The geometry of the first transition state is standard because one O atom of CO_2 has just moved away from the Ta-Ta-CO_2 plane of $\mathbf{Ta_2H_4{\bullet}CO_2}$ in order to allow the terminal hydride to bridge from the Ta center to the C atom of CO_2. All other bond lengths or angles are mostly unchanged.

The intermediate $\mathbf{Ta_2H_3{\bullet}HCO_2}$ presents a nearly symmetrical μ-η^2:η^2-HCO_2 moiety. The Ta-Ta distance is 2.95 Å, which is not consistent with a formate unit between two Ta(IV) centers unless the two d electrons remain unpaired. NBO analysis shows that there are no unpaired electrons in the d orbitals of the Ta centers or the presence of a Ta-Ta bond. The Lewis configuration extracted from the NBO shows a covalent bond between Ta1 and the C atom and two dative bonds from both negatively charged O atoms to each Ta center. The system can thus be

described with two electrons delocalized between both Ta-C bonds and formally Ta(V) centers. The formation of the experimental product involves the transition state **TS2-CO_2**, which corresponds to the transfer of the second terminal hydride to the C atom of the HCO_2 unit. The activation barrier is calculated to be +20.5 kcal/mol, which is high but still kinetically accessible. The geometry of this transition state looks like that of **TS1-CO_2**, discussed above. The formation of **2.5** is calculated to be exergonic by -17.4 kcal/mol with respect to the dinuclear formate complex **Ta_2H_3•HCO_2**. The computed structure of **2.5** is similar to the experimental one, for example, with C-O, Ta-O, and Ta-Ta bond lengths of 1.40 [1.388(10) Å exp], 1.95 Å [1.982(8) Å exp], and 2.80 Å [2.7693(9) Å exp], respectively. The HOMO still corresponds to the σ interaction of the two d orbitals of Ta, confirming the Ta(IV) oxidation state. The importance of the metal is clearly evident because calculations using copper surfaces detail quite different intermediates.[182]

The reaction of CO_2 with the highly reducing ditantalum tetrahydride complex **2.1** proceeds by a migratory insertion process followed by reductive elimination, as summarized in Scheme 2.6.

2.2.3 Conclusions

Of particular interest is how CO_2 interacts with the starting hydride. By using a computational approach, a low-energy structure emerged, wherein CO_2 binds reductively with tetrahydride **2.1** to generate **Ta_2H_4•CO_2**, wherein two of the bridging hydrides become terminal and the CO_2 unit is formally a CO_2^{2-} moiety. One of the interesting insights that result from these calculations is the importance of the terminal hydride unit in the transformation documented in this work. While the starting tetrahydride **2.1** contains four bridging hydrides in its ground state, each

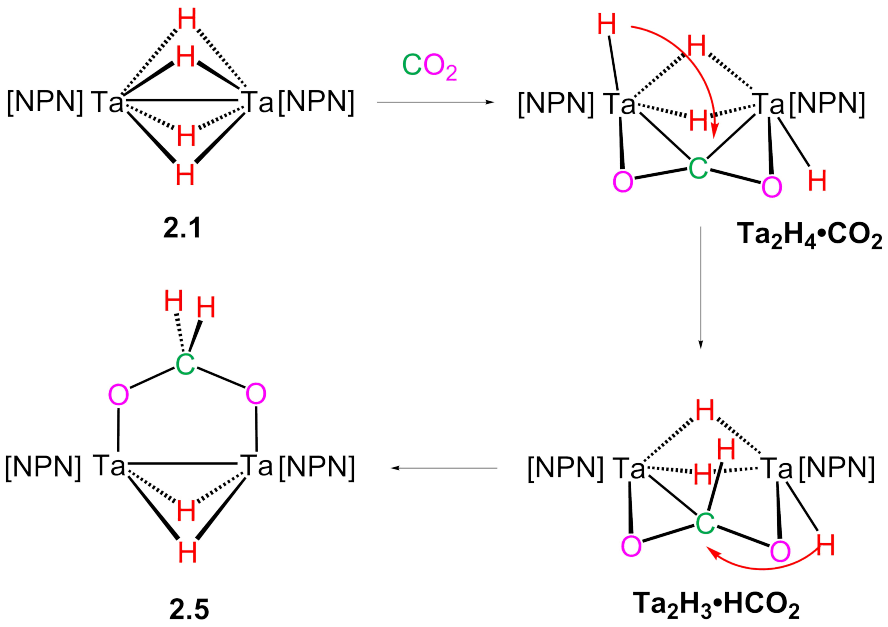

Scheme 2.6

step in the process involves a terminal hydride interacting with a small organic moiety in a bridging position. In the first transfer, the μ-η^2:η^2-formato complex **Ta_2H_3•HCO_2** is generated and finally the methylene diolate product **2.5**; this latter process is formally a dinuclear C-H reductive elimination, wherein the two Ta(V) centers of **Ta_2H_3•HCO_2** are converted to Ta(IV) moieties in **2.5**.

While dinuclear complexes offer unique activation modes for small molecules, mainly by invoking simultaneous interactions with two metal centers, in this work, we show that the strongly reducing ditantalum complex in concert with available hydrides can convert the important C_1 source CO_2 to a reduced form, in this case, a methylene diolate fragment.

Chapter 3

Synthesis of Base Metal Complexes of the Type [fc(NP)]M

The only place where success comes before work is in the dictionary
— Vince Lombardi

3.1 Synthesis of Iron and Cobalt Complexes of a Ferrocene-Linked Diphosphinoamide Ligand and Characterization of a Weak Iron-Cobalt Interaction

3.1.1 Introduction

The recent interest in the use of earth abundant or base metals (e.g. Fe, Co, Ni) in lieu of precious metals (e.g., Ru, Rh, Pd) in homogeneous catalysis is due to lower cost, higher availability and decreased environmental and health issues, especially with Fe-based systems.[183] From a burgeoning spate of publications,[3,57,81,90,184–196] it has emerged that the chemistry of the base metals can be more complicated than that of the precious metals. This is particularly the case because paramagnetic complexes are often found for these elements, especially with Fe and Co,[197–201]

and simple two-electron oxidative addition and reductive elimination processes, which are a staple for precious metal catalytic cycles, are not as common for base metal catalyst precursors.[1,202]

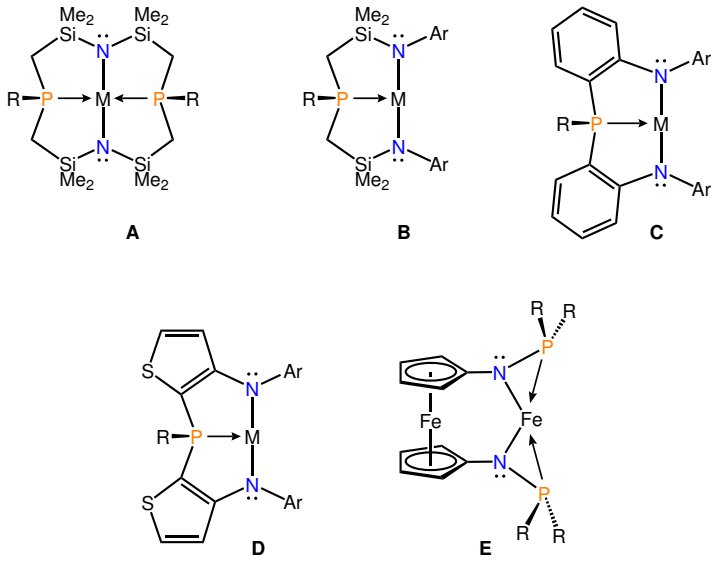

Scheme 3.1

The kinds of ligand environments used to generate base metal complexes are not too different from those found for the precious metals.[198,203,204] To promote versatility we have been exploring ligand sets that incorporate amido and phosphine donors into chelating arrays.[92,205] We have already shown that these kinds of donors can stabilize complexes of the early and late transition metal elements[92–94,206] including a number of the aforementioned base metals.[198,199] Ongoing efforts in our group have focused on the effect of the linkers that connect the disparate donor environments on the structures and reactivity of the resultant metal complexes. We have previously reported (Scheme 3.1) metal complexes stabilized by diamido donors with one or two phosphine units connected in macrocyclic

(**A**)[207–210] or chelating arrays using *o*-phenylene (P−C_6H_4−N: **C**),[99–101,211] 2,3-thiophenyl (P−C_4H_2S−N:) **D**:[143] or methylene-dimethysilyl (P−CH_2SiMe_2−N **A**,**B**)[207–210,212] linkers. More recently, we have investigated[109,137] phosphinoamide donors[110,111,213] in which there is no linker between the amido and the phosphine donor, and have the general formula $[R_2P{-}NR']^-$. Of particular interest is the use of a ferrocenediamine scaffold to generate a diphosphinoamido donor set as depicted in **E**[137] in Scheme 3.1. One intriguing feature of this system is the presence of the ferrocene unit that can undergo redox chemistry and therefore act in a non-innocent fashion.[214]

In this contribution we outline the coordination chemistry of 1,1'-ferrocenebis-(diisopropylphosphinoamide) with Fe(II) and Co(II) precursors, which generate new structural motifs in base metal chemistry that result from this linkerless donor set. What emerges from this study is that a weak metal-metal bond can arise from the interaction of the closed-shell iron center of ferrocene with an open-shell base metal center.

3.1.2 Results and Discussion

1,1'-Ferrocenediamine[130] is easily converted to 1,1'-ferrocenebis(diisopropylphosphinoamine), $fc(NHP^iPr_2)_2$, **1.50**, as previously reported.[137] Deprotonation of **1.50** with KH leads to formation of the dipotassium derivative, $K_2[fc(NP^iPr_2)_2]$, **3.1**, which can be stored under nitrogen as a solid for several weeks without significant degradation. An X-ray single crystal structural analysis (See Figure A.3) of this material indicates that it is polymeric in the solid state; nevertheless, it serves as a useful metathesis reagent as described below.

The reaction of **3.1** with $FeBr_2(THF)_2$ results in the formation of a species that

has the empirical formula, Fe[fc(NP)$_2$], **3.2**, as a red brown solid. Complex **3.2** is paramagnetic, and assuming a monomeric structure, exhibits a lower than expected effective magnetic moment (μ_{eff} Evans Method: 3.3 μ_B, Gouy: 3.2 μ_B), and gives rise to an NMR spectrum that contains 10 paramagnetically-shifted singlets over the range of $\delta + 120$ to -80.

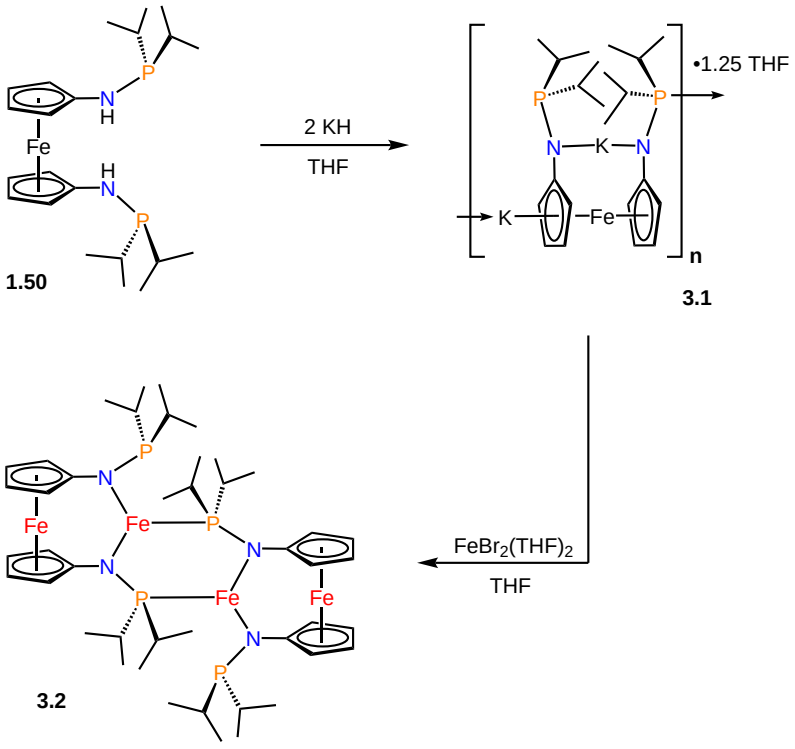

Scheme 3.2

From the NMR evidence alone, it is clear that **3.2** cannot be a mononuclear complex with a geometry similar to **E** in Scheme 3.1 (M = Fe), as one would predict only five resonances in the ^{1}H NMR spectrum on the basis of C_{2v} symmetry. In addition the μ_{eff} value does not match simple spin-only values expected for a high spin (HS) or low spin (LS) monomeric Fe(II) complex. Fortunately, single crystals

can be grown by slow evaporation of hexanes; the solid-state molecular structure is shown in Figure 3.1, along with selected bond lengths and angles.

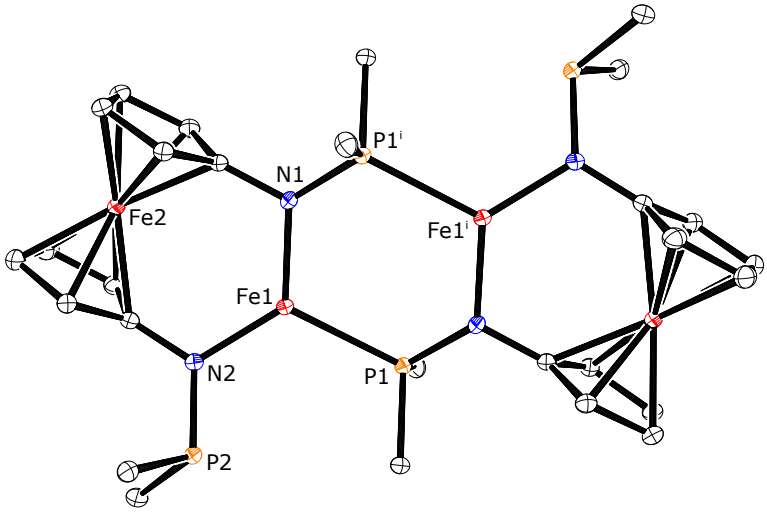

Figure 3.1: ORTEP diagram of **3.2** with ellipsoids drawn at 50% probability. All H atoms and ^{i}Pr methyl groups have been omitted for clarity. Selected bond lengths (Å) and angles (deg): Fe2-Fe1 3.5341(4); Fe1-Fe1^{i} 3.9241(5); Fe1-P1 2.4443(4); N1-Fe1 1.9459(12); N2-Fe1 1.9217(12); N1-P1 1.6692(13); N2-P2 1.6993(12); N2-Fe1-N1 123.47(5); N1-Fe1-P1 115.71(4); P1-Fe1-N2 120.81(4).

In the solid state, **3.2** is dimeric with bridging and terminal phosphine donors generating two three-coordinate Fe(II) centers, in addition to the ferrocene Fe(II) units. Complex **3.2** displays C_i symmetry where the inversion center of the molecular structure sits in the middle of an elongated six-membered heterocyclic ring made up of two Fe(II) centers and two phosphinoamide moieties. The bridging phosphinoamides in **3.2**, (N1-P1 $\approx$ 1.67 Å), are similar to other iron N-Aryl phosphinoamide complexes,[111] all of which are longer than typical N-alkyl substituted phosphinoamides[111,215] due to competing delocalization of the nitrogen based lone pair into π^* orbitals of the arene rings. The trigonal planar coordination geometry

of **3.2** results in an unstrained ligand backbone characterized by the tilt angle of 0.13°[216–219] and bite angle of 107.34° (See Figure 3.2 for depiction of Cp tilt (α) and bite (δ) angles). Other examples of trigonal planar iron phosphinoamide complexes have been reported by the Thomas group[111,115] and in all cases the N-P axes are perpendicular to the donor atom plane.

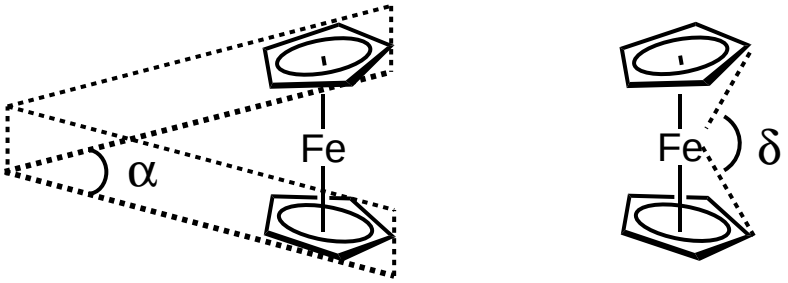

Figure 3.2: Cp tilt angle (left) and bite angle (right).

Using a dimeric structure, the room temperature effective magnetic moment of **3.2** was determined to be 6.7 μ_B by the Evans method, and 6.6 μ_B using a Gouy balance; the agreement between methods indicates that the dimer formulation exists in both the solution and solid state. As already mentioned, the paramagnetically shifted ^{1}H NMR spectrum of **3.2** displays 10 shifted singlets in C_6D_6 as shown in Figure 3.3. In d_8-THF, a slightly shifted set of 10 singlets is again observed, indicating that the dimeric structure is maintained in the presence of excess ethereal donors. However, when **3.2** is dissolved in d_5-pyridine, a simplified spectrum is observed in which 5 signals can be detected (Figure 3.3). When the pyridine solution is evaporated to dryness and the residue dissolved in C_6D_6, the original 10 line pattern is again observed, indicating that in the presence of pyridine, a different structure is generated, but reversion to the dimer **3.2** occurs when the pyridine is removed.

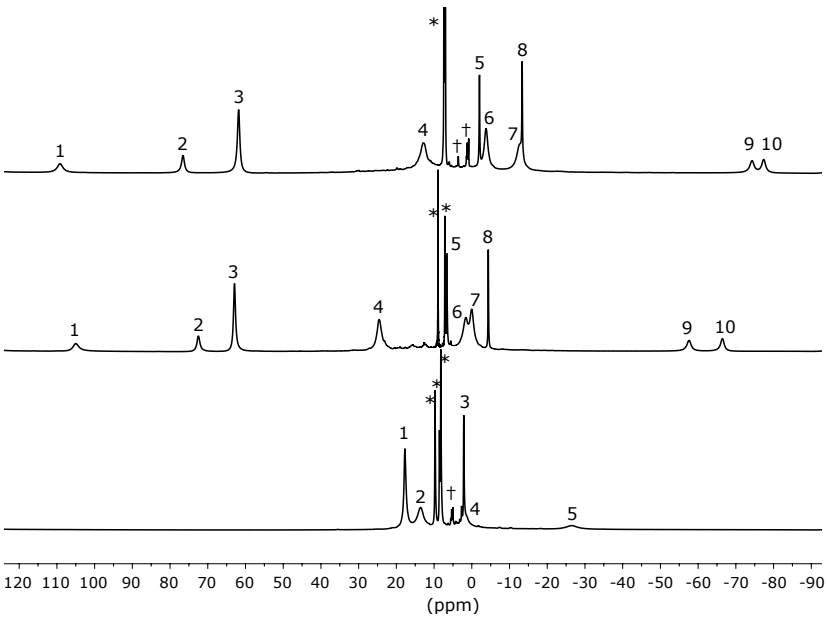

Figure 3.3: 300 MHz ^{1}H NMR spectra of **3.2** in C_6D_6 (top), d_8 -THF (middle), d_5 - pyridine (bottom): * denotes residual proton peak(s) of the NMR solvent; † denotes protonated ligand, **1.50**.

In an effort to investigate this apparent change in symmetry, the reaction of **3.2** with *p*-dimethylaminopyridine (DMAP) was examined, which resulted in the isolation of the mononuclear complex **3.3**. This mononuclear derivative can also be accessed by direct reaction of the potassium salt **3.1** with $FeBr_2(THF)_2$ in the presence of a slight excess of DMAP and the NMR spectrum of **3.3** is similar to that of **3.2** in d_5 - pyridine. The effective magnetic moment of **3.3** in solution (5.1 μ_B) is within the range expected for a HS Fe(II) center (Scheme 3.3).

The single crystal X-ray structure of **3.3** is shown in Figure 3.4, along with selected bond lengths and angles. The iron center in **3.3** displays a distorted tetrahedral geometry, with a large N1-Fe2-N1^i angle for the ferrocene based nitrogen donors (120.66°) and a more constricted N2-Fe2-N2^i angle for the DMAP donors

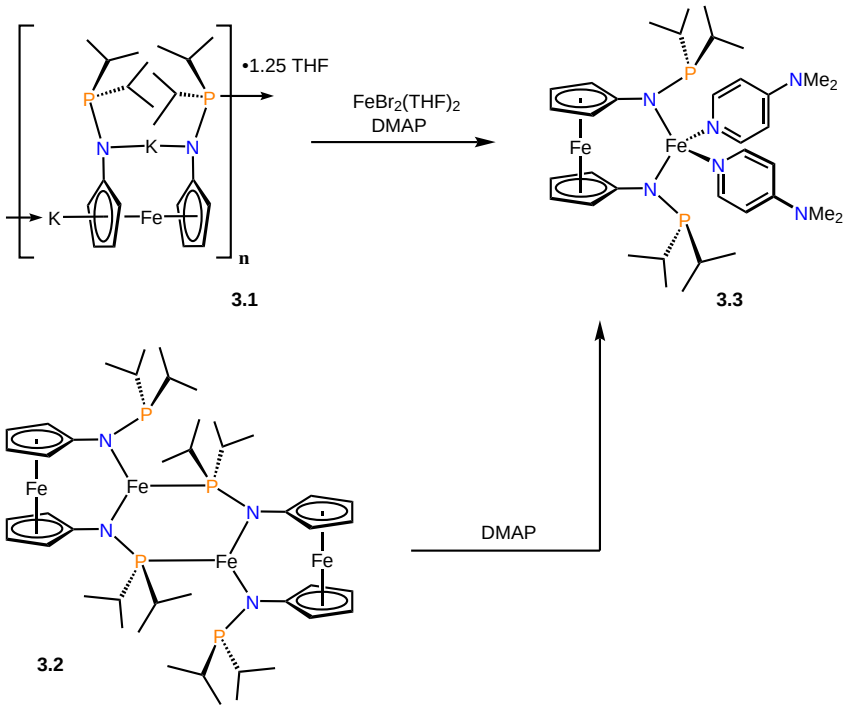

Scheme 3.3

(91.55°). This type of distortion is common in four-coordinate complexes with 1,1'-diaminoferrocene based ligands[132,220] due to the large bite angle imposed. The N-P bond lengths are very typical of an aryl-phosphinoamide and similar to that found for the unbound N-P unit in the dimer **3.2**. Upon changing the coordination geometry from trigonal planar in **3.2** to tetrahedral in **3.3** we observe an elongation of the Fe-Fe distance to 3.60 Å which is typical for tetrahedrally bound systems displaying no interaction with the ferrocene backbone.[132,133,220,221]

The ^{57}Fe Mössbauer spectra of **3.2** and **3.3** are shown in Figure 3.5; each compound displays two doublets arising from the two unique Fe(II) centers. The spectrum of **3.2** was fit as a pair of quadrupolar doublets. Based on the isomer shift and quadrupolar splitting of **1.50** (See Figure C.1) and other ferrocene based lig-

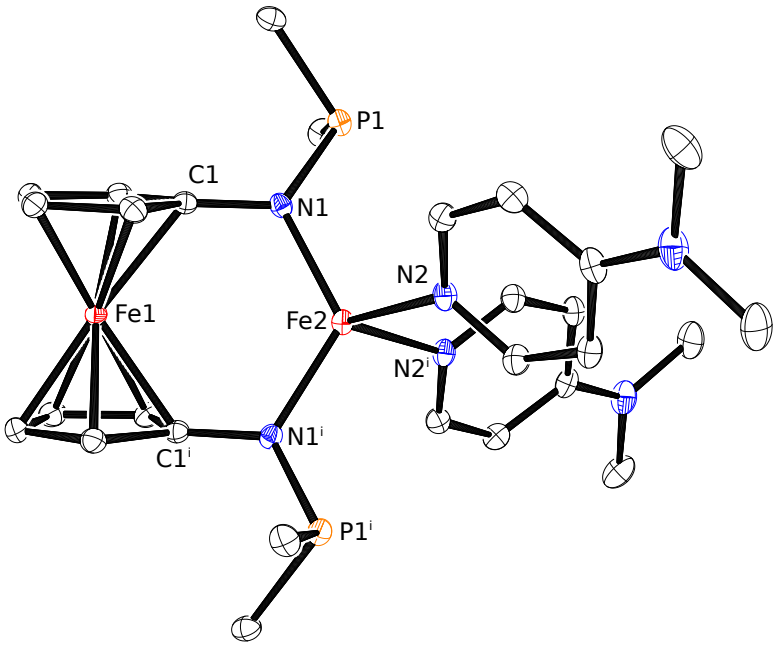

Figure 3.4: ORTEP diagram of **3.3** with ellipsoids drawn at 50% probability. All H atoms and ^{i}Pr methyl groups have been omitted for clarity. Selected bond lengths (Å) and angles (deg): Fe2-Fe1 3.6059(5); Fe1-N1 1.9650(15); Fe1-N2 2.1223(14); N1-P1 1.6855(15); N1-Fe1-N1^{i} 120.66(8); N2-Fe1-N2^{i} 91.55(8); N1-Fe1-N2 106.15(6).

ands[221–224] the doublet with ΔEq = 2.34 mm/s was assigned to the ferrocene iron center. The doublet with ΔEq = 1.02 mm/s, assigned to the trigonal planar Fe(II) center, displays an isomer shift value of 0.43 mm/s consistent with a HS Fe(II) ion. Trigonal planar iron complexes with a diamido phosphine donor set are relatively uncommon,[78,225,226] and to our knowledge, only one other has been characterized by Mössbauer spectroscopy (See Table 3.1).[111] While the quadrupolar splitting (1.02 mm/s) of the trigonal planar iron in **3.2** is substantially smaller than that of [Fe(NP)$_2$(NP)FeCl], there is some ambiguity in the latter as to whether the tetrahedral or trigonal planar iron center is being observed. However, the quadrupolar

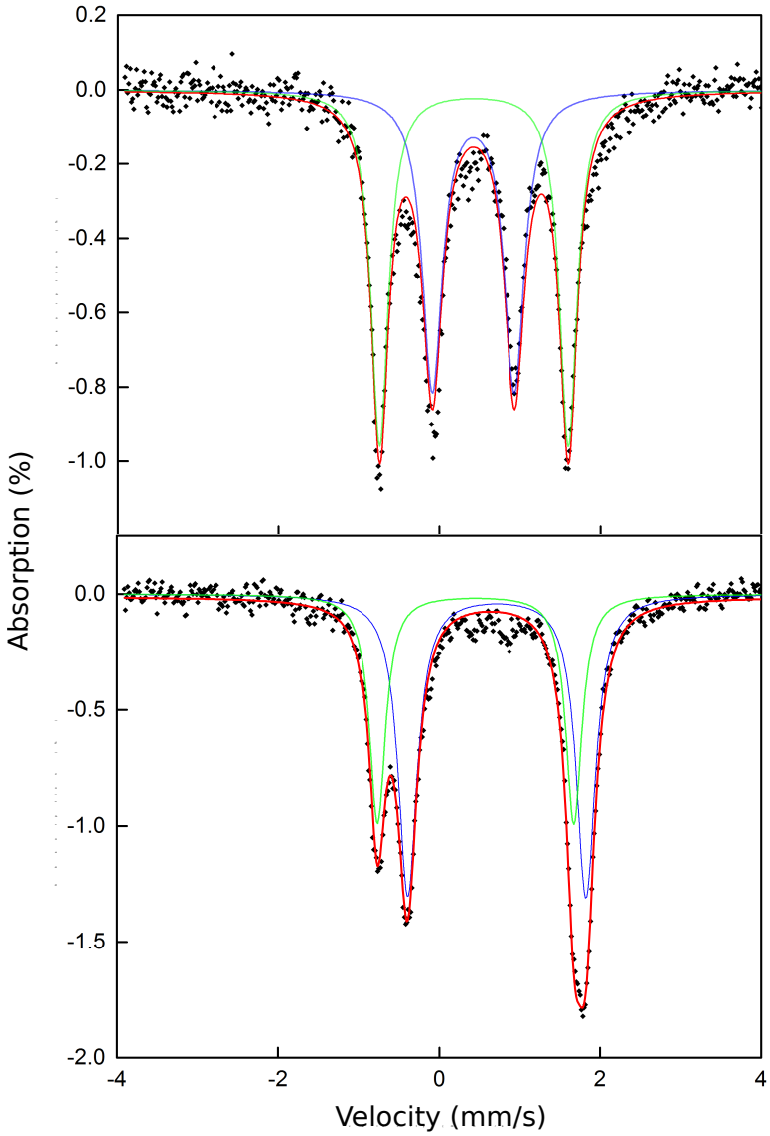

Figure 3.5: Zero field ^{57}Fe Mössbauer spectra of **3.2** (top) and **3.3** (bottom) recorded at room temperature. Black diamonds are data points from the Mössbauer experiment, green curves are fits for the ferrocene iron (δ = 0.43 mm/s, ΔEq = 2.34 mm/s for **3.2**; δ = 0.45 mm/s, ΔEq = 2.36 mm/s for **3.3**), blue curves are fits for the non-ferrocene iron centers (δ = 0.43 mm/s, ΔEq = 1.02 mm/s for **3.2**; δ = 0.71 mm/s, ΔEq = 2.22 mm/s for **3.3**), and red curves are fits for total contributions.

splitting of **3.2** is consistent with other trigonal planar species[227,228] particularly the electron-rich, dimeric $[Fe(N(SiMe_3)_2)_2]_2$.[229] Not surprisingly, in the mononuclear complex **3.3** the ferrocene iron displays nearly identical Mössbauer parameters to the ferrocene iron in **3.2**. The second doublet, attributed to the tetrahedral Fe(II) center, displays a typical isomer shift and quadrupolar splitting for HS tetrahedral Fe(II).[190,230–232]

To further investigate the coordination chemistry of $K_2[fc(NP)_2]$, **3.1**, we performed a salt metathesis with $CoCl_2(py)_4$. We were able to isolate a solid by conducting the reaction of **3.1** and $CoCl_2(py)_4$ in a hydrocarbon solvent such as pentane or toluene, to precipitate the product (compound **3.4**) directly. If the reaction is conducted in a more polar solvent the product rapidly decomposes. Fortunately, single crystals could be obtained by performing the metathesis in toluene at high concentration; the solid-state molecular structure is shown in Figure 3.6 along with selected bond lengths and angles. In order to confirm that the solid state molecular structure was consistent with the bulk sample we performed a powder X-ray diffraction analysis, see Figure 3.7.

The overall dimeric structure of **3.4** is similar to that of the iron-based **3.2**, but with one striking difference: whereas in **3.2** the non-ferrocene iron adopts a trigonal planar geometry, the cobalt center of **3.4** adopts a nearly square planar geometry as a result of an interaction with the iron of the ferrocene backbone. While the Co-Fe bond length in **3.4** is very similar to the sum of the van der Waals radii, the dramatic difference in Fe-M distances between **3.2**, 3.5341(3) Å and **3.4**, 2.8451(10) Å, suggests an electronic interaction is responsible for this nearly 0.7 Å contraction, as steric effects should be similar between the two complexes. One of the further consequences of this Fe-Co interaction in **3.4** is the disposition of the nitrogen

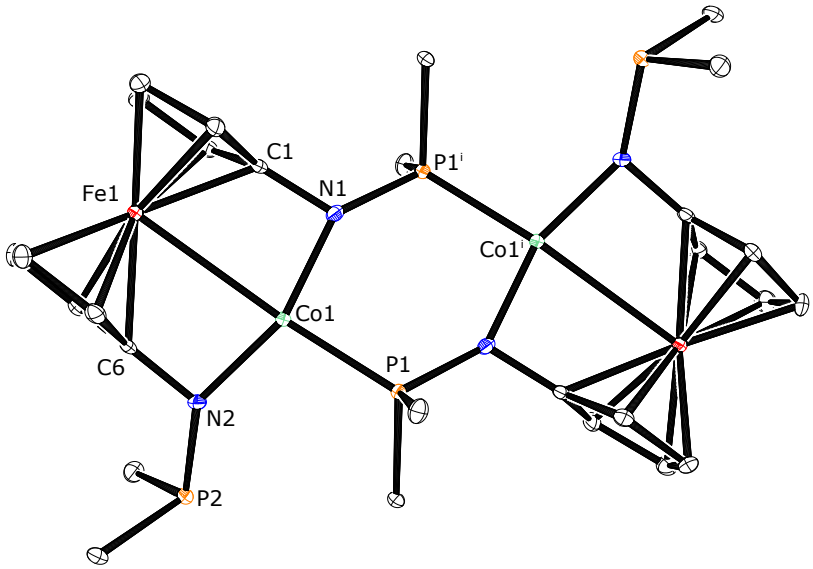

Figure 3.6: ORTEP diagram of **3.4** with ellipsoids drawn at 50% probability. All H atoms and ^{i}Pr methyl groups have been omitted for clarity. Selected bond lengths (Å) and angles (deg): Fe1-Co1 2.8451(10); N1-Co1 1.854(2); N2-Co1 1.877(2); N1-P1 1.676(2); N2-P2 1.697(2); Co1-P1 2.1562(11); N1-Co1-N2 159.64(9); P1-Co1-Fe1 166.90(2); N1-Co1-Fe1 80.50(7); N1-Co1-P1 96.19(6); C1-N1-Co1 95.64(15).

atoms, N1 and N2, in the 1,1'-diaminoferrocene backbone. The C1-N1-Fe1 angle of 115.12(2)° in **3.2** shows a relatively strain-free sp^2-hybridized nitrogen atom, in contrast to the more acute C1-N1-Co1 angle of 95.64(15)° in **3.4**. In addition, the Cp plane angle of the ferrocene backbone increases from 0.1° in **3.2** to 6.9° in **3.4**, which indicates more strain of the rigid backbone in the latter complex. Interactions between the iron of ferrocene and a metal bound by donor atoms in the 1,1' position are known including Fe-Pd[233–238] and Fe-Pt[239,240] interactions. Outside of the two aforementioned metals, only a few examples[133,134,221,241] of this kind of interaction have been reported. To our knowledge, **3.4** represents the first example of a ferrocene-stabilized group 9 metal. It is only the second example

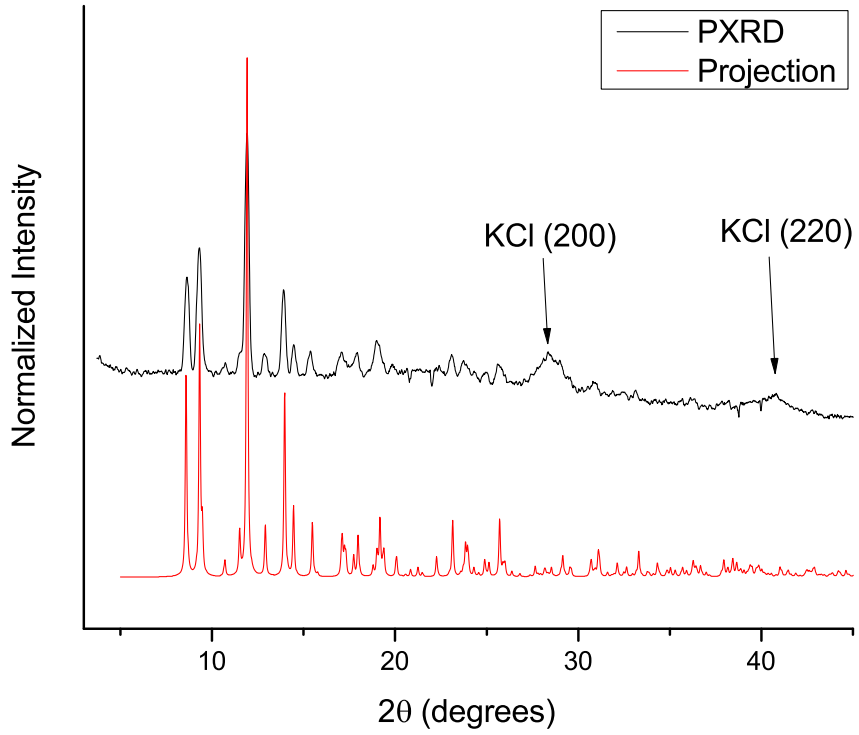

Figure 3.7: PXRD for bulk **3.4** compared to a projection obtained from single crystal X-ray diffraction data of **3.4**.

with a 1st row transition metal, the other being a titanium complex which can be thought of as a Lewis acid Lewis base interaction (d^6 Fe(II) $\rightarrow$ d^0 Ti(IV)).[133]

While the ferrocene iron centers in **1.50**, **3.2** and **3.3** display similar isomer shift and quadrupole splitting values, the Mössbauer spectrum of **3.4** displays a single quadrupole doublet for the ferrocene center, which has a contracted quadrupolar splitting of 2.01 mm/s. Figure 3.8 shows the overlay of the fits for the ferrocene centers in **3.2** and **3.4** illustrating the smaller quadrupolar splitting of the dicobalt derivative, **3.4**, compared to the diiron, **3.2**. A similar ferrocene-metal interaction has been recently characterized[221] for a closed-shell ruthenium complex of a

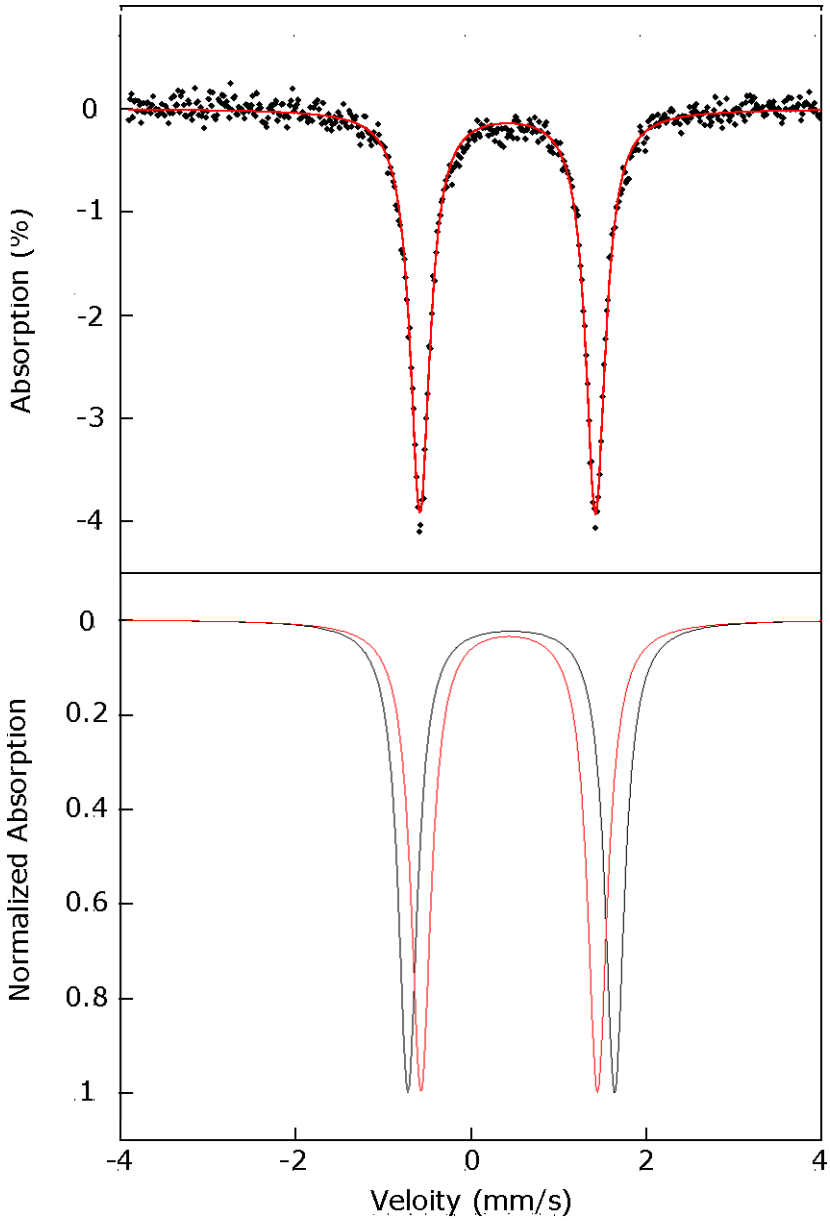

Figure 3.8: Zero field ^{57}Fe Mössbauer spectrum of **3.4** collected at room temperature fit as a quadrupolar doublet; δ = 0.42 mm/s, ΔEq = 2.01 mm/s (top) and an overlay of the ferrocene center fits for **3.2** in black and **3.4** in red, showing the contraction of the latter (bottom).

ferrocene diamide ligand. While the fc-M bond lengths are similar (Fe-Ru: 2.80 Å; Fe-Co: 2.84 Å), the ruthenium complex displays an even smaller quadrupolar splitting, 1.81 mm/s, possibly due to greater orbital overlap with the larger 4d metal ruthenium.

Table 3.1: Mössbauer parameters for **3.2**, **3.3**, **3.4** and related compounds.

Compound	Isomer Shift (mm/s)	Quadrupolar Splitting (mm/s)
1	0.48	2.52
3.2[a]	0.43	2.34
	0.43	1.02
3.3[a]	0.45	2.36
	0.71	2.22
3.4	0.42	2.01
$[Fe(NP)_2(NP)FeCl]$[b]	0.60	1.80
$(Fe(N(SiMe_3)_2)_2)_2$	0.58	1.02

[a] The iron of the ferrocene moiety is listed above; [b] (NP) : $N^iPrP^iPr_2$

3.1.3 Magnetic Measurements

In an effort to determine the spin states and gain insight into the electronic structure of **3.2**, **3.3** and **3.4** we performed Variable Temperature (VT)-magnetometry. Figure 3.9 shows the plots of effective magnetic moment (μ_{eff}) vs. T for **3.2**, **3.3** and **3.4**. The monomeric **3.3** displays a fairly constant μ_{eff} value from 300 K down to 55 K, with an average value of 5.1 μ_B. After 55 K the data undergo a brief rise to a maximum of 5.3 μ_B at 22 K before falling steeply to a minimum of 4.2 μ_B at 1.8 K. This data can be fit with a Curie-Weiss Law with parameters of C = 3.222(4) cm^3 K mol^{-1} and Θ = -1.89(6) K (see Figure D.1 for fit). The room temperature μ_{eff} value for **3.3** is higher than the spin only value of 4.9 μ_B expected[242] for high spin d^6; however, this is common with tetrahedral Fe(II) centers due to spin-orbit-coupling.[243] Examining **3.2** we see a room temperature magnetic moment of 6.6 μ_B

per dimer that slowly begins to decrease until ~125 K at which point μ_{eff} decreases to a minimum of 1.4 μ_B at 1.8 K. The gradual decrease of μ_{eff} with decreasing temperature is consistent with an antiferromagnetic exchange between the two trigonal planar iron centers. The combination of weak anti-ferromagnetic coupling and zero-field splitting creates a situation where modelling is not of significant value and was not pursued. We tentatively assign **3.2** as having two central HS Fe(II) centers (spin only: 9.8 μ_B) with weak antiferromagnetic coupling between the two trigonal planar iron centers. It should be noted that performing Evans method[244,245] on a C_6D_6 solution of **3.2**, yields a room temperature magnetic moment of 6.7 μ_B. The agreement between room temperature measurements in the solid state and in solution indicates that the dimeric nature of **3.2** is maintained in solution. The proposed antiferromagnetic exchange is likely intramolecular mediated through the N-P bridges or by direct exchange and not by intermolecular exchange processes. Due to a large Fe-Fe distance of 3.9241(5) Å, we prefer magnetic exchange through the amidophosphine bridges as a rationale for the low magnetic moment.

In Figure 3.9, the overall shape of the μ_{eff} vs T curves for **3.2** and **3.4** are similar; however, the most striking difference is the low μ_{eff} for **3.4** throughout the entire temperature range. Starting at 4.2 μ_B at 300 K (confirmed by Gouy balance) μ_{eff} gradually decreases to 3.0 μ_B at 16 K, indicative of weak antiferromagnetic coupling. Below 16 K μ_{eff} sharply falls to a value of 1.2 μ_B at 1.8 K, which is attributed to a combination of Zeeman and zero field splitting; again modelling was not pursued. The low room temperature value of μ_{eff} is higher than the spin only value but consistent with other LS square planar Co(II) centers with some second-order spin-orbit coupling.[199,242,246] Based on structural and magnetic analysis of **3.2** and **3.4** it is evident that the electronic structures of these two compounds are

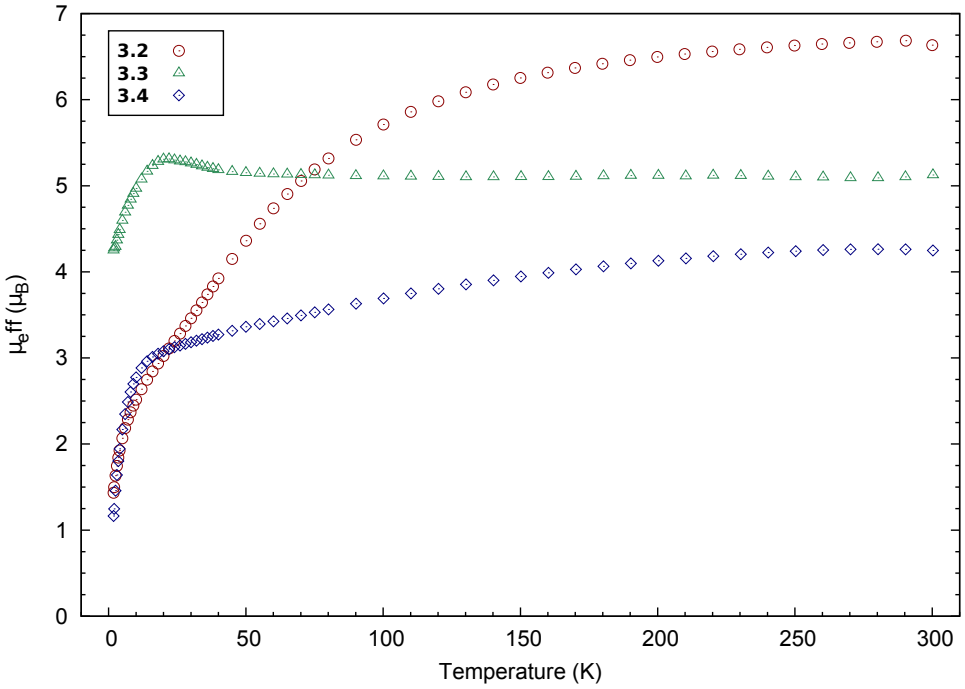

Figure 3.9: Variable-temperature effective magnetic moment (μ_{eff}) for **3.2**, **3.3** and **3.4** collected under an applied DC field of 1 T.

drastically different. The observation of LS Co(II) centers in the dimer further supports a Fe-Co interaction in **3.4**, as the additional donor interactions would result in a stronger ligand field and therefore a low spin complex.

3.1.4 DFT Calculations

In order to confirm the spin state assignments obtained from VT-magnetomerty, and investigate the Fe-Co interaction in **3.4** we turned to DFT methods. We performed geometry optimizations on the full molecules of **3.2** and **3.4** using the atomic coordinates obtained from the solid-state molecular structures as an initial geometry. Both LS and HS configurations for **3.2** (S = 0 and S = 4) and **3.4** (S = 1 and S = 3) were evaluated at the BP86[247,248] level of theory using triple-ζ-valence

basis sets. The HS (S = 4) and LS (S = 1) spin states were found to be more stable for **3.2** and **3.4** respectively, supporting the spin state assignments made based on VT-magnetometry. In both cases, the geometry obtained *in silico* for the more stable spin state is very similar (See Figure B.1 and Figure B.2 in Appendix B) to the geometry obtained by single crystal diffraction studies; the less stable spin states show large distortions from the experimentally determined coordinates. A few of the observed and calculated bond metrics are compared in Table 3.2, for a more expansive set see Table B.3.

Table 3.2: Computed and experimental bond metrics for **3.2** and **3.4**.

Bond Metric	**3.2**			**3.4**		
	expt	S = 0	S = 4	expt	S = 1	S = 3
Fe – M (Å)	3.5341(4)	2.914	3.522	2.845(1)	2.871	3.203
M – P (Å)	2.4442(4)	2.160	2.439	2.156(1)	2.182	2.403
N–M–N (°)	123.47(5)	157.17	124.85	159.64(9)	158.90	139.97

With the spin states confirmed we examined the bonding between Fe and Co in **3.4**. Through NBO analysis, the Mayer bond order[249,250] for the Fe-Co unit was calculated to be 0.21, indicative of a weak but significant bonding interaction. In comparison, **3.2** displays a Fe-Fe Mayer bond order of 0.04. Due to the scarcity of weak M-M bonds between 3d metals that have been characterized using the Mayer bond order, direct comparison is difficult. The carbonyl cluster $Fe_3(CO)_{12}$ and dimeric $[CpCoH(CO)]_2$ display bond orders of 0.42[251] and 0.342[252] respectively, and are described as single bonds. However, other complexes of 1,1'-substituted ferrocene based ligands, which display a Fe-M interaction have been studied. For complexes with Pd(0.26), Pt(0.31) and Ru(0.26) the Mayer bond order is typically less than other metal metal single bonds.[134,221]

Gratifyingly, three of the high lying molecular orbitals show bonding interactions between the iron and cobalt centers. HOMO-6 in **3.4** is a highly delocalized orbital (See Figure B.11) which displays an Fe-Co σ interaction. In addition a pair of π bonding orbitals can be found, HOMO - 9/10 see Figure 3.10. For **3.2** the high lying orbitals, HOMO $\rightarrow$ HOMO-20, were examined for similar interactions and none were found; a complete set of frontier molecular orbitals for **3.2** and **3.4** are shown in Figure B.3 to Figure B.11.

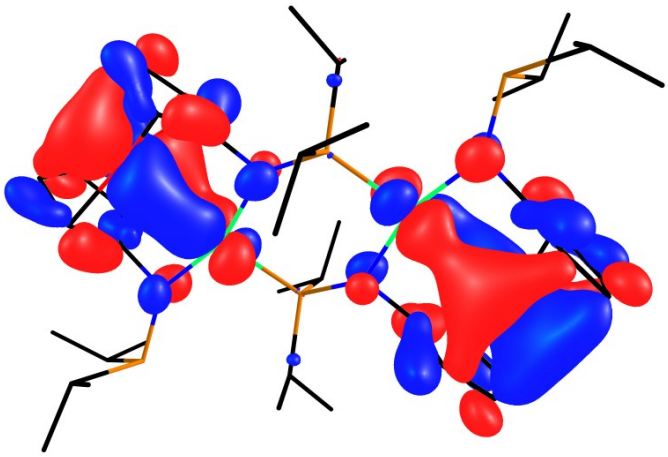

Figure 3.10: HOMO-9_α for **3.4**. HOMO-10_α, HOMO-7_β and HOMO-8_β are similar.

The optimized coordinates of **3.4** were then used in subsequent analysis using NBO 6.0.[253] Analysis of the natural bond orbitals reveals a sigma overlap between a filled valence orbital on iron and an empty σ^* orbital between cobalt and phosphorus, as shown in Figure 3.11. The natural localized molecular orbitals generated from these natural bond orbitals are predominately iron based with a 2.2% contribution from cobalt.

Furthermore, NBO second order perturbation analysis of donor-acceptor inter-

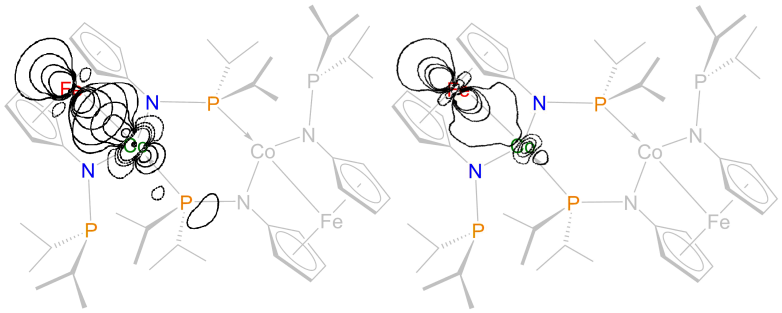

Figure 3.11: Contour plots of Left: NBO 91 (Fe) and NBO 250 (Co-P*) overlap. Right NLMO 91.

actions reveals several stabilizations from filled orbitals on cobalt to empty orbitals in the ferrocene unit (11.41 kcal/mol) and vice versa (7.79 kcal/mol). In addition to direct interactions, there are several donations from filled cobalt-ligand bonding orbitals to empty orbitals on iron (10.42 kcal/mol) for a total of 29.62 kcal/mol. Note that these energy values are described for only one Fe-Co pair. For a detailed list of relevant second order interactions see Table B.4 The nearly equal energy contributions of Fe $\rightarrow$ Co and Co $\rightarrow$ Fe are surprising given that a recently reported iron-ruthenium interaction[221] showed only donation from filled ferrocene-based orbitals to empty ruthenium-based orbitals.

3.1.5 Summary and Conclusions

Using the dianionic ferrocene-based diphosphinoamide ligand precursor, we have been able to prepare dimeric base metal complexes that incorporate iron(II) and cobalt(II) centers symmetrically bridged by phosphinoamide units. Each of these dimers exhibits similar structures that involve a central six-membered heteroatom

ring flanked by closed shell ferrocene units that also display uncoordinated phosphine moieties. The key difference in these structures is evident in the geometries of the open-shell iron and cobalt centers. In the diiron dimer **3.2**, each iron is trigonal planar, while in the dicobalt dimer **3.4**, each cobalt displays a square planar geometry, due to a significant interaction with each ferrocene iron center. This interaction has been confirmed by DFT analysis showing bonding orbitals encompassing the iron and cobalt centers and NBO analysis suggesting that a filled valence orbital on ferrocene donates to an low-lying σ^*_{Co-P} orbital.

Other ferrocene $\rightarrow$ M bonding interactions are well known and have been reported for M = Pd, Pt, Ru and Ti, all of which display closed-shell configurations. To our knowledge, this is the first example of a ferrocene $\rightarrow$ M bond to an open-shell metal ion. A rationale for the difference in the interaction of the two dimeric complexes reported here is likely that the HS Fe(II) centers in **3.2** do not have available orbitals for donation from the ferrocene unit, whereas in **3.4** the low-spin Co(II) centers mimic closed-shell Pd(II) and Pt(II) ions with available metal-based orbitals for interaction with the ferrocene Fe centers. Chapter 4 will focus on the reactivity of these structurally unique dimers.

3.2 Attempted Synthesis of Group 10 Phosphinoamides

3.2.1 Introduction

In the previous section we examined the coordination chemistry of a bisamidophosphine ferrocene ligand by performing salt metathesis reactions of **3.1** with iron and cobalt halides to produce metal complexes of the type $([fc(NP^iPr_2)_2]M)_2$. During these syntheses, we discovered that the iron center of the ferrocene backbone can

act as a donor to the cobalt center, yielding the square-planar coordination environment observed in **3.4**. While square planar Co(II) complexes like **3.4** are becoming more common because of their potential application in catalysis ,[3,254–263] the number of square planar d^7 metal complexes pales in comparison to the plethora of square planar d^8 complexes based on group 10 metals. For this reason, we wondered if the group 10 metal complexes would be more stable than the cobalt derivative **3.4**. Therefore, we endeavoured to synthesize compounds of the type $([fc(NP^iPr_2)_2]M)_2$ where M = Ni, Pd, Pt. If indeed these diamagnetic complexes were more stable than **3.4**, this would allow us to characterize the Fe$\rightarrow$ M donation in solution and examine any potentially non-innocent effects this interaction would have on small molecule activation.

3.2.2 Attempted Synthesis of Group 10 Complexes

Initial synthetic efforts were directed toward platinum in order to take advantage of the NMR spectroscopic handle provided by the spin-active ^{195}Pt nucleus. We initially tried the same salt metathesis methodology, shown to be successful with iron and cobalt. However, using the dipotassium salt **3.1** and a variety of PtL_2X_2 (Scheme 3.4) metathesis reagents resulted in intractable mixtures, which, when analyzed by solution phase ^{31}P NMR spectroscopy, did not display any evidence of phosphorus-platinum coupling. Salt metathesis with Pd(II) sources (Scheme 3.4) resulted in similarly intractable mixtures. In addition, based on the observation of black precipitate in both the Pd and Pt reaction mixtures, we concluded that reductive elimination to Pt^0 was too facile with this electron rich ligand set.

An alternative synthetic strategy was attempted involving a two step coordination and deprotonation protocol using $PtCl_2(PPh_3)_2$ as the metal precursor. Stirring

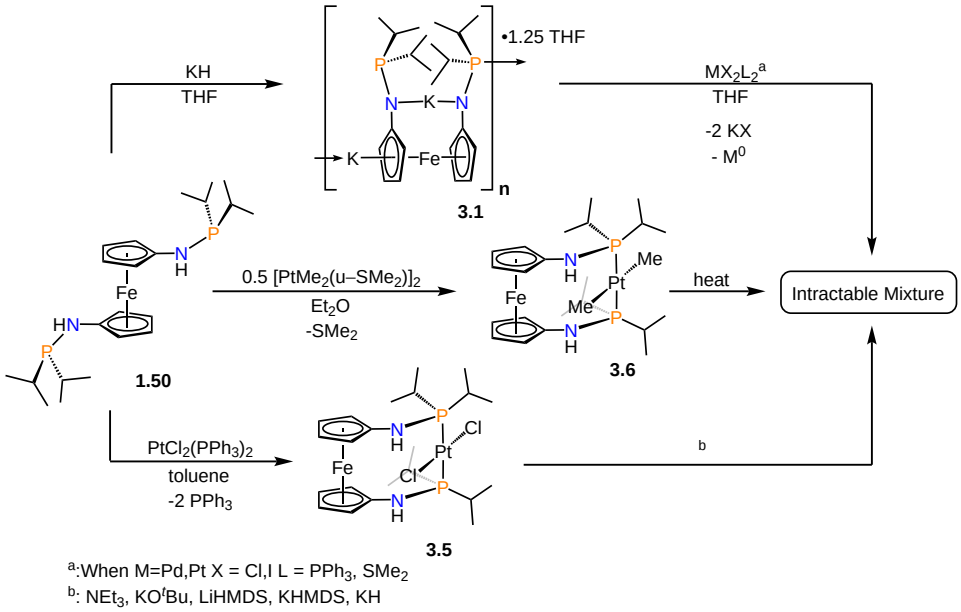

Scheme 3.4: Attempted synthesis of $([fc(NP^{i}Pr_2)_2]M)_2$ where M = Pd, Pt

a solution of the diphosphinoamine **1.50** with $PtCl_2(PPh_3)_2$ and monitoring by ^{31}P NMR spectroscopy leads to a spectrum with two new resonances corresponding to a major and minor product. Both resonances display coupling to platinum and are separated by a mere 0.71 ppm. The $^{1}J_{P,Pt}$ coupling constants for the major and minor products are 2547 Hz and 2565 Hz, respectively, consistent with a platinum-phosphorus bond. Due to the similar chemical shifts and coupling constants we tentatively assigned these resonances to *cis*/*trans* isomers of $[fc(NHP^{i}Pr_2)_2]PtCl_2$. The ^{1}H NMR spectrum displays two N-H resonances at 5.64 and 5.95 ppm, with the major N-H resonance split into a *virtual* triplet, which, upon ^{31}P decoupling collapses to a singlet. Virtual coupling requires strong coupling between the equivalent phosphorus nuclei suggesting that the major product is the species with the *trans* arrangement of the phosphorus atoms, shown for **3.5** in Scheme 3.4. Unfor-

tunately, deprotonation of this complex with a wide variety of bases led to either no reaction (NEt_3, KO^tBu) or decomposition to an intractable mixture (KHMDS, LiHMDS, KH, MeLi). As we were unable to generate $([fc(NP^iPr_2)_2]Pt)_2$ using this route, complete characterization of **3.5**, including determination of the solid state molecular structure, was not pursued.

A third synthetic route was envisioned whereby a platinum alkyl complex of **1.50** could undergo alkane elimination to generate the desired $([fc(NP^iPr_2)_2]Pt)_2$. After converting $PtCl_2(SMe_2)_2$ to $(Pt(\mu\text{-}SMe_2)Me_2)_2$[264] addition of **1.50** resulted in conversion, as evidenced by ^{31}P NMR spectroscopy, to a single product **3.6**, with $^1J_{P,Pt}$ = 2029 Hz. Characterization by ^1H NMR spectroscopy reveals the same pattern as **3.5** with one additional resonance for the methyl groups at 0.97 ppm. Gentle heating (50°C) of **3.6** results in no reaction and more aggressive heating (100°C) results in decomposition of **3.6** and formation of a platinum mirror on the inside of the NMR tube. No resonances are observed in the ^1H NMR spectrum for methane or ethane, however, several low intensity signals were observed between 0 and 1 ppm.

Our inability to synthesize phosphinoamide complexes of platinum and palladium led to investigations of the coordination chemistry of Ni(II), another d^8 metal ion, unique from its heavier congeners due to its ability to adopt both square planar and tetrahedral coordination geometries.[265,266] We began by performing salt metathesis between **3.1** and a variety of NiX_2L_2 compounds where X = Cl, Br and L = DME, THF, PPh_3. In all of the reactions a new diamagnetic compound, **3.7** in Scheme 3.5, was observed by ^{31}P NMR spectroscopy in varying purity.

The original synthesis of **3.7** was performed using $NiCl_2(PPh_3)_2$, however, subsequent syntheses have utilized the much cheaper and more atom economical

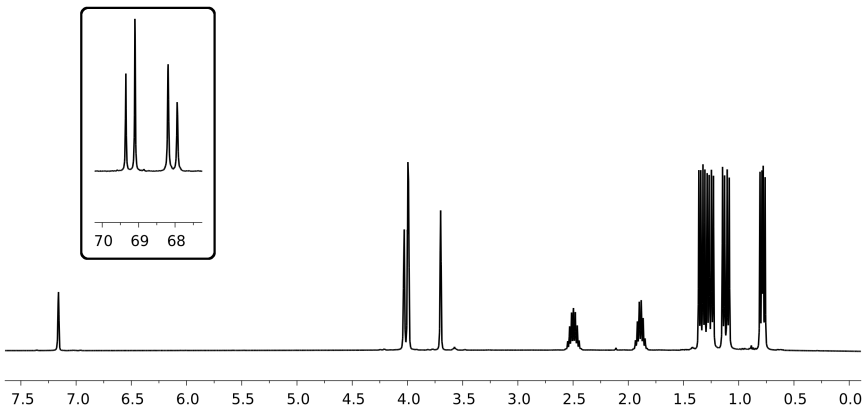

Figure 3.12: $^{31}P\{^{1}H\}$ (162 MHz, insert) and ^{1}H NMR (400 MHz) spectra of compound **3.7** in C_6D_6

$NiBr_2$. Examination of the ^{31}P and ^{1}H NMR spectra of **3.7**, shown in Figure 3.12, suggested that we had indeed synthesized the desired $([fc(NP^{i}Pr_2)_2]Ni)_2$ complex. The ^{31}P NMR spectrum displays two resonances coupled to one another ($^{3}J_{P,P}$ = 40.7 Hz) with very similar chemical shifts ($\Delta\delta = 1.16$ ppm). The ^{1}H NMR spectrum is consistent with inequivalent ligand arms, displaying 4 sets of resonances for the *iso*-propyl protons, as would be expected for a complex with an analogous structure to **3.4**. The stability of **3.7** was demonstrated by multiple heating and cooling cycles from 25°C to 80°C followed by ^{1}H NMR analysis, showing no significant compound degradation.

Single crystals of **3.7** were grown by cooling a toluene/hexanes solution to -40 °C, and the solid-state molecular structure was established by single-crystal X-ray diffraction, and shown in Figure 3.13. Surprisingly, the structure shows a compound containing no nickel and a new P-N bond formed between the phosphorus of one phosphinoamide and the nitrogen of the other ligand arm, a completely unexpected result. Examination of the bond lengths obtained from the solid-state

molecular structure shows that the N1-P1 bond length (1.565(3) Å) is substantially shorter than the other two P-N distances (> 1.7 Å) suggesting that an oxidation of one amidophosphine has occurred and there is now a formal double bond between N1-P1. The N1-P1 distance of **3.7** is comparable to other phosphinimines from our group (1.5594(1) Å) and others (∼1.58 Å).[267]

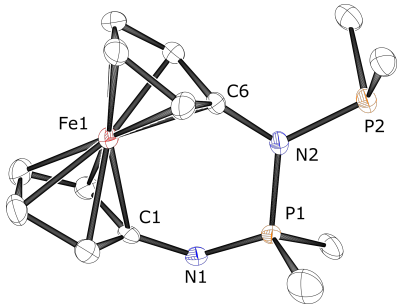

Figure 3.13: ORTEP diagram of **3.7** with ellipsoids drawn at 50% probability. All H atoms and ^{i}Pr methyl groups have been omitted for clarity. Selected bond lengths (Å) and angles (deg): N1-P1 1.565(3); N2-P2 1.750(3); P1-N2 1.720(3) C1-N1 1.391(5); C6-N2 1.443(5); Fe1-P1 3.5182(12); N1-P1-N2 114.95(16); P1-N1-C1 126.4(3); P1-N2-C6 119.4(2); P1-N2-P2 1.479(5); Cp tilt angle 9.40(17).

The salt metathesis reaction with nickel is more complicated than with iron or cobalt. Balancing the equation, Ni^0 and KBr must be produced in the reaction. We attempted to identify a putative Ni intermediate in the reaction by trapping with PMe_2Ph. Adding 5 eq of PMe_2Ph to the reaction of the dipotassium salt **3.1** and $NiBr_2$ yields a reaction mixture with a resonance at -9.5 ppm in the ^{31}P NMR spectrum, attributed to $Ni(PMe_2Ph)_4$. All other resonances in the spectrum could be attributed to compound **3.7** and excess PMe_2Ph.[268] The addition of PMe_2Ph did not allow us to observe a Ni intermediate, however, the observation of $Ni(PMe_2Ph)_4$ is evidence for the production of Ni^0 during the course of the reac-

tion. We propose that a Ni(II) intermediate like $(fc(NP^iPr_2)_2Ni)_2$ (or a monomeric complex $fc(NP^iPr_2)_2NiL_x$) is initially formed before rapid reductive elimination occurs to yield **3.7** (Scheme 3.5). All attempts to isolate or characterize the proposed $(fc(NP^iPr_2)_2Ni)_2$ intermediate, including low temperature ^{31}P and ^1H NMR studies, were unsuccessful.

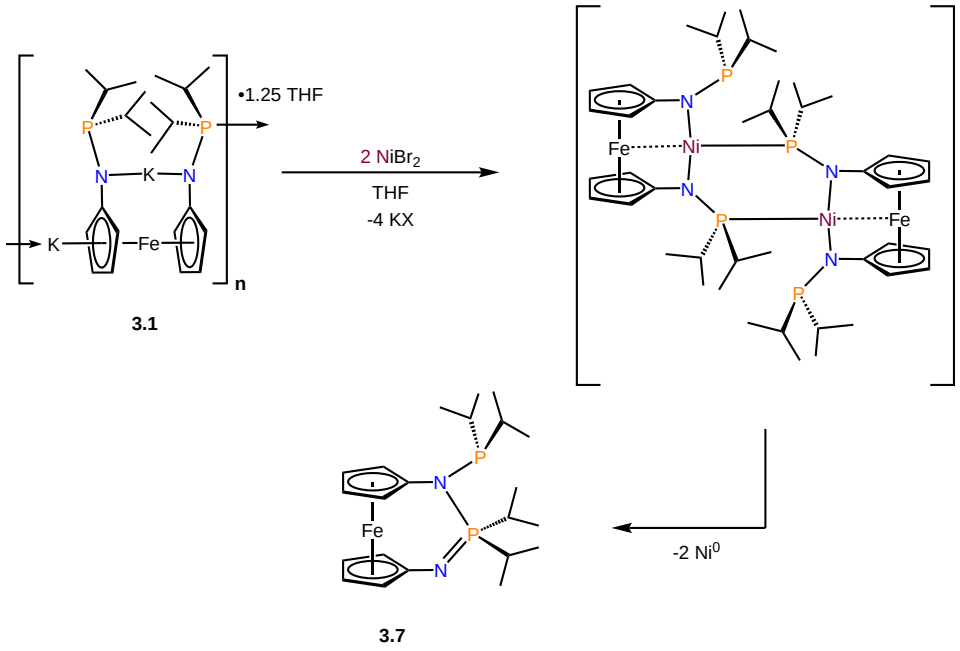

Scheme 3.5: Synthesis of **3.7**.

The similar chemical shifts of the two phosphine environments (Figure 3.12) in **3.7** was surprising given that one is a P(V) phosphinimine and one is a P(III) phosphinoamine. We undertook VT-NMR spectroscopy studies to identify any exchange processes and, under gentle heating (328 K), observed the coalescence of the phosphorus resonances (Figure 3.14). This was surprising as the exchange of the inequivalent phosphorus atoms requires cleavage and formation of a P-N bond on the NMR time scale. Repeating this experiment with multiple heating and

cooling cycles does not result in product decomposition; the original spectra are observed every time upon returning to room temperature. Unfortunately, we were not able to fully resolve the two signals at low temperature because at temperatures below 209 K solubility issues prevent the collection of quality data. There is no indication from Figure 3.14 that the signals are fully separated even at 209 K.

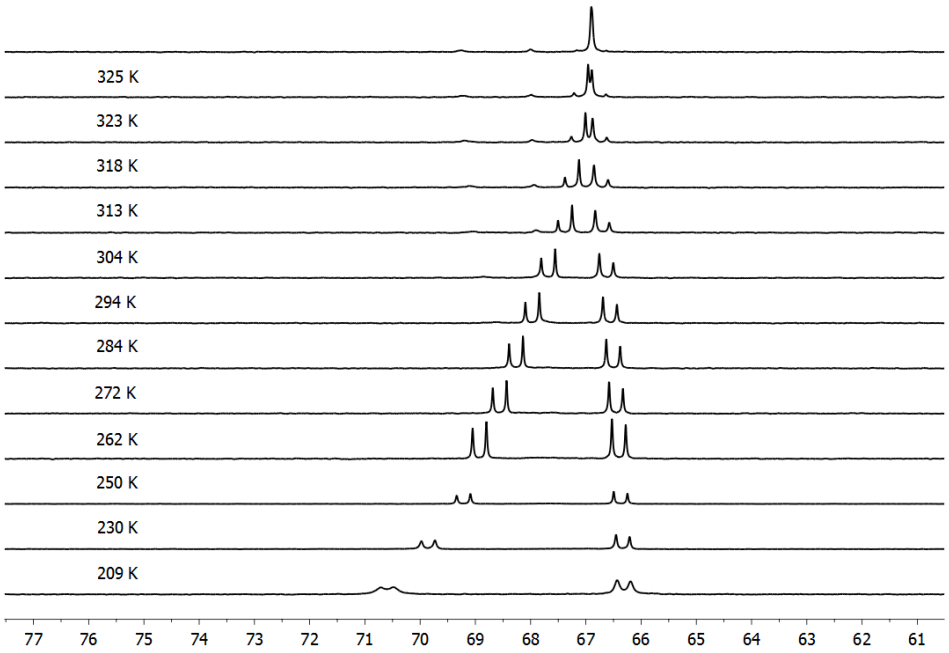

Figure 3.14: VT-^{31}P (162 MHz) NMR spectra of compound **3.7** in d_8-toluene

To the best of our knowledge compounds like **3.7** where a $R_2P{-}NR{-}PR_2{=}NR$ linkage is present are virtually unknown, with only one report of the protonated cation $R_2P{-}NR{-}PR_2{-}NHR^+$.[269] However, aryl phosphoramidines $ArNHPR_2NAr$ and the deprotonated phosphoaramidinates are known and the latter have been shown to stabilize copper(I) carbenes[270] and zirconium complexes competent in ethylene polymerization.[271] In these systems, no ligand rearrangements are re-

ported even at elevated temperatures up to 353 K, indicating that the phosphoramidinate linkage is not inherently labile. We suggest that the chemical exchange in **3.7** is triggered by a delocalization of electron density from the Cp ring into the aminophosphine arm of the ligand, breaking the P-N single bond (**A** in Scheme 3.6). The iminophosphoranide produced (**B**) can attack the phosphorus atom resulting in a rearomatization of the Cp ring (**C**). However, the lone pair of the phosphorus(III) center could also trigger the same P-N bond cleavage and this possibility can not be ruled out.

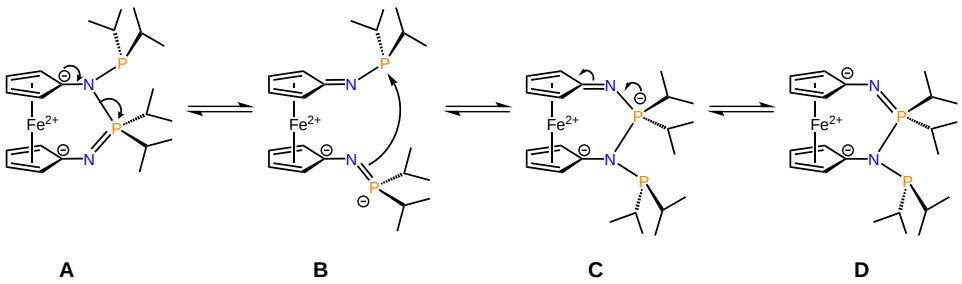

Scheme 3.6: Proposed mechanism of exchange in **3.7**.

3.2.3 Nickel Complexes of Unlinked Phosphinoamides

As previousely mentioned, compounds of the type RN=PR'_2-NR-PR'_2 are unknown. If the reaction between $NiBr_2$ and **3.1** could be generalized to unlinked phosphinoamides this reaction could provide a simple route to neutral unsymmetric imine / phosphine ligands like compound **3.8** in Scheme 3.7. A potential reaction scheme is shown in Scheme 3.7, whereby unsymmetric ligands could be constructed in two steps starting from anilines and chlorophosphines. In order to investigate this possibility we began by synthesizing a monomeric phosphinoamine that we had previously used,[109] $ArNHP^iPr_2$, where Ar = 3,5-dimethylphenyl, **3.9**. Subsequently, **3.9**

was treated with potassium hydride and the resulting phosphinoamide, **3.10**, was fully characterized.

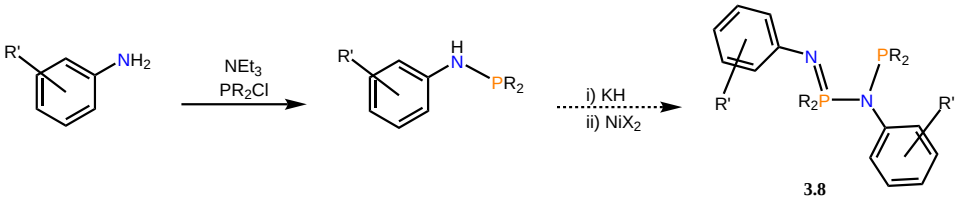

Scheme 3.7: Attempted synthesis of asymmetric P,N ligands.

Treating **3.10** with $NiBr_2$ results in an immediate reaction to form a new compound. While the symmetry displayed in the ^{1}H and ^{31}P NMR spectra is consistent with coupled phosphinoamides, the chemical shifts of the phosphorus resonances were highly separated (68.8 ppm and 29.9 ppm) in contrast to that observed for **3.7**. In addition, the integration of aryl and *iso*-propyl proton resonances indicates that there are twice as many $P^{i}Pr_2$ groups as NAr groups. Again, clarity was established only after single crystals were grown for X-ray diffraction. The solid-state molecular structure is shown in Figure 3.15, and shows a very strange and unexpected compound, **3.11**, which contains two nickel ions, two bridging phosphinoamide ligands and two terminal phosphide ligands. The Fenske group has previously reported salt metathesis of $Li[PhNPPh_2]$ with $NiCl_2(PPh_3)_2$ and have found that during salt metathesis ligand rearangments are common,[272] however, neither of the compounds reported are analogous to compound **3.11**.

Examining the solid-state molecular structure more closely we see that the nickel atoms have adopted a square planar geometry (sum of internal angles 359.7°, τ_4[273] = 0.25) involving a Ni-Ni bond. Metal-metal interactions are known in nickel(II) dimers,[274,275] however, in these cases the square-pyramidal nickel atom

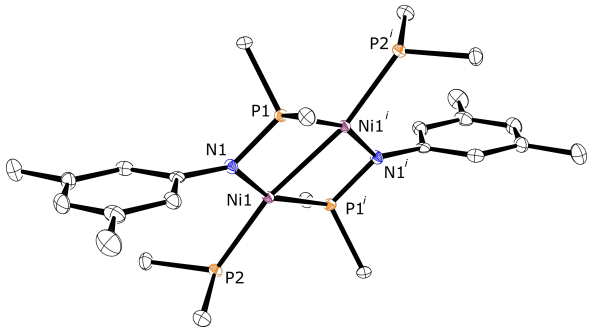

Figure 3.15: ORTEP diagram of **3.11** with ellipsoids drawn at 50% probability. All H atoms and ^{i}Pr methyl groups have been omitted for clarity. Selected bond lengths (Å) and angles (deg): Ni1-Ni1^{i} 2.4741(6); Ni1-N1 1.9008(5); Ni1-P1 2.5983(7); Ni1-P1^{i} 2.1239(5); Ni1-P2 2.1952(5); N1-P1 1.6402(4); P2-Ni1-N1 100.12(2); P2-Ni1-P1^{i} 102.78(2); P1-N1-Ni1 94.121(18); 109.08(2).

is surrounded by 4 donor atoms from the ligands and the metal-metal interaction is normal to the donor plane. In contrast, the Ni(II) ions in **3.11** are bound by only three donor atoms and the metal-metal bond is in the donor plane. Another interesting structural feature of **3.11** is the short N1-P1, P1-Ni1^{i} and long N1-Ni1 distances. As discussed in Chapter 1, the N-P bond length of phosphinoamine ligands can be invaluable in characterizing the ligand as one of two possible resonance structures (see Figure 1.3): phosphinoamide or iminophosphoranide. In this case, the contracted P-N bond in combination with a weaker and longer N-Ni, compared to **3.2** and **3.4**, bond suggests that the iminophosphoranide resonance structure is a better description of this compound.

Although **3.11** is structurally interesting it seems as though our goal of a general methodology for the coupling of amidophosphines is not possible by this route. The product obtained, **3.11**, clearly does not account for all the starting materials and by mass balance the by-product should be ArNNAr where Ar = 3,5-

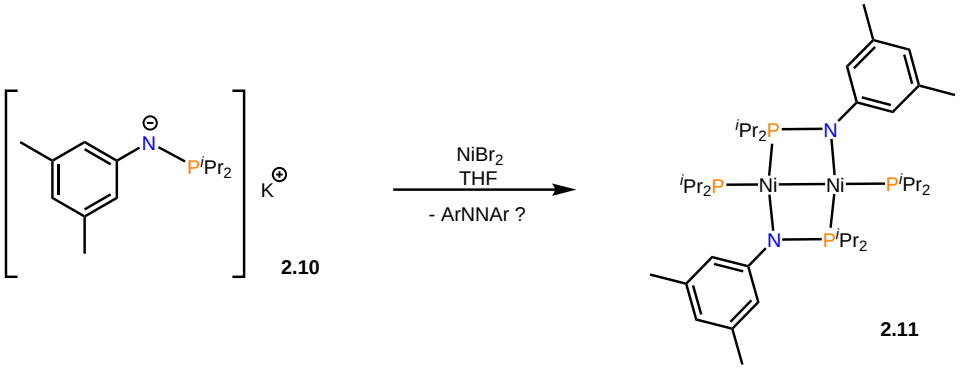

Scheme 3.8: Reaction between **3.10** and $NiBr_2$.

dimethylphenyl. However, we were unable to detect this byproduct using GC-MS or ^{1}H NMR spectroscopy.

3.3 Conclusions and Future Directions

The diphosphinoamide ligand, compound **1.50**, has been successfully installed on iron(II) and cobalt(II) using a salt metathesis methodology. While both compounds display the same overall dimeric structure, the cobalt(II) complex shows an additional interaction with the iron atom in the ferrocene backbone. This interaction has been characterized using X-ray crystallography and ^{57}Fe Mössbauer spectroscopy, and studied using DFT. The iron compound, **3.2**, has been shown to maintain its dimeric structure in solution until a significantly strong donor such as pyridine or *p*-dimethylaminopyridine is added. On the other hand, **3.4** undergoes rapid decomposition in solution before it can be characterized. Attempts at forming complexes of group 10 metals led to a reductive elimination and formation of **3.7** in the case of nickel. Attempts to generalize this reaction to intermolecular coupling of phosphinoamides were unsuccessful. Moving forward, **3.2** will be subjected to a battery of

experiments with the aim of characterizing how this polyiron system behaves under reducing and oxidizing conditions as well as its binding and activation modes for a variety of small molecules. It is impractical to study the reactivity of **3.4** due to it's instability in solution and while the reactivity of **3.3** could be interesting it is beyond the scope of this thesis.

Chapter 4

Small Molecule Activation with an Iron Phosphinoamide Dimer

Success consists of going from failure to failure without loss of enthusiasm. — Winston Churchill

4.1 Reactions with Hydrogen and Carbon Monoxide

4.1.1 Reaction with Hydrogen

As discussed in Chapter 1, iron complexes containing amido and imine donors can catalyze hydrogenation/dehydrogenation and transfer hydrogenation reactions.[57,58,60,61] Unfortunately we quickly discovered that compound **3.2** is not an appropriate catalyst for acceptorless alcohol dehydrogenation or transfer hydrogenation reactions. Compound **3.2** reacts rapidly with alcohols producing the protonated bis(phosphinoamine) ligand, **1.50**, as evidenced by ^{1}H NMR spectroscopy. No additional products are observed by ^{1}H NMR spectroscopy and a likely end-state for the iron is the insoluble material, isolated from the reaction mixture. Interestingly, reaction of compound **3.2** or **3.1** with acetonitrile also produces compound

1.50. The fact that compound **3.2** reacts with acetonitrile but not toluene allows us to put limits on the pK_a of compound **1.50** (31.3 – 41).[276,277]

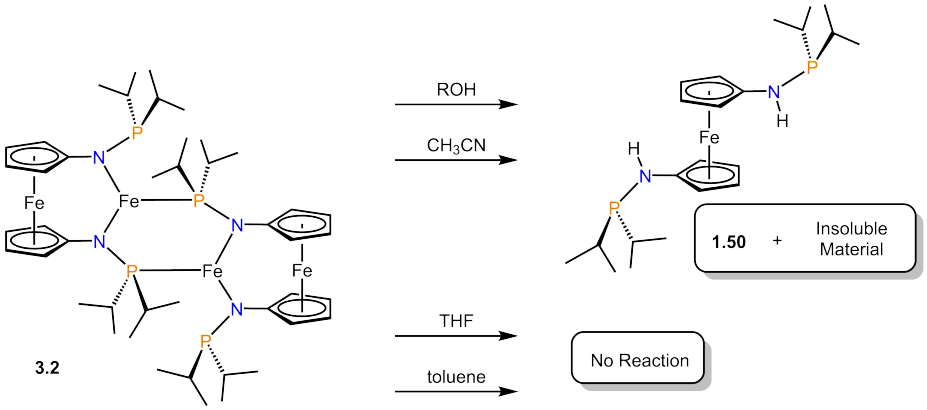

Scheme 4.1: Reaction of phosphinoamide salts with various solvents

In order to investigate whether compound **3.2** could catalyze hydrogenation reactions we examined reactions of **3.2** with H_2. When a toluene solution of **3.2** was exposed to H_2 gas, a color change was observed from dark brown to light orange, along with concomitant formation of a dark precipitate. When the volatiles were removed and the residue was redissolved in C_6D_6 a crude NMR spectrum was obtained that contains resonances attributed to **1.50** in the diamagnetic region of the spectrum and no major resonances in the paramagnetic regions. In order to determine whether adventitious water was responsible for the formation of **1.50**, side by side hydrogenations of **3.2** and the potassium salt **3.1** were performed, as shown in Scheme 4.2. While hydrogenation of the iron dimer (**3.2**) produced protonated ligand, no reaction was observed in the hydrogenation of compound **3.1**, thus eliminating the possibility of any trace H_2O.

The production of compound **1.50** suggests a heterolytic cleavage of H_2 occurs over the Fe–N bonds in compound **3.2**. We propose that once all the Fe–N

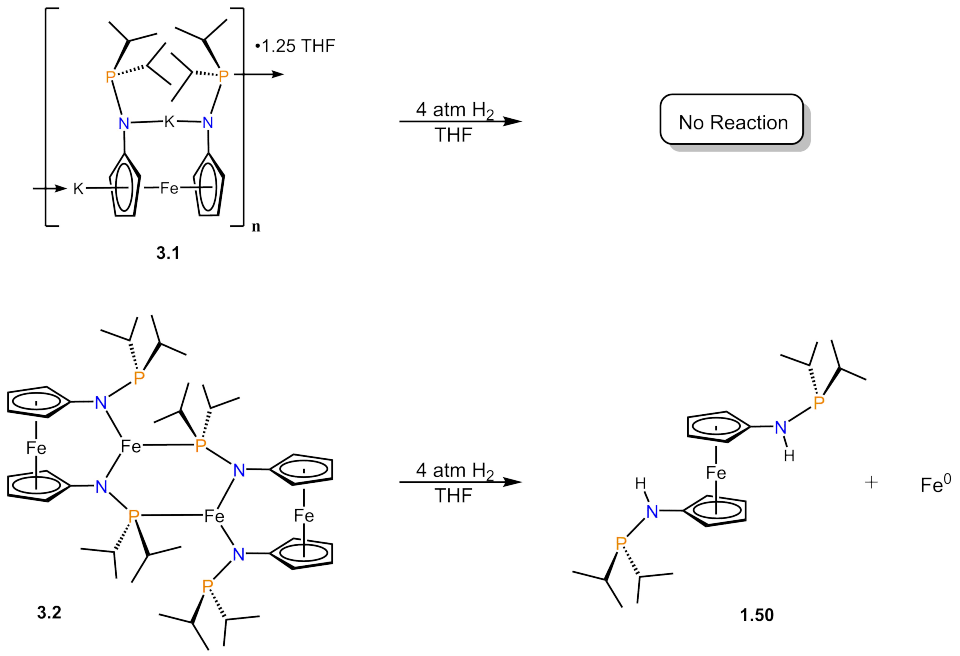

Scheme 4.2: Reaction of phosphinoamide salts with dihydrogen

bonds are hydrogenated, the resulting "[fc(NHP^{i}Pr$_2$)$_2$]FeH$_2$" intermediate decomposes via reductive elimination forming H_2, Fe^0 and **1.50**. We were able to support this proposal by observing that the solids produced in the reaction mixture are attracted to a bar magnet and are therefore ferromagnetic, consistent with Fe^0 formation. Simultaneous to our investigation, the Morris group reported that asymmetric transfer hydrogenation reactions of ketones using iron complexes thought to be homogeneous[278] were actually catalyzed by Fe^0 nanoparticles formed *in situ*.[279] Interestingly, these nanoparticles were able to catalyze enantioselective transfer hydrogenation and the authors suggest that chirality of the ligand is imparted *via* coordination to the surface of the nanoparticle. We attempted transfer hydrogenation and direct hydrogenation of ketones using compound **3.2** as a precatalyst but no conversion was observed.

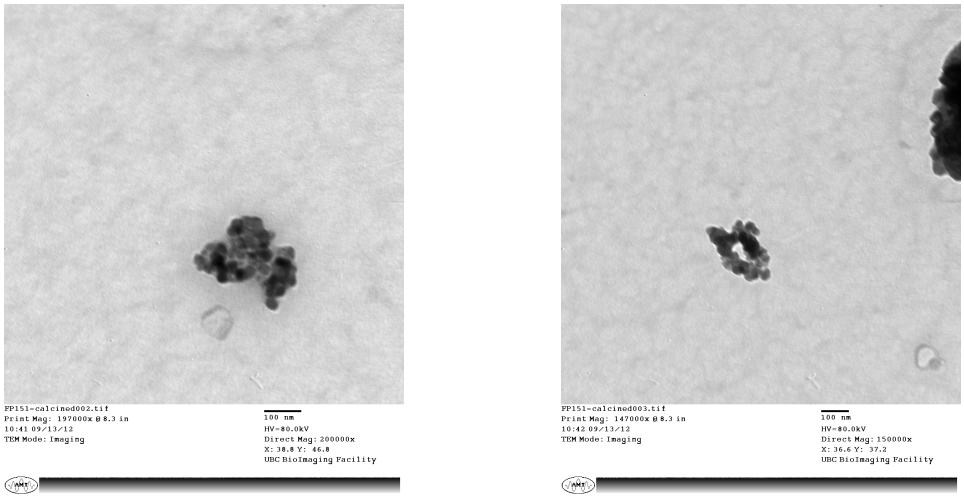

Figure 4.1: Selected TEM images of a carbonized reaction mixture of **3.2** and H_2 showing inconsistent morphologies and particle sizes

We sought to evaluate the morphology of the Fe(0) produced in the hydrogenation of compound **3.2** for comparison to the active Fe(0) nanoparticles reported by Morris and coworkers. After exposing **3.2** to 4 atm of H_2 for 12 h the volatiles were removed *in vacuo* and the resulting residue was heated to 700 °C in a tube furnace for 16 h to remove the organic residues. The resulting solids were analyzed by Transmission Electron Tomography (TEM) and some representative images are shown in Figure 4.1. The TEM images show inhomogeneous particles with a wide range of diameters (100 nm - 2000 nm) and inconsistent morphologies. No further study of these particles was undertaken.

4.1.2 Reactions with Carbon Monoxide

The iron catalysts for ketone hydrogenation (compound **1.6** - **1.9** in Scheme 1.4) have higher coordination numbers and lower spin states (HS vs LS) than com-

pound **3.2** and contain one or more CO ligand. We hypothesized that addition of CO ligands to compound **3.2** would increase the ligand field enough to create a low spin complex, similar to compound **1.8**. Exposing a toluene solution of **3.2** to 1 atm of carbon monoxide for 16 h produces an intractable mixture of paramagnetic materials. If the reaction mixture is left under a carbon monoxide atmosphere for several days without stirring, low yields (2 - 5%) of dark red crystals of a new compound, **4.1**, are obtained. The solid state molecular structure shown in Figure 4.2 depicts a surprising disassembly of the ferrocene-based ligand. The short C1-N1, C2-C3, C4-C5 and long C1-C2 and C1-C5 bond lengths indicate that each $^{i}Pr_2PNC_5H_4$ fragment has been oxidized by two electrons producing a neutral cyclopentadieneimine fragment. These ligands coordinate to the iron centers in a $\mu(\eta^4$Cp - P) coordination mode, yielding a dimeric piano stool complex reminiscent of the Knölker complexes discussed in Chapter 1. It should be noted that the reaction between compound **3.2** and excess carbon monoxide (shown in Scheme 4.3) is completely atom economical and can be thought of as a reduction of the iron atoms by the $^{i}Pr_2PNC_5H_4$ fragment, however, due to the low yields of this compound complete characterization was not pursued.

If the amount of carbon monoxide is limited to one equivalent, a new highly asymmetric species, **4.2**, is observed by ^{1}H NMR spectroscopy in the crude reaction mixture. After purification, black crystals of compound **4.2** can be obtained. Redissolving these crystals produces the same ^{1}H NMR spectrum (Figure 4.3) as the crude reaction mixture. Single crystals of compound **4.2** can be grown by slow evaporation of hexanes and the solid-state molecular structure is shown in Figure 4.4. One carbon monoxide ligand is bound to one of the non-ferrocene iron centers and one of the ligand arms has reversed its coordination geometry from

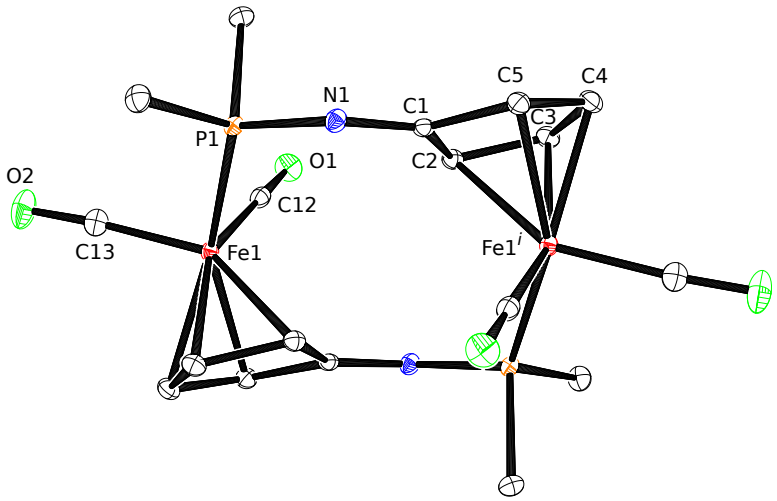

Figure 4.2: ORTEP diagram of **4.1** with ellipsoids drawn at 50% probability. All H atoms and ^{i}Pr methyl groups have been omitted for clarity. Selected bond lengths (Å) and angles (deg): Fe1^{i}-C2 2.1443(12); Fe1^{i}-C3 2.0748(13); Fe1^{i}-C4 2.0742(14); Fe1^{i}-C5 2.1317(12); Fe1^{i}-C1 2.3636(12); C1-N1 1.3252(15); C2-C3 1.4291(16); C4-C5 1.4152(16); C1-C2 1.4527(16); C1-C5 1.4668(16) N1-P1 1.6642(11); C12-O1 1.1532(15); C1-N1-P1 123.78(9); Fe1-C12-O1 176.45(10).

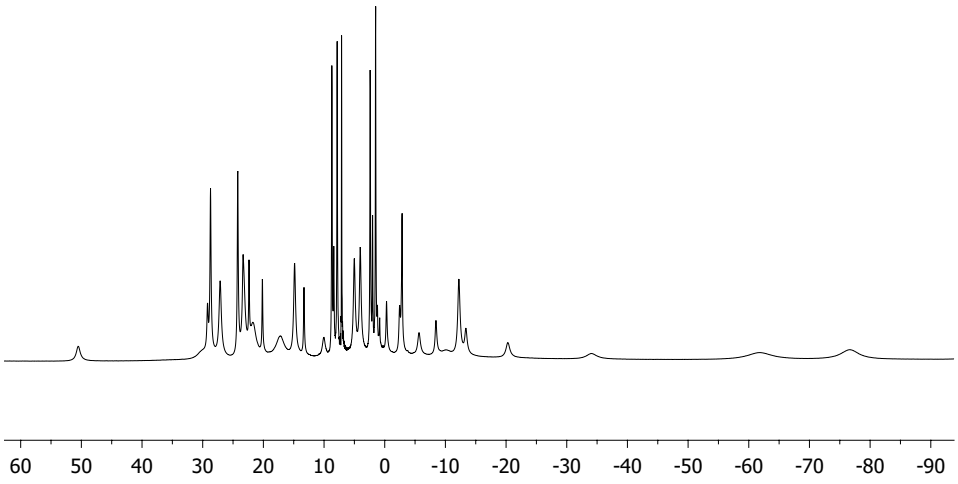

Figure 4.3: 300 MHz ^{1}H NMR spectra of **4.2** in C_6D_6

μ-N,P to μ-P,N, as shown in Scheme 4.3. As a result, the non-ferrocene iron centers are formally Fe(I)/Fe(III). It is tempting to suggest that the binding of carbon monoxide results in an electron transfer and ligand rearrangement between the interior iron centers. ^{57}Fe Mössbauer spectra of compound **4.2** were collected at room temperature and 77 K in order to help assign the oxidation states of the iron centers, see Figure C.3. The data collected was fit with four doublets, however, the data quality is low enough that other fits are possible and conclusive oxidation states could not be assigned.

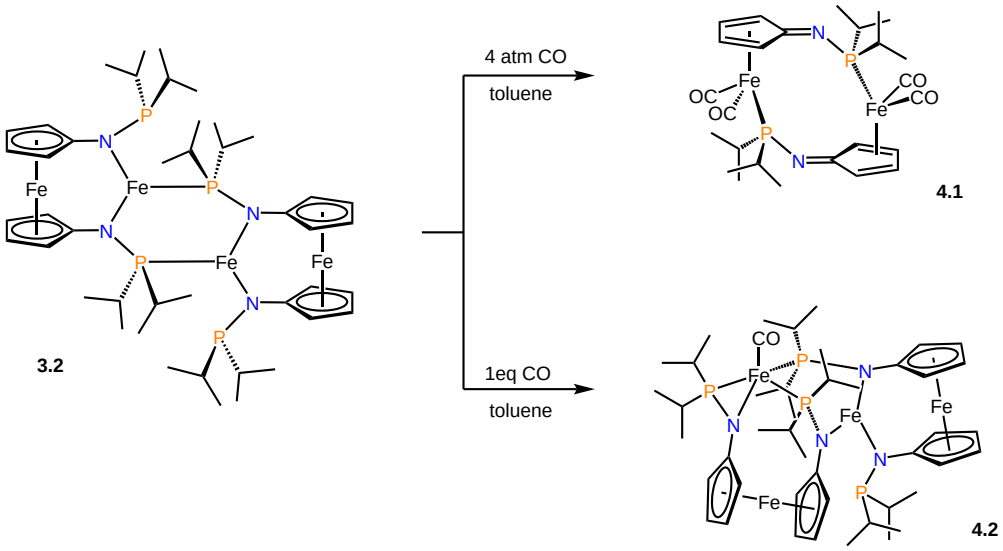

Scheme 4.3: Reactions of compound **3.2** with carbon monoxide

The IR stretching frequency of the CO ligand in compound **4.2** is 1880 cm^{-1}. Direct comparison of this stretching frequency is difficult because, to the best of our knowledge, no high spin iron complexes containing CO ligand(s) have been reported. Octahedral low-spin iron complexes reported by the Morris (**1.8**) and Milstein (**1.9**) group both contain carbonyl ligands with similar stretching frequen-

cies to the CO ligand in **4.2**, μ_{IR} = 1894 and 1865 respectively. Therefore the CO ligated iron center in **4.2** is consistent with a low spin iron carbonyl.[56,62] To answer the original question, whether addition of a CO ligand would produce a more stable hydrogenation catalyst, compound **3.2** was exposed to one atmosphere of hydrogen and again we observed decomposition to insoluble material and protonated ligand, **1.50**.

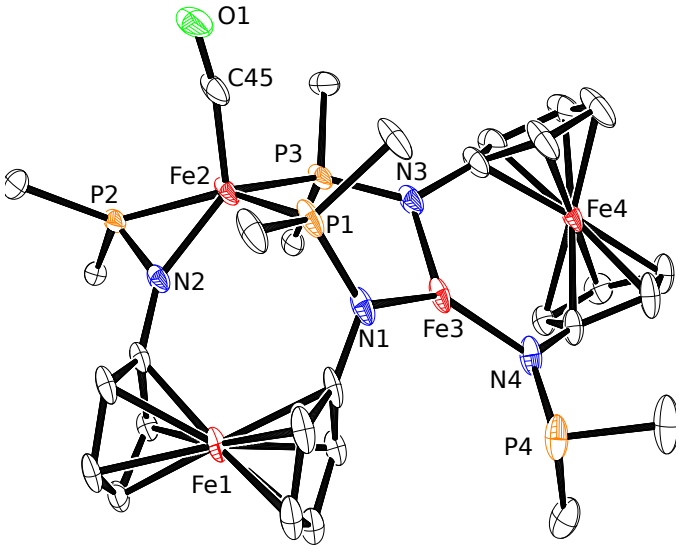

Figure 4.4: ORTEP diagram of **4.2** with ellipsoids drawn at 50% probability. All H atoms and ^{i}Pr methyl groups have been omitted for clarity. Selected bond lengths (Å) and angles (deg): C45-O1 1.162(3); N1-P1 1.6726(19); N2-P2 1.6659(17); N3-P3 1.6617(17); N4-P4 1.6886(19); Fe2-N2 1.8559(15); Fe2-P2 2.2321(8); Fe2-P1 2.2441(10); Fe2-P3 2.2432(9); Fe3-N1 2.0033(16); Fe3-N3 1.9968(18); Fe3-N4 1.9287(17); Fe2-C45-O1 169.79(18) P1-Fe2-P3 96.59(3); P1-Fe2-C45 97.23(9); N1-Fe3-N3 108.48(7); N1-Fe3-N4 131.24(7); N3-Fe3-N4 120.16(7).

The above results suggest that phosphinoamide ligands are not suitable for cooperative activation of dihydrogen due to complex instability. Modifications to the ligand scaffold providing a larger chelate ring, *vide infra* could help remediate

these issues by keeping the Fe–H N–H pair stable long enough to react with an incoming substrate. Moving forward we will investigate the oxidation and reduction of compound **3.2** and investigate its reactivity with various small molecules.

4.2 Redox Behaviour of ([fc(NP^{i}Pr$_2$)$_2$]Fe)$_2$, Formation of a Fe-Fe Bond and Cleavage of Azobenzene

The impressive transformations facilitated by heterogeneous catalysts[280–285] and multimetallic co-factors in metalloenzymes, such as nitrogenase,[286–289] have led to interest in the study of polynuclear molecular systems.[142,290–292] The ability of metalloenzymes to perform multielectron reductions[293,294] using iron-based cofactors is particularly noteworthy considering the conditions of the intracellular environment. Despite significant efforts, the binding and activation of substrates by these polynuclear sites remain poorly understood.[294–298] Attempts to create synthetic models of these polyiron sites has been of increasing interest,[295,299–304] as such studies may reveal insights into complex redox processes. Of particular note, recent reports of polyiron complexes supported by abiological ligands detail the activation of substrates relevant to nitrogen fixation.[90,115,305–307] Such studies are important because these synthetic systems can be more easily studied than the naturally occurring enzymes, which allows for a more detailed description of their electronic structures, factors affecting metal-metal bonding, and substrate binding.[308,309]

Betley and coworkers have contributed to this area with the isolation of the trinuclear, high-spin cluster of Fe(II) centers (**A** in Scheme 4.4), which is capable of cleaving the N-N bond of azobenzene (PhN=NPh) with no external reductant.[90] We have previously reported the tetrairon dimer **3.2** that contains two ferrocenyl

diphosphinoamides supporting two high spin Fe(II) ions; this ancillary ligand system also can be used to generate a mixed tetranuclear Fe_2-Co_2 system that displays interesting Fe–Co interactions (compound **3.4**).[310] Based on reports from our group and others that show how dinitrogen can be activated and functionalized by dinuclear or trinuclear complexes,[5,89,91,95,96,144,191] we investigated the redox reactivity of **3.2** to examine structural changes, as well as interaction with small molecules related to dinitrogen fixation. In this section, we report the oxidation and reduction of **3.2**, and the cleavage of azobenzene by **3.2**.

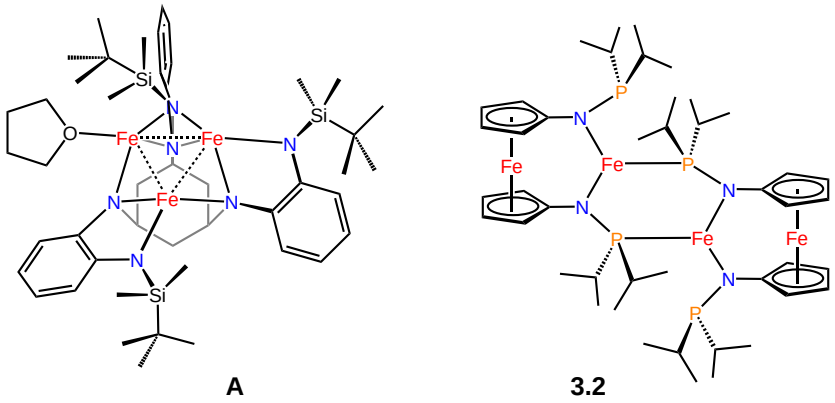

Scheme 4.4: Polyiron Complexes

Initially, we sought to use cyclic voltammetry to study the redox behaviour of **3.2** but the results were poor, with multiple irreversible waveforms observed in both the reductive and oxidative regimes (see Figure E.1 in Appendix E) suggesting that compound **3.2** undergoes a chemical reaction following reduction or oxidation. We then examined chemical oxidants and reductants. Although **3.2** reacts rapidly with numerous oxidants of the type Ag(Y) and X_2 (Y= OTf^-, Cl^-, BPh_4^-, X = Br, I) the cleanest reactions were obtained using the molecular iodine equivalent 1,2-diiodoethane. Treatment of **3.2** with four equivalents of 1,2-diiodoethane re-

sulted in conversion to a new paramagnetic product. Limiting the equivalents of 1,2-diiodoethane simply results in partial conversion to the same product. The stoichiometry of the reaction suggested that the oxidation was more than a simple Fe(II)/Fe(III) event. Recrystallization from toluene/hexanes mixture results in the formation of dark red crystals of a new paramagnetic product, **4.3**, with an empirical formula of $[fc(NP^{i}Pr_2)_2]FeI_4$ (56 %). X-ray analysis of **4.3** revealed the solid state molecular structure, shown in Figure 4.5. The P-N bond shortens from **3.2** (1.6993(12) Å) to **4.3** (1.603(7) Å) demonstrating that the electron-rich phosphinoamide arms of the ligand have been oxidized while both iron atoms remain in the Fe(II) oxidation state. We suggest that irreversible oxidation of the P-N bond is contributing to the poor quality of CV data in the oxidative regime.

Attempts to generate a dinitrogen complex by reduction of **3.2** under mild conditions (Na/Hg or cobaltacene under 4 atm N_2) were unsuccessful. Upon reduction with excess KC_8 **3.2** does not coordinate dinitrogen but rather undergoes a rearrangement to form an iron-iron bond between the two internal iron centers (Figure 4.5). The Fe1-Fe2 distance decreases from 3.9241(5) Å in **3.2** to 2.4760(6) Å in **4.4**, similar to the diiron (Fe^{I}/Fe^{II}) trisphosphinoamide complex reported by the Thomas group (2.4645 Å).[115] In order for the iron centers in **4.4** to get close enough to form a bond, the ferroceene backbones of the ligand must twist to become perpendicular to each other (cp plane to cp plane angle = 84.75°- 86.05°). The iron-iron bond, formed upon reduction of **3.2** illustrates the potential for the storage of reducing equivalents in this system. Compound **4.4** is stable as a solid in the glovebox freezer for up to a week; however, in a C_6D_6 solution **4.4** reverts back to over 50% compound **3.2** in less than 48 hours. The magnetic moment of **4.4** (7.8 μ_B) indicates that the complex maintains a maximally high spin S=7/2

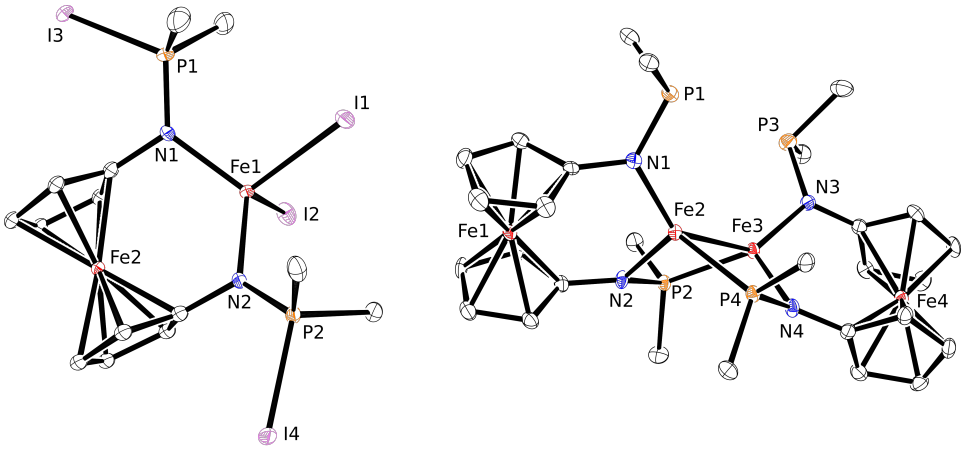

Figure 4.5: ORTEP diagram of **4.3** (left) and anionic portion of **4.4** (right) with ellipsoids drawn at 50% probability. All H atoms and ^{i}Pr methyl groups have been omitted for clarity. Selected bond lengths (Å) and angles (deg) of **4.3**: Fe1-Fe2 3.4836(17); N1-P1 1.607(7); N2-P2 1.603(7); Fe1-I1 2.6889(13); Fe1-I2 2.6428(13); P1-I3 2.408(3); P2-I4 2.409(3); I1-Fe-I2 104.97(4); N1-Fe-N2 115.7(3); cp tilt[216, 219] 2.78; and **4.4**: Fe1-Fe2 3.7016(10); Fe2-Fe3 2.4755(7); Fe3-Fe4 3.6954(10); N1-P1 1.690(3); N2-P2 1.651(3); Fe2-N2 1.975(3); Fe2-N1 1.983(3); Fe2-P2 2.7252(11); Fe3-P2 2.3607)10); N1-Fe2-N2 11.49(11); N2-Fe2-P4 110.22(8); N1-Fe2-Fe3 136.97(8); cp tilt[216,219] for Fe1 1.18 and Fe4 0.88.

ground state. It has been observed that diiron systems displaying a M-M bond contract upon oxidation[311] with the rationale being a depopulation of the M-M anti-bonding orbitals. However, in a recent contribution, Betley and coworkers report that the same triiron system that activates PhNNPh (**A** in Scheme 4.4) displays a contracted Fe-Fe distance (0.13 Å) upon reduction.[309] Compound **3.2**, **1.30** and **A** in Figure Scheme 4.4 represent rare examples of polyiron compounds that display increased iron-iron interactions upon reduction while maintaining a high-spin state, and therefore population of metal-metal anti-bonding orbitals. The reactivity of **4.4** with nitrogen rich substrates such as PhNNPh has so far led to complicated

mixtures, no doubt due to the high reactivity of this complex.

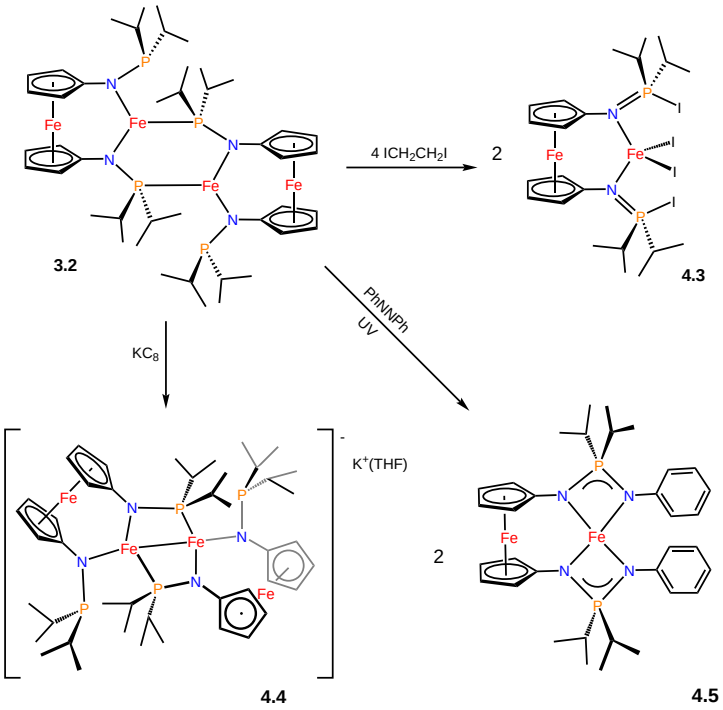

Scheme 4.5: Reactivity of **3.2**

While **3.2** was unable to coordinate dinitrogen even under reducing conditions, we wondered how **3.2** would react with the N=N double bond in azobenzene. Cleavage of PhNNPh is known for iron[312] and ruthenium[313] carbonyl clusters, which involve transfer of the putative metal imidos to CO to form isocyanates. More recently, a trinuclear ruthenium hydride[314] and a trinuclear iron complex[90] were shown to cleave PhNNPh into metal imido fragments. We thought that complex **3.2**, containing four iron(II) centers, would also have the available reducing equivalents to cleave the PhNNPh bond.

Exposing compound **3.2** to azobenzene does not result in a reaction as evidenced by ^{1}H NMR spectroscopy. Even heating the mixture to 70 °C for 12 hours

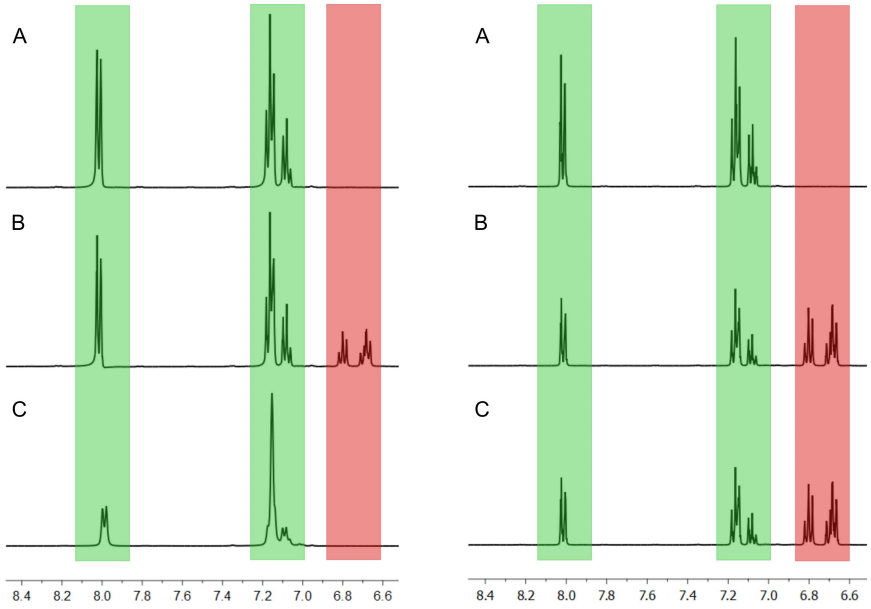

Figure 4.6: ^{1}H NMR spectra (400 MHz, 298 K) of A: (left and right) Initial solution of *trans*-PhNNPh; B: (left) Solution after irradiation at 350 nm for 25 min (right) Solution after irradiation at 350 nm for 60 min; C: 30 minutes after mixing with (left) and without (right) compound **3.2**. Green: *trans*-PhNNPh and red:*cis*-PhNNPh

does not result in any new signals in either the paramagnetic or diamagnetic ^{1}H NMR spectra. However, when a solution of **3.2** and PhNNPh in C_6D_6 was irradiated with UV light (350 nm) a reaction was observed by NMR spectroscopy to a new paramagnetic product, **4.5**. Initially we hypothesized that **3.2** could only react with *cis*-PhNNPh due to steric congestion. To test this we produced a mixture of *cis*/*trans*-PhNNPh by photolysis and added compound **3.2** in the absence of UV light. No reaction was observed, however, **3.2** does seems to catalyze the *cis*/*trans* isomerization of azobenzene (See Figure 4.6). Compound **4.5** could only be produced when both reactants are exposed to UV light together, indicating that the

role of UV radiation is more than isomerization of azobenzene. Single crystals of **4.5** were obtained by cooling a solution of pentane, and the solid state structure is shown in Figure 4.7.

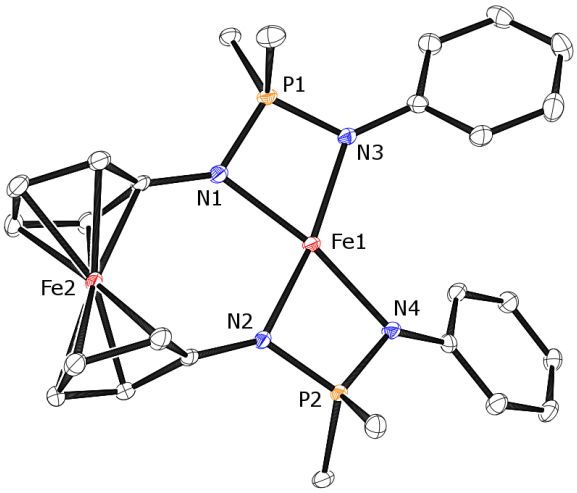

Figure 4.7: ORTEP diagram of **4.5** with ellipsoids drawn at 50% probability. All H atoms and ^{i}Pr methyl groups have been omitted for clarity. Selected bond lengths (Å) and angles (deg): Fe1-Fe2 4.0103(4); N1-P1 1.6142(13); P1-N3 1.6260(14); N1-Fe1 2.0558(13); P1-Fe1 2.7176(5); N3-Fe1 2.0634(14); N1-P1-N3 96.90(7); N1-Fe1-N2 98.04(5); N1-Fe1-N3 72.13(5); N3-Fe1-N4 118.01(5).

Unexpectedly two new P-N bonds were formed and the resulting N–P–N fragment has similar P1-N1 and P1-N3 bond lengths of 1.6119(14) Å and 1.6260(14) Å respectively, indicate a delocalized diiminophosphorinato anion. Interestingly the ferrocene linker forces the iron center to adopt a distorted square-planar geometry (τ_4[273] = 0.19). Compound **4.5** displays a room temperature magnetic moment of 2.9 μ_B, consistent with the spin only value of two unpaired electrons (S = 1) and other square planar Fe(II) complexes.[232] Replacing PhNNPh with tolNNtol (tol = 4-methylphenyl) results in conversion to a new paramagetic product, **4.6**, which

displays a very similar ^{1}H NMR spectrum to compound **4.5**. Using a 50:50 mixture of PhNNPh and tolNNtol in a reaction with compound **3.2** and analysis by mass spectrometry allowed us to observe the parent peak for the "mixed" species, [fc(NP^{i}Pr$_2$NPh)(NP^{i}Pr$_2$Ntol)]Fe, suggesting that the reaction is not a concerted reaction between ArNNAr and [fc(NP^{i}Pr$_2$)$_2$]Fe.

Diiminophosphinato ligands have been used to support metal metal bonds in alkali earth metals,[315–317] rare earth element polymerization catalysts[318–322] and group 10 cross-coupling catalysts.[323–325] To the best of our knowledge, this is the first report of a bis(diiminophosphorinato)iron complex, however, a diiron system with a bridging diiminophosphorinato backbone has been reported.[215] While diiminophosphorinatos are most commonly synthesized from phosphines and organic azides, synthesis from azobenzene is precedented. Recently, a reaction between the Ti/Co phosphinoamide complex, (THF)Ti(ArNPR$_2$)$_3$Co(N$_2$) (Ar = 2,4,6-trimethylphenyl , R = ^{i}Pr), and azobenzene has been reported to result in cleavage of azobenzene and formation of one diiminophosphorinato and one bridging metal imido.[326] We suggest that an iron imido is produced in the reaction between PhNNPh and compound **3.2**, but this imido quickly reacts with a phosphinoamide arm of the ligand. The complex most similar to **3.2** is Fe(^{i}PrNPPh$_2$)$_3$Fe(PMe$_3$),[115] which reacts with organic azides to produce an iron imido. However, this imido is not reported to react with the bound amidophosphine ligands and we suggest that the geometric differences between the two complexes, namely the presence of an η^1-N phosphinoamide in compound **3.2**, is responsible for the divergent reaction profiles of these complexes.

In this report, we present a polyiron complex that, under photolytic conditions, cleaves azobenzene through a proposed but undetected iron imido. We also

note that **3.2** undergoes a ligand rearrangement forming a metal-metal bond upon reduction while maintaining a high-spin S = 7/2 state. From a ligand design perspective, it appears that amidophosphine donors are too electron-rich to study oxidation of high-spin iron clusters. Further work will involve determining whether the proposed imido, generated during the reaction of **3.2** with PhNNPh, can be trapped before transfer to the phosphine. New ligand designs will focus on scaffolds that can support higher nuclearity iron systems that are more redox-innocent, and stay dimeric throughout redox processes and reactions with nitrogen-rich small molecules.

4.3 Cooperative Activation of Polar Multiple Bonds

In the previous section we described the redox behavior of compound **3.2** and showed that the site of oxidation is the phosphinoamide arms. Based on this observation we investigated the reactivity of **3.2** with electrophilic carbon centers of CO_2, PhCHO and PhCN to determine whether the phosphinoamide would be the most nucleophilic site. Metal-bound phosphinoamides react with carbon-based electrophiles as initially reported for zirconium phosphinoamides and nitriles.[327] Later, reports of CO_2 activation by $(CO)_2CpM(R_2PNR')$ (M = Fe,Ru) emerged;[328] however, in all of the aforementioned cases, the $[R_2PNR']^-$ anion is best described by the iminophosphide resonance structure (See Figure 1.3). A better comparison to compound **3.2** can be found in a report from the Stephan group,[128] where a ruthenium amidophosphine complex (**B** in Scheme 4.6) was found to insert CO_2 between the metal phosphorous bond forming a 5-membered ring from the metal, amidophosphine and CO_2 molecule. The ruthenium amidophosphine complex reported by the Stephan group is an active (albeit poor) catalyst for the hydroboration

of CO_2. We wondered if our iron complex featuring four amidophosphines and a more ridgid ferrocene-backbone, **3.2**, would activate CO_2 using the same metal-ligand cooperativity observed for compound **B**.

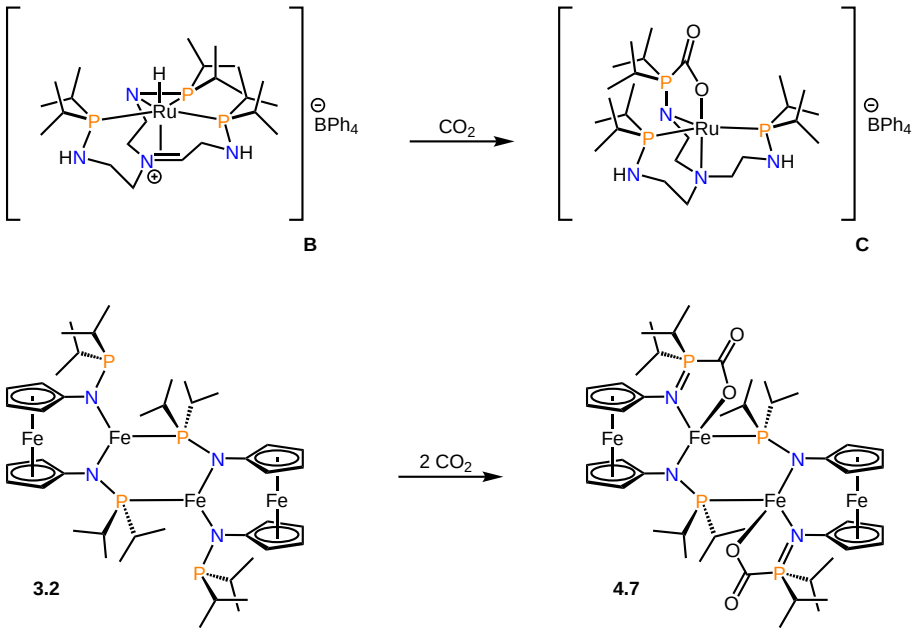

Scheme 4.6: Reactions between metal-bound amidophosphines and CO_2

Treatment of a solution of **3.2** with excess carbon dioxide results in decomposition to an intractable mixture of diamagnetic and paramagnetic materials. However, when the equivalents of CO_2 are limited, a light orange solution was observed from which light yellow crystals, **4.7**, were isolated. A solution made from these crystals shows 15 paramagnetically shifted peaks in the ^{1}H NMR spectrum (See Figure 4.8), 5 more than the would be expected for a dimeric structure similar to compound **3.2**.

The solid state molecular structure of **4.7** is shown in Figure 4.9 and reveals the expected asymmetric dimeric structure, shown in Scheme 4.6, which clearly shows

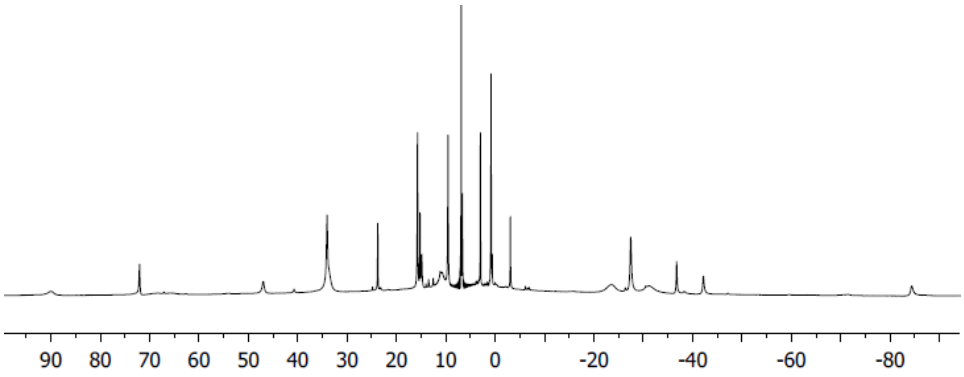

Figure 4.8: 300 MHz ^{1}H NMR spectrum of **4.7** in C_6D_6

that a cooperative CO_2 binding event has taken place utilizing the electron-rich amidophosphine as a Lewis base. In addition, one equivalent of **1.50** is present in the lattice, bound by hydrogen bonding between the phosphinoamine N–H groups and the oxygen atoms of **4.7**, which explains the 5 extra signals observed in the ^{1}H NMR spectrum. When ultra-pure CO_2 was used under rigorously dry conditions the same color change was observed, however, these reaction mixtures failed to yield crystalline material. We propose that the activation of CO_2 occurs regardless of whether adventitious water is present or not, but that crystallization requires an appropriate hydrogen bond donor. From the bond length contraction of N2–P2 from 1.6993(12) Å in **3.2** to 1.617(4) Å in **4.7** and concomitant elongation of the Fe-N2 bond from 1.9218(12) Å in **3.2** to 2.061(3) Å in **4.7**, it is clear that the CO_2 activation proceeds via oxidation of the phosphinoamide unit. The solution magnetic moment of **4.7** (5.9 μB) was measured by the Evans method and is lower than the expected spin-only value for two high-spin Fe(II) centers (9.8 μB). From the magnetic moment, we conclude that the dimeric structure remains intact in solution and suggest that an increase in antiferromagnetic coupling is responsible

for the decreased magnetic moment in **4.7** compared to the starting material (μ_{eff} = 6.7 μB). Although compound **3.2** is able to cooperatively activate two equivalents of CO_2, neither **3.2** nor **4.7** catalyze the hydroboration of CO_2, as observed by ^{11}B NMR spectroscopy.

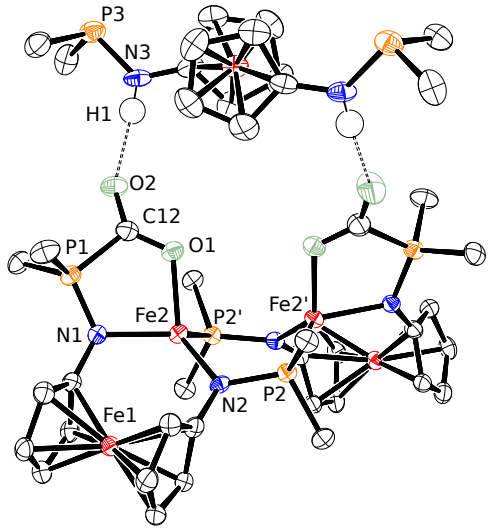

Figure 4.9: ORTEP diagram of **4.7** and co-crystallized protonated ligand, **1.50**, with ellipsoids drawn at 50% probability. All H atoms and ^{i}Pr methyl groups have been omitted for clarity. Selected bond lengths (Å) and angles (deg): Fe1-Fe2 3.6854(9); Fe2-Fe2' 3.5592(11); Fe2-N1 2.061(3); Fe2-N2 1.956(3); Fe2-P2' 2.4635(11); Fe2-O1 2.084(3); N1-P1 1.617(4); N2-P2 1.673(3); N3-P3 1.695(4); P1-C12 1.857(5); C12-O1 1.262(6); C12-O2 1.221(6); O2-H1 2.04(6); N3-H1 0.84(6); N1-Fe2-N2 114.24(13); N2-Fe2-P2' 109.32(10); N1-Fe2-O1 85.99(13).

After observing that the outer sphere cooperative activation of CO_2 is more favorable than a direct, exclusive interaction with the iron centers, we turned our attention to another substrate with an electrophilic carbon center, benzaldehyde. In order to determine the stoichiometry of the reaction between benzaldehyde and compound **3.2** we performed small scale reactions with 1, 2, 4 and ~100 equiv-

alents of benzaldehyde in deuterated solvent and monitored the reactions by ^{1}H NMR spectroscopy. Addition of 1 or 2 equivalents of benzaldehyde resulted in a mixture of products evidenced by the numerous peaks in the ^{1}H NMR spectra. When 4 or $\sim$100 equivalents were added to compound **3.2**, conversion to one major product, compound **4.8**, was observed suggesting that all four amidophosphine arms had been substituted (Scheme 4.7). In order to investigate whether a cooperative activation would occur with a less electrophilic substrate we examined the stoichiometry of the reaction between **3.2** and benzonitrile in an identical manner to the reaction with benzaldehyde. Treatment of **3.2** with benzonitrile provided a similar ^{1}H NMR spectrum of a new paramagnetic compound, **4.9**, regardless of the stoichiometry of benzonitrile (1,2,4 or 100 equiv.) suggesting only a single phosphinoamide arm was functionalized. While **4.9** does not react with additional equivalents of benzonitrile, a reaction can be observed by ^{1}H NMR spectroscopy upon addition of a more electrophilic substrate like benzaldehyde or methyl benzoate, however these products could not be characterized. It is interesting to note that unlike the addition of excess CO_2, addition of excess benzaldehyde ($>$ 4 eq) or benzonitrile ($>$ 1 eq) does not result in further reaction. We hypothesize that the small steric profile of CO_2 allows for further deleterious reactions.

Single crystals of both **4.8** and **4.9** were grown and the solid state molecular structures are show in Figure A.4 and Figure A.5 respectively. The relevant N–P bond lengths in compounds **4.7** - **4.9** are contracted by $\sim$ 0.1 Å compared to the starting material, compound **3.2**, indicating that the phosphinoamides have been converted to iminophosphoranes. The intrairon distance between the non-ferrocene irons has decreased for compounds **4.7** - **4.9** by 0.36, 0.61, and 1.03 Å respectively, however, only the Fe–Fe distance of compound **4.9** (2.8932(13) Å) is below the

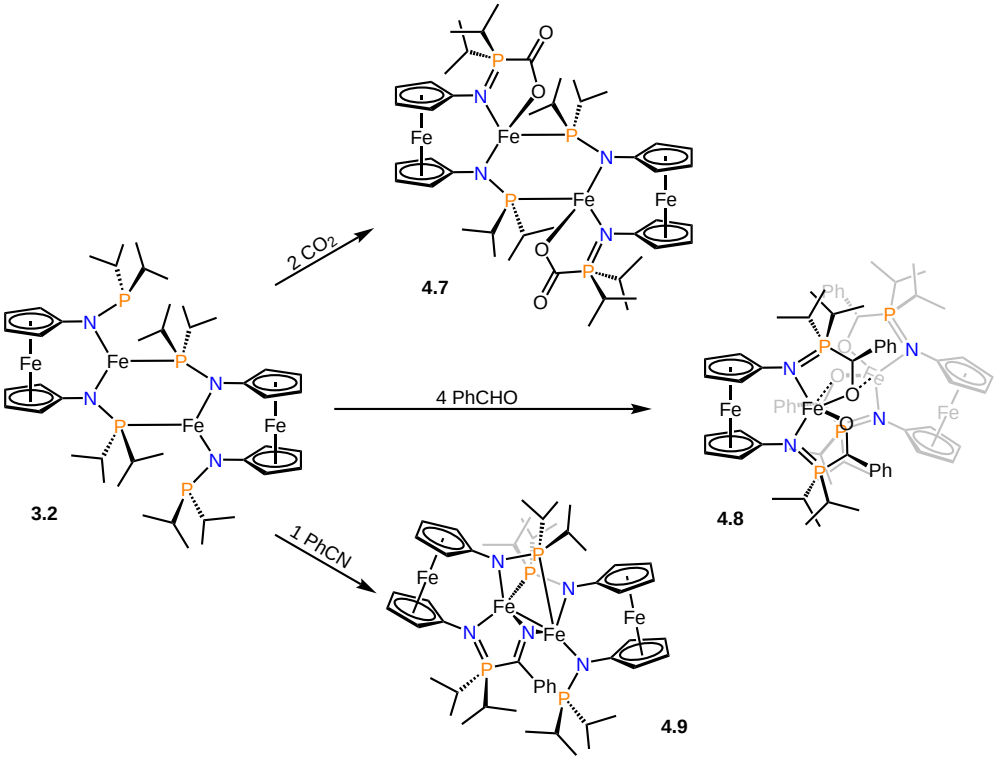

Scheme 4.7: Reactions between compound **3.2** and electrophilic carbon centers

sum of the covalent radii (3.06(8) Å).[329]

It appears that amidophosphines are not suitable ligands for the study of the interaction of polyiron systems with CO_2 due to the propensity of these complexes to activate polar unsaturated bonds in a cooperative fashion. Future work should look at modified ligand designs without the electron-rich amidophosphine donors, therefore avoiding this type of metal-ligand cooperativity. This could be done by introducing electronic spacers between the nitrogen and phosphorus atom, or by removing the phosphorus donor entirely, *vide infra*. Further study of the reactions between compound **3.2** and polar unsaturated molecules could investigate the po-

tential application of these complexes as catalysts in functionalization reactions such as hydrosilyation.

Chapter 5

Future Work and Conclusions

I was taught that the way of progress is neither swift nor easy
—Marie Curie

5.1 Thesis Synopsis

This thesis is divided into two distinct branches, one focused on an amidophosphine-supported ditantalum tetrahydride, and the other focused on the synthesis and reactivity of polyiron complexes. The goal of the first branch was to investigate the transformations of carbon monoxide and carbon dioxide by the ditantalum tetrahydride, **2.1**. This work was preceded by two discoveries by Dr. Joachim Ballmann. First, that compound **2.1** can completely reduce carbon monoxide to methane, resulting in an oxo bridged ditantalum species, **2.4**. Second, when compound **2.1** is exposed to carbon dioxide, two hydrides are transfered resulting in a bridging diolate. The second branch involved investigating the coordination chemistry of the 1,1'-bis(phosphinoamide)ferrocene, **1.50** with base metals and probing the ability of these complexes to activate small molecules with a focus on dinitrogen. This ligand set had been previously developed by Dr. Nathan Halcovitch to prevent

ligand redistribution in early transition metal phosphinoamide complexes.

Chapter 2 covers all of the tantalum amidophosphine chemistry, and consists of two publications. Based on our previous reports of a ditantalum tetrahydride, **2.1**, which spontaneously activates dinitrogen in a side-on-end-on binding mode,[144] we examined the reaction between **2.1** and isoelectronic carbon monoxide. We found, however, that instead of a side-on-end-on activation product, we obtained a new ditantalum species containing no new carbon atoms, and a bridging oxide, compound **2.4**. The fate of the carbon atom was identified as methane based on an experiment using labeled ^{13}CO. After consulting with our computational collaborators they suggested three separate mechanistic pathways for the reaction. All three have energy barriers that are within the error of the calculations and thus, experimental evidence was required to reveal the operative mechanism. The critical difference between the mechanisms is that in one, all 4 tantalum hydrides are used to produce the methane, while in the others, a proton from one of the N-Ph rings is removed by a Ta-CH_3. An isotopic labeling study reveals two different isotopologues of compound **2.1**, one where only the hydrides are deuterated and one where all hydrides and all *ortho* N-Ph protons were deuterated. Using these two isotopologues in reactions with carbon monoxide we trapped the product methane and analyzed its mass by GC-MS. These results support a mechanism that involves a transient Ta(III)=Ta(III) double bond, which rapidly cyclometalates the N-Ph ring by oxidative addition of a C-H bond. To probe the catalytic potential of these transformations, regeneration of the tetrahydride **2.1** was pursued through treatment of **2.4** with E-H reagents (Et_3SiH, $^nBuSiH_3$, $LiAlH_4$, $NaBH_4$, $THF{\cdot}BH_3$). However, in all cases either no reaction was observed or many phosphorus containing species were observed by ^{31}P NMR spectroscopy, none of which were compound **2.1**.

Section 2.2 details the reaction of tetrahydride **2.1** with carbon dioxide. In this case, retention of the O–C–O framework is observed after two hydride transfers resulting in a diolate-bridged ditantalumdihydride, **2.5**. My main contributions to this publication were finishing the characterization of compound **2.5** and using d^4-**2.1** to prove that the hydrogen atoms of the methylene diolate originate from the hydrides of **2.1**. In addition to the published material, we sought to observe reaction intermediates consistent with the minima suggested by DFT calculations. Regardless of temperature, the product and starting material were observed exclusively.

Chapter 3 details the coordination chemistry of the 1,1'-bis(phosphinoamide)fe-rrocene ligand, **1.50**, with base metals. We isolated complexes of iron(II) (**3.2**) and cobalt(II) (**3.4**), which exist in a dimeric form. Interestingly the cobalt complex, which is only stable in the solid state, displays weak bonding interactions between the iron of the ferrocene backbone and the cobalt center. This interaction was characterized by ^{57}Fe Mössbauer spectroscopy, SQUID magnetometry and modeled with DFT calculations. The calculations suggest that this interaction is comprised of donation from the iron center to the cobalt center (Fe $\rightarrow$ Co) and back donation from the cobalt center to antibonding orbitals in the ferrocene backbone (Co $\rightarrow$ fc*). We sought to synthesize the analogous nickel(II) complexes, however, elimination of Ni(0) and oxidation of the dianionic ligand to compound **3.7** was too facile.

Chapter 4 covers a selection of reactions between the dimeric iron phosphinoamide **3.2** and various small molecules. Treatment with dihydrogen led to heterolytic cleavage of H_2 across the Fe–N bond, which unfortunately results in decomposition to Fe(0) and compound **1.50**. Addition of carbon monoxide to com-

pound **3.2** is more complicated than originally imagined and resulted in a ligand rearrangement. This illustrates the reluctance of compound **3.2** to break apart into monomers. Reactions with polar unsaturated organic molecules led to nucleophilic attack of the organic substrate by the phosphorus atom of the ligand, forming metallocycles. To our dismay, compound **3.2** does not react with N_2 when reduced with KC_8 under 4 atmospheres of dinitrogen. Instead, reduction of compound **3.2** results in formation of a metal-metal bond between the iron centers resulting in a bimetallic Fe-Fe unit with an average formal oxidation state of +1.5 for each iron center, $[Fe_2]^{3+}$. Reaction of **3.2** with ArNNAr under photolytic conditions led to the cleavage of the N=N double bond. We propose that an unobserved iron imido intermediate is formed prior to imido transfer to the phosphorus atom, resulting in two $[NPNAr]^-$ ligand arms on the 1,1'ferrocene backbone in compound **4.5** and **4.6**. Reactions between compound **3.2** and oxidants generally afford multiple products, however, using the iodine equivalent ICH_2CH_2I conversion to a single product is observed where both phosphinoamide arms have been oxidized, **4.3**. Throughout Chapter 4 the phosphinoamide arms of compound **3.2** were found to be non-innocent, often acting as nucleophilic iminophosphide, which complicated investigation of small molecule activation by two iron centers.

5.2 Future Directions

5.2.1 Re-Designing the 1,1'-diphosphinoamide Ligand for Polymetallic Complex Formation

The ferrocene-linked phosphinoamide ligand undergoes bond-forming reactions and displays redox non-innocence in many of the reactions performed with compound **3.2**. Typically the phosphinoamide functions as a nucleophile, leaving the

oxidation state of the iron unchanged, which illustrates the metal ligand cooperativity in these iron phosphinoamide complexes. However, due to the strong P–C bond formed when reacting with organic electrophiles, the ability of these complexes to catalytically functionalize organic electrophiles is likely unrealistic. Unfortunately, the observed ligand cooperativity precluded reactivity at the metal center and/or the ferrocene backbone. In order to eliminate phosphinoamide involvement we redesigned the ligand by placing an electronic spacer between the nitrogen and phosphorus atoms. Initially we decided to keep the spacer as short as possible to encourage short intermetallic distances and thus chose a methylene linker. Professor Connie Lu has recently pioneered the use of methylene linked tris(amidophosphine) as ligands for homo- and heterobimetallic base metal complexes. Highlighting their successes with these ligands is a dicobalt complex capable of catalytic silyation of dinitrogen.[89]

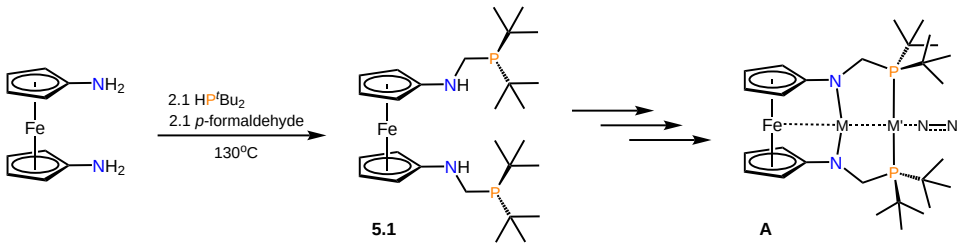

Scheme 5.1: Synthesis of ferrocene-linked bis(amidophosphine)

Starting from 1,1'-diaminoferrocene we envisioned a reaction with ditertbutylphosphine and *p*-formaldehyde producing a novel tetradentate ligand set **5.1**. RNH–CH_2–PR_2 linkages can be formed by a condensation reaction between a primary amine and a dialkylphosphinomethanol,[330] which can be generated from secondary phosphines and *p*-formaldehyde. Using this methodology we developed a melt procedure for the synthesis of compound **5.1** depicted in Scheme 5.1. Upon toluene ex-

traction and precipitation from pentane, an orange semi-solid was isolated. Characterization by ^{1}H NMR spectroscopy and elemental analysis confirmed the identity as the desired bis(aminophosphine), compound **5.1**. With the bis(aminophosphine) now available, we anticipate that a variety of bimetallic compounds of the form **A** in Scheme 5.1 can be synthesized and evaluated as catalysts for dinitrogen functionalization.

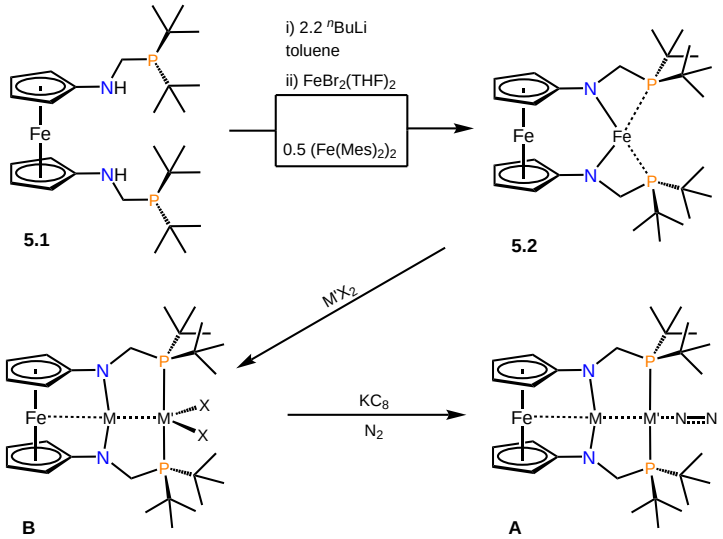

Scheme 5.2: Installing multiple metals in the ferrocene-linked bis(amidophosphine)

After succesfully synthesizing the neutral form of the methylene-linked ligand, we turned our attention to installing base metals into the donor pockets. Taking cues from the Lu group, we decided to install the first metal center by a deprotonation / salt metathesis route, shown in Scheme 5.2 (top). We began by deprotonating compound **5.1** with ^{n}BuLi; monitoring the reaction by ^{1}H NMR we observed the disapearence of the N–H resonance after 1 hour. Removing the volatiles, and washing with pentane afforded a red powder, which was immediately redissolved

in THF and treated with $FeBr_2(THF)_2$ resulting in a dark red solution. After allowing the salt metathesis reaction to proceed for 16 hours, the paramagnetic complex **5.2** was isolated as dark red needles. Unfortunately this compound persistently crystallizes with a fine needle morphology, which is not suitable for X-ray diffraction. However, using elemental analysis we were able to confirm that the needles have the expected empirical formula $C_{28}H_{48}N_2P_2Fe_2$. The ^{1}H NMR spectrum of **5.2** displays 5 signals, which are assigned as 1 very broad methylene resonance, 2 Cp resonances, and 2 *tert*-butyl resonances based on integration, see Figure 5.1. Inequivalency in the *tert*-butyl resonances is inconsistent with a C_{2v} symmetric structure like the one shown in Scheme 5.2 and led to uncertainty in our assignment.

To support our characterization we investigated an alternative synthetic route to compound **5.2**. A protonolysis reaction between **5.1** and Fe_2Mes_4 (Mes = 2,4,6-trimethylphenyl) was examined. Treatment of **5.1** with Fe_2Mes_4 results in an immediate color change to a dark red solution and after 4 hours the volatiles were removed *in vacuo* yielding a dark red powder. This powder displayed a similar set of 5 signals as was previously observed for the material obtained by salt metathesis. Crude spectra for both syntheses of compound **5.2** are shown in Figure 5.1.

The convergence of the salt metathesis and protonolysis reactions to a single product, strongly supports the identity of those products being compound **5.2**. For comparison, the Lu lab does not attempt to isolate the "metalloligand", rather a second metal is added *in situ*, which improves the crystallinity. Considerable efforts are still required to uncover the potential of this ligand set, including installation of a second metal, proving that **5.1** is a suitable pro-ligand for construction of bimetallic complexes of the type $[fc(NCH_2P^iPr_2)_2]FeMX_n$. Additionally, us-

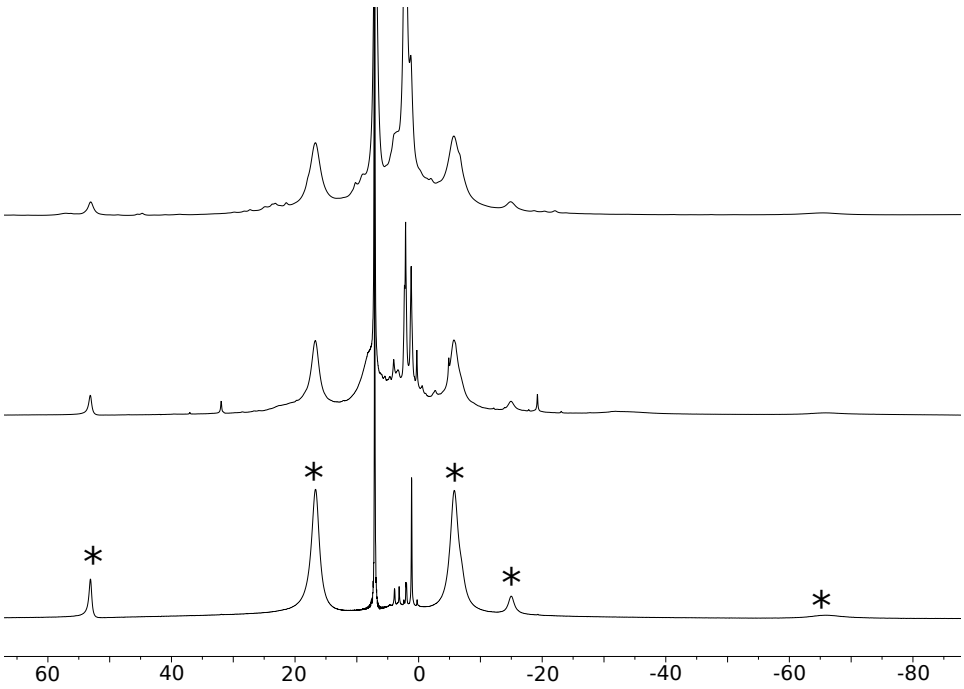

Figure 5.1: ^{1}H NMR (400 MHz) spectra of compound **5.2** in C_6D_6 from protonolysis reaction between **5.1** and Fe_2Mes_4 (top) salt metathesis reaction between **5.1**, ^{n}BuLi and $FeBr_2(THF)_2$ (middle) and after recrystallization (bottom). The peaks attributed to **5.2** are indicated with a *

ing a different base metal for the initial protonolysis with compound **5.1** such as $Co(py)_2(CH_2SiMe_3)_2$ could offer access to a new set of bimetallic combinations. Following synthesis and isolation of bimetallic compounds, reduction under nitrogen could offer insight into the effect of different electronic configurations on dinitrogen coordination complexes.

5.2.2 More Ligands Based on 1,1'-diaminoferrocene

The 1,1'-diaminoferrocene scaffold has been employed by the Arnold and Diaconescu groups in dianionic bidentate ligands bearing silane and arene substituents as a means to tune the electronic and steric environments.[131–134,136,220] However,

ligands synthesized from this backbone with higher denticities (**1.50** and **5.1**) are rare. For example, the bis(salen) ligand developed by Arnold and coworkers[331] demonstrates a tetradentate ligand environment with group 4 metals. These salen complexes have application in catalytic ring-opening polymerization of lactones, as reported by Diaconescu and coworkers. Interestingly, the authors showed that substrate selectivity was oxidation state dependent with regards to the ferrocene scaffold.[214] The ligands synthesized in this thesis were designed in pursuit of polymetallic systems, but many other ligands based on the 1,1'diaminoferrocene scaffold have intriguing potential. We will now present a variety of ligand designs that offer promising reactivity potential.

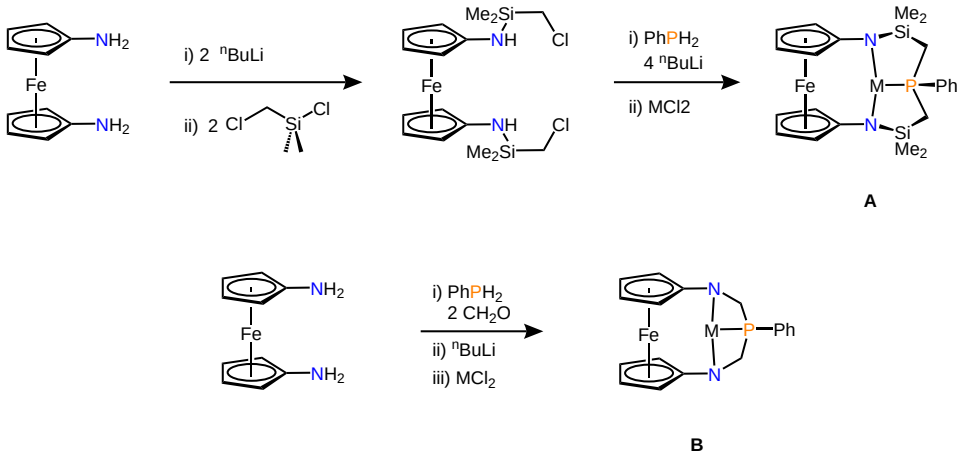

Scheme 5.3: Proposed synthesis of novel cyclic ligands with 1,1'diaminoferrocene backbones

As discussed in Chapter 1, the tridentate amidophosphine, **[NPN]^{Si}**, has allowed us to uncover unprecedented reactivity in tantalum complexes. By replacing the N-Ph groups of **[NPN]^{Si}** with the Cp rings of 1,1'-diaminoferrocene, a macrocyclic [NPN] ligand (**A** in Scheme 5.3) can be envisioned. This macrocyclic de-

sign, which has a small internal binding pocket would likely coordinate facially to large transition metals like tantalum, similar to the coordination geometry observed in **[NPN]^{Si}**$TaMe_3$, the precursor to the side-on-end-on dinitrogen complex, compound **2.2**. An even smaller macrocycle (**B** in Scheme 5.3) could be accessed by employing a simple CH_2 linker. This smaller macrocycle would further reduce the steric projection of the ligand, allowing for more unencumbered dimerization. A proposed synthesis of each ligand set is shown in Scheme 5.3 based on previous synthetic reports from our group[144] and others.[332]

The Meyer group uses pyrazole backbones for tethering two coordination pockets, which are typically polydentate ligands that have been previously reported to support monometallic complexes. These pyrazole-tethered ligands have been coordinated to a variety of transition metals including a diruthenium water oxidation catalyst.[85] Building from this idea we suggest the 1,1'diaminoferrocene backbone could serve a similar role as the pyrazole backbone. For example, established ligands like **[NPN]^{Si}**, α-diimines, bisiminopyridine, aminopyridines could be tethered producing ligands **A** - **D** in Scheme 5.4. These ligands would be well suited for bimetallic coordination and potentially allow for detailed study of multimetallic transformations *in situ*. In addition, having two metal centers in close proximety could allow for novel activation modes for dinitrogen and other small molecules. This concept of using 1,1'diaminoferrocene backbone to tether previously established ligands is currently being explored by members of our group.

5.2.3 Future Work with Iron Compounds

After discovering compound **3.2**, we imagined a wide array of small molecules that could be activated by the two Fe(II) centers. We intended to systematically

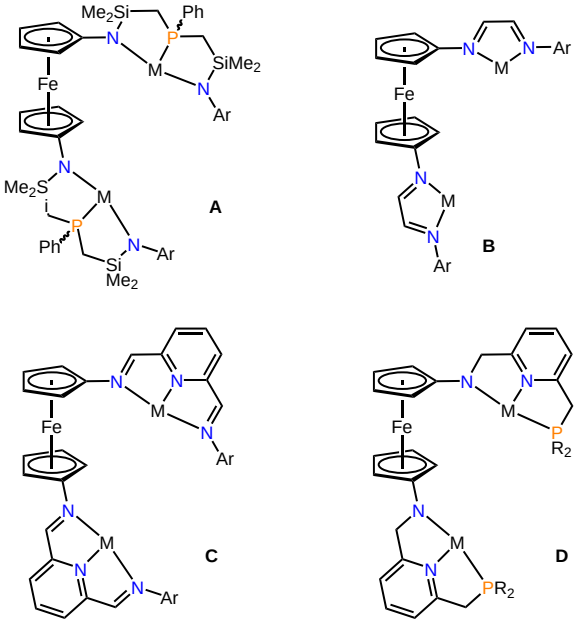

Scheme 5.4: Ligands designed for bimetallic coordination with 1,1'-diaminoferrocene backbones based on previously established ligands.

study reactions between compound **3.2** and various small molecules, oxidants and reductants, but unfortunately most reactions led to inconclusive results. For example, a systematic study of different oxidation reactions similar to the reaction of **3.2** with diiodoethane was undertaken to see the effects of adding elemental oxygen, sulfur, as well as one electron oxidants like silver(I) and ferrocinium salts. In all cases compound **3.2** undergoes a reaction but crystalline material could not be isolated from the reaction, and the paramagnetic nature of the product(s) precludes structural characterization by NMR spectroscopy. Paramagnetic ^{1}H NMR spectra are particularly difficult to analyze in this case because the putative Fe(III) formed in these reaction typically displays line broadening that is 10-1000 times wider than Fe(II).[333] In addition to the oxidants mentioned, activation of P_4, NO and CS_2

appeared promising but the reaction mixtures failed to yield crystalline material.

Employing **3.2** as a metalloligand we exposed compound **3.2** to additional equivalents of $FeBr_2(THF)_2$ in an effort to synthesize compound **A** (Scheme 5.5), which led to the observation of an unusual reaction. The results of this reaction looked initially promising based on the ^{1}H NMR spectrum containing 5 peaks, consistent with C_{2v} symmetric coordination of $[fc(NP^iPr_2)_2]^{2-}$. Single crystals suitable for X-ray diffraction were isolated in low yields ($\leq$ 10 %) and, to our surprise, the solid state molecular structure reveals a compound with 10 new iron centers (**5.3** in Scheme 5.5); multiple views of the solid state molecular structure are shown in Figure A.6. Along with the iron centers there are 16 bromide ligands (all but two are bridging) and two oxide ligands. Balancing the charges all iron centers remain Fe(II), however, the source of the μ–oxo ligands is troubling. Hypothesizing that adventitious water was causing the formal elimination of HBr we attempted to increase the yield of this reaction by adding stoichiometric amounts of water to the solvent; the presence of water proved ineffective. Characterization of this compound beyond X-ray crystallographic analysis is difficult. Traditional C,H,N elemental analysis is consistent with the the expected empirical formula $C_{44}H_{72}Br_{16}Fe_{14}N_4O_2P_4$, however the solution molecular structure can not be confirmed by this route as the ^{1}H NMR spectrum is broad and very symmetric. It is easy to imagine various cluster formulations that would give rise to similar ^{1}H NMR spectra. We attempted to characterize this cluster using mass spectrometry, however, no parent ions were detected. Reassuringly, this synthesis is reproducible, and additional trials afforded crystals with unit cell parameters consistent with **5.3**. To date, characterization of **5.3** and associated byproducts necessary for mass balance remains elusive.

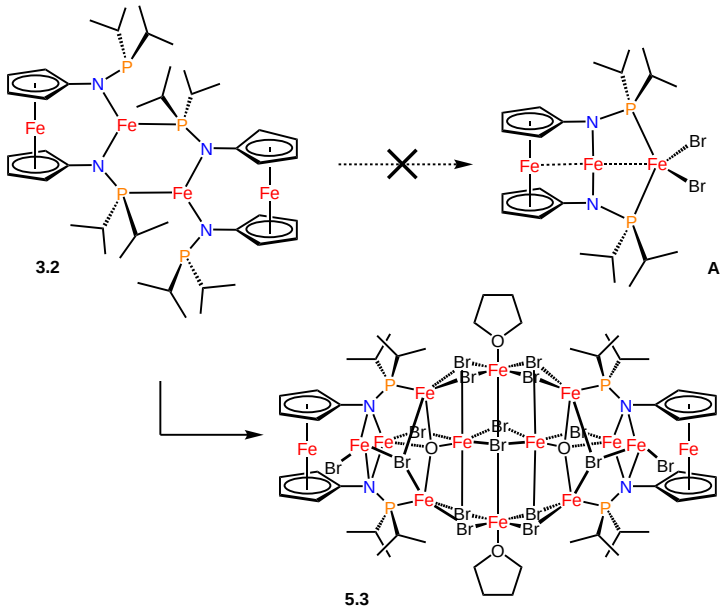

Scheme 5.5: Formation of an $FeBr_2$ cluster

In **5.3**, the bis(phosphinoamide)ferrocene ligand appears to cap a $FeBr_2$ cluster which resembles an ionic lattice of $FeBr_2$. The striking symmetry of this cluster is illustrated with multiple views of the solid state molecular structure shown in Appendix A. As emphasized in Chapter 1, polyiron complexes are found as active sites in nitrogenase as well as all-iron compounds capable of cleaving the N-N bond of dinitrogen. In the context of N_2 reduction, the existence of compound **5.3** is intriguing due to the large number of metal centers. Controlled synthesis and potential for homogenous catalysis remain unanswered questions, however, the number of coordination sites and reducing equivalents is enticing.

5.3 Final Conclusions

This dissertation is the result of countless hours spent coaxing compounds into crystallization and staring at very broad NMR spectra. As outlined in Chapter 1, iron is a versatile metal, with economic and environmental benefits, but using it comes with a host of issues, the most noticeable being the intense reliance on crystallography, which impedes rapid progress. The phosphinoamide functional group plays a feature role in this dissertation. While unlinked phosphinoamides have been used to form polyiron complexes in the Thomas lab,[115] which form iron imidos, the susceptibility for the N–P units to undergo redox or bond forming transformations precluded diverse reactivity at the metal center. We attribute this non-innocence to the coordination mode of the phosphinoamide, specifically, the η^1-N binding resulting in a dissociated phosphine. Phosphinoamide ligands are intriguing for their simplicity and wide array of coordination modes. However, as we have seen repeatedly they are often non-innocent, especially when exposed to oxidants and electrophiles. Harnessing the cooperative activation illustrated in section 4.3 could result in cooperative catalysis, analagous to the ruthenium tris(phosphinoamine) system developed by the Stephan group.[128] Alternatively, modifications to the ligand arms of compound **1.50**, as detailed in section 5.2, could alleviate these problems and allow for the study of polymetallic systems unimpeded by ligand cooperativity. Construction of trimetallic systems based on the methylene-linked amidophosphine **5.1** show promise, and as a linear M-M-M-N-N unit has never been synthesized there is potential for a highly activated N_2 unit.[89]

Chapter 6

Experimental Details

6.1 General Procedures

6.1.1 Laboratory Equipment and Procedures

Unless otherwise noted all procedures were performed using standard Schlenk technique or inside a glovebox (MBraun) equipped with a freezer (-40 °C) under an atmosphere of dry dinitrogen using oven-dried (200 °C) glassware and cooled under dynamic vacuum. A ”bomb”, as referenced in the experimental procedures below, is a thick-walled glass reactor fitted with a Kontes needle valve.

6.1.2 Solvents

Anhydrous hexanes, toluene, diethyl ether and tetrahydrofuran were purchased from Aldrich, sparged with dinitrogen and dried further by passage through towers containing activated alumina and molecular sieves. Pentane and Hexamethyldisiloxane (HMDSO) were refluxed over sodium benzophenone ketal, distilled under positive N_2 pressure and degassed via several freeze-pump-thaw cycles. C_6D_6 was stirred over sodium benzophenone ketal, vacuum transferred and freeze-pump-

thaw degassed; toluene-d^8, THF-d^8 and and pyridine-d^5 were stirred over activated molecular sieves and freeze-pump-thaw degassed. Gaseous reagents (H_2, D_2, CO_2, CO) were dried by passage through a trap containing activated molecular sieves prior to use.

6.1.3 Starting Materials

Paraformaldehyde, tolNNtol, PhNNPh and ^{n}BuLi (1.6 M in hexanes) were purchased from commercial suppliers and used as received. KH was purchased from Aldrich, placed on a glass frit, washed with anhydrous pentane under dinitrogen and dried *in vacuo*. $NiBr_2$ was purchased from Aldrich, oven-dried and cooled under dynamic vacuum. DMAP and ICH_2CH_2I were purchased from Aldrich and recrystallized from diethyl ether/hexane and diethyl ether respectively. PhCHO and PhCN were purchased from Aldrich, fractionaly distilled and stored over activated molecular sieves. $FeBr_2(THF)_2$ was preparred by Soxhlet extraction of $FeBr_2$ with anhydrous THF under dinitrogen and recrystallized from the THF solution. ^{t}Bu$_2$PH was prepared by reducing ^{t}Bu$_2$PCl with lithium aluminum hydride and fractional distillation of the reaction mixture. [P($CH_2SiMe_2NPh)_2$]$TaMe_3$,[145] fc($NHP^iPr_2)_2$,[137] $CoCl_2py_4$,[28] $ArNHP^iPr_2$,[109] KC_8,[334] and 1,1'-diaminoferrocene[130] were prepared according to literature methods.

6.1.4 Instrumentation and Methods of Analysis

^{1}H, ^{13}C and ^{31}P NMR spectra were recorded on a Bruker Avance 300 or 400 MHz spectrometer. ^{1}H and ^{13}C NMR chemical shifts were referenced to residual solvents signals from the deuterated solvents. ^{31}P NMR chemical shifts were referenced to external samples of phosphoric acid (85 % in aqueous solution) at $\delta = 0$

ppm.

Elemental analyses (EA) determinations were performed using a Carlo Erba Elemental Analyzer 1108, and were performed in the Department of Chemistry at the University of British Columbia by Mr. Derek Smith.

Suitable single crystals were selected in a glovebox, coated in STP motor oil and mounted on a glass loop. Single crystal X-ray data sets were collected on a Bruker DUO Apex II diffractometer with graphite-monochromated Mo Kα radiation (λ = 0.71073 Å) at a temperature of 90 K. Data were collected and integrated using the Bruker SAINT software package.[335] Absorption corrections were performed using the multiscan technique (SADABS).[336] The structures were solved by direct methods and refined using all reflections with the SHELX-2013[337] program package. All non-hydrogen atoms were refined anisotropically. All structures were solved and refined using the WinGX (version 1.80.05)[338] or Olex2 (version 1.2.5)[339] software packages. Crystallographic tables containing unit cell and refinement information are located in Appendix A.

Powder X-ray diffraction experiments were performed on a Bruker Apex II diffractometer with Cu K_α radiation (λ = 1.54184 Å) using an area detector. Powder samples were packed in a borosilicate glass capillary (0.7 mm diameter, from Charles Supper Company) under nitrogen and then flame sealed. Two measurements were taken on the sample, centering the X-ray beam on two different positions of the capillary to ensure reproducibility.

^{57}Fe Mössbauer spectra were recorded using a W.E.B. Research Mössbauer spectroscopy system at room temperature. A ^{57}Co (in rhodium matrix) source with a strength of 25 mCi was used. The detector was a Reuters-Stokes Kr/CO_2 proportional counter. The sample powders were loaded in a high-density polyethylene flat

washer, wrapped in parafilm and secured with Kapton tape. The sample chamber was evacuated to -28 ”Hg and back filled to -25 ”Hg with He. The velocity was scanned between 4 and -4 mms^{-1} using a constant acceleration triangle waveform, and calibrated against a Fe foil measured at 295 K in zero magnetic field. All isomer shifts (δ) are relative to Fe foil. Fitting of the data was performed using WMOSS software, which is available free of charge at http://wmoss.org/.

Magnetic susceptibility data were acquired in the solid state using a Quantum Designs MPMS5 SQUID magnetometer for VT measurements, or Mk 1 Johnson Matthey magnetic susceptibility balance at room temperature. Magnetic moments in solution were obtained using Evans NMR method.[244,245]

GC-MS analysis of head space gases was performed on a Agilent Technologies 5975B instrument. The ionization was done by electron impact at 1494 EMV. The Column used was a HP5MS - 5 % phenyl methyl siloxane. The program was as follows: 3 minutes at 50 °C ramp at 10 °C/min to 180 °C, hold at 180 °C for 5 min. The elution time for head space gases was 1.9 min. A image of the apparatus used is provided in Figure F.1

6.1.5 Computational Details for Chapter 3

DFT Calculations were carried out using the Gaussian 09[162] package. Calculations were performed at the BP86 level of theory,[247,248] using triple- -potential (TZP) basis sets and effective core potentials on Fe and Co. Calculation of NBOs,[340] NLMOs,[341] and Mayer Bond Order was performed using NBO 6.0.[253] Images of orbitals were generated using NBOPro6,[253] as well as Chemcraft.[342]

6.2 Synthesis of Compounds

6.2.1 Complexes Pertaining to Chapter 2

$PhP(CH_2SiMe_2NPh)_2Ta(\mu\text{-}O)(\mu\text{-}H)Ta(\kappa\text{-}o\text{-}C\text{-}C_6H_4\text{-}NSiMe_2CH_2)PhP(CH_2SiMe_2NPh)$ (2.4)

A pale yellow solution of [NPN]$TaMe_3$ (600 mg, 0.908 mmol) in Et_2O (50 ml) was transferred into a thick-wall glass vessel equipped with a Teflon valve and thoroughly degassed via three freeze-pump-thaw cycles. The vessel was immersed in liquid dinitrogen, filled with H_2 gas and sealed under atmospheric pressure. The reaction mixture was allowed to warm to room temperature, while the pressure inside the vessel slowly rose to approximately four atmospheres. After stirring at room temperature overnight, a deep purple solution of ([NPN]Ta)$_2(\mu\text{-H})_4$ (**2.1**) was obtained. The vessel was cooled in liquid nitrogen, the headspace evaporated and the solution thoroughly degassed at -78°C. The vessel was immersed in liquid dinitrogen and carbon monoxide (10 mL, 0.409 mmol, 0.9 eq) condensed into the vessel from a calibrated glass bulb. Note that exposure to dinitrogen has to be avoided during this procedure, due to the N_2-sensitivity of **2.1**. The vessel was then sealed under static vacuum and the reaction mixture slowly warmed to room temperature. Within 30 min the purple solution turned brown-orange. After stirring for another 15 min, all volatiles were removed in vacuum. Hexamethyldisiloxane (approx. 10 mL) was added to the tacky residue, resulting in the precipitation of the product as a brown powder, which was filtered off, rinsed with hexamethyldisiloxane (2 x 2 ml) and dried in vacuum. Yield: 310 mg, 0.249 mmol, 61%. $^{31}P\{^1H\}$ NMR (δ in ppm, C_6D_6 293 K, 162 MHz) 20.2 (s), 12.1 (s); ^1H NMR (δ in ppm, C_6D_6 293 K, 400 MHz) 7.93 (m, 2H), 7.74 (m, 2H), 7.31 (m, 4H), 7.05

(m, 8H), 6.85 (m, 4H), 6.72 (m, 3H), 6.59 (t, 1H, J = 7.2 Hz), 6.47 (d, 2H, J = 7.3 Hz), 6.34 (dd, 1H, J = 5.3Hz, 7.8Hz), 6.04 (t, 1H, J = 7.3Hz), 5.48 (app t, 1H, J = 5.8Hz), 4.98 (d, 1H, J = 6.5 Hz), 1.57 (m, 5H), 1.27 (m, 1H), 1.06 (m, 1H), 0.81 (m, 1H), 0.45 (s, 3H), 0.41 (s, 3H), 0.35 (s, 3H), 0.08 (s, 3H), -0.07 (s, 3H), -0.10 (s, 3H), -0.20 (s, 3H), -0.29 (s, 3H); $^{13}C\{^{1}H\}$ NMR (δ in ppm, C_6D_6 293 K, 101 MHz) 163.5 (d, $^{2}J_{CP}$ = 12.7 Hz), 160.8 (d, $^{2}J_{CP}$ = 8.62 Hz), 156.4 (d, $^{3}J_{CP}$ = 7.27 Hz), 155.2 (d, $^{3}J_{CP}$ = 5.61 Hz), 154.8 (d, $^{3}J_{CP}$ = 6.31 Hz) 138.24 (d, $^{1}J_{CP}$ = 28.12 Hz), 136.5 (d, $^{1}J_{CP}$ = 27.58 Hz), 133.8 (d, $^{3}J_{CP}$ = 13.63 Hz) 131.8 (d, $^{3}J_{CP}$ = 11.50 Hz) 130.4 (s), 129.1 (s), 129.0 (s), 129.0 (s), 128.7 (s), 128.6 (s), 127.6 (s), 127.3 (s), 127.2 (s), 127.1 (s), 126.0 (s), 125.3 (s), 122.6 (s), 122.2 (s), 121.5 (s), 107.2 (s), 98.1 (s), 19.5 (d, $^{2}J_{CP}$ = 3.64 Hz), 17.7 (s), 14.8 (s), 13.9 (s), 5.21 (s), 3.56 (d, $^{3}J_{CP}$ = 4.42 Hz), 3.03 (s), 2.49 (d, $^{3}J_{CP}$ = 7.07 Hz), 2.38 (s), 2.09 (s), 1.12 (d, $^{3}J_{CP}$ = 10.6 Hz) 0.53 (d, $^{3}J_{CP}$ = 5.69 Hz). MS (EI) *m/z* (%) 1246 (100%) [M+]. Anal. Calcd. for $C_{48}H_{62}N_4O_1P_2Si_4Ta_2$: C, 46.22; H, 5.01; N, 4.49. Found: C, 46.17; H, 5.24; N, 4.33

Reaction of ^{13}CO with (PhP($CH_2SiMe_2NPh)_2$Ta)$_2(\mu-H)_4$

A pale yellow solution of [NPN]TaMe_3 (53 mg, 0.0401 mmol) in C_6D_6 (5 ml) was transferred into a thick-wall glass vessel equipped with a Teflon valve and thoroughly degassed via three freeze-pump-thaw cycles. The vessel was immersed in liquid dinitrogen, filled with H_2 gas and sealed under atmospheric pressure. The reaction mixture was allowed to warm to room temperature, while the pressure inside the vessel slowly rose to approximately four atmospheres. After stirring at room temperature overnight, a deep purple solution of [([NPN]Ta)$_2(\mu$-H)$_4$ (**2.1**) was obtained. After removing the over-pressure of hydrogen the solution was cannula transferred to an NMR tube equipped with a Teflon valve and the tube was filled

with C_6D_6 (3 mL) until 1 mL of headspace remained. The NMR tube was immersed in liquid nitrogen and the volatiles were removed under high vacuum. ^{13}CO (1 mL, 0.409 mmol) was condensed into the NMR tube from a break seal flask. The NMR tube was sealed and allowed to warm to room temperature. Within 30 min the solution had turned brown-orange, indicative that the reaction was complete. The reaction mixture was characterized by NMR spectroscopy. $^{31}P\{^1H\}$ NMR (δ in ppm, C_6D_6 293 K, 162 MHz) 20.2 (s), 12.1 (s); ^1H NMR (δ in ppm, C_6D_6 293 K, 400 MHz) 7.93 (m, 2H), 7.74 (m, 2H), 7.31 (m, 4H), 7.05 (m, 8H), 6.85 (m, 4H), 6.72 (m, 3H), 6.59 (t, 1H, J = 7.2 Hz), 6.47 (d, 2H, 7.3 Hz), 6.34 (dd, 1H, J = 5.3Hz, 7.8Hz), 6.04 (t, 1H, J = 7.3Hz), 5.48 (app t, 1H, J = 5.8Hz), 4.98 (d, 1H, J = 6.5 Hz), 1.57 (m, 5H), 1.27 (m, 1H), 1.06 (m, 1H), 0.81 (m, 1H), 0.45 (s, 3H), 0.41 (s, 3H), 0.35 (s, 3H), 0.08 (s, 3H), -0.07 (s, 3H), -0.10 (s, 3H), -0.20 (s, 3H), -0.29 (s, 3H); $^{13}C\{^1H\}$ NMR (δ in ppm, C_6D_6 293 K, 101 MHz) 133.8 (d, $^3J_{CP}$ = 13.63 Hz), 131.8 (d, $^3J_{CP}$ = 11.50 Hz), 130.4 (s), 129.1 (s), 129.0 (s), 129.0 (s), 128.7 (s), 128.6 (s), 127.6 (s), 127.3 (s), 127.2 (s), 127.1 (s), 126.0 (s), 125.3 (s), 122.6 (s), 122.2 (s), 121.5 (s), 17.7 (s), 14.8 (s), 13.9 (s), 5.21 (s), 3.56 (d, $^3J_{CP}$ = 4.42 Hz), 3.03 (s), 2.49 (d, $^3J_{CP}$ = 7.07 Hz), 2.38 (s), 2.09 (s),), 1.12 (d, $^3J_{CP}$ = 10.6 Hz) 0.53 (d, $^3J_{CP}$ = 5.69 Hz), -4.26 (s).

[PhP(CH_2SiMe_2NPh)$_2$Ta(μ−H)]$_2$(μ−OCH_2O) (2.5)

A solution of [PhP(CH_2SiMe_2NPh)$_2$Ta]$_2$(μ−H)$_4$ (**2.1**) in Et_2O (50 ml) was prepared from [PhP(CH_2SiMe_2NPh)$_2$]$TaMe_3$ (600 mg, 0.908 mmol) and thoroughly degassed. Subsequently, the thick-wall glass vessel was immersed in liquid dinitrogen and carbon dioxide (10 mL, 0.409 mmol, 0.9 eq) condensed in from a calibrated glass bulb. The vessel was sealed under static vacuum and warmed to room temperature. A brown solution was obtained after stirring at room temperature for

1 h. The solvent was evaporated to afford a brown residue, which was recrystallized from a minimum amount of pentane (approx. 10 ml) at -40°C. The product was collected on a sintered glass frit, washed with cold pentane (2 x 1 ml) and dried under vacuum. Yield: 345 mg, 0.22 mmol, 60%. ^{1}H NMR (C_6D_6, 400 MHz): δ 0.12 (s, 12H, $SiCH_3$), 0.15 (s, 12H, $SiCH_3$), 1.18 (m, 8H, $SiCH_2P$), 6.11 (s, 2H, OCH_2O), 6.81 (t, $^{2}J_{H,P}$ = 4.8 Hz, 2H, TaH_2Ta), 6.89 (d, $^{3}J_{H,H}$ =7.4 Hz, 8H, *o*-NPh), 6.96 (t, $^{3}J_{H,H}$ = 7.3 Hz, 4H, *p*-NPh), 7.03 - 7.14 (m, 6H, *m*-PPh and *p*-PPh), 7.18 (t, $^{3}J_{H,H}$ = 7.6 Hz, 8H, *m*-N-Ph), 7.74 (m, 4H, *o*-PPh). ^{1}H{^{31}P} NMR (C_6D_6), selected peaks only: 1.18 (m, 8H, $SiCH_2P$), 6.81 (s, 2H, TaH_2Ta), 7.74 (d, $^{3}J_{H,H}$ = 7.0 Hz, 4H, *o*-PPh). ^{31}P{^{1}H} NMR (C_6D_6, 161 MHz): δ 13.1 (s). ^{13}C APT NMR (C_6D_6, 101 MHz): δ 2.4 (s, $SiCH_3$), 16.2 (s, $SiCH_2P$), 110.6 (s, OCH_2O), 122.7, 128.4, 129.7, 130.2, 132.4 and 132.7 (*o*-, *m*- and *p*-Ph carbons), 138.9 (d, $^{1}J_{C,P}$ = 25 Hz, *ipso*-PPh carbon), 153.9 (s, *ipso*-NPh carbon). MS (EI) m/z (%): 1278 (100%) [M]+. Elemental Anal.: Calcd. for $C_{49}H_{64}N_4O_2P_2Si_4Ta_2$: C 46.01; H 5.20 N 4.38. Found: C 45.36; H 5.19; N 4.20

[PhP(CH$_2$SiMe$_2$-*o*-D$_2$-NPh)$_2$Ta(μ−D)]$_2$(μ−OCD$_2$O) (**d$_{12}$-2.5**)

A sample of **d$_{12}$-2.5** was prepared in a manner identical to that for **2.5** using D_2 gas. ^{1}H NMR (C_6D_6, 400 MHz): δ 0.12 (s, 12H, $SiCH_3$), 0.15 (s, 12H, $SiCH_3$), 1.18 (m, 8H, $SiCH_2P$), 6.96 (t, $^{3}J_{H,H}$ = 7.3 Hz, 4H, *p*-NPh), 7.03 - 7.14 (m, 6H, *m*-PPh and *p*-PPh), 7.18 (d, $^{3}J_{H,H}$ = 7.6 Hz, 8H, *m*-N-Ph), 7.74 (m, 4H, *o*-PPh). ^{31}P{^{1}H} NMR (C_6D_6, 400 MHz): δ 13.1 (s). ^{2}H NMR (Et_2O, 61.4 MHz): δ 6.2 (s_{br}, OCD_2O), 6.6 - 8.0 (s_{br}, TaD_2Ta and *o*-D_2-NPh).

[PhP(CH$_2$SiMe$_2$NPh)$_2$Ta(μ−H)]$_2$(μ−O^{13}CH$_2$O) (**^{12}C-2.5**)

A sample of ^{13}C-**2.5** was prepared in a manner identical to that for **2.5** using ^{13}C-enriched carbon dioxide. ^{1}H NMR (C_6D_6, 400 MHz), selected peaks only: δ 6.11

(d, $^{1}J_{C,H}$ = 164 Hz, 2H, OCH_2O). $^{13}C\{^{1}H\}$ NMR (C_6D_6, 400 MHz), selected peaks only: δ 110.6 (s, OCH_2O), ^{13}C NMR (gated-decoupling, C_6D_6, 101 MHz), selected peaks only: δ 110.6 (t, $^{1}J_{C,H}$ = 164 Hz OCH_2O).

6.2.2 Complexes Pertaining to Chapter 3

$[fc(NP^{i}Pr_2)_2]K_2(THF)_{1.25}$ (3.1)

To an oven-dried Schlenk flask was added $fc(NHP^{i}Pr_2)_2$ (2.563 g, 5.717 mmol) and KH (1.829 g, 45.74 mmol). THF (100 mL) was added via cannula resulting in an orange suspension that was stirred for 16 hours resulting in a deep red solution with white precipitate. The solution is filtered through Celite, to remove excess KH, and reduced to dryness *in vacuo* resulting in a red sticky solid. The red solid is suspended in pentane, filtered with a glass frit, washed with pentane (3 x 15 mL) and dried *in vacuo*. Yield: 2.93 g, 4.767 mmol, 83%. $^{31}P\{^{1}H\}$ NMR (δ in ppm, DMSO-d^6, 293 K, 162 MHz) 70.1 (s); ^{1}H NMR (δ in ppm, DMSO-d^6, 293 K, 400 MHz) 3.60 (s, 5H, THF), 3.18 (s, 4H, Cp), 2.96 (s, 4H, Cp), 1.76 (s, 5H, THF), 1.29 (broad sept, 4H, J = 5.4 Hz, ^{i}Pr CH), 1.01 (d, 12H, J = 5.4 Hz, ^{i}Pr CH_3), 0.86 (d, 12H, J = 4.7 Hz, ^{i}Pr CH_3); $^{13}C\{^{1}H\}$ NMR (δ in ppm, DMSO-d^6 , 293 K, 101 MHz, *ipso*-Cp carbon not found) 66.97 (s, THF O$-CH_2$), 58.76 (s, Cp), 56.65 (d, $^{3}J_{C,P}$ = 17.17 Hz, Cp), 27.99 (d, $^{1}J_{C,P}$ = 15.31 Hz, P-CH), 25.09 (s, CH_2 THF), 20.14 (d, $^{2}J_{C,P}$ = 18.81 Hz, CH_3), 18.59 (d, $^{2}J_{C,P}$ = 10.52 Hz, CH_3). Anal. Calcd for $C_{108}H_{184}O_5N_8P_8Fe_4K_8$: C, 52.76; H, 7.54; N, 4.56. Found: C, 52.64; H, 7.61; N, 4.60.

$([fc(NP^{i}Pr_2)_2]Fe)_2$ (3.2)

To an oven-dried Schlenk flask containing $K_2[fc(NHP^{i}Pr_2)_2](THF)$ (2.50 g, 4.07 mmol) and $FeBr_2(THF)_2$ (1.50 g,4.17 mmol) was added THF (100 mL), resulting

in a brown slurry that was allowed to stir for 12 hours. The resulting solution was filtered through Celite, reduced to dryness and washed with cold pentane (3 x 5 mL). The resulting brown solids were isolated and further dried *in vacuo*. Yield: 1.48 g, 1.47 mmol, 72%. $^{31}P\{^{1}H\}$ NMR (δ in ppm, C_6D_6, 293 K, 121 MHz): 962.0 (s). ^{1}H NMR (δ in ppm, C_6D_6, 293 K, 300 MHz) 109.51 (s), 76.95 (s), 62.13 (s), 12.98 (s), -2.08 (s), -3.73 (s), -13.12 (s), -13.42 (s), -74.46 (s), -77.70(s). MS (EI) m/z (%): 1004 (14%) [M]+. Anal. Calcd for $C_{44}H_{72}N_4P_4Fe_4$: C, 52.62; H, 7.23; N, 5.58. Found: C, 52.39; H, 7.36; N, 5.40. μ_{eff} (solution 25 °C) 6.7 μ_B. μ_{eff} (solid, Gouy balance, 25°C) 6.6 μ_B.

[fc(NP^{i}Pr$_2$)$_2$]Fe(DMAP)$_2$ (3.3)

Synthesis A: To an oven-dried Schlenk flask containing ([fc(NP^{i}Pr$_2$)$_2$]Fe)$_2$ (0.452 g, 0.45 mmol) and 4-dimethylaminopyridine (0.220 g, 1.80 mmol) was added Et_2O (50 mL) via cannula at room temperature. After stirring for 16 hours, the volatiles were removed *in vacuo* and the resulting solids were suspended in Et_2O (10 mL) and filtered to give yellow powder. Yield: 0.430 g, 0.576 mmol, 64%. ^{1}H NMR (δ in ppm, C_6D_6, 293 K, 300 MHz): 57.82 (s), 31.76 (s), 15.90 (s), 12.13 (s), 0.44 (s), -1.34 (s), -26.91 (s), -56.99 (s). Anal. Calcd for $C_{36}H_{56}N_6P_2Fe_2$: C, 57.92; H, 7.56; N, 11.26. Found: C, 57.61; H, 7.52; N, 11.28. μ_{eff} (solution 25°C) 4.9 μ_B. μ_{eff} (solid, Gouy balance, 25°C) 5.1 μ_B.

Synthesis B: To an oven-dried Schlenk flask containing K_2[fc(NP^{i}Pr$_2$)$_2$](THF) (0.100 g, 0.167 mmol), $FeBr_2(THF)_2$ (0.060 g, 0.167 mmol) and 4-dimethylaminopyridine (0.040 g, 0.327 mmol) was added THF (25 mL) via cannula at room temperature. After 16 hours, the volatiles were removed *in vacuo* and the resulting orange-red solids were extracted with toluene (15 mL), filtered through Celite and reduced to dryness. The resulting orange-yellow solids were suspended in Et_2O (5

mL), filtered, and dried *in vacuo* resulting in a fine yellow powder. Yield: 0.088 g, 0.117 mmol, 71%.

([fc(NP^{i}Pr$_2$)$_2$]Co)$_2$ (3.4)

To an oven-dried Schlenk flask containing K_2[fc(NP^{i}Pr$_2$)$_2$] (0.200 g, 0.335 mmol) and $CoCl_2(py)_4$ (0.152 g, 0.341 mmol) was added pentane (50 mL) via cannula. The resulting slurry was allowed to stir at room temperature for 16 hours at which point the resulting dark brown solids were filtered away from the light orange supernatant and dried *in vacuo*. Due to solubility and stability issues, the resulting KCl cannot be separated from the product therefore all calculations are based on a molecular formula including four equivalents of KCl and the characterization is all performed in the solid state. Yield: 82%. Very small quantities of X-ray quality crystals can be obtained by performing the reaction in saturated toluene, without stiring and decanting the supernatant away from the crystals which grow on the side of the vial. To confirm that the solid state molecular structure is representative of the bulk powder isolated; a PXRD analysis was performed. MS (EI) m/z (%): 1010.2081 (100%) [M]+. Anal. Calcd for $C_{44}H_{72}N_4P_4Fe_2Co_2K_4Cl_4$: C, 40.38; H, 5.55; N, 4.28. Found: C, 40.15; H, 5.34; N, 3.97. μ_{eff} (solid, Gouy balance, 25°C) 2.7 μ_{B}.

fc(NP^{i}Pr$_2$=N(P^{i}Pr$_2$) (3.7)

To an oven-dried Schlenk flask containing H_2[fc(NP^{i}Pr$_2$)$_2$] (0.050 g, 0.11 mmol) and KH (0.030 g, 0.75 mmol) was added THF (5 mL) and the solution was allowed to stir for 16 hours. The solution was filtered through Celite into an oven dried Schlenk flask containing $NiBr_2$ (29 mg, 0.13 mmol) suspended in THF (1 mL) and allowed to stir for 2 hours, turning the red solution dark brown. The volatiles were removed *in vacuo* and the resulting solids were extracted with toluene (3 x

1 mL). The toluene solutions were combined, reduced to 2 mL, and cooled to -40 °C, resulting in crystallisation of the product. The toluene solution was decanted for successive crystallization and the black crystals were dried *in vacuo*. Yield: 43 mg, 86% . $^{31}P\{^{1}H\}$ NMR (δ in ppm, C_6D_6, 293 K, 162 MHz): 69.2 (d, $^{2}J_{P,P}$ = 40.7 Hz, P_A), 68.1 (d, $^{2}J_{P,P}$ = 40.7 Hz, P_B); ^{1}H NMR (δ in ppm, C_6D_6, 293 K, 400 MHz): 4.03 (m, 2H, fcC−H), 4.00 (m, 4H, fcC−H), 3.70 (m, 2H, fcC−H), 2.50 (sept, 2H, $^{3}J_{H,H}$ = 7.0 Hz, ^{i}Pr C-H_A), 1.89 (sept, 2H, $^{3}J_{H,H}$ = 6.9 Hz, ^{i}Pr C-H_B), 1.33 (dd, 6H, $^{3}J_{H,P}$ = 15.0 Hz, $^{3}J_{H,H}$ = 7.1 Hz ^{i}Pr CH_{3A}), 1.26 (dd, 6H, $^{3}J_{H,P}$ = 15.5 Hz, $^{3}J_{H,H}$ = 7.2 Hz ^{i}Pr CH_{3A}), 1.12 (dd, 6H, $^{3}J_{H,P}$ = 17.0 Hz, $^{3}J_{H,H}$ = 7.4 Hz ^{i}Pr CH_{3B}), 0.78 (dd, 6H, $^{3}J_{H,P}$ = 11.5 Hz, $^{3}J_{H,H}$ = 7.0 Hz ^{i}Pr CH_{3B}); ^{13}C APT NMR (δ in ppm, C_6D_6, 101 MHz): δ, 106.31 (d, $^{2}J_{C,P}$ = 13.4 Hz, *ipso* cp), 91.66 (d, $^{2}J_{C,P}$ = 6.0 Hz,*ipso* cp), 69.20 (s, cp), 67.89 (d, $^{3}J_{C,P}$ = 6.7 Hz, cp), 66.71 (s, cp), 66.52 (s, cp), 28.85 (dd, J = 77.8, 9.7 Hz, CH or CH3), 27.04 (d, J = 20.4 Hz, CH or CH3), 22.18 (d, J = 24.9 Hz, CH or CH3), 18.28 (t, J = 3.2 Hz, CH or CH3), 17.94 (dd, J = 5.3, 3.2 Hz, CH or CH3), 17.77 (d, J = 12.2 Hz, CH or CH3). Anal. Calcd for $C_{22}H_{36}FeN_2P_2$: C, 59.20; H, 8.13; N, 6.28. Found: C, 58.91; H, 8.11; N, 5.96.

K[ArNP^{i}Pr$_2$] (3.10)

To an oven-dried Schlenk flask containing ArNHP^{i}Pr$_2$ (Ar = 3,5-dimethylphenyl) (0.500 g, 2.11 mmol) and KH (0.210 g, 5.24 mmol) was added THF (50 mL), resulting in a colorless solution, and allowed to stir at room temperature. After 16 hours, the excess KH was filtered off through a Celite plug, and the volatiles were removed *in vacuo* yielding a white solid. The white solids were suspended in benzene (20 mL) and stirred for 30 min yielding a white suspension. Filtration of this suspension yields a crystalline white powder. Yield: 0.520 g, 90%. $^{31}P\{^{1}H\}$

NMR (δ in ppm, THF-d^8, 293 K, 162 MHz) 56.2 (s); ^{1}H NMR (δ in ppm, THF-d^8, 293 K, 400 MHz) 6.21 (s, 2H, *o*-Ar), 5.54 (s, 1H, *p*-Ar), 1.95 (s, 6H, Ar-CH_3), 1.47 (sept, $^3J_{H,H}$ = 7.0 Hz, 2H, ^{i}Pr-CH), 0.94 (dd, $^3J_{H,H}$ = 7.0 Hz,$^3J_{H,P}$ = 10.3 Hz, 12H, ^{i}Pr-CH_3). ^{13}C APT NMR (δ in ppm, THF-d^8, 101 MHz, *ipso*-Ar carbon not found) 137.60 (s, Ar **C**-CH_3), 116.87 (s, *o/p*Ar **C**-H), 116.69 (s, *o/p*Ar **C**-H), 29.03 (d, $^1J_{C,P}$ = 16.2 Hz, ^{i}Pr **C**H), 27.17 (s, Ar **C**H_3), 20.50 (d, $^2J_{C,P}$ = 21.3 Hz, ^{i}Pr **C**H_3), 18.90 (d, $^2J_{C,P}$ = 9.84 Hz, ^{i}Pr **C**H_3). Anal. Calcd for $C_{14}H_{23}KNP$: C, 61.50; H, 8.42; N, 5.09. Found: C, 61.22; H, 8.65; N, 4.75.

([ArNP^{i}Pr$_2$]Ni(P^{i}Pr$_2$))$_2$ (3.11)

To a slurry of $NiBr_2$ (20 mg, 0.092 mmol) in THF (2 mL) was added dropwise a solution of K[ArNP^{i}Pr$_2$] (Ar = 3,5-dimethylphenyl) (0.050 g, 0.182 mmol) in THF (2 mL) and the solution was allowed to stir at room temperature for 2 hours. The solution was reduced to dryness and the red/orange residue was extracted with pentane (2 x 3 mL) and filtered through Celite yielding an intense orange solution. This solution was concentrated to ($\sim$1 mL) and cooled to -40°C resulting in the formation of dark red crystals. Yield (0.018 g, 46 %). ^{31}P{^{1}H} NMR (δ in ppm, C_6D_6, 293 K, 162 MHz) 68.8 (d, $^2J_{P,P}$ = 44.8 Hz), 29.9 (d, $^2J_{P,P}$ = 44.8 Hz); ^{1}H NMR (δ in ppm, C_6D_6, 293 K, 400 MHz) 6.71 (s, 2H, *o*-Ar), 6.42 (s, 1H, *p*-Ar), 2.10 (s, 6H, Ar-CH_3), 1.47 (sept, $^3J_{H,H}$ = 7.0 Hz, 2H, ^{i}Pr-CH), 1.29 (sept, $^3J_{H,H}$ = 7.0 Hz, 2H, ^{i}Pr-CH), 0.99 (dd, $^3J_{H,H}$ = 7.0 Hz,$^3J_{H,P}$ = 9.8 Hz, 12H, ^{i}Pr-CH_3) 0.96 (dd, $^3J_{H,H}$ = 7.0 Hz,$^3J_{H,P}$ = 10.7 Hz, 12H, ^{i}Pr-CH_3).

6.2.3 Complexes Pertaining to Chapter 4

((C$_5$H$_4$NP^{i}Pr$_2$)Fe(CO)$_2$)$_2$ (4.1)

To an oven dried bomb was added a solution of ([fc(NP^{i}Pr$_2$)$_2$]Fe)$_2$ (0.100 g, 0.0996

mmol) in toluene (5 mL). The solution was degassed *via* 3 freeze-pump-thaw cycles and then exposed to 1 atm of CO at 77 K. The flask was allowed to warm to room temperature without stirring for 14 days resulting in the formation of dark red crystals. Yield 0.006 g, 0.01 mmol, 5%.

fc(NP^{i}Pr$_2$)$_2$Fe(CO)fc(NP^{i}Pr$_2$)$_2$Fe (4.2)

To an oven dried bomb was added a solution of ([fc(NP^{i}Pr$_2$)$_2$]Fe)$_2$ (0.100 g, 0.0996 mmol) in toluene (5 mL). The solution was degassed *via* 3 freeze-pump-thaw cycles and then exposed to CO (2.4 mL, 0.1 mmol) at 77 K. The flask was allowed to warm to room temperature with stirring for 16 hours. The volatiles were removed *in vacuo* and the resulting solids were extracted with a 3:1 hexanes:toluene mixture (4 mL) filtered through Celite and recrystallized at -40 °C, resulting in dark brown crystals. Yield 0.085 g, 0.083 mmol, 83%. ^{1}H NMR (δ in ppm, C_6D_6, 293 K, 400 MHz) 51.86 (s), 29.23 (s) 28.73 (s), 27.16 (s), 24.23 (s), 23.38 (s), 22.39 (s), 20.19 (s), 17.30 (s), 14.89 (s), 13.33 (s), 10.08 (s), 1.04 (s), -0.24 (s), -2.81 (s), -5.60 (s), -8.40 (s), -12.16 (s), -13.30 (s), -20.22 (s), -33.88 (s), -61.15 (s), -75.86 (s). Anal. Calcd for $C_{45}H_{72}Fe_4N_4OP_4$: C, 52.35; H, 7.03; N, 5.43. Found: C, 51.98; H, 6.85; N, 5.71. μ_{CO} = 1880cm^{-1}. μ_{eff} = 5.3 μB.

fc(NP^{i}Pr$_2$I)$_2$FeI$_2$ (4.3)

To an oven-dried Schlenk flask was added ([fc(NP^{i}Pr$_2$)$_2$]Fe)$_2$ (0.100 g, 0.0996 mmol) and toluene (5 mL). A solution of ICH_2CH_2I (0.118 g, 0.419 mmol) in toluene (5 mL) was added dropwise and the resulting solution was allowed to stir for 16 h. The volatiles were removed *in vacuo* and the resulting solids were recrystallized from a 50/50 mixture of toluene and hexanes resulting in dark red crystalline solids, which were dried *in vacuo*. Yield 0.112 g, 55.7 %. ^{1}H NMR (δ in ppm, C_6D_6, 293 K, 400 MHz) 18.36 (s), 4.74 (s), 3.19 (s), 0.88 (s), -9.33 (s).

Anal. Calcd for $C_{29}H_{44}Fe_2I_4N_2P_2$: C, 31.61; H, 4.02; N, 2.54. Found: C, 31.94; H, 4.12; N, 2.50. μ_{eff} (solution 25 °C) 5.4 μ_B.

[(fc(NP^{i}Pr$_2$)$_2$Fe)$_2$][K(THF)$_6$] (4.4)

To an oven-dried Schlenk flask was added ([fc(NP^{i}Pr$_2$)$_2$]Fe)$_2$ (0.100 g, 0.0996 mmol) and toluene (5 mL) and chilled to -30 °C. In a separate Schlenk flask KC_8 was suspended in toluene (5 mL) and chilled to -30 °C. The ([fc(NP^{i}Pr$_2$)$_2$]Fe)$_2$ solution was cannula transferred to the KC_8 slurry and allowed to warm to room temperature with stirring for 6 h. The resulting slurry is filtered through Celite and and the volatiles were removed *in vacuo* leaving a black residue. The residue was dissolved in a minimal amount of THF, layered with hexanes and cooled to -35 °C resulting in the formation of black crystals which were filtered and dried *in vacuo*. Yield: 0.094 g, 0.064 mmol, 64%. ^{1}H NMR (δ in ppm, C_6D_6, 293 K, 400 MHz) 188.42 (s), 36.80 (s), 34.10 (s), 25.32 (s), 15.14 (s), 12.08 (s), 11.51 (s), -2.75 (s), -17.86 (s), -29.72 (s). Anal. Calcd for $C_{68}H_{120}Fe_4KN_4O_6P_4$: C, 55.33; H, 8.19; N, 3.80. Found: C, 55.11; H, 7.82 ; N, 3.98. μ_{eff} (solution 25 °C) 7.8 μ_B.

fc(NP^{i}Pr$_2$NPh)$_2$Fe (4.5)

An oven dried bomb was loaded with (Fe[fc(NP^{i}Pr$_2$)$_2$])$_2$ (0.100 g, 0.0996 mmol), PhNNPh (0.020 g, 0.110 mmol) and toluene (10 mL). The bomb was sealed, removed from the glovebox and irradiated with UV-light (350 nm) for 20 hours. The solution was then filtered, removing minimal solids, and reduced *in vacuo* to 1 mL. Pentane (1 mL) was added and the solution was cooled to -40 °C resulting in formation of an orange powder. Yield: 0.057 g, 0.083 mmol, 83 %. ^{1}H NMR (δ in ppm, C_6D_6, 293 K, 400 MHz) 98.3 (s), 30.2 (s), 28.9 (s), 8.0 (s), 0.32 (s), -0.6 (s), -10.7 (s), -13.6 (s). Anal. Calcd for $C_{68}H_{120}Fe_4KN_4O_6P_4$: C, 55.33; H, 8.19; N, 3.80. Found: C, 54.98 ; H, 8.36 ; N, 4.11. μ_{eff} (solution 25 °C) 2.9 μ_B.

fc(NP^{i}Pr$_2$Ntol)$_2$Fe (4.6) An oven dried NMR tube was loaded with (Fe[fc(NP^{i}Pr$_2$)$_2$])$_2$ (0.010 g, 0.0099 mmol), tolNNtol (0.004 g, 0.019 mmol) and toluene (10 mL). The NMR tube was sealed, removed from the glovebox and irradiated with UV-light (350 nm) for 20 hours. The solution was then filtered, removing minimal solids. ^{1}H NMR (δ in ppm, C_6D_6, 293 K, 400 MHz) 98.9 (s), 30.1 (s), 28.3 (s), 25.9 (s), 8.1 (s), 0.6 (s), -0.51 (s), -13.4 (s).

((fc(NP^{i}Pr$_2$)(NP^{i}Pr$_2$CO$_2$))Fe)$_2$ (4.7)

To an oven dried bomb was delivered a solution of ([fc(NP^{i}Pr$_2$)$_2$]Fe)$_2$ (0.061 g, 0.0607 mmol) in THF ($\sim$ 10 mL). The solution was degassed *via* 3 freeze-pump-thaw cycles and CO_2 (3 mL, 0.12 mmol) was delivered at 77 K. The solution was allowed to warm to room temperature and stirred for 4 hours. The resulting yellow solution was reduced *in vacuo* and the resulting yellow-brown solids were recrystalized from toluene ($\sim$ 1 mL) at -40 °C. Yield: 0.047 g, 0.0430 mmol, 64 %. ^{1}H NMR (δ in ppm, C_6D_6, 293 K, 400 MHz) 90.2 (s), 72.3 (s), 47.3 (s), 34.3 (s), 24.1 (s), 16.0 (s), 11.1 (s), 9.8 (s), -2.8 (s), -23.2 (s), -27.2 (s), -30.6 (s), -36.5 (s), -41.9 (s), -84.1 (s). Anal. Calcd for $C_{46}H_{72}Fe_4N_4O_4P_4 \bullet C_{22}H_{38}FeN_2P_2$ C, 53.01; H, 7.20; N, 5.45. Found: C, 53.33 ; H, 7.46 ; N, 5.02. μ_{eff} (solution 25 °C) 5.9 μ_B.

(fc(NP^{i}Pr$_2$CHPhO)$_2$Fe)$_2$ (4.8)

To an oven-dried vial containing ([fc(NP^{i}Pr$_2$)$_2$]Fe)$_2$ (100 mg, 0.0996 mmol) and toluene (2 mL) was added benzaldehyde (40 mg, 0.38 mmol), resulting in an orange solution that was allowed to stir for 30 min. The solution was reduced to dryness *in vacuo* resulting in an orange-yellow solid. The orange-yellow solid was dissolved in minimal hexanes, and the solution was filtered through Celite. The orange filtrate was allowed to recrystallize at -40 °C, resulting in the formation of a yellow solid, which was filtered through a glass frit and dried *in vaccuo*. Yield:

69 mg, 0.048 mmol, 48% yield. ^{1}H NMR (δ in ppm, C_6D_6, 293 K, 400 MHz) 94.6 (s), 68.1 (s), 35.3 (s), 34.1 (s), 18.6 (s), 15.7 (s), 13.4 (s), 12.6 (s), 10.6 (s), 10.1 (s), 2.8 (s), -6.6 (s), -7.1 (s), -21.1 (s), -29.4 (s), -32.8 (s), -39.4 (s), -43.9 (s), -82.0 (s). Anal. Calcd for $C_{72}H_{96}Fe_4N_4O_4P_4$: C, 60.52; H, 6.77; N, 3.92 Found: C, 60.04 ; H, 6.56 ; N, 4.11. μ_{eff} (solution 25 °C) 5.8 μ_B.

(fc(NP^{i}Pr$_2$)(NP^{i}Pr$_2$CPhN))Fefc(NP^{i}Pr$_2$)$_2$Fe (4.9)

To an oven-dried 50 mL round bottom flask containing ([fc(NP^{i}Pr$_2$)$_2$]Fe)$_2$ (200 mg, 0.199 mmol) and toluene (2 mL) was added benzonitrile (20 mg, 0.19 mmol), resulting in a dark purple solution that was allowed to stir for 30 min. The solution was reduced to dryness *in vacuo*, resulting in a black solid. The black solid was suspended in hexane, filtered through a glass frit, washed with hexane (3 x 2 mL) and dried *in vacuo*, resulting in a red powder. Yield 145 mg, 0.131 mmol, 69% yield. ^{1}H NMR (δ in ppm, d^8-THF, 293 K, 300 MHz) 18.99 (s), 18.52 (s), 18.06 (s), 17.57 (s), -3.40 (s). -4.54 (s), -34.24 (s). Anal. Calcd for $C_{51}H_{77}Fe_4N_5P_4$: C, 55.31; H, 7.01; N, 6.32 Found: C, 55.11 ; H, 6.81 ; N, 6.87. μ_{eff} (solution 25 °C) 6.4 μ_B.

6.2.4 Complexes Pertaining to Chapter 5

fc(NHCH$_2$P^{t}Bu$_2$)$_2$ (5.1)

To an oven-dried Schlenk flask containing fcNH$_2$ (2.9 g, 0.013 mol) and *p*-CH$_2$O (0.80 g, 0.027 mol) was added ^{t}Bu$_2$PH (5.0 mL, 3.9 g, 0.027 mol). The flask was heated to 110 °C under a dinitrogen atmosphere for 2.5 h until the formation of water vapor had stopped. The resulting orange-brown solids were extracted with toluene filtered through Celite, and the resulting solution was cooled to -40 °C, forming a waxy orange solid. Yield 4.01 g, 0.0076 mmol, 58.5% yield. ^{31}P{^{1}H}

NMR (δ in ppm, d^8-toluene, 293 K, 162 MHz) 28.3 (s); ^{1}H NMR (δ in ppm, d^8-toluene, 293 K, 400 MHz) 3.94 (s, 4H), 3.89 (s, 4H), 3.18 (d, 4H, $^2J_{HP}$ = 5.9 Hz), 2.42 (broad s, 2H), 1.17 (d, 36 H, $^3J_{HP}$ = 10.9 Hz); ^{13}C{^{1}H} NMR (δ in ppm, d^8-toluene, 293 K, 101 MHz) 112.4 (d, $^3J_{CP}$ = 13.5 Hz), 63.4 (s), 56.1 (s), 42.2 (d, $^1J_{CP}$ = 14.8 Hz), 31.2 (d, $^1J_{CP}$ = 21.0 Hz), 29.9 (d, $^2J_{CP}$ = 13.3 Hz) Anal. Calcd. for $C_{28}H_{50}FeN_2P_2$: C, 63.15; H, 9.46; N, 5.26. Found: C, 63.21; H, 9.49; N, 5.22.

fc(NCH$_2$P^{t}Bu$_2$)$_2$Fe (5.2)

Synthesis A: To a solution of fc(NCH$_2$P^{t}Bu$_2$)$_2$ (0.25g, 0.47 mmol) in ether (15 mL) was added 1.6 M ^{n}BuLi in hexanes (0.57 mL, 0.91 mmol) at -78 °C. The solution was allowed to warm to room temperature over 3 h. This solution was added dropwise to an oven dried Schlenk containing $FeBr_2(THF)_2$ (0.16 g, 0.44 mmol) suspended in THF (5 mL). The reaction was allowed to stir for 16 h at which point the volatiles were removed *in vacuo*. The resulting red solids were extracted with hexanes, filtered through Celite and recrystallized from hexanes at -40 °C affording red needle-shaped crystals. Yield 0.088 g, 0.15 mmol, 32% yield. ^{1}H NMR (δ in ppm, C_6D_6, 293 K, 400 MHz) 53.1 (s), 16.8 (s), -5.7 (s), -14.9 (s), -66.1 (s). Anal. Calcd. for $C_{28}H_{48}N_2P_2Fe_2$: C 57.36; H, 8.25; N, 4.78. Found: C, 57.55, 8.31, 4.44.

Synthesis B: To an oven dried Schlenk containing fc(NCH$_2$P^{t}Bu$_2$)$_2$ (0.050 g, 0.094 mmol) in toluene (5 mL) was added dropwise a solution of Fe_2Mes_2 (0.027 g, 0.045 mmol) in toluene (5 mL). The resulting red solution was allowed to stir at room temperature for 2.5 h. The solution was reduced to dryness *in vacuo* and the resulting solids were recrystallized from hexanes. Yield 0.026 g, 0.044 mmol, 47% yield.

Bibliography

(1) Chirik, P. J.; Wieghardt, K. *Science* **2010**, *327*, 794.

(2) Chirik, P. J. In *Catalysis without Precious Metals*; Wiley-VCH Verlag GmbH & Co. KGaA: 2010, pp 83–110.

(3) Chirik, P. J. *Acc. Chem. Res.* **2015**, *48*, 1687.

(4) Čorić, I.; Holland, P. L. *J. Am. Chem. Soc.* **2016**, *138*, 7200.

(5) McWilliams, S. F.; Holland, P. L. *Acc. Chem. Res.* **2015**, *48*, 2059.

(6) Holland, P. L. *Acc. Chem. Res.* **2015**, *48*, 1696.

(7) U.S. Pharmacopeial Convention., http://www.usp.org/usp-nf/key-issues/elemental-impurities (accessed 08/02/2016).

(8) Haynes, W. M.; Lide, D. R., *CRC handbook of chemistry and physics : a ready-reference book of chemical and physical data*; CRC Press: Boca Raton, Fla., 2011.

(9) Lewis, J. C.; Bergman, R. G.; Ellman, J. A. *Acc. Chem. Res.* **2008**, *41*, 1013.

(10) Colby, D. A.; Bergman, R. G.; Ellman, J. A. *Chem. Rev.* **2010**, *110*, 624.

(11) Colby, D. A.; Tsai, A. S.; Bergman, R. G.; Ellman, J. A. *Acc. Chem. Res.* **2012**, *45*, 814.

(12) Trnka, T. M.; Grubbs, R. H. *Acc. Chem. Res.* **2001**, *34*, 18.

(13) Vougioukalakis, G. C.; Grubbs, R. H. *Chem. Rev.* **2010**, *110*, 1746.

(14) Dierick, S.; Markó, I. E. In *Encyclopedia of Reagents for Organic Synthesis*; John Wiley & Sons, Ltd: 2001.

(15) Dierick, S.; Markó, I. E. In *N-Heterocyclic Carbenes*; Wiley-VCH Verlag GmbH & Co. KGaA: 2014, pp 111–150.

(16) Gildner, P. G.; Colacot, T. J. *Organometallics* **2015**, *34*, 5497.

(17) Johansson-Seechurn, C. C. C.; Kitching, M. O.; Colacot, T. J.; Snieckus, V. *Angew. Chem. Int. Ed.* **2012**, *51*, 5062.

(18) Halpern, J.; Okamoto, T.; Zakhariev, A. *J. Mol. Catal.* **1977**, *2*, 65.

(19) Amatore, C.; Jutand, A. In *Handbook of Organopalladium Chemistry for Organic Synthesis*; John Wiley & Sons Inc.: 2003, pp 943–972.

(20) Fors, B. P.; Buchwald, S. L. *J. Am. Chem. Soc.* **2010**, *132*, 15914.

(21) Kochi, J. K. *Acc. Chem. Res.* **1974**, *7*, 351.

(22) Skinner, H. A.; Connor, J. A. *Pure Appl. Chem.* **1985**, *57*, 79.

(23) Li, C.; Nolan, S. P. *Organometallics* **1995**, *14*, 1327.

(24) Li, C.; Stevens, E. D.; Nolan, S. P. *Organometallics* **1995**, *14*, 3791.

(25) Luo, L.; Li, C.; Cucullu, M. E.; Nolan, S. P. *Organometallics* **1995**, *14*, 1333.

(26) Mandich, M. L.; Halle, L. F.; Beauchamp, J. L. *J. Am. Chem. Soc.* **1984**, *106*, 4403.

(27) Tilset, M.; Parker, V. D. *J. Am. Chem. Soc.* **1989**, *111*, 6711.

(28) Zhu, D.; Janssen, F. F.B. J.; Budzelaar, P. H. M. *Organometallics* **2010**, *29*, 1897.

(29) Cámpora, J.; Naz, A. M.; Palma, P.; Álvarez, E.; Reyes, M. L. *Organometallics* **2005**, *24*, 4878.

(30) Madden, C.; Vaughn, M. D.; Dez-Prez, I.; Brown, K. A.; King, P. W.; Gust, D.; Moore, A. L.; Moore, T. A. *J. Am. Chem. Soc.* **2012**, *134*, 1577.

(31) Sono, M.; Roach, M. P.; Coulter, E. D.; Dawson, J. H. *Chem. Rev.* **1996**, *96*, 2841.

(32) Burgess, B. K.; Lowe, D. J. *Chem. Rev.* **1996**, *96*, 2983.

(33) Sellmann, D.; Sutter, J. *Acc. Chem. Res.* **1997**, *30*, 460.

(34) Hosseinzadeh, P.; Lu, Y. *Biochim. Biophys. Acta.* **2016**, *1857*, 557.

(35) Seefeldt, L. C.; Dance, I. G.; Dean, D. R. *Biochemistry* **2004**, *43*, 1401.

(36) Frankel, E. N.; Jones, E. P.; Davison, V. L.; Emken, E.; Dutton, H. J. *J. Am. Oil Chem. Soc.* **1965**, *42*, 130.

(37) Frankel, E. N.; Emken, E. A.; Davison, V. L. *J. Org. Chem.* **1965**, *30*, 2739.

(38) Schroeder, M. A.; Wrighton, M. S. *J. Am. Chem. Soc.* **1976**, *98*, 551.

(39) Markó, L.; Radhi, M. A.; Ötvös, I. *J. Organomet. Chem.* **1981**, *218*, 369.

(40) Nishiguchi, T.; Fukuzumi, K. *J. Chem. Soc., Chem. Commun.* **1971**, 139.

(41) Bianchini, C.; Meli, A.; Peruzzini, M.; Vizza, F.; Zanobini, F.; Frediani, P. *Organometallics* **1989**, *8*, 2080.

(42) Bianchini, C.; Meli, A.; Peruzzini, M.; Frediani, P.; Bohanna, C.; Esteruelas, M. A.; Oro, L. A. *Organometallics* **1992**, *11*, 138.

(43) Wienhofer, G.; Westerhaus, F. A.; Jagadeesh, R. V.; Junge, K.; Junge, H.; Beller, M. *Chem. Comm.* **2012**, *48*, 4827.

(44) Fong, H.; Moret, M.-E.; Lee, Y.; Peters, J. C. *Organometallics* **2013**, *32*, 3053.

(45) Small, B. L.; Brookhart, M.; Bennett, A. M. A. *J. Am. Chem. Soc.* **1998**, *120*, 4049.

(46) Bart, S. C.; Lobkovsky, E.; Chirik, P. J. *J. Am. Chem. Soc.* **2004**, *126*, 13794.

(47) Bart, S. C.; Hawrelak, E. J.; Lobkovsky, E.; Chirik, P. J. *Organometallics* **2005**, *24*, 5518.

(48) Darmon, J. M.; Stieber, S. C. E.; Sylvester, K. T.; Fernndez, I.; Lobkovsky, E.; Semproni, S. P.; Bill, E.; Wieghardt, K.; DeBeer, S.; Chirik, P. J. *J. Am. Chem. Soc.* **2012**, *134*, 17125.

(49) Knowles, W. S.; Noyori, R. *Acc. Chem. Res.* **2007**, *40*, 1238.

(50) Knowles, W. S. *Angew. Chem. Int. Ed.* **2002**, *41*, 1998.

(51) Noyori, R. *Angew. Chem. Int. Ed.* **2002**, *41*, 2008.

(52) Enthaler, S.; Hagemann, B.; Erre, G.; Junge, K.; Beller, M. *Chem. Asian J.* **2006**, *1*, 598.

(53) Casey, C. P.; Guan, H. *J. Am. Chem. Soc.* **2007**, *129*, 5816.

(54) Fleischer, S.; Zhou, S.; Junge, K.; Beller, M. *Angew. Chem. Int. Ed.* **2013**, *52*, 5120.

(55) Menashe, N.; Shvo, Y. *Organometallics* **1991**, *10*, 3885.

(56) Lagaditis, P. O.; Lough, A. J.; Morris, R. H. *J. Am. Chem. Soc.* **2011**, *133*, 9662.

(57) Zuo, W.; Tauer, S.; Prokopchuk, D. E.; Morris, R. H. *Organometallics* **2014**, *33*, 5791.

(58) Sues, P. E.; Demmans, K. Z.; Morris, R. H. *Dalton Trans.* **2014**, *43*, 7650.

(59) Sandoval, C. A.; Ohkuma, T.; Muiz, K.; Noyori, R. *J. Am. Chem. Soc.* **2003**, *125*, 13490.

(60) Gunanathan, C.; Milstein, D. *Acc. Chem. Res.* **2011**, *44*, 588.

(61) Langer, R.; Leitus, G.; Ben-David, Y.; Milstein, D. *Angew. Chem. Int. Ed.* **2011**, *50*, 2120.

(62) Langer, R.; Diskin-Posner, Y.; Leitus, G.; Shimon, L. J. W.; Ben-David, Y.; Milstein, D. *Angew. Chem. Int. Ed.* **2011**, *50*, 9948.

(63) Ivanovic-Burmazovic, I.; van Eldik, R. *Dalton Trans.* **2008**, 5259.

(64) Cummins, D. C.; Yap, G. P. A.; Theopold, K. H. *Eur. J. Inorg. Chem.* **2016**, *2016*, 2349.

(65) Pinaka, A.; Vougioukalakis, G. C. *Coord. Chem. Rev.* **2015**, *288*, 69.

(66) Cable, R. A.; Green, M.; Mackenzie, R. E.; Timms, P. L.; Turney, T. W. *J. Chem. Soc., Chem. Commun.* **1976**, 270b.

(67) Berke, H.; Bankhardt, W.; Huttner, G.; v. Seyerl, J.; Zsolnai, L. *Ber.* **1981**, *114*, 2754.

(68) Hills, A.; Hughes, D. L.; Jimenez-Tenorio, M.; Leigh, G. J.; Rowley, A. T. *J. Chem. Soc., Dalton Trans.* **1993**, 3041.

(69) Komiya, S.; Akita, M.; Yoza, A.; Kasuga, N.; Fukuoka, A.; Kai, Y. *J. Chem. Soc., Chem. Commun.* **1993**, 787.

(70) George, T. A.; Rose, D. J.; Chang, Y.; Chen, Q.; Zubieta, J. *Inorg. Chem.* **1995**, *34*, 1295.

(71) Kandler, H.; Gauss, C.; Bidell, W.; Rosenberger, S.; Brgi, T.; Eremenko, I. L.; Veghini, D.; Orama, O.; Burger, P.; Berke, H. *Chem. Eur. J.* **1995**, *1*, 541.

(72) Fryzuk, M. D.; Johnson, S. A. *Coord. Chem. Rev.* **2000**, *200-202*, 379.

(73) Betley, T. A.; Peters, J. C. *J. Am. Chem. Soc.* **2003**, *125*, 10782.

(74) Moret, M.-E.; Peters, J. C. *J. Am. Chem. Soc.* **2011**, *133*, 18118.

(75) Chomitz, W. A.; Arnold, J. *Chem. Comm.* **2007**, 4797.

(76) Parks, J. E.; Holm, R. H. *Inorg. Chem.* **1968**, *7*, 1408.

(77) Smith, J. M.; Lachicotte, R. J.; Pittard, K. A.; Cundari, T. R.; Lukat-Rodgers, G.; Rodgers, K. R.; Holland, P. L. *J. Am. Chem. Soc.* **2001**, *123*, 9222.

(78) Smith, J. M.; Sadique, A. R.; Cundari, T. R.; Rodgers, K. R.; Lukat-Rodgers, G.; Lachicotte, R. J.; Flaschenriem, C. J.; Vela, J.; Holland, P. L. *J. Am. Chem. Soc.* **2006**, *128*, 756.

(79) Rodriguez, M. M.; Bill, E.; Brennessel, W. W.; Holland, P. L. *Science* **2011**, *334*, 780.

(80) Figg, T. M.; Holland, P. L.; Cundari, T. R. *Inorg. Chem.* **2012**, *51*, 7546.

(81) Zall, C. M.; Clouston, L. J.; Young, V. G.; Ding, K.; Kim, H. J.; Zherebetskyy, D.; Chen, Y.-S.; Bill, E.; Gagliardi, L.; Lu, C. C. *Inorg. Chem.* **2013**, *52*, 9216.

(82) Clouston, L. J.; Siedschlag, R. B.; Rudd, P. A.; Planas, N.; Hu, S.; Miller, A. D.; Gagliardi, L.; Lu, C. C. *J. Am. Chem. Soc.* **2013**, *135*, 13142.

(83) Rudd, P. A.; Liu, S.; Planas, N.; Bill, E.; Gagliardi, L.; Lu, C. C. *Angew. Chem. Int. Ed.* **2013**, *52*, 4449.

(84) Tereniak, S. J.; Carlson, R. K.; Clouston, L. J.; Young, V. G.; Bill, E.; Maurice, R.; Chen, Y.-S.; Kim, H. J.; Gagliardi, L.; Lu, C. C. *J. Am. Chem. Soc.* **2013**, *136*, 1842.

(85) Neudeck, S.; Maji, S.; Lpez, I.; Meyer, S.; Meyer, F.; Llobet, A. *J. Am. Chem. Soc.* **2013**, *136*, 24.

(86) Dalle, K. E.; Gruene, T.; Dechert, S.; Demeshko, S.; Meyer, F. *J. Am. Chem. Soc.* **2014**, *136*, 7428.

(87) Das, B.; Daver, H.; Singh, A.; Singh, R.; Haukka, M.; Demeshko, S.; Meyer, F.; Lisensky, G.; Jarenmark, M.; Himo, F.; Nordlander, E. *Eur. J. Inorg. Chem.* **2014**, *2014*, 2204.

(88) Kindermann, N.; Dechert, S.; Demeshko, S.; Meyer, F. *J. Am. Chem. Soc.* **2015**, *137*, 8002.

(89) Siedschlag, R. B.; Bernales, V.; Vogiatzis, K. D.; Planas, N.; Clouston, L. J.; Bill, E.; Gagliardi, L.; Lu, C. C. *J. Am. Chem. Soc.* **2015**, *137*, 4638.

(90) Powers, T. M.; Betley, T. A. *J. Am. Chem. Soc.* **2013**, *135*, 12289.

(91) Lee, Y.; Sloane, F. T.; Blondin, G.; Abboud, K. A.; Garca-Serres, R.; Murray, L. J. *Angew. Chem. Int. Ed.* **2015**, *54*, 1499.

(92) Fryzuk, M. D. *Can. J. Chem.* **1992**, *70*, 2839.

(93) Fryzuk, M. D.; Montgomery, C. D. *Coord. Chem. Rev.* **1989**, *95*, 1.

(94) Fryzuk, M. D.; Haddad, T. S.; Berg, D. J. *Coord. Chem. Rev.* **1990**, *99*, 137.

(95) Fryzuk, M. D.; Love, J. B.; Rettig, S. J.; Young, J. V. G. *Science* **1997**, *275*, 1445.

(96) Fryzuk, M. D.; MacKay, B. A.; Johnson, S. A.; Patrick, B. O. *Angew. Chem. Int. Ed.* **2002**, *41*, 3709.

(97) Fryzuk, M. D.; MacKay, B. A.; Patrick, B. O. *J. Am. Chem. Soc.* **2003**, 3234.

(98) Morello, L.; Love, J. B.; Patrick, B. O.; Fryzuk, M. D. *J. Am. Chem. Soc.* **2004**, *126*, 9480.

(99) MacLachlan, E. A.; Fryzuk, M. D. *Organometallics* **2005**, *24*, 1112.

(100) MacLachlan, E. A.; Hess, F. M.; Patrick, B. O.; Fryzuk, M. D. *J. Am. Chem. Soc.* **2007**, *129*, 10895.

(101) Parker, K. D. J.; Fryzuk, M. D. *Organometallics* **2014**, *33*, 6122.

(102) Wambach, T. C.; Ahn, J. M.; Patrick, B. O.; Fryzuk, M. D. *Organometallics* **2013**, *32*, 4431.

(103) Zhu, T.; Wambach, T. C.; Fryzuk, M. D. *Inorg. Chem.* **2011**, *50*, 11212.

(104) Ménard, G.; Jong, H.; Fryzuk, M. D. *Organometallics* **2009**, *28*, 5253.

(105) Fei, Z.; Dyson, P. J. *Coord. Chem. Rev.* **2005**, *249*, 2056.

(106) Zubiri, M. R. I.; Milton, H. L.; Cole-Hamilton, D. J.; Slawin, A. M. Z.; Derek Woollins, J. *Polyhedron* **2004**, *23*, 693.

(107) Blanc, C.; Agbossou-Niedercorn, F. *Tetrahedron: Asymmetry* **2004**, *15*, 757.

(108) Trinquier, G.; Ashby, M. T. *Inorg. Chem.* **1994**, *33*, 1306.

(109) Halcovitch, N. R.; Fryzuk, M. D. *Dalton Trans.* **2012**, *41*, 1524.

(110) Greenwood, B. P.; Forman, S. I.; Rowe, G. T.; Chen, C.-H.; Foxman, B. M.; Thomas, C. M. *Inorg. Chem.* **2009**, *48*, 6251.

(111) Kuppuswamy, S.; Bezpalko, M. W.; Powers, T. M.; Turnbull, M. M.; Foxman, B. M.; Thomas, C. M. *Inorg. Chem.* **2012**, *51*, 8225.

(112) Wetzel, T. G.; Dehnen, S.; Roesky, P. W. *Angew. Chem. Int. Ed.* **1999**, *38*, 1086.

(113) Thapa, I.; Gambarotta, S.; Korobkov, I.; Duchateau, R.; Kulangara, S. V.; Chevalier, R. *Organometallics* **2010**, *29*, 4080.

(114) Thapa, I.; Gambarotta, S.; Korobkov, I.; Murugesu, M.; Budzelaar, P. *Organometallics* **2012**, *31*, 486.

(115) Kuppuswamy, S.; Powers, T. M.; Johnson, B. M.; Bezpalko, M. W.; Brozek, C. K.; Foxman, B. M.; Berben, L. A.; Thomas, C. M. *Inorg. Chem.* **2013**, *52*, 4802.

(116) Nagashima, H.; Sue, T.; Oda, T.; Kanemitsu, A.; Matsumoto, T.; Motoyama, Y.; Sunada, Y. *Organometallics* **2006**, *25*, 1987.

(117) Sunada, Y.; Sue, T.; Matsumoto, T.; Nagashima, H. *J. Organomet. Chem.* **2006**, *691*, 3176.

(118) Sue, T.; Sunada, Y.; Nagashima, H. *Eur. J. Inorg. Chem.* **2007**, *2007*, 2897.

(119) Tsutsumi, H.; Sunada, Y.; Shiota, Y.; Yoshizawa, K.; Nagashima, H. *Organometallics* **2009**, *28*, 1988.

(120) Greenwood, B. P.; Rowe, G. T.; Chen, C.-H.; Foxman, B. M.; Thomas, C. M. *J. Am. Chem. Soc.* **2010**, *132*, 44.

(121) Krogman, J. P.; Foxman, B. M.; Thomas, C. M. *J. Am. Chem. Soc.* **2011**, *133*, 14582.

(122) Krogman, J. P.; Bezpalko, M. W.; Foxman, B. M.; Thomas, C. M. *Inorg. Chem.* **2013**, *52*, 3022.

(123) Zhou, W.; Marquard, S. L.; Bezpalko, M. W.; Foxman, B. M.; Thomas, C. M. *Organometallics* **2013**, *32*, 1766.

(124) Kuppuswamy, S.; Cooper, B. G.; Bezpalko, M. W.; Foxman, B. M.; Powers, T. M.; Thomas, C. M. *Inorg. Chem.* **2012**, *51*, 1866.

(125) Kuppuswamy, S.; Powers, T. M.; Krogman, J. P.; Bezpalko, M. W.; Foxman, B. M.; Thomas, C. M. *Chem. Sci.* **2013**, *4*, 3557.

(126) Kuppuswamy, S.; Bezpalko, M. W.; Powers, T. M.; Wilding, M. J. T.; Brozek, C. K.; Foxman, B. M.; Thomas, C. M. *Chem. Sci.* **2014**, *5*, 1617.

(127) Gwynne, E. A.; Stephan, D. W. *Organometallics* **2011**, *30*, 4128.

(128) Sgro, M. J.; Stephan, D. W. *Angew. Chem. Int. Ed.* **2012**, *51*, 11343.

(129) Sgro, M. J.; Stephan, D. W. *Chem. Comm.* **2013**, *49*, 2610.

(130) Shafir, A.; Power, M. P.; Whitener, G. D.; Arnold, J. *Organometallics* **2000**, *19*, 3978.

(131) Elliott, A. G.; Green, A. G.; Diaconescu, P. L. *Dalton Trans.* **2012**, *41*, 7852.

(132) Shafir, A.; Power, M. P.; Whitener, G. D.; Arnold, J. *Organometallics* **2001**, *20*, 1365.

(133) Shafir, A.; Arnold, J. *J. Am. Chem. Soc.* **2001**, *123*, 9212.

(134) Duhovi, S.; Oria, J. V.; Odoh, S. O.; Schreckenbach, G.; Batista, E. R.; Diaconescu, P. L. *Organometallics* **2013**, *32*, 6012.

(135) Broderick, E. M.; Gutzwiller, N. P.; Diaconescu, P. L. *Organometallics* **2010**, *29*, 3242.

(136) Shafir, A.; Arnold, J. *Inorg. Chim. Acta* **2003**, *345*, 216.

(137) Halcovitch, N. R.; Fryzuk, M. D. *Organometallics* **2013**, *32*, 5705.

(138) Allgeier, A. M.; Mirkin, C. A. *Angew. Chem. Int. Ed.* **1998**, *37*, 894.

(139) Housecroft, C. E.; Sharpe, A. G., *Inorganic Chemistry*, 3rd ed.; Pearson: Harlow: 2008.

(140) Parshall, G.; Ittel, S. D., *Homogeneous Catalysis. The Application and Chemistry of Catalysis by Soluble Transition Metal Complexes*, 2nd ed.; Wiley Interscience: 1992.

(141) Schlögl, R. *Angew. Chem. Int. Ed.* **2003**, *42*, 2004.

(142) Fryzuk, M. D. *Chem. Rec.* **2003**, *3*, 2.

(143) Fryzuk, M. D. *Acc. Chem. Res* **2009**, *42*, 127.

(144) Fryzuk, M. D.; Johnson, S. A.; Patrick, B. O.; Albinati, A.; Mason, S. A.; Koetzle, T. F. *J. Am. Chem. Soc.* **2001**, *123*, 3960.

(145) Fryzuk, M. D.; Johnson, S. A.; Rettig, S. J. *J. Am. Chem. Soc.* **1998**, *120*, 11024.

(146) Shaver, M. P.; Fryzuk, M. D. *Organometallics* **2005**, *24*, 2606.

(147) Belmonte, P. A.; Cloke, F. G. N.; Schrock, R. R. *J. Am. Chem. Soc.* **1983**, *105*, 2643.

(148) Miller, R. L.; Toreki, R.; LaPointe, R. E.; Wolczanski, P. T.; Van Duyne, G. D.; Roe, D. C. *J. Am. Chem. Soc.* **1993**, *115*, 5570.

(149) Toreki, R.; LaPointe, R. E.; Wolczanski, P. T. *J. Am. Chem. Soc.* **1987**, *109*, 7558.

(150) Matsuo, T.; Kawaguchi, H. *J. Am. Chem. Soc.* **2005**, *127*, 17198.

(151) Shima, T.; Hou, Z. *J. Am. Chem. Soc.* **2006**, *128*, 8124.

(152) Neithamer, D. R.; LaPointe, R. E.; Wheeler, R. A.; Richeson, D. S.; Van Duyne, G. D.; Wolczanski, P. T. *J. Am. Chem. Soc.* **1989**, *111*, 9056.

(153) Miller, R. L.; Wolczanski, P. T.; Rheingold, A. L. *J. Am. Chem. Soc.* **1993**, *115*, 10422.

(154) Christian, G.; Stranger, R.; Petrie, S.; Yates, B. F.; Cummins, C. C. *Chem. - Eur. J.* **2007**, *13*, 4264.

(155) Andrae, D.; Häußermann, U.; Dolg, M.; Stoll, H.; Preuß, H. *Theor. Chem. Acta* **1990**, *77*, 123.

(156) Martin, J. M. L.; Sundermann, A. *J. Chem. Phys.* **2001**, *114*.

(157) Hehre, W. J.; Ditchfield, R.; Pople, J. A. *J. Chem. Phys.* **1972**, *56*, 2257.

(158) Bergner, A.; Dolg, M.; Kchle, W.; Stoll, H.; Preu, H. *Mol. Phys.* **1993**, *80*, 1431.

(159) Höllwarth, A.; Böhme, M.; Dapprich, S; Ehlers, A.; Gobbi, A.; Jonas, V.; Köhler, K.; Stegmann, R.; Veldkamp, A.; Frenking, G. *Chem. Phys. Lett.* **1993**, *208*, 237.

(160) Becke, A. D. *J. Chem. Phys.* **1993**, *98*, 5648.

(161) Burke, K.; Perdew, J.; Yang, W., *Electronic Density-Functional Theory: Recent Progress and New Directions*; Springer US: 1998.

(162) Frisch, M. J.; Trucks, G. W.; Schlegel, H. B.; Scuseria, G. E.; Robb, M. A.; Cheeseman, J. R.; Scalmani, G.; Barone, V.; Mennucci, B.; Petersson, G. A.; Nakatsuji, H.; Caricato, M.; Li, X.; Hratchian, H. P.; Izmaylov, A. F.; Bloino, J.; Zheng, G.; Sonnenberg, J. L.; Hada, M.; Ehara, M.; Toyota, K.; Fukuda, R.; Hasegawa, J.; Ishida, M.; Nakajima, T.; Honda, Y.; Kitao, O.; Nakai, H.; Vreven, T.; Montgomery Jr., J. A.; Peralta, J. E.; Ogliaro, F.; Bearpark, M.; Heyd, J. J.; Brothers, E.; Kudin, K. N.; Staroverov, V. N.; Kobayashi, R.; Normand, J.; Raghavachari, K.; Rendell, A.; Burant, J. C.; Iyengar, S. S.; Tomasi, J.; Cossi, M.; Rega, N.; Millam, J. M.; Klene, M.; Knox, J. E.; Cross, J. B.; Bakken, V.; Adamo, C.; Jaramillo, J.; Gomperts, R.; Stratmann, R. E.; Yazyev, O.; Austin, A. J.; Cammi, R.; Pomelli, C.; Ochterski, J. W.; Martin, R. L.; Morokuma, K.; Zakrzewski, V. G.; Voth, G. A.; Salvador, P.; Dannenberg, J. J.; Dapprich, S.; Daniels, A. D.; Farkas, Foresman, J. B.; Ortiz, J. V.; Cioslowski, J.; Fox, D. J. *Gaussian* 09 Revision E.01., Gaussian Inc. Wallingford CT 2009.

(163) Reed, A. E.; Curtiss, L. A.; Weinhold, F. *Chem. Rev.* **1988**, *88*, 899.

(164) Fryzuk, M. D.; Johnson, S. A.; Rettig, S. J. *Organometallics* **2000**, *19*, 3931.

(165) Watson, L. A.; Eisenstein, O. *J. Chem. Ed.* **2002**, *79*, 1269.

(166) Cavigliasso, G.; Christian, G.; Stranger, R.; Yates, B. F. *Dalton Trans.* **2009**, 956.

(167) Ariafard, A.; Brookes, N. J.; Stranger, R.; Yates, B. F. *J. Am. Chem. Soc.* **2008**, *130*, 11928.

(168) EPA Green House Gas Emissions., http://www.epa.gov/climatechange/ghgemissions/gases/co2.html (accessed 12/12/2016).

(169) Darensbourg, D. J. *Inorg. Chem.* **2010**, *49*, 10765.

(170) Tanaka, R.; Yamashita, M.; Nozaki, K. *J. Am. Chem. Soc.* **2009**, *131*, 14168.

(171) Wesselbaum, S.; vomStein, T.; Klankermayer, J.; Leitner, W. *Angew. Chem. Int. Ed.* **2012**, *51*, 7499.

(172) Jessop, P. G.; Jo, F.; Tai, C.-C. *Coord. Chem. Rev.* **2004**, *248*, 2425.

(173) Bernskoetter, W. H.; Tyler, B. T. *Organometallics* **2011**, *30*, 520.

(174) Cokoja, M.; Bruckmeier, C.; Rieger, B.; Herrmann, W. A.; Kühn, F. E. *Angew. Chem. Int. Ed.* **2011**, *50*, 8510.

(175) Finn, C.; Schnittger, S.; Yellowlees, L. J.; Love, J. B. *Chem. Commun.* **2012**, *48*, 1392.

(176) Sakakura, T.; Choi, J.-C.; Yasuda, H. *Chem. Rev.* **2007**, *107*, 2365.

(177) Aresta, M., *Carbon Dioxide Recovery and Utilization*, Wiley-VCH: Weinheim, Germany, 2010.

(178) Knobloch, D. J.; Toomey, H. E.; Chirik, P. J. *J. Am. Chem. Soc.* **2008**, *130*, 4248.

(179) Ballmann, J.; Yeo, A.; MacKay, B. A.; van Rijt, S.; Patrick, B. O.; Fryzuk, M. D. *Chem. Commun.* **2010**, *46*.

(180) Rankin, M. A.; Cummins, C. C. *J. Am. Chem. Soc.* **2010**, *132*, 10021.

(181) Tardif, O.; Hashizume, D.; Hou, Z. *J. Am. Chem. Soc.* **2004**, *126*, 8080.

(182) Peterson, A. A.; Abild-Pedersen, F.; Studt, F.; Rossmeisl, J.; Nørskov, J. K. *Energy Environ. Sci.* **2010**, *3*, 1311.

(183) *Catalysis without Precious Metals*; Bullock, R. M., Ed.; Wiley-VCH: 2010.

(184) Chen, C.; Dugan, T. R.; Brennessel, W. W.; Weix, D. J.; Holland, P. L. *J. Am. Chem. Soc.* **2014**, *136*, 945.

(185) Frazier, B. A.; Williams, V. A.; Wolczanski, P. T.; Bart, S. C.; Meyer, K.; Cundari, T. R.; Lobkovsky, E. B. *Inorg. Chem.* **2013**, *52*, 3295.

(186) Frazier, B. A.; Wolczanski, P. T.; Lobkovsky, E. B.; Cundari, T. R. *J. Am. Chem. Soc.* **2009**, *131*, 3428.

(187) Friedfeld, M. R.; Margulieux, G. W.; Schaefer, B. A.; Chirik, P. J. *J. Am. Chem. Soc.* **2014**, *136*, 13178.

(188) Hennessy, E. T.; Betley, T. A. *Science* **2013**, *340*, 591.

(189) Hennessy, E. T.; Liu, R. Y.; Iovan, D. A.; Duncan, R. A.; Betley, T. A. *Chem. Sci.* **2014**, *5*, 1526.

(190) Hoyt, J. M.; Shevlin, M.; Margulieux, G. W.; Krska, S. W.; Tudge, M. T.; Chirik, P. J. *Organometallics* **2014**, *33*, 5781.

(191) MacLeod, K. C.; Vinyard, D. J.; Holland, P. L. *J. Am. Chem. Soc.* **2014**, *136*, 10226.

(192) Powers, T. M.; Gu, N. X.; Fout, A. R.; Baldwin, A. M.; Hernndez Snchez, R.; Alfonso, D. M.; Chen, Y.-S.; Zheng, S.-L.; Betley, T. A. *J. Am. Chem. Soc.* **2013**, *135*, 14448.

(193) Sazama, G. T.; Betley, T. A. *Inorg. Chem.* **2014**, *53*, 269.

(194) Tereniak, S. J.; Carlson, R. K.; Clouston, L. J.; Young, V. G.; Bill, E.; Maurice, R.; Chen, Y.-S.; Kim, H. J.; Gagliardi, L.; Lu, C. C. *J. Am. Chem. Soc.* **2014**, *136*, 1842.

(195) Schmidt, V. A.; Hoyt, J. M.; Margulieux, G. W.; Chirik, P. J. *J. Am. Chem. Soc.* **2015**, *137*, 7903.

(196) Camacho-Bunquin, J.; Ferguson, M. J.; Stryker, J. M. *J. Am. Chem. Soc.* **2013**, *135*, 5537.

(197) Dean, R. K.; Fowler, C. I.; Hasan, K.; Kerman, K.; Kwong, P.; Trudel, S.; Leznoff, D. B.; Kraatz, H.-B.; Dawe, L. N.; Kozak, C. M. *Dalton Trans.* **2012**, *41*, 4806.

(198) Fryzuk, M. D.; Leznoff, D. B.; Ma, E. S. F.; Rettig, S. J.; Young, V. G. *Organometallics* **1998**, *17*, 2313.

(199) Fryzuk, M. D.; Leznoff, D. B.; Thompson, R. C.; Rettig, S. J. *J. Am. Chem. Soc.* **1998**, *120*, 10126.

(200) Hayes, C. E.; Leznoff, D. B. *Dalton Trans.* **2012**, *41*, 5743.

(201) King, E. R.; Sazama, G. T.; Betley, T. A. *J. Am. Chem. Soc.* **2012**, *134*, 17858.

(202) Chirik, P. J. *Inorg. Chem.* **2011**, *50*, 9737.

(203) Zhang, G.; Vasudevan, K. V.; Scott, B. L.; Hanson, S. K. *J. Am. Chem. Soc.* **2013**, *135*, 8668.

(204) Askevold, B.; Nieto, J. T.; Tussupbayev, S.; Diefenbach, M.; Herdtweck, E.; Holthausen, M. C.; Schneider, S. *Nat. Chem.* **2011**, *3*, 532.

(205) Fryzuk, M. D.; Haddad, T. S. *J. Chem. Soc., Chem. Commun.* **1990**, 1088.

(206) Fryzuk, M. D.; MacNeil, P. A. *Organometallics* **1983**, *2*, 355.

(207) Fryzuk, M. D.; Kozak, C. M.; Bowdridge, M. R.; Jin, W.; Tung, D.; Patrick, B. O.; Rettig, S. J. *Organometallics* **2001**, *20*, 3752.

(208) Fryzuk, M. D.; Love, J. B.; Rettig, S. J. *Chem. Commun.* **1996**, 2783.

(209) Fryzuk, M. D.; Johnson, S. A.; Rettig, S. J. *J. Am. Chem. Soc.* **2001**, *123*, 1602.

(210) Fryzuk, M. D.; Kozak, C. M.; Mehrkhodavandi, P.; Morello, L.; Patrick, B. O.; Rettig, S. J. *J. Am. Chem. Soc.* **2002**, *124*, 516.

(211) MacLachlan, E. A.; Fryzuk, M. D. *Organometallics* **2006**, *25*, 1530.

(212) Morello, L.; Yu, P.; Carmichael, C. D.; Patrick, B. O.; Fryzuk, M. D. *J. Am. Chem. Soc.* **2005**, *127*, 12796.

(213) Kuppuswamy, S.; Powers, T. M.; Johnson, B. M.; Brozek, C. K.; Krogman, J. P.; Bezpalko, M. W.; Berben, L. A.; Keith, J. M.; Foxman, B. M.; Thomas, C. M. *Inorg. Chem.* **2014**, *53*, 5429.

(214) Wang, X.; Thevenon, A.; Brosmer, J. L.; Yu, I.; Khan, S. I.; Mehrkhodavandi, P.; Diaconescu, P. L. *J. Am. Chem. Soc.* **2014**, *136*, 11264.

(215) Malassa, A.; Schulze, B.; Stein-Schaller, B.; Grls, H.; Weber, B.; Westerhausen, M. *Eur. J. Inorg. Chem.* **2011**, *2011*, 1584.

(216) Sadeh, S.; Schatte, G.; Müller, J. *Chem. Eur. J.* **2013**, *19*, 13408.

(217) Schumann, H.; Hartmann, U.; Wassermann, W.; Dietrich, A.; Gürlitz, F. H.; Pohl, L.; Hostalek, M. *Chem. Ber.* **1990**, *123*, 2093.

(218) Herbert, D. E.; Mayer, U. F.; Manners, I. *Angew. Chem. Int. Ed.* **2007**, *46*, 5060.

(219) Green, J. C. *Chem. Soc. Rev.* **1998**, *27*, 263.

(220) Carver, C. T.; Diaconescu, P. L. *J. Am. Chem. Soc.* **2008**, *130*, 7558.

(221) Green, A. G.; Kiesz, M. D.; Oria, J. V.; Elliott, A. G.; Buechler, A. K.; Hohenberger, J.; Meyer, K.; Zink, J. I.; Diaconescu, P. L. *Inorg. Chem.* **2013**, *52*, 5603.

(222) Sirbu, D.; Turta, C.; Benniston, A. C.; Abou-Chahine, F.; Lemmetyinen, H.; Tkachenko, N. V.; Wood, C.; Gibson, E. *RSC Adv.* **2014**, *4*, 22733.

(223) Kaub, C.; Augenstein, T.; Bauer, T. O.; Rothe, E.; Esmezjan, L.; Schnemann, V.; Roesky, P. W. *Inorg. Chem.* **2014**, *53*, 4491.

(224) Mereacre, V.; Schlageter, M.; Powell, A. K. *J. Magn. Magn Mater.* **2015**, *381*, 478.

(225) Lin, P.-H.; Smythe, N. C.; Gorelsky, S. I.; Maguire, S.; Henson, N. J.; Korobkov, I.; Scott, B. L.; Gordon, J. C.; Baker, R. T.; Murugesu, M. *J. Am. Chem. Soc.* **2011**, *133*, 15806.

(226) Ruddy, A. J.; Kelly, C. M.; Crawford, S. M.; Wheaton, C. A.; Sydora, O. L.; Small, B. L.; Stradiotto, M.; Turculet, L. *Organometallics* **2013**, *32*, 5581.

(227) Mund, G.; Vidovic, D.; Batchelor, R. J.; Britten, J. F.; Sharma, R. D.; Jones, C. H. W.; Leznoff, D. B. *Chem. Eur. J* **2003**, *9*, 4757.

(228) MacDonnell, F. M.; Ruhlandt-Senge, K.; Ellison, J. J.; Holm, R. H.; Power, P. P. *Inorg. Chem.* **1995**, *34*, 1815.

(229) Evans, D. J.; Hughes, D. L.; Silver, J. *Inorg. Chem.* **1997**, *36*, 747.

(230) Liu, Y.; Luo, L.; Xiao, J.; Wang, L.; Song, Y.; Qu, J.; Luo, Y.; Deng, L. *Inorg. Chem.* **2015**, *54*, 4752.

(231) Muresan, N.; Lu, C. C.; Ghosh, M.; Peters, J. C.; Abe, M.; Henling, L. M.; Weyhermller, T.; Bill, E.; Wieghardt, K. *Inorg. Chem.* **2008**, *47*, 4579.

(232) Hawrelak, E. J.; Bernskoetter, W. H.; Lobkovsky, E.; Yee, G. T.; Bill, E.; Chirik, P. J. *Inorg. Chem.* **2005**, *44*, 3103.

(233) Seyferth, D.; Hames, B. W.; Rucker, T. G.; Cowie, M.; Dickson, R. S. *Organometallics* **1983**, *2*, 472.

(234) Akabori, S.; Kumagai, T.; Shirahige, T.; Sato, S.; Kawazoe, K.; Tamura, C.; Sato, M. *Organometallics* **1987**, *6*, 2105.

(235) Mann, G.; Shelby, Q.; Roy, A. H.; Hartwig, J. F. *Organometallics* **2003**, *22*, 2775.

(236) Metallinos, C.; Tremblay, D.; Barrett, F. B.; Taylor, N. J. *J. Organomet. Chem.* **2006**, *691*, 2044.

(237) Klapp, L. R. R.; Bruhn, C.; Leibold, M.; Siemeling, U. *Organometallics* **2013**, *32*, 5862.

(238) Blass, B. L.; Hernández Sánchez, R.; Decker, V. A.; Robinson, M. J.; Piro, N. A.; Kassel, W. S.; Diaconescu, P. L.; Nataro, C. *Organometallics* **2016**, *35*, 462.

(239) Akabori, S.; Kumagai, T.; Shirahige, T.; Sato, S.; Kawazoe, K.; Tamura, C.; Sato, M. *Organometallics* **1987**, *6*, 526.

(240) Gramigna, K. M.; Oria, J. V.; Mandell, C. L.; Tiedemann, M. A.; Dougherty, W. G.; Piro, N. A.; Kassel, W. S.; Chan, B. C.; Diaconescu, P. L.; Nataro, C. *Organometallics* **2013**, *32*, 5966.

(241) Ramos, A.; Otten, E.; Stephan, D. W. *J. Am. Chem. Soc.* **2009**, *131*, 15610.

(242) Carlin, R. L., *Magnetochemistry*; Springer-Verlag: Heidelberg: 1986.

(243) Stokes, S. L.; Davis, W. M.; Odom, A. L.; Cummins, C. C. *Organometallics* **1996**, *15*, 4521.

(244) Evans, D. F. *J. Chem. Soc.* **1959**, 2003.

(245) Schubert, E. M. *J. Chem. Ed.* **1992**, *69*, 62.

(246) Hebden, T. J.; St.John, A. J.; Gusev, D. G.; Kaminsky, W.; Goldberg, K. I.; Heinekey, D. M. *Angew. Chem. Int. Ed.* **2011**, *50*, 1873.

(247) Becke, A. D. *Phys. Rev. A* **1988**, *38*, 3098.

(248) Perdew, J. P. *Phys. Rev. B* **1986**, *33*, 8822.

(249) Mayer, I. *Chem. Phys. Lett.* **1983**, *97*, 270.

(250) Bridgeman, A. J.; Cavigliasso, G.; Ireland, L. R.; Rothery, J. *J. Chem. Soc., Dalton Trans.* **2001**, 2095.

(251) Chevreau, H.; Martinsky, C.; Sevin, A.; Minot, C.; Silvi, B. *New J. Chem.* **2003**, *27*, 1049.

(252) Phillips, A. D.; Ienco, A.; Reinhold, J.; Bttcher, H.-C.; Mealli, C. *Chem. Eur. J* **2006**, *12*, 4691.

(253) Glendening, E.; Badenhoop, J.; Reed, A. E.; Carpenter, J. E.; Bohmann, J. A.; Morales, C.; Landis, C.; Weinhold, F. NBO 6.0., 2013.

(254) Cantalupo, S. A.; Fiedler, S. R.; Shores, M. P.; Rheingold, A. L.; Doerrer, L. H. *Angew. Chem. Int. Ed.* **2012**, *51*, 1000.

(255) Friedfeld, M. R.; Shevlin, M.; Margulieux, G. W.; Campeau, L.-C.; Chirik, P. J. *J. Am. Chem. Soc.* **2016**, *138*, 3314.

(256) Lagaditis, P. O.; Schluscha, B.; Demeshko, S.; Wrtele, C.; Schneider, S. *Inorg. Chem.* **2016**, *55*, 4529.

(257) Nguyen, A. I.; Hadt, R. G.; Solomon, E. I.; Tilley, T. D. *Chem. Sci.* **2014**, *5*, 2874.

(258) Rozenel, S. S.; Padilla, R.; Arnold, J. *Inorg. Chem.* **2013**, *52*, 11544.

(259) Rozenel, S. S.; Padilla, R.; Camp, C.; Arnold, J. *Chem. Comm.* **2014**, *50*, 2612.

(260) Scheuermann, M. L.; Semproni, S. P.; Pappas, I.; Chirik, P. J. *Inorg. Chem.* **2014**, *53*, 9463.

(261) Xu, R.; Chakraborty, S.; Yuan, H.; Jones, W. D. *ACS Catalysis* **2015**, *5*, 6350.

(262) Yu, R. P.; Darmon, J. M.; Milsmann, C.; Margulieux, G. W.; Stieber, S. C. E.; DeBeer, S.; Chirik, P. J. *J. Am. Chem. Soc.* **2013**, *135*, 13168.

(263) Zhang, G.; Scott, B. L.; Hanson, S. K. *Angew. Chem. Int. Ed.* **2012**, *51*, 12102.

(264) Hill, G. S.; Irwin, M. J.; Levy, C. J.; Rendina, L. M.; Puddephatt, R. J.; Andersen, R. A.; McLean, L. In *Inorganic Syntheses*; Wiley & Sons.: 2007, pp 149–153.

(265) Fryzuk, M. D.; MacNeil, P. A. *J. Am. Chem. Soc.* **1981**, *103*, 3592.

(266) Fryzuk, M. D.; MacNeil, P. A.; Rettig, S. J.; Secco, A. S.; Trotter, J. *Organometallics* **1982**, *1*, 918.

(267) Wang, Z.-X.; Qi, C.-Y. *Organometallics* **2007**, *26*, 2243.

(268) Breunig, J. M.; Gupta, P.; Das, A.; Tussupbayev, S.; Diefenbach, M.; Bolte, M.; Wagner, M.; Holthausen, M. C.; Lerner, H.-W. *Chem. Asian J.* **2014**, *9*, 3163.

(269) Gudat, D.; Nieger, M.; Niecke, E. *J. Chem. Soc., Dalton Trans.* **1989**, 693.

(270) Hofmann, P.; Shishkov, I. V.; Rominger, F. *Inorg. Chem.* **2008**, *47*, 11755.

(271) Vollmerhaus, R.; Shao, P.; Taylor, N. J.; Collins, S. *Organometallics* **1999**, *18*, 2731.

(272) Fenske, D.; Maczek, B.; Maczek, K. *Z. Anorg. Allg. Chem.* **1997**, *623*, 1113.

(273) Yang, L.; Powell, D. R.; Houser, R. P. *Dalton Trans.* **2007**, 955.

(274) Corbett, M.; Hoskins, B. F. *Chem. Commun.* **1968**, 1602.

(275) Pang, K.; Figueroa, J. S.; Tonks, I. A.; Sattler, W.; Parkin, G. *Inorg. Chim. Acta* **2009**, *362*, 4609.

(276) Matthews, W. S.; Bares, J. E.; Bartmess, J. E.; Bordwell, F. G.; Cornforth, F. J.; Drucker, G. E.; Margolin, Z.; McCallum, R. J.; McCollum, G. J.; Vanier, N. R. *J. Am. Chem. Soc.* **1975**, *97*, 7006.

(277) Bordwell, F. G.; Algrim, D.; Vanier, N. R. *J. Org. Chem.* **1977**, *42*, 1817.

(278) Meyer, N.; Lough, A. J.; Morris, R. H. *Chem. Eur. J.* **2009**, *15*, 5605.

(279) Sonnenberg, J. F.; Coombs, N.; Dube, P. A.; Morris, R. H. *J. Am. Chem. Soc.* **2012**, *134*, 5893.

(280) Suntivich, J.; May, K. J.; Gasteiger, H. A.; Goodenough, J. B.; Shao-Horn, Y. *Science* **2011**, *334*, 1383.

(281) Kurzman, J. A.; Dettelbach, K. E.; Martinolich, A. J.; Berlinguette, C. P.; Neilson, J. R. *Chem. Mater.* **2015**, *27*, 3462.

(282) Cheng, Y.; Jiang, S. P. *Prog. Nat. Science: Mat. Int.* **2015**, *25*, 545.

(283) Dhakshinamoorthy, A.; Asiri, A. M.; Garcia, H. *Chem. Eur. J.* **2016**, *22*, 8012.

(284) Inderwildi, O. R.; Jenkins, S. J. *Chem. Soc. Rev.* **2008**, *37*, 2274.

(285) Roduner, E.; Kaim, W.; Sarkar, B.; Urlacher, V. B.; Pleiss, J.; Gläser, R.; Einicke, W.; Sprenger, G. A.; Beifuβ, U.; Klemm, E.; Liebner, C.; Hieronymus, H.; Hsu, S.; Plietker, B.; Laschat, S. *ChemCatChem* **2013**, *5*, 82.

(286) Kim, J; Rees, D. *Science* **1992**, *257*, 1677.

(287) Einsle, O.; Tezcan, F. A.; Andrade, S. L. A.; Schmid, B.; Yoshida, M.; Howard, J. B.; Rees, D. C. *Science* **2002**, *297*, 1696.

(288) Lancaster, K. M.; Roemelt, M.; Ettenhuber, P.; Hu, Y.; Ribbe, M. W.; Neese, F.; Bergmann, U.; DeBeer, S. *Science* **2011**, *334*, 974.

(289) Spatzal, T.; Aksoyoglu, M.; Zhang, L.; Andrade, S. L. A.; Schleicher, E.; Weber, S.; Rees, D. C.; Einsle, O. *Science* **2011**, *334*, 940.

(290) Muetterties, E. L. *Science* **1977**, *196*, 839.

(291) Hazari, N. *Chem. Soc. Rev.* **2010**, *39*, 4044.

(292) Tanaka, H.; Nishibayashi, Y.; Yoshizawa, K. *Acc. Chem. Res.* **2016**, *49*, 987.

(293) Kurtz Jr., M. D. *J. Biol. Inorg. Chem.* **1997**, *2*, 159.

(294) Holm, R. H.; Kennepohl, P.; Solomon, E. I. *Chem. Rev.* **1996**, *96*, 2239.

(295) Lee, S. C.; Holm, R. H. *Chem. Rev.* **2004**, *104*, 1135.

(296) Venkateswara Rao, P.; Holm, R. H. *Chem. Rev.* **2004**, *104*, 527.

(297) Bjornsson, R.; Neese, F.; Schrock, R. R.; Einsle, O.; DeBeer, S. *J. Biol. Inorg. Chem.* **2015**, *20*, 447.

(298) Barney, B. M.; Igarashi, R. Y.; Dos Santos, P. C.; Dean, D. R.; Seefeldt, L. C. *J. Biol. Chem.* **2004**, *279*, 53621.

(299) Wolff, T. E.; Berg, J. M.; Warrick, C.; Hodgson, K. O.; Holm, R. H.; Frankel, R. B. *J. Am. Chem. Soc.* **1978**, *100*, 4630.

(300) Mizobe, Y.; Mascharak, P. K.; Palermo, R. E.; Holm, R. H. *Inorg. Chim. Acta* **1983**, *80*, L65.

(301) Coucouvanis, D.; Mosier, P. E.; Demadis, K. D.; Patton, S.; Malinak, S. M.; Kim, C. G.; Tyson, M. A. *J. Am. Chem. Soc.* **1993**, *115*, 12193.

(302) Fomitchev, D. V.; McLauchlan, C. C.; Holm, R. H. *Inorg. Chem.* **2002**, *41*, 958.

(303) Coucouvanis, D.; Han, J.; Moon, N. *J. Am. Chem. Soc.* **2002**, *124*, 216.

(304) Ohta, S.; Ohki, Y.; Hashimoto, T.; Cramer, R. E.; Tatsumi, K. *Inorg. Chem.* **2012**, *51*, 11217.

(305) Powers, T. M.; Fout, A. R.; Zheng, S.-L.; Betley, T. A. *J. Am. Chem. Soc.* **2011**, *133*, 3336.

(306) Gehring, H.; Metzinger, R.; Braun, B.; Herwig, C.; Harder, S.; Ray, K.; Limberg, C. *Dalton Trans.* **2016**, *45*, 2989.

(307) Ermert, D. M.; Gordon, J. B.; Abboud, K. A.; Murray, L. J. *Inorg. Chem.* **2015**, *54*, 9282.

(308) Hernández Sánchez, R.; Zheng, S.-L.; Betley, T. A. *J. Am. Chem. Soc.* **2015**, *137*, 11126.

(309) Hernández Sánchez, R.; Bartholomew, A. K.; Powers, T. M.; Ménard, G.; Betley, T. A. *J. Am. Chem. Soc.* **2016**, *138*, 2235.

(310) Pick, F. S.; Thompson, J. R.; Savard, D. S.; Leznoff, D. B.; Fryzuk, M. D. *Inorg. Chem.* **2016**, *55*, 4059.

(311) Lee, D.; Krebs, C.; Huynh, B. H.; Hendrich, M. P.; Lippard, S. J. *J. Am. Chem. Soc.* **2000**, *122*, 5000.

(312) Bruce, M. I.; Humphrey, M. G.; Shawkataly, O. B.; Snow, M. R.; Tiekink, E. R. T. *J. Organomet. Chem.* **1986**, *315*, C51.

(313) Smieja, J. A.; Gozum, J. E.; Gladfelter, W. L. *Organometallics* **1986**, *5*, 2154.

(314) Nakajima, Y.; Suzuki, H. *Organometallics* **2005**, *24*, 1860.

(315) Hawley, A. L.; Stasch, A. *Eur. J. Inorg. Chem* **2015**, *2015*, 258.

(316) Stasch, A. *Angew. Chem. Int. Ed.* **2014**, *53*, 10200.

(317) Stasch, A. *Chem. Eur. J.* **2012**, *18*, 15105.

(318) Li, S.; Miao, W.; Tang, T.; Dong, W.; Zhang, X.; Cui, D. *Organometallics* **2008**, *27*, 718.

(319) Liu, B.; Han, B.-Y.; Zhang, C.-L.; Li, S.-H.; Sun, G.-P.; Cui, D.-M. *Chin. J. Polym. Sci.* **2015**, *33*, 792.

(320) Liu, B.; Li, L.; Sun, G.; Liu, J.; Wang, M.; Li, S.; Cui, D. *Macromolecules* **2014**, *47*, 4971.

(321) Liu, B.; Liu, D.-T.; Li, S.-H.; Sun, G.-P.; Cui, D.-M. *Chin. J. Polym. Sci.* **2016**, *34*, 104.

(322) Liu, B.; Sun, G.; Li, S.; Liu, D.; Cui, D. *Organometallics* **2015**, *34*, 4063.

(323) Zhang, Q.; Zhang, X.-Q.; Wang, Z.-X. *Dalton Trans.* **2012**, *41*, 10453.

(324) Peganova, T. A.; Kalsin, A. M.; Ustynyuk, N. A.; Vasil'ev, A. A. *Russ. Chem. Bull.* **2014**, *63*, 2305.

(325) Guo, W.-J.; Wang, Z.-X. *J. Org. Chem.* **2013**, *78*, 1054.

(326) Wu, B.; Gramigna, K. M.; Bezpalko, M. W.; Foxman, B. M.; Thomas, C. M. *Inorg. Chem.* **2015**, *54*, 10909.

(327) Mahieu, A.; Igau, A.; Jaud, J.; Majoral, J.-P. *Organometallics* **1995**, *14*, 944.

(328) Kubo, K.; Baba, T.; Mizuta, T.; Miyoshi, K. *Organometallics* **2006**, *25*, 3238.

(329) Cordero, B.; Gomez, V.; Platero-Prats, A. E.; Reves, M.; Echeverria, J.; Cremades, E.; Barragan, F.; Alvarez, S. *Dalton Trans.* **2008**, 2832.

(330) Rudd, P. A.; Liu, S.; Gagliardi, L.; Young, V. G.; Lu, C. C. *J. Am. Chem. Soc.* **2011**, *133*, 20724.

(331) Shafir, A.; Fiedler, D.; Arnold, J. *J. Chem. Soc., Dalton Trans.* **2002**, 555.

(332) Wilson, A. D.; Newell, R. H.; McNevin, M. J.; Muckerman, J. T.; Rakowski DuBois, M; DuBois, D. L. *J. Am. Chem. Soc.* **2006**, *128*, 358.

(333) Relaxation, C. *Coord. Chem. Rev.* **1996**, *150*, 77.

(334) Bergbreiter, D. E.; Killough, J. M. *J. Am. Chem. Soc.* **1978**, *100*, 2126.

(335) SAINT Version 7.03A., Bruker AXS Inc., Madison, Wisconsin USA, (1997-2003).

(336) SADABS Bruker Nonius: area detector scaling and absorption correction. Version 2.10., Bruker AXS Inc., Madison, Wisconsin, USA, (2003).

(337) Sheldrick, G. M. *Acta Cryst. A* **2008**, *A64*, 112.

(338) Farrugia, L. J. *J. Appl. Cryst.* **1999**, *32*, 837.

(339) Dolomanov, O. V.; Bourhis, L. J.; Gildea, R. J.; Howard, J. A. K.; Puschmann, H. *J. Appl. Cryst.* **2009**, *42*, 339.

(340) Carpenter, J. E.; Weinhold, F. *J. Mol. Struc.-THEOCHEM* **1988**, *169*, 41.

(341) Reed, A. E.; Weinhold, F. *J. Chem. Phys.* **1985**, *83*, 1736.

(342) Zhurko, G. A. Chemcraft., 2013.

Appendix A

Crystallographic Appendix

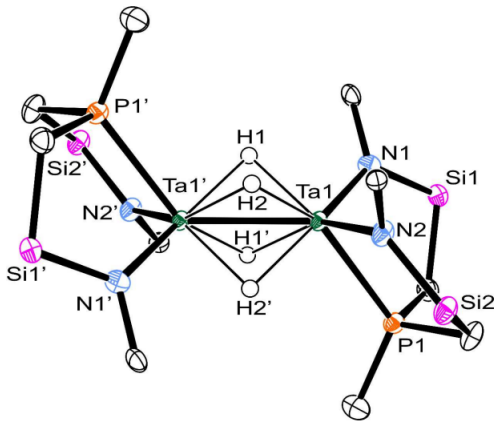

Figure A.1: ORTEP plot (30% thermal ellipsoids) of the molecular structure of **2.1** (*refinement incomplete*). Silyl-methyl and ligand N,P-phenyl-ring carbons (except ipso positions) have been omitted for clarity. Selected bond lengths (Å, rounded to two decimal places) and angles (°, rounded to integer values): Ta1-Ta1′ 2.57; Ta1-N1 2.08; Ta1-N2 2.09; Ta1-P1 2.56; Ta-H ranging from 1.87 to 1.92; N1-Ta1-N2 113; H-Ta-H (*cis*) 61 to 64; H-Ta-H (*trans*) 91 to 94; P1-Ta1-Ta1-P1 180; H1-H1-H2-H2 0.

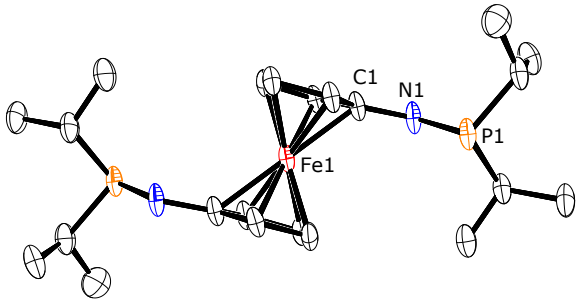

Figure A.2: ORTEP diagram of **1.50** with ellipsoids drawn at 50% probability. All H atoms have been omitted for clarity. elected bond lengths (Å) and angles (deg): C1-N1 1.4021(4); N1-P1 1.7130(3). Cp plane angle = 0° due to inversion center at Fe1

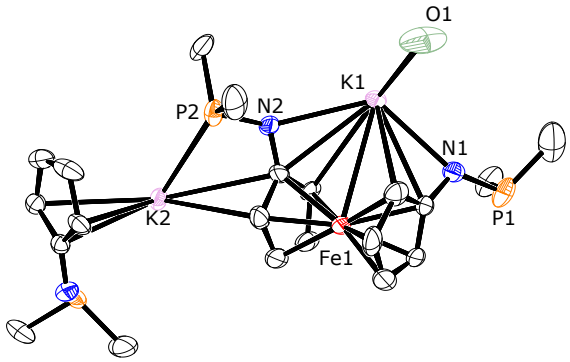

Figure A.3: ORTEP diagram of **3.1** with ellipsoids drawn at 50% probability. All H atoms, ^{i}Pr methyl groups and carbons from the THF molecules have been omitted for clarity. The figure represents 1/3 of the asymmetric unit with an extra Cp ring shown to illustrate connectivity. Refinement not complete.

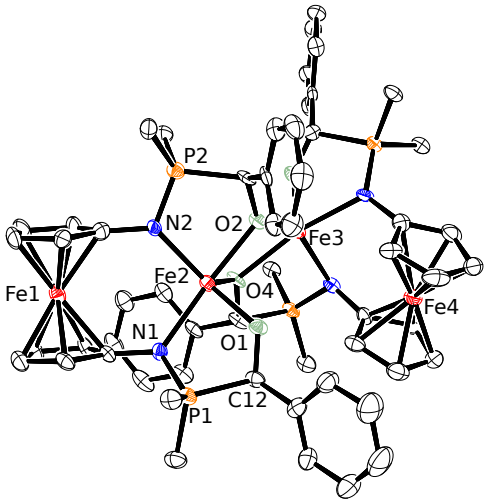

Figure A.4: ORTEP diagram of **4.8** with ellipsoids drawn at 50% probability. All H atoms and ^{i}Pr methyl groups have been omitted for clarity. Selected bond lengths (Å) and angles (deg): Fe1-Fe2 4.0122(11); Fe2-Fe3 3.3087(11); N1-P1 1.607(4); N2-P2 1.618(4); P1-C12 1.857(5); Fe2-N1 2.239(4); Fe2-N2 2.108(4); Fe2-O1 1.987(4); Fe2-O2 2.132(4); Fe3-O2 2.040(3); Fe2-O3 2.077(3); Fe3-O3 2.177(4); P1-C12-O1 105.7(4); N1-Fe2-O1 81.13(15); O2-Fe2-N1 170.87(14); O2-Fe2-O1 91.90(14); Fe2-O2-Fe3 104.92(15); Fe2-O3-Fe3 102.09(14).

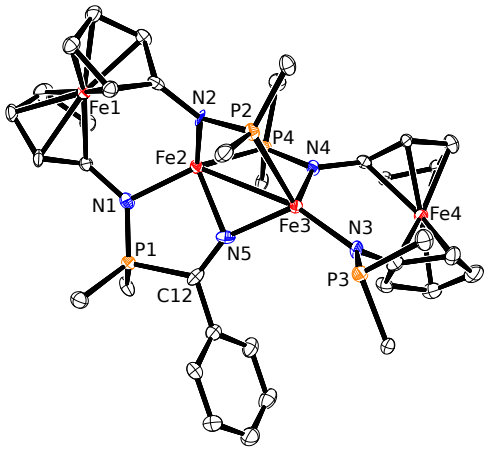

Figure A.5: ORTEP diagram of **4.9** with ellipsoids drawn at 50% probability. All H atoms and ^{i}Pr methyl groups have been omitted for clarity. Selected bond lengths (Å) and angles (deg): Fe1-Fe2 3.4980(14); Fe2-Fe3 2.8932(13); Fe3-Fe4 3.7358(14); N1-P1 1.600(5); N2-P2 1.656(5); N3-P3 1.682(5); N4-P4 1.656(5); Fe2-N1 2.017(5); Fe2-N2 1.935(5); Fe2-P4 2.4187(19); Fe2-N5 2.008(5); Fe3-N3 1.972(5); Fe3-N4 2.021(5); Fe3-P2 2.5703(19); Fe3-N5 2.011(5); Fe2-N5-Fe3 92.1(2); N1-Fe2-N2 112.7(2); N1-Fe2-N5 87.6(2); N2-Fe2-P4 109.56(14); N3-Fe3-N4 112.0(2); N3-Fe3-N5 122.8(2); N3-Fe3-P2 120.85(6).

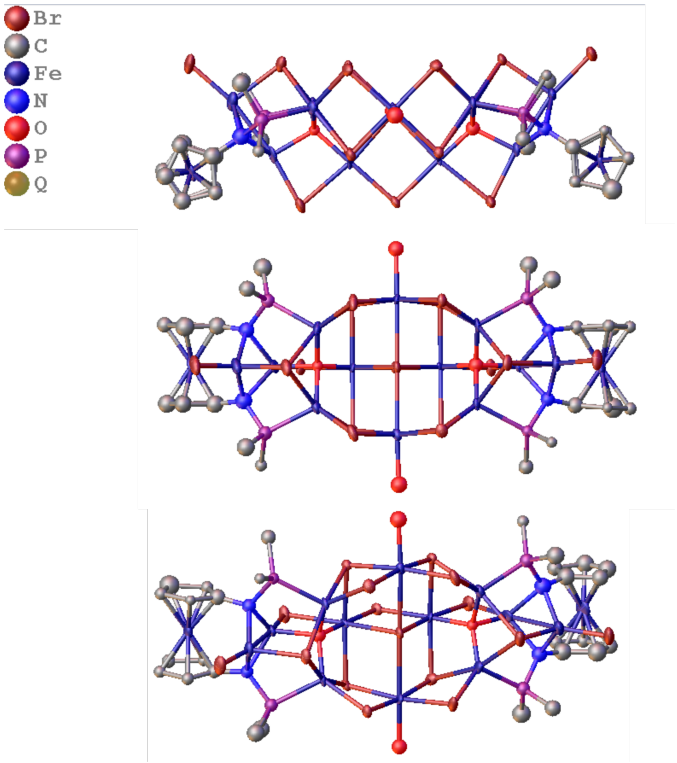

Figure A.6: ORTEP plot (30% thermal ellipsoids) of **5.3** All H atoms and ^{i}Pr methyl groups have been omitted for clarity.

Table A.1: Crystal data and refinement details for **2.5**

Compound	**2.5**
empirical formula	$C_{49}H_{64}N_4O_2P_2Si_4Ta_2$
formula weight	1277.24
crystal size [mm]	0.18 x 0.16 x 0.10
crystal system	monoclinic
space group	*C2/c* (No. 15)
a [Å]	22.1884(16)
b [Å]	11.7359(9)
c [Å]	25.096(2)
α [°]	90
β [°]	97.377(2)
γ [°]	90
V [Å^3]	6480.9(9)
ρ [g cm^3]	1.309
Z	4
$F(000)$	2356
μ [mm^{-1}]	3.531 (Mo-Kα)
T_{min}/T_{max}	0.431/0.702
hkl range	-22 – 26, $\pm$13, $\pm$ 29
θ range [°]	1.64 – 25.02
meassured refl.	21114
unique refl.	5695
refined parameters	285
completeness to θ [%]	99.9
goodness-of-fit	0.966
$R1$, $wR2$ ($I > 2\sigma(I)$)	0.0519, 0.1245
$R1$, $wR2$ (all data)	0.0737, 0.1328
res. el. dens. [e- Å^3]	4.172/-1.544

Table A.2: Crystal data and refinement details for **1.50** and **3.1**

Compound	**1.50**	**3.1**
empirical formula	$C_{22}H_{38}FeN_2P_2$	$C_{26}H_{36}FeK_2N_2OP_2$
formula weight	448.34	588.58
crystal size [mm]	0.44 x 0.20 x 0.18	0.17 x 0.16 x 0.08
crystal system	monoclinic	triclinic
space group	$C2/c$ (No. 15)	$P-1$ (No. 2)
a [Å]	18.063(5)	16.608(4)
b [Å]	14.407(4)	16.689(3)
c [Å]	10.848(3)	19.732(2)
α [°]	90.00	112.329(11)
β [°]	122.754(5)	106.485(3)
γ [°]	90.00	106.206(4)
V [Å^3]	2374.0(12)	5147.9(11)
ρ [g cm^3]	1.254	1.138
Z	4	8
$F(000)$	960	1846
μ [mm^{-1}]	0.779 (Mo-Kα)	0.789 (Mo-Kα)
T_{min}/T_{max}	0.3763 / 0.7452	0.6120 / 0.7460
hkl range	$\pm$ 21, $\pm$ 17, $\pm$ 12	$\pm$ 23, -23 – 25, $\pm$ 27
θ range [°]	1.95 – 25.10	1.242 – 30.149
meassured refl.	14339	27690
unique refl.	1858	27690
refined parameters	132	848
completeness to θ [%]	98.6	91.1
goodness-of-fit	1.091	1.024
$R1$, $wR2$ ($I > 2\sigma(I)$)	0.0737, 0.2029	0.1165, 0.2644
$R1$, $wR2$ (all data)	0.0786, 0.2084	0.1452, 0.2771
res. el. dens. [e- Å^3]	1.586/-0.891	3.3284/-2.43

Table A.3: Crystal data and refinement details for **3.2** and **3.3**

Compound	**3.2**	**3.3**
empirical formula	$C_{22}H_{36}Fe_2N_2P_2$	$C_{36}H_{56}Fe_2N_6P_2$
formula weight	502.17	746.51
crystal size [mm]	0.22 x 0.20 x 0.14	0.14 x 0.10 x 0.05
crystal system	monoclinic	monoclinic
space group	$P21/n$ (No. 14)	$C2/c$ (No. 15)
a [Å]	10.3912(8)	21.5781(11)
b [Å]	12.2273(10)	10.6543(5)
c [Å]	19.1171(15)	17.4825(8)
α [°]	90.00	90.00
β [°]	96.112(2)	112.2320(10)
γ [°]	90.00	90.00
V [Å^3]	2415.1(3)	3720.4(3)
ρ [g cm^3]	1.381	1.333
Z	4	4
$F(000)$	1056	1584
μ [mm^{-1}]	1.344 (Mo-Kα)	0.900 (Mo-Kα)
T_{min}/T_{max}	0.6139 / 0.7456	0.6633 / 0.7459
hkl range	-12 – 13, -15 – 10, $\pm$ 24	$\pm$ 29, $\pm$ 14, $\pm$ 24
θ range [°]	1.98 – 27.59	2.04 – 29.45
meassured refl.	21051	19671
unique refl.	5580	5155
refined parameters	253	215
completeness to θ [%]	99.6	99.5
goodness-of-fit	1.026	1.023
$R1$, $wR2$ ($I > 2\sigma(I)$)	0.0237, 0.0599	0.0348, 0.0785
$R1$, $wR2$ (all data)	0.0292, 0.0634	0.0568, 0.0872
res. el. dens. [e- Å^3]	0.521 / -0.266	0.710 / -0.313

Table A.4: Crystal data and refinement details for **3.4** and **3.7**

Compound	**3.4**	**3.7**
empirical formula	$C_{22}H_{36}CoFeN_2P_2$	$C_{22}H_{36}FeN_2P_2$
formula weight	505.25	446.32
crystal size [mm]	0.10 x 0.08 x 0.07	0.25 x 0.11 x 0.05
crystal system	monoclinic	monoclinic
space group	$P21/n$ (No. 14)	$P21$ (No. 4)
a [Å]	9.969(5)	9.745(2)
b [Å]	12.244(5)	10.920(3)
c [Å]	19.170(5)	10.448(3)
α [°]	90.00	90.00
β [°]	98.468(5)	91.151(5)
γ [°]	90.00	90.00
V [Å^3]	2314.4(16)	1111.7(5)
ρ [g cm^3]	1.450	1.333
Z	4	2
$F(000)$	1060	476
μ [mm^{-1}]	1.492 (Mo-Kα)	0.832 (Mo-Kα)
T_{min}/T_{max}	0.6585 / 0.7456	0.6435 / 0.7453
hkl range	$\pm$ 12, $\pm$ 15 , $\pm$ 24	-11 – 12, $\pm$ 13, $\pm$ 12
θ range [°]	1.98 – 27.52	1.95 – 26.14
meassured refl.	18977	15384
unique refl.	5307	4391
refined parameters	253	252
completeness to θ [%]	99.5	99.5
goodness-of-fit	1.014	1.065
$R1$, $wR2$ ($I > 2\sigma(I)$)	0.0354, 0.0674	0.0338, 0.0807
$R1$, $wR2$ (all data)	0.0601, 0.0751	0.0373, 0.0824
res. el. dens. [e- Å^3]	0.618 / -0.359	0.776 / -0.321

Table A.5: Crystal data and refinement details for **3.11** and **4.1**

Compound	**3.11**	**4.1**
empirical formula	$C_{20}H_{37}NNiP_2$, 0.5(C_5H_{12})	$C_{26}H_{36}Fe_2N_2O_4P_2$
formula weight	444.19	614.21
crystal size [mm]	0.31 x 0.09 x 0.06	0.10 x 0.10 x 0.05
crystal system	monoclinic	monoclinic
space group	$P21/n$ (No. 14)	$C2/c$ (No. 15)
a [Å]	15.919(5)	23.955(5)
b [Å]	8.787(3)	11.231(4)
c [Å]	17.620(6)	9.830(4)
α [°]	90.00	90.00
β [°]	97.814(8)	90.664(5)
γ [°]	90.00	90.00
V [Å^3]	2441.9(14)	2644.5(19)
ρ [g cm^3]	1.208	1.543
Z	4	4
F(000)	956	1280
μ [mm^{-1}]	0.933 (Mo-Kα)	1.254 (Mo-Kα)
T_{min}/T_{max}	0.761/0.946	0.6617/0.7460
hkl range	$\pm$ 19, $\pm$ 10, -21 – 19	$\pm$ 33, $\pm$ 15, $\pm$ 13
θ range [°]	1.854 – 26.234	1.700 – 30.026
meassured refl.	18629	27810
unique refl.	4872	3855
refined parameters	243	163
completeness to θ [%]	99.1	99.8
goodness-of-fit	1.028	1.045
$R1$, $wR2$ ($I > 2\sigma(I)$)	0.0411, 0.0912	0.0228, 0.0592
$R1$, $wR2$ (all data)	0.0663, 0.1014	0.0269, 0.0610
res. el. dens. [e- Å^3]	0.840/-0.510	0.486/-0.267

Table A.6: Crystal data and refinement details for **4.2** and **4.3**

Compound	**4.2**	**4.3**
empirical formula	$C_{45}H_{72}Fe_4N_4OP_4$	$0.5(C_{29}H_{44}Fe_2I_4N_2P_2)$
formula weight	1032.34	550.95
crystal size [mm]	0.18 x 0.15 x 0.12	0.06 x 0.06 x 0.02
crystal system	triclinic	monoclinic
space group	$P-1$ (No. 2)	Cc (No. 9)
a [Å]	13.920(3)	14.8284(13)
b [Å]	14.903(7)	17.0000(15)
c [Å]	16.3381(11)	14.5439(13)
α [°]	109.772(4)	90
β [°]	101.935(4)	90.654(2)
γ [°]	106.720(5)	90
V [Å^3]	2884.3(17)	3666.0(6)
ρ [g cm^3]	1.189	1.996
Z	2	8
$F(000)$	1084	2104
μ [mm^{-1}]	1.128 (Mo-Kα)	4.268 (Mo-Kα)
T_{min}/T_{max}	0.6980/0.7458	0.6284/0.7453
hkl range	$\pm$ 18, $\pm$ 20, $\pm$ 22	-18 – 10, $\pm$ 20, $\pm$ 17
θ range [°]	1.751 – 28.729	1.822 – 26.099
meassured refl.	56376	26127
unique refl.	14822	6304
refined parameters	548	302
completeness to θ [%]	99.2	99.8
goodness-of-fit	1.007	1.136
$R1$, $wR2$ ($I > 2\sigma(I)$)	0.0317, 0.0719	0.0243, 0.0572
$R1$, $wR2$ (all data)	0.0534, 0.0811	0.0252, 0.0575
res. el. dens. [e- Å^3]	0.443/-0.443	0.564/-0.507

Table A.7: Crystal data and refinement details for **4.4** and **4.5**

Compound	**4.4**	**4.5**
empirical formula	$C_{68}H_{120}Fe_4KN_4O_6P_4$	$C_{34}H_{46}Fe_2N_4P_2$
formula weight	1475.24	684.39
crystal size [mm]	0.23 x 0.05 x 0.05	0.12 x 0.11 x 0.08
crystal system	monoclinic	monoclinic
space group	$P21/c$ (No. 14)	$P21/n$ (No. 14)
a [Å]	14.292(3)	13.6777(7)
b [Å]	21.153(5)	13.5134(6)
c [Å]	24.731(6)	17.7979(8)
α [°]	90	90
β [°]	91.213(5)	94.0140(10)
γ [°]	90	90
V [Å^3]	7475(3)	3281.6(3)
ρ [g cm^3]	1.311	1.385
Z	4	4
$F(000)$	3145	1440
μ [mm^{-1}]	0.951 (Mo-Kα)	1.011 (Mo-Kα)
T_{min}/T_{max}	0.6530/0.7456	0.6760/0.7456
hkl range	-18 – 17, -26 – 27, ± 32	± 17, ± 17, ± -23 – 15
θ range [°]	1.720 – 27.548	1.818 – 27.503
meassured refl.	68997	30760
unique refl.	17128	7523
refined parameters	792	563
completeness to θ [%]	99.5	99.9
goodness-of-fit	0.985	1.022
$R1$, $wR2$ ($I > 2\sigma(I)$)	0.0482, 0.0958	0.0279, 0.0638
$R1$, $wR2$ (all data)	0.0917, 0.1123	0.0372, 0.0675
res. el. dens. [e- Å^3]	0.980/-1.005	0.421/-0.236

Table A.8: Crystal data and refinement details for **4.7** and **4.8**

Compound	**4.7**	**4.8**
empirical formula	$C_{34}H_{55}N_3P_3Fe_{2.5}$	$C_{73.5}H_{99.5}Fe_4N_4O_4P_4$
formula weight	770.34	1450.85
crystal size [mm]	0.29 x 0.18 x 0.08	0.24 x 0.11 x 0.07
crystal system	Monoclinic	Triclinic
space group	$C2/c$ (No. 15)	$P-1$ (No. 2)
a [Å]	18.292(3)	13.1417(11)
b [Å]	28.392(4)	23.350(2)
c [Å]	18.367(4)	27.418(2)
α [°]	90	88.065(2)
β [°]	116.591(2)	76.473(2)
γ [°]	90	81.651(3)
V [Å^3]	8530(2)	8093.3(12)
ρ [g cm^3]	1.200	1.191
Z	8	4
$F(000)$	3248	3060
μ [mm^{-1}]	0.985 (Mo-Kα)	0.826 (Mo-Kα)
T_{min}/T_{max}	0.6054/0.7452	0.6368/0.7452
hkl range	-21 – 22, -34 – 20, -22 – 20	$\pm$ 15, $\pm$ 27, $\pm$ 32
θ range [°]	1.490 – 25.390	1.166 – 25.159
meassured refl.	22830	103776
unique refl.	7774	28748
refined parameters	418	1633
completeness to θ [%]	99.1	99.0
goodness-of-fit	1.163	0.981
$R1$, $wR2$ ($I > 2\sigma(I)$)	0.0584, 0.1569	0.0645, 0.1259
$R1$, $wR2$ (all data)	0.0895, 0.1740	0.1384, 0.1516
res. el. dens. [e- Å^3]	1.134/-0.584	0.666/-0.479

Table A.9: Crystal data and refinement details for **4.9**

Compound	**4.9**
empirical formula	$C_{57}H_{91}Fe_4N_5P_4$
formula weight	1193.62
crystal size [mm]	0.18 x 0.11 x 0.07
crystal system	monoclinic
space group	$P21/c$ (No. 14))
a [Å]	14.1719(3)
b [Å]	31.7623(6)
c [Å]	13.7659(3)
α [°]	90
β [°]	110.7260(10)
γ [°]	90
V [Å^3]	5791.7(2)
ρ [g cm^3]	1.369
Z	4
$F(000)$	2528
μ [mm^{-1}]	9.225 (Cu-Kα)
T_{min}/T_{max}	0.4185/0.7530
hkl range	$\pm$ 16, $\pm$ 37, -15 – 16
θ range [°]	2.782 – 67.860
meassured refl.	43002
unique refl.	10186
refined parameters	649
completeness to θ [%]	97.2
goodness-of-fit	1.007
$R1$, $wR2$ ($I > 2\sigma(I)$)	0.0722, 0.1731
$R1$, $wR2$ (all data)	0.1239, 0.2045
res. el. dens. [e- Å^3]	0.948/-0.858

Appendix B

Computational Appendix

Table B.1 Optimized xyz coordinated for **3.2**

C	-3.69183100	-3.04030900	3.61032100
H	-4.43243700	-3.63115700	3.04283000
C	-3.76036400	-3.44043100	5.09624600
H	-3.66095200	-4.52693500	5.24577400
H	-4.72679500	-3.13343900	5.53263300
H	-2.96350700	-2.94465700	5.67778200
C	-4.00660600	-1.54569500	3.43233300
H	-3.90886100	-1.22990800	2.38124300
H	-3.32081200	-0.92358600	4.03254200
H	-5.03605200	-1.32183200	3.76285900
Fe	-1.10130300	-1.57670500	0.52167400
Fe	-3.52181300	-3.08340100	-1.54606500
P	-1.96076900	-3.40926900	2.91340300
P	1.04009300	-0.91509700	1.48280100
N	1.46852000	0.71745700	1.17848500
N	-2.05902400	-3.08290000	1.21595000
C	-4.93221900	-4.34630400	-0.77496800
H	-5.97120500	-4.39475800	-1.09676900
C	2.46372900	1.35023000	1.96680900
C	1.02704500	-1.22659100	3.34458900
H	0.58351800	-2.24026900	3.37963600
C	-2.97589500	-3.71423100	0.34859200

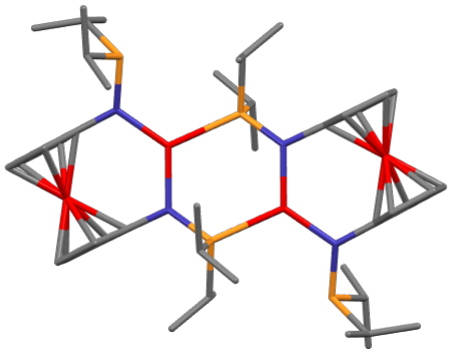

C	3.89670200	1.12201300	1.95155400
H	4.41763200	0.43471500	1.28821900
C	4.50212400	1.96443900	2.94669200
H	5.56602800	2.02912200	3.16878700
C	-1.88690200	-5.30495000	3.12753900
H	-1.76998800	-5.38885100	4.22589100
C	-4.40487000	-3.48797700	0.24945400
H	-4.97125100	-2.77156600	0.83999000
C	-3.11505700	-6.13148600	2.70829600
H	-4.03902700	-5.79085000	3.20095400
H	-2.96755200	-7.19112200	2.98550900
H	-3.27918800	-6.09156500	1.62115500
C	-2.63734200	-4.69948300	-0.66029000
H	-1.63077600	-5.06114300	-0.86094100
C	3.46262600	2.74652000	3.56167600
H	3.60510500	3.50647400	4.32812800
C	2.21467000	2.38390600	2.95119700
H	1.23706400	2.81076700	3.16535900
C	2.37892700	-1.24454300	4.07870600
H	3.10748300	-1.92236800	3.60764400
H	2.22147200	-1.60222400	5.11165100
H	2.83188000	-0.24485300	4.13765200
C	2.46149800	-1.99392000	0.85392500
H	3.37237000	-1.67200000	1.38927400
C	0.01918700	-0.28438000	4.02231200
H	-0.96464700	-0.32662800	3.52778300
H	0.37135000	0.75752900	4.01199900
H	-0.12608700	-0.58654800	5.07335900
C	2.64962200	-1.75550800	-0.65218600
H	2.83833400	-0.69122000	-0.87532700
H	1.75152300	-2.06416800	-1.21365200
H	3.50702300	-2.33671100	-1.03250500
C	2.18189300	-3.47457800	1.15621700
H	2.17142100	-3.68594300	2.23651500
H	2.95483800	-4.11417600	0.69661400
H	1.20301600	-3.77707800	0.74642200
C	-0.59849600	-5.84730700	2.48675200
H	0.29220200	-5.30623500	2.84279100
H	-0.63197700	-5.75437200	1.38987300
H	-0.46614500	-6.91613600	2.72897300

C	-3.83998500	-5.09442900	-1.33754900
H	-3.90989500	-5.80777400	-2.15706200
C	3.69183100	3.04030900	-3.61032100
H	4.43243700	3.63115700	-3.04283000
C	3.76036400	3.44043100	-5.09624600
H	3.66095200	4.52693500	-5.24577400
H	4.72679500	3.13343900	-5.53263300
H	2.96350700	2.94465700	-5.67778200
C	4.00660600	1.54569500	-3.43233300
H	3.90886100	1.22990800	-2.38124300
H	3.32081200	0.92358600	-4.03254200
H	5.03605200	1.32183200	-3.76285900
Fe	1.10130300	1.57670500	-0.52167400
Fe	3.52181300	3.08340100	1.54606500
P	1.96076900	3.40926900	-2.91340300
P	-1.04009300	0.91509700	-1.48280100
N	-1.46852000	-0.71745700	-1.17848500
N	2.05902400	3.08290000	-1.21595000
C	4.93221900	4.34630400	0.77496800
H	5.97120500	4.39475800	1.09676900
C	-2.46372900	-1.35023000	-1.96680900
C	-1.02704500	1.22659100	-3.34458900
H	-0.58351800	2.24026900	-3.37963600
C	2.97589500	3.71423100	-0.34859200
C	-3.89670200	-1.12201300	-1.95155400
H	-4.41763200	-0.43471500	-1.28821900
C	-4.50212400	-1.96443900	-2.94669200
H	-5.56602800	-2.02912200	-3.16878700
C	1.88690200	5.30495000	-3.12753900
H	1.76998800	5.38885100	-4.22589100
C	4.40487000	3.48797700	-0.24945400
H	4.97125100	2.77156600	-0.83999000
C	3.11505700	6.13148600	-2.70829600
H	4.03902700	5.79085000	-3.20095400
H	2.96755200	7.19112200	-2.98550900
H	3.27918800	6.09156500	-1.62115500
C	2.63734200	4.69948300	0.66029000
H	1.63077600	5.06114300	0.86094100
C	-3.46262600	-2.74652000	-3.56167600
H	-3.60510500	-3.50647400	-4.32812800

C	-2.21467000	-2.38390600	-2.95119700
H	-1.23706400	-2.81076700	-3.16535900
C	-2.37892700	1.24454300	-4.07870600
H	-3.10748300	1.92236800	-3.60764400
H	-2.22147200	1.60222400	-5.11165100
H	-2.83188000	0.24485300	-4.13765200
C	-2.46149800	1.99392000	-0.85392500
H	-3.37237000	1.67200000	-1.38927400
C	-0.01918700	0.28438000	-4.02231200
H	0.96464700	0.32662800	-3.52778300
H	-0.37135000	-0.75752900	-4.01199900
H	0.12608700	0.58654800	-5.07335900
C	-2.64962200	1.75550800	0.65218600
H	-2.83833400	0.69122000	0.87532700
H	-1.75152300	2.06416800	1.21365200
H	-3.50702300	2.33671100	1.03250500
C	-2.18189300	3.47457800	-1.15621700
H	-2.17142100	3.68594300	-2.23651500
H	-2.95483800	4.11417600	-0.69661400
H	-1.20301600	3.77707800	-0.74642200
C	0.59849600	5.84730700	-2.48675200
H	-0.29220200	5.30623500	-2.84279100
H	0.63197700	5.75437200	-1.38987300
H	0.46614500	6.91613600	-2.72897300
C	3.83998500	5.09442900	1.33754900
H	3.90989500	5.80777400	2.15706200

Table B.2 Optimized xyx coordinates for **3.4**

Co	1.19084800	1.75658600	-0.35145100
Fe	3.16981200	2.88394300	1.39634600
P	0.61484800	-1.06375300	1.36118100
P	1.92220200	3.60908000	-3.11667800
N	1.86988400	3.13178300	-1.44631300
N	1.08396100	0.56378000	1.07649400
C	2.07394200	1.16603600	1.86466300
C	2.76536000	3.65374300	-0.50686700
C	1.84929100	2.23851000	2.82256500
H	0.88037500	2.68640600	3.02921300
C	4.17312400	3.32184400	-0.33012700
H	4.72634900	2.60411500	-0.93018000
C	-0.34165800	-0.32236200	3.90192500
H	-1.30242000	-0.27636200	3.36768800
H	-0.54429100	-0.65363900	4.93490400
H	0.07574300	0.69438500	3.94778800
C	1.83577200	-3.60619200	1.05520700
H	1.72567700	-3.80903000	2.13147400
H	0.91508100	-3.95275600	0.55885900
H	2.68179300	-4.20899300	0.68158500
C	2.07260200	-2.11780200	0.76077900
H	2.94738000	-1.77022500	1.33927600
C	1.98701200	-1.34797700	3.95555400
H	2.69167600	-2.06031300	3.49989700
H	2.47566400	-0.36448700	4.00200800
H	1.81580800	-1.68175700	4.99446400
C	1.93919500	5.52052000	-3.15064600
H	1.93063700	5.70003600	-4.24381400
C	3.14263900	6.27057400	-2.55432500
H	4.10187800	5.93298700	-2.97596900
H	3.05522000	7.35191500	-2.76584600
H	3.19464800	6.15128600	-1.46200200
C	3.10064500	2.58480600	3.42166300
H	3.26024300	3.35789800	4.17136100
C	0.61161300	6.06134200	-2.59396200
H	-0.25524000	5.58018600	-3.07376800

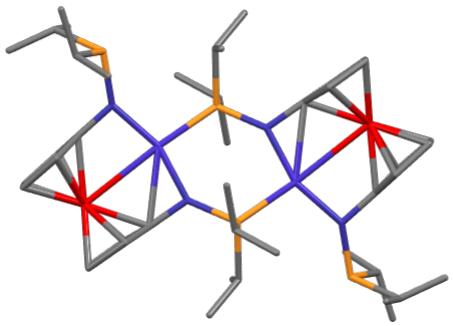

H	0.53351300	5.88537200	-1.50950700
H	0.53404800	7.14948100	-2.76371400
C	0.63230900	-1.30146700	3.22665800
H	0.16785300	-2.30286800	3.30851600
C	2.43156200	4.59983700	0.55040500
H	1.44003500	5.01574800	0.71354500
C	3.70466600	3.25298400	-3.68746800
H	4.40762400	3.75995500	-3.00276100
C	3.51251500	0.92356900	1.84554700
H	4.01958500	0.20966600	1.20080700
C	4.68979500	4.09564800	0.75725000
H	5.70983900	4.06453800	1.13671300
C	4.12608700	1.77058800	2.82295800
H	5.19066300	1.82383800	3.04486700
C	3.91350800	3.79911500	-5.11307900
H	3.87028600	4.89853400	-5.15790300
H	4.90038200	3.49113000	-5.50073200
H	3.14929400	3.40259500	-5.80437200
C	2.33450900	-1.87043000	-0.73182700
H	2.46456100	-0.79664800	-0.94703400
H	3.24348400	-2.40783100	-1.05396600
H	1.48661700	-2.22622300	-1.33889800
C	3.61464800	4.88231100	1.30264100
H	3.68490800	5.54548100	2.16328800
C	3.97212900	1.73942400	-3.64549600
H	3.74970700	1.31028000	-2.65571500
H	3.34439400	1.21105600	-4.38213500
H	5.02748600	1.52392400	-3.88914500
Co	-1.19084800	-1.75658600	0.35145100
Fe	-3.16981200	-2.88394300	-1.39634600
P	-0.61484800	1.06375300	-1.36118100
P	-1.92220200	-3.60908000	3.11667800
N	-1.86988400	-3.13178300	1.44631300
N	-1.08396100	-0.56378000	-1.07649400
C	-2.07394200	-1.16603600	-1.86466300
C	-2.76536000	-3.65374300	0.50686700
C	-1.84929100	-2.23851000	-2.82256500
H	-0.88037500	-2.68640600	-3.02921300
C	-4.17312400	-3.32184400	0.33012700
H	-4.72634900	-2.60411500	0.93018000

C	0.34165800	0.32236200	-3.90192500
H	1.30242000	0.27636200	-3.36768800
H	0.54429100	0.65363900	-4.93490400
H	-0.07574300	-0.69438500	-3.94778800
C	-1.83577200	3.60619200	-1.05520700
H	-1.72567700	3.80903000	-2.13147400
H	-0.91508100	3.95275600	-0.55885900
H	-2.68179300	4.20899300	-0.68158500
C	-2.07260200	2.11780200	-0.76077900
H	-2.94738000	1.77022500	-1.33927600
C	-1.98701200	1.34797700	-3.95555400
H	-2.69167600	2.06031300	-3.49989700
H	-2.47566400	0.36448700	-4.00200800
H	-1.81580800	1.68175700	-4.99446400
C	-1.93919500	-5.52052000	3.15064600
H	-1.93063700	-5.70003600	4.24381400
C	-3.14263900	-6.27057400	2.55432500
H	-4.10187800	-5.93298700	2.97596900
H	-3.05522000	-7.35191500	2.76584600
H	-3.19464800	-6.15128600	1.46200200
C	-3.10064500	-2.58480600	-3.42166300
H	-3.26024300	-3.35789800	-4.17136100
C	-0.61161300	-6.06134200	2.59396200
H	0.25524000	-5.58018600	3.07376800
H	-0.53351300	-5.88537200	1.50950700
H	-0.53404800	-7.14948100	2.76371400
C	-0.63230900	1.30146700	-3.22665800
H	-0.16785300	2.30286800	-3.30851600
C	-2.43156200	-4.59983700	-0.55040500
H	-1.44003500	-5.01574800	-0.71354500
C	-3.70466600	-3.25298400	3.68746800
H	-4.40762400	-3.75995500	3.00276100
C	-3.51251500	-0.92356900	-1.84554700
H	-4.01958500	-0.20966600	-1.20080700
C	-4.68979500	-4.09564800	-0.75725000
H	-5.70983900	-4.06453800	-1.13671300
C	-4.12608700	-1.77058800	-2.82295800
H	-5.19066300	-1.82383800	-3.04486700
C	-3.91350800	-3.79911500	5.11307900
H	-3.87028600	-4.89853400	5.15790300

H	-4.90038200	-3.49113000	5.50073200
H	-3.14929400	-3.40259500	5.80437200
C	-2.33450900	1.87043000	0.73182700
H	-2.46456100	0.79664800	0.94703400
H	-3.24348400	2.40783100	1.05396600
H	-1.48661700	2.22622300	1.33889800
C	-3.61464800	-4.88231100	-1.30264100
H	-3.68490800	-5.54548100	-2.16328800
C	-3.97212900	-1.73942400	3.64549600
H	-3.74970700	-1.31028000	2.65571500
H	-3.34439400	-1.21105600	4.38213500
H	-5.02748600	-1.52392400	3.88914500

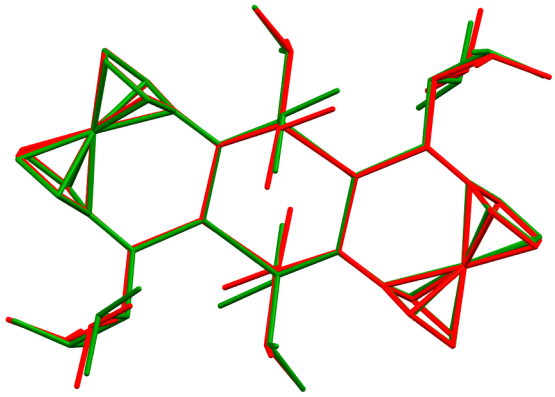

Figure B.1 Overlay of solid state molecular structure (red) and calculated geometry (green) for **3.2**

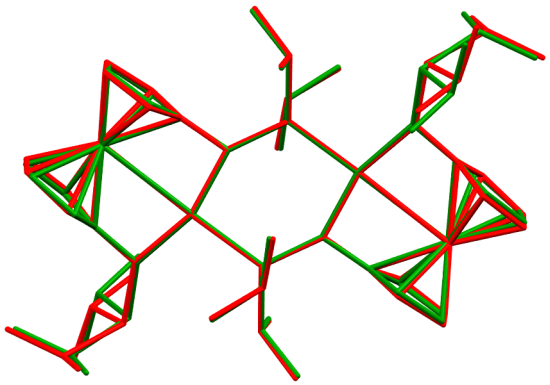

Figure B.2 Overlay of solid state molecular structure (red) and calculated geometry (green) for **3.4**

Table B.3 Comparison of calculated and experimental bond metrics for **3.2** and **3.4**. Bond lengths in Å and angles in °

Complex	Bond Metric	Calculated	Experimental
	N - P_i	1.72	1.67
	N - P_t	1.73	1.70
	Fe - N_i	1.94	1.95
	Fe - N_t	1.91	1.92
3	Fe - P	2.44	2.44
	Fe_{fc} ····· Fe	3.52	3.53
	Fe ····· Fe	3.98	3.92
	N - Fe - N	124.8	123.5
	Cp Plane Angle	2.1	0.1
	N - P_i	1.72	1.68
	N - P_t	1.74	1.70
	Co - N_i	1.86	1.85
	Co - N_t	1.88	1.88
5	Co - P	2.18	2.16
	Fe_{fc} ····· Co	2.87	2.84
	Co ····· Co	4.30	4.23
	N - Co - N	158.9	159.6
	Cp Plane Angle	8.2	6.9

Molecular Orbitals of 3.2

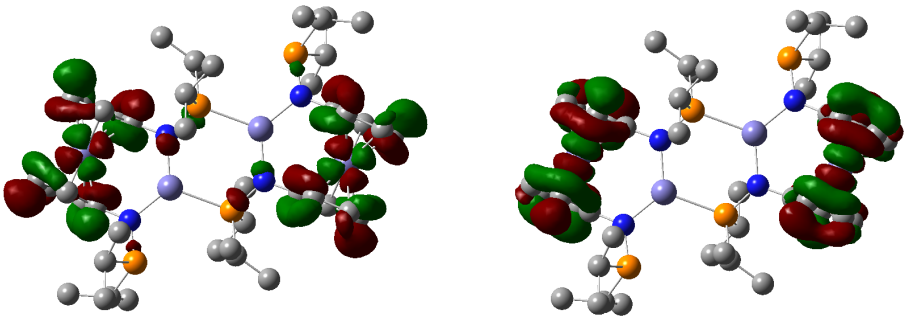

Figure B.3 LUMO$_\alpha$ (left) and LUMO+1$_\alpha$ (right) for **3.2** (Isosurface value = 0.02)

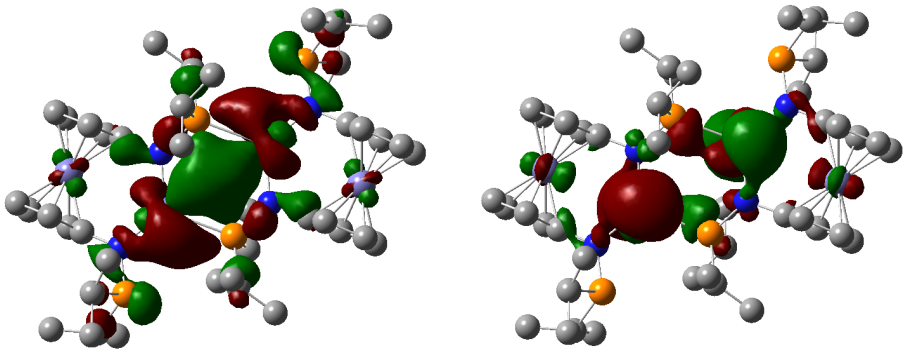

Figure B.4 LUMO$_\beta$ (left) and LUMO+1$_\beta$ (right) for **3.2** (Isosurface value = 0.02)

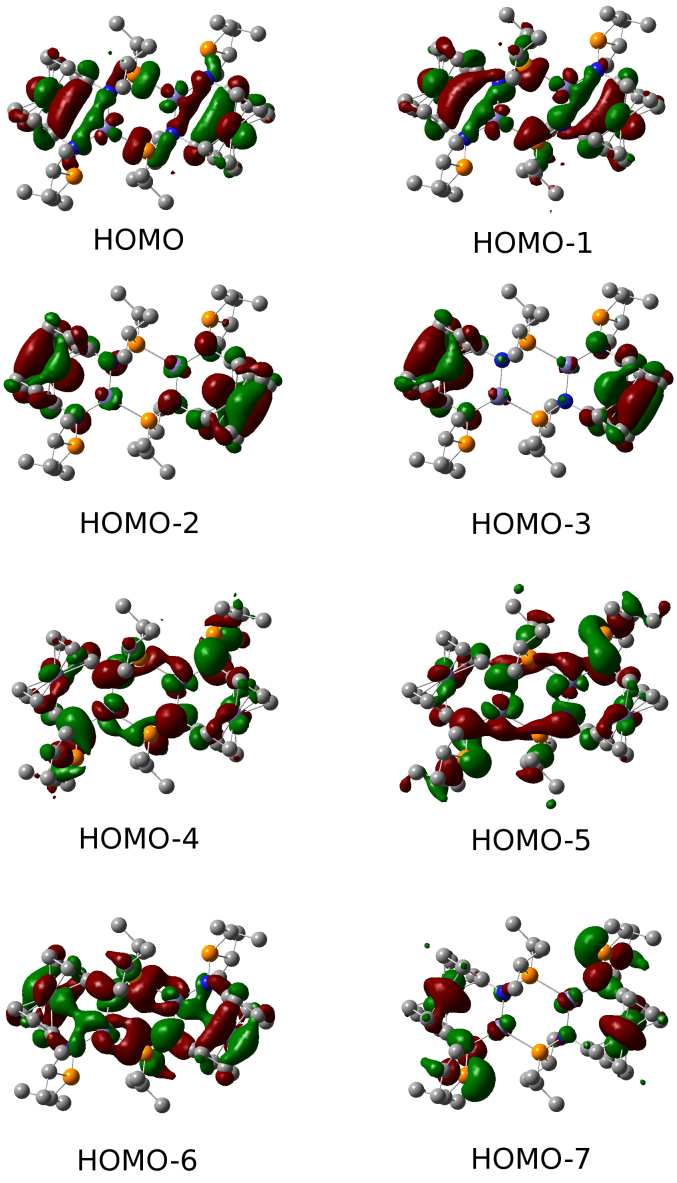

Figure B.5 HOMO$_\alpha$ to HOMO-7$_\alpha$ for **3.2** (Isosurface value = 0.02)

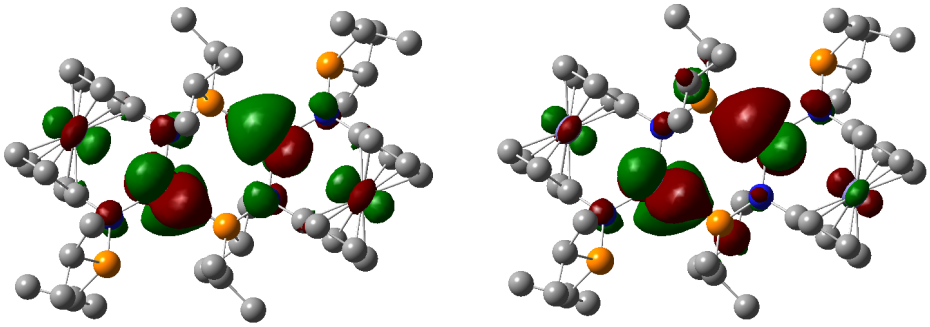

Figure B.6 HOMO$_\beta$ (left) and HOMO-1$_\beta$ (right) for **3.2** (Isosurface value = 0.02)

Molecular Orbitals of 3.4

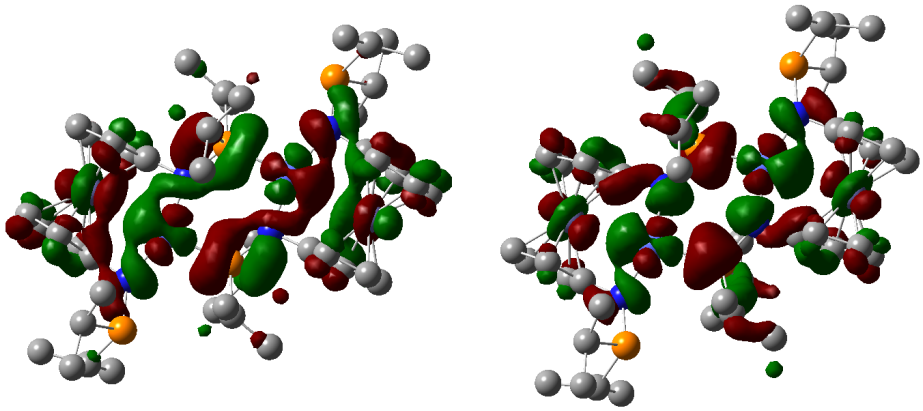

Figure B.7 LUMO$_\alpha$ (left) and LUMO+1$_\alpha$ (right) for **3.4** (Isosurface value = 0.02)

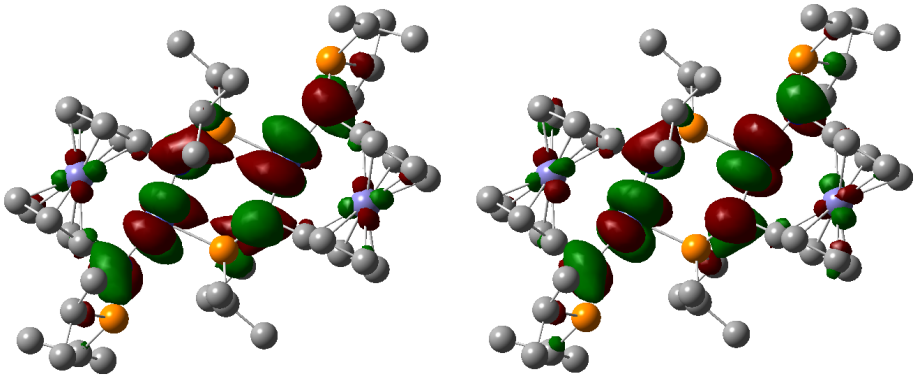

Figure B.8 LUMO$_\beta$ (left) and LUMO+1$_\beta$ (right) for **3.4** (Isosurface value = 0.02)

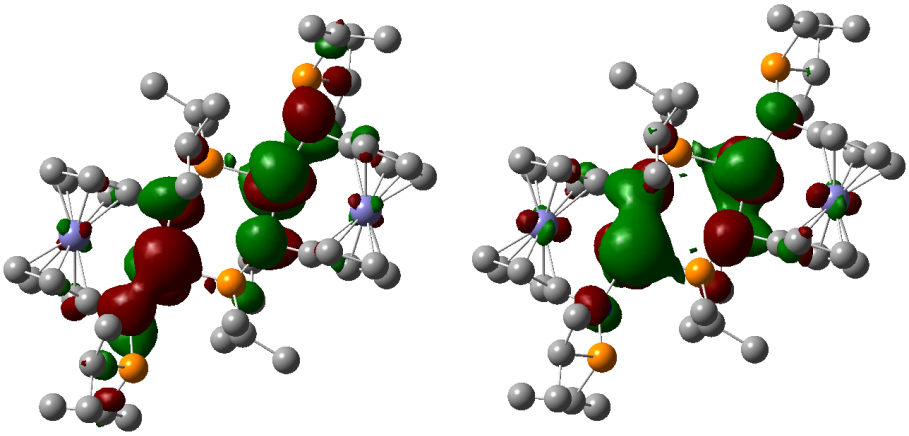

Figure B.9 HOMO$_\alpha$ (left) and HOMO-1$_\alpha$ (right) for **3.4** (Isosurface value = 0.02)

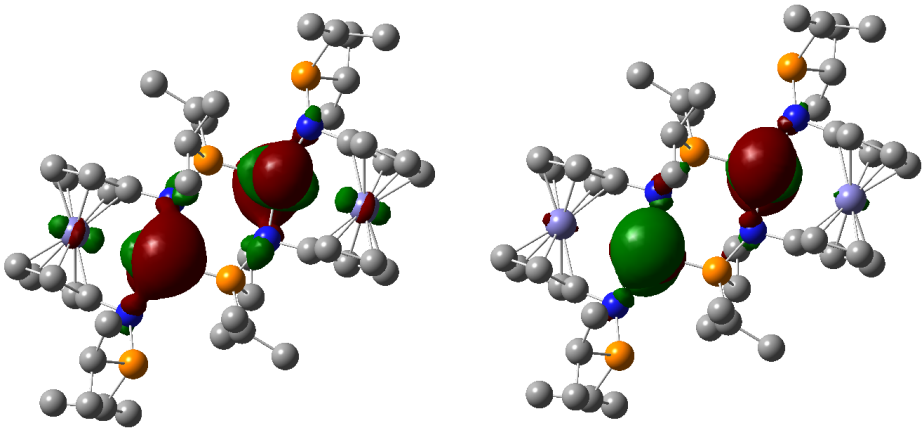

Figure B.10 HOMO$_\beta$ (left) and HOMO-1$_\beta$ (right) for **3.4** (Isosurface value = 0.02)

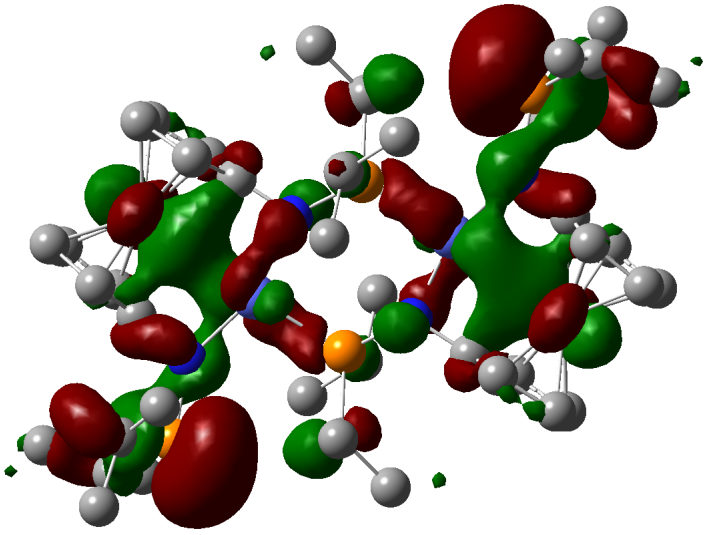

Figure B.11 HOMO-6$_\alpha$ for **3.4** (Isosurface value = 0.02)

Table B.4 Second order perturbation theory analysis of **3.4**

Spin	Donor	Acceptor	Energy (kcal/mol)
α	86. LP (2)Co 1	247. LV (1)Fe 2	1.84
β	85. LP (1)Co 1	246. LV (1)Fe 2	3.00
α	88. LP (4)Co 1	389. 3C*(1)Fe2-C7-C8	3.18
β	87. LP (3)Co 1	389. 3C*(1)Fe2-C7-C8	3.39
β	88. LP (1)Fe 2	245. LV (1)Co 1	1.16
α	89. LP (1)Fe 2	249. BD*(1)Co 1- N 6	0.99
β	88. LP (1)Fe 2	249. BD*(1)Co 1- N 6	0.94
α	89. LP (1)Fe 2	250. BD*(1)Co 1- P 67	2.33
β	88. LP (1)Fe 2	250. BD*(1)Co 1- P 67	2.37
α	107. BD (1)Co 1- N 6	247. LV (1)Fe 2	3.58
β	105. BD (1)Co 1- N 6	246. LV (1)Fe 2	2.37
α	107. BD (1)Co 1- N 6	389. 3C*(1)Fe2-C7-C8	3.15
β	105. BD (1)Co 1- N 6	389. 3C*(1)Fe2-C7-C8	3.52
α	108. BD (1)Co 1- P 67	247. LV (1)Fe 2	3.00
β	106. BD (1)Co 1- P 67	246. LV (1)Fe 2	3.39

Appendix C

Mössbauer Appendix

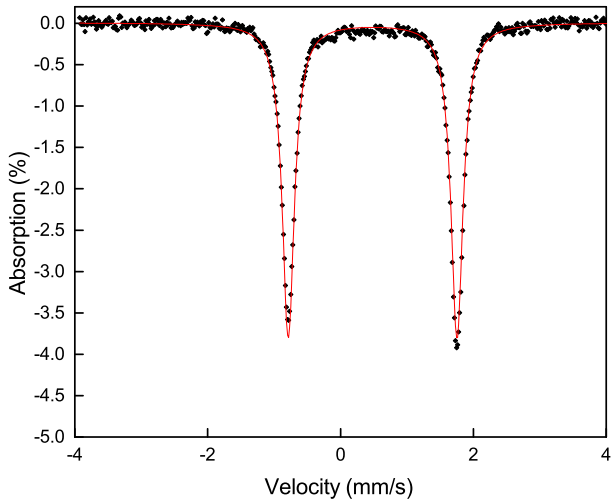

Figure C.1 Zero field ^{57}Fe Mössbauer spectra of **1.50**. See Table 3.1 for isomer shifts and quadrupole splittings.

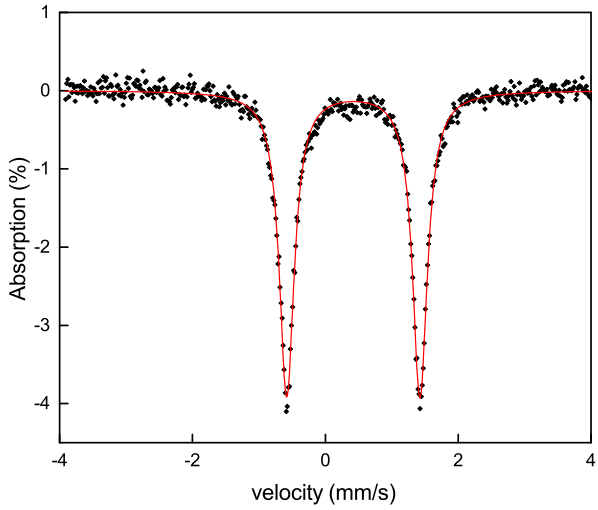

Figure C.2 Zero field ^{57}Fe Mössbauer spectra of **3.4**. δ = 0.42mm/s; ΔEq = 2.01mm/s.

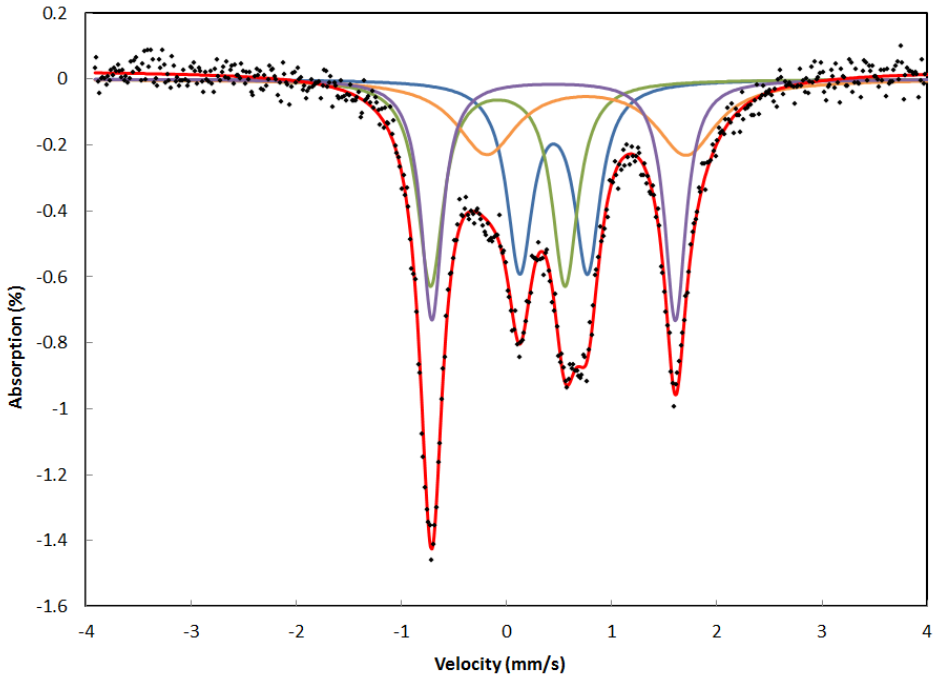

Figure C.3 Zero field ^{57}Fe Mössbauer spectra of **4.2**. Fits of the four iron centers (purple) δ = 0.45 mm/s, ΔEq = 2.31 mm/s; (green) δ = -0.08 mm/s, ΔEq = 1.29 mm/s; (orange) δ = 0.76 mm/s, ΔEq = 1.89 mm/s; (blue) δ = 0.45 mm/s, ΔEq = 0.66 mm/s.

Appendix D

SQUID Magnetometry

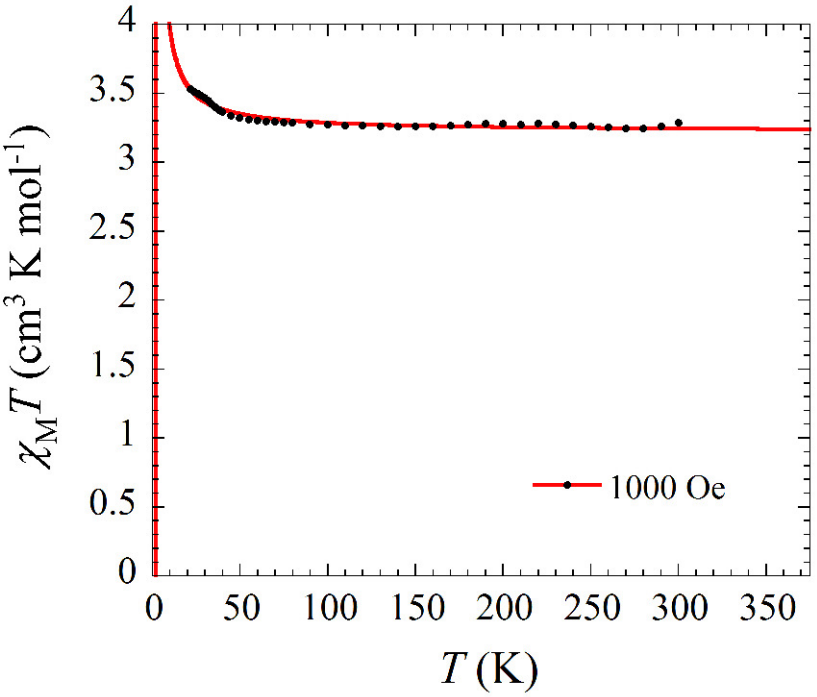

Figure D.1 Plot of $\chi_M T$ vs T for **3.4** fit with a Curie-Weiss law, C = 3.222(4) cm^3 K $mol^{-}1$ and Θ = -1.89(6) K.

Appendix E

Cyclic Voltammetry

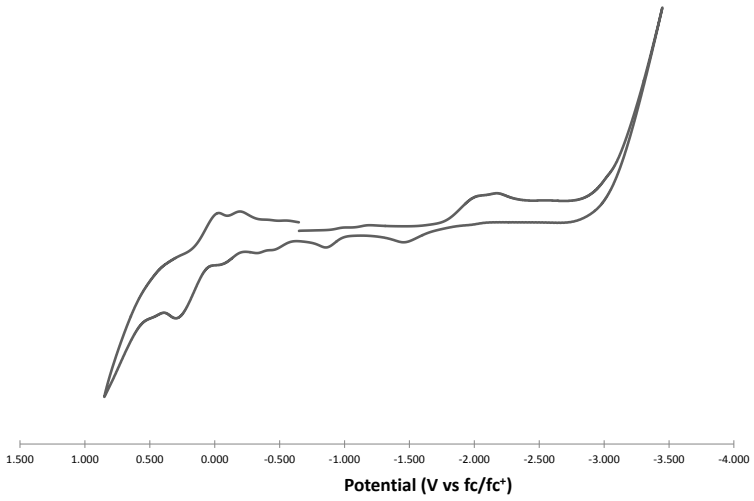

Figure E.1 Cyclic voltammogram of complex **3.2** (in 0.1 M [^{n}Bu$_4$N][PF$_6$] in THF; scan rate = 100 mv s^{-1}

Appendix F

Gas Chromatography Mass Spectrometry

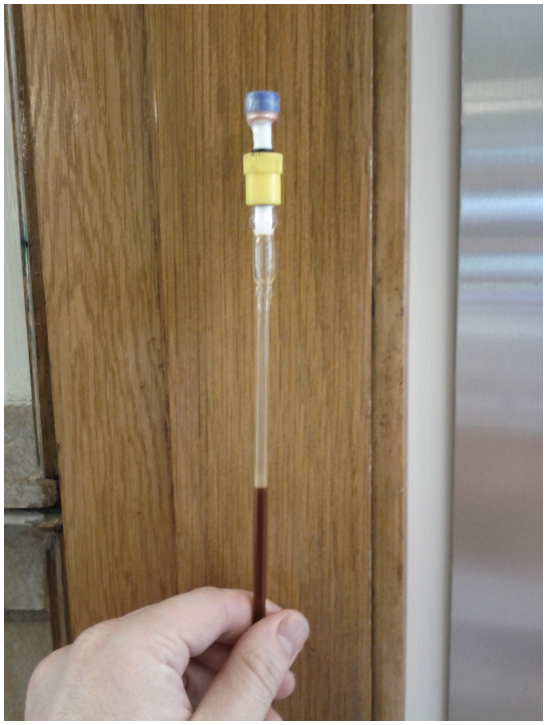

Figure F.1 Adapter used for head space analysis